U.PORTO

FEUP FACULDADE DE ENGENHARIA
UNIVERSIDADE DO PORTO

Master's Dissertation in Mechanical Engineering on:

Finite Element Model updating of a structure with sparse nonlinearities

Author

Cristiano Dias Cunha - up201605845

Supervisor at FEUP

Prof. Pedro Leal Ribeiro

Supervisor at Siemens

Eng. Giancarlo Kosova

Porto, 11th October, 2021

"There is no passion to be found playing small, in settling for a life that is less than the one you are capable of living"

Neslon Mandela

Acknowledgements

First of all I would like to thank to my company supervisor Eng. Giancarlo Kosova for all its patience, knowledge and dedication that he gave me in order to achieve the work that is presented at this thesis. Secondly, I must also refer my academical supervisor, Prof. Pedro Leal Ribeiro, that despite of all limitations associated to doing a thesis in a company located in a different country, was always available to assist and help me during this journey. Similarly, I have to thank to Siemens Digital Industry Software for the opportunity that was gave to me, for which I am very grateful, and give my congratulations for allowing so many students from different places around Europe to have this experience. It is certainly an example of what should be the collaboration between the academical and the industrial world.

Since this thesis represents the end of my journey at FEUP, Faculdade de Engenharia da Universidade do Porto, a special thanks must be given to all Professors, laboratorial personal staff and all human resources that are part of the Mestrado Integrado em Engenharia Mecanica, because they are the ones responsible for maintaining this prestigious and so well recognized course, that allows me to have today the "doors open" for what I expect to be an exciting career and adventure. As this is also a result of a long educational journey, I must also thank to all teachers and personal staff that crossed my path.

Like someone, once said, an equally or maybe more important thing than the diploma that those 5 years provide, are the human relations and the friendships that resulted from it, so I have to express my gratitude to all my friend that shared with me these 5 years. It is clear to me that the best memories at FEUP are all about the moments that I shared with them.

A special thanks must be given to my parents, Agostinho and Isabel, because without them it would have been impossible to become an Engineer and the first member of the family with superior education. Because, unlike my parents, uncles, grandparents, and so many people around the world nowadays, I was fortunate to have the possibility of fight for all my dreams and goals, and to become what I wanted to be, and that was only possible with the hard work and sacrifices of my parents.

Abstract

One of the greatest simplifications done at engineering is the approximation of many behaviours by linear functions, but in some circumstances that consideration doesn't allow a correct prediction of the phenomenon intended to be studied. In those situations, the only option is the consideration of the nonlinearities, and that unfortunately possesses some important obstacles like the unknown nature of the nonlinearity in some situations, or the high computational cost. In that context, one of the nonlinear identification techniques known as structural model updating is applied to an airplane mockup with two localized nonlinearities. Its application on this thesis evolves three different stages that are the construction of the numerical model, the characterization of the nonlinearity, and the update of the numerical model. For the second step among the different available techniques, a technique known as Acceleration Surface Method, that is based on the Restoring Force Surface method is used, and the advantages and limitations of the technique are explored and presented in different moments of this thesis. To face the second challenge, a model order reduction technique, based on Rubin and MacNeal approximations is studied, and then applied to the numerical linear model, that is later coupled with a local nonlinear data-driven model, forming consequently a hybrid nonlinear model. To validate the capacity of the reduced order model to predict and simulate the responses of the system, its results are compared with the ones obtained experimentally.

Keywords: Nonlinear dynamics; Nonlinear identification; Structural model updating; Acceleration surface method; Model order reduction.

Resumo

Uma das maiores simplificações feitas em engenharia é aproximação de diversos fenómenos por meio de funções lineares, quem em algumas circunstâncias não permitem prever de forma correta o fenómeno que se pretende estudar. Nessas situações a solução é considerar o comportamento não linear, mas tal infelizmente possui importantes obstáculos como o desconhecimento da natureza da não linearidade, em certas situações, e o elevado custo computacional. Nesse contexto, uma das técnicas da identificação não linear, conhecida por "structural model updating" é aplicado a um modelo à escala, de um avião com duas não linearidades localizadas. A sua aplicação nesta tese envolve três fases distintas que são a construção de um modelo numérico, a caracterização da não linearidade, e a atualização do modelo numérico. Para a segunda etapa, dentro das diferentes alternativas existentes, foi adotada uma técnica conhecida por Método da Superfície de Aceleração que é baseado no método da Superfície da Força de Restauração, a para esse método as vantagens e limitações da sua utilização são exploradas e apresentadas em diversos momentos ao longo desta tese. Para enfrentar o segundo desafio, uma técnica de "model order reduction" baseada nas aproximações de Rubin e MacNeal é estudada, e posteriormente aplicada ao modelo numérico linear, que posteriormente é acoplado com o modelo local não linear baseado em dados experimentais, obtendo-se consequentemente um modelo não linear híbrido. Para validar a capacidade do modelo de ordem reduzida em prever e simular as respostas do sistema, os seus resultados são comparados com aqueles que foram obtidos experimentalmente.

Palavras-chave: Dinâmica não linear; Identificação não linear; Structural Model Updating; Método da superfície de aceleração; Model order reduction.

Contents

Abstract iii

Resumo v

List of Figures xi

List of Tables xix

Notation xxi

1 Introduction 1
- 1.1 Context . . . 1
- 1.2 Motivation . . . 1
- 1.3 Goals . . . 2
- 1.4 Outline . . . 2

2 Brief literature review 5
- 2.1 Nonlinear dynamics . . . 5
  - 2.1.1 Causes . . . 5
  - 2.1.2 Nonlinear oscillations and resonance . . . 6
- 2.2 Nonlinear identification . . . 7
  - 2.2.1 Detection . . . 7
  - 2.2.2 Characterization and parametrization . . . 8
  - 2.2.3 Structural Model Updating . . . 9

3 Nonlinear integration and time-frequency transformation 11
- 3.1 Numerical integration methods . . . 11
  - 3.1.1 Newmark - nonlinear systems . . . 12
- 3.2 Time-frequency transformation . . . 15
  - 3.2.1 Fourier Transform . . . 15
  - 3.2.2 Wavelet transform . . . 16
  - 3.2.3 Final remarks . . . 17

4 Nonlinear characterization 19
- 4.1 Restoring force surface (RFS) method . . . 19
  - 4.1.1 RFS - application example . . . 21
  - 4.1.2 ASM - application example . . . 25

5 Model order reduction **31**
5.1 Introduction . . . 32
5.2 Craig-Brampton model . . . 33
5.3 Rubin and MacNeal approximations . . . 34
5.4 Conclusion . . . 37
5.5 Implementation in Newmark algorithm . . . 37
5.6 Application example - cantilever beam . . . 39

6 Structural modelling and experimental measurements **47**
6.1 Finite element model . . . 47
6.2 Experimental procedure . . . 50
6.3 Data processing phase . . . 54
6.3.1 Natural modes - Polymax® . . . 54
6.3.2 Acceleration integration procedure . . . 56
6.4 Performed experiments . . . 58

7 Linear model validation and nonlinear characterization **61**
7.1 Linear model validation . . . 61
7.1.1 Experimental modal model . . . 61
7.1.2 Linear model correlation . . . 65
7.2 Nonlinear characterization . . . 68
7.2.1 Subharmonic resonance . . . 88

8 Structural model update **91**
8.1 Linear model . . . 92
8.2 Nonlinear model . . . 102
8.2.1 Cubic stiffness . . . 103
8.2.2 Polynomial stiffness . . . 123
8.2.3 Piecewise stiffness . . . 144
8.3 Conclusions on the structural model updating . . . 145

9 Conclusion **147**
9.1 Main conclusions . . . 147
9.2 Future works . . . 149

References **151**

List of Figures

2 Brief literature review **5**
2.1 Response curves for a resonantly excited and damped SDOF nonlinear system with softening behaviour (left) and hardening behaviour (right) 6
2.2 Sine-sweep answer example 8

3 Nonlinear integration and time-frequency transformation **11**
3.1 Working principle of the Fourier Transform 15
3.2 Difference between a sine and a wavelet wave 16
3.3 Scaling process in the Wavelet Transform 17
3.4 Resolution in a STFT and a in a WT 17

4 Nonlinear characterization **19**
4.1 Nonlinear 5DOF system 20
4.2 Nonlinear 1DOF system 21
4.3 Restoring force surface - linear case 22
4.4 Stiffness and damping curves - linear case 23
4.5 Restoring force surface - nonlinear case 23
4.6 Stiffness and damping curves - nonlinear case 24
4.7 Restoring force surface - nonlinear case with linear sine-sweep 24
4.8 Stiffness and damping curves - nonlinear case - linear sweep 25
4.9 Acceleration surface for the SDOF system 25
4.10 Stiffness and damping curves for the SDOF system using ASM 26
4.11 Acceleration surface 27
4.12 Stiffness and damping curves 27
4.13 Time-frequency plot with the indication of the different harmonics 28
4.14 Time-frequency plot using time at X axis 28
4.15 Acceleration surface considering the nonlinearity between DOF 3 and 5 29
4.16 Stiffness curve considering the nonlinear connection between DOF 3 and 5 . . . 29
4.17 Stiffness curve for the nonlinear connection between DOF 3 and 5 considering the full equation 30

5 Model order reduction **31**
5.1 Model order reduction procedure and its particularities for Craig-Brampton and Rubin-MacNeal 32

5.2 a) Fixed-interface modes for a cantilever beam; b) Constraint modes for a cantilever beam . . . 33
5.3 Simcenter3D® model. . . . 39
5.4 Natural modes of the beam: a) first natural mode; b) second natural mode. . . . 39
5.5 1st modal answer of the beam . . . 40
5.6 2nd modal answer of the beam . . . 40
5.7 Time-frequency plot of the undamped answer . . . 41
5.8 Time-frequency plot of the damped answer . . . 41
5.9 Accelerations surface obtained with the reduced order model and Simcenter3D® 42
5.10 Stiffness curves obtained with the reduced order model and Simcenter3D®. . . . 42
5.11 Damping curves obtained with the reduced order model and Simcenter3D®. . . . 43
5.12 Acceleration surface - nonlinear case . . . 43
5.13 Stiffness and damping curves - nonlinear case . . . 44
5.14 Acceleration surface - nonlinear undamped case . . . 44
5.15 Acceleration surface - nonlinear case from 5-100Hz . . . 45

6 Structural modelling and experimental measurements 47
6.1 Airplane technical drawing . . . 47
6.2 Pylon technical drawing . . . 48
6.3 Geometrical simplifications done at the pylon . . . 49
6.4 Pylon finite element model . . . 49
6.5 Finite element model of the airplane with wings with indication of the sensor locations . . . 50
6.6 Natural shapes of the airplane with the pylons . . . 52
6.7 Experimental setup - a) Overall setup b) Tape beneath the sensors c) Connection between the shaker and the airplane . . . 53
6.8 Example of a stabilisation diagram . . . 56
6.9 Butterworth highpass filter parameters . . . 57
6.10 Acceleration integration procedure . . . 58

7 Linear model validation and nonlinear characterization 61
7.1 Stabilization diagram . . . 62
7.2 MAC for the modal modes generated by Testlab® . . . 62
7.3 3rd and 11th modes obtained by Testlab® . . . 64
7.4 MAC between the numerical and experimental modesets . . . 65
7.5 Comparison between the 13th modes on Testlab® - a) - and Simcenter3D® - b) 66
7.6 Comparison between the 14th modes on Testlab® - a) - and Simcenter3D® - b) 66
7.7 FRF curves from left and right pylon . . . 66
7.8 Frequency error between the experimental and the numerical model . . . 67
7.9 Sweep 1 answers for 0.01V and 0.02V at LPylon:2 . . . 69
7.10 Sweep 1 answers for 0.04V and 0.06V at LPylon:2 . . . 69
7.11 Sweep 1 answers for 0.07V and 0.08V at LPylon:2 . . . 70
7.12 Sweep 1 answer for 0.09V at LPylon:2 . . . 70
7.13 Sweep 2 answers for 0.01V and 0.02V at LPylon:2 . . . 71
7.14 Sweep 2 answers for 0.04V and 0.06V at LPylon:2 . . . 71
7.15 Sweep 2 answers for 0.07V and 0.08V at LPylon:2 . . . 72
7.16 Sweep 2 answers for 0.09V at LPylon:2 . . . 72

7.17 Sweep 2 answers for 0.02V with sweep-rates of 0.4 oct/min and 1.0 oct/min . . 73
7.18 Sweep-up and sweep-down for 0.02V with sweep-rates of 0.4 oct/min 73
7.19 Acceleration surface for 0.07 V when filtering the force and the answer for LPylon:2 75
7.20 Acceleration surface for 0.08 V when filtering the force and the answer for LPylon:2 76
7.21 Damping curves for 0.07 V when filtering the force and the answer for LPylon:2 76
7.22 Damping curves for 0.08 V when filtering the force and the answer for for LPylon:2 77
7.23 Overlaid damping curves when using filtering the force and the answer for 0.07 V for LPylon:2 77
7.24 Acceleration surface for 0.07 V when "filtering the force" for LPylon:2 78
7.25 Stiffness curve for 0.01 V when filtering the force and the answer 78
7.26 Stiffness curve for 0.02 V when filtering the force and the answer 79
7.27 Stiffness curve for 0.04 V when filtering the force and the answer 79
7.28 Stiffness curve for 0.06 V when filtering the force and the answer 80
7.29 Stiffness curve for 0.07 V when filtering the force and the answer 80
7.30 Stiffness curve for 0.08 V when filtering the force and the answer 81
7.31 Stiffness curve for 0.09 V when filtering the force and the answer 81
7.32 Overlaid stiffness curves when "filtering the force" 82
7.33 Overlaid stiffness curves when filtering the answer 82
7.34 Overlaid stiffness curve for 0.07 V when filtering the force and the answer . . . 83
7.35 Overlaid stiffness curve for 0.08 V when filtering the force and the answer . . . 83
7.36 Stiffness curve for 0.06 V for *sweep1* and *sweep2* when filtering the force and the answer 84
7.37 Stiffness curve when isolating the first mode through a bandpass filter 84
7.38 Stiffness curve for right and left pylon when "filtering the force" 85
7.39 Overlaid stiffness curve for right and left pylon when "filtering the force" . . . 85
7.40 Time-frequency plot for *sweep1* excitation at 0.08 V from 6.3-10 Hz. 86
7.41 Stiffness curve for excitation frequency 45-65 Hz for 0.06 V 88
7.42 Stiffness curve for excitation frequency 53-63 Hz for 0.06 V 89
7.43 Overlaid stiffness curves of the experiments 6-100Hz and 45-65Hz by applying a bandpass filter at 6.4-8Hz 89
7.44 Overlaid stiffness curves of 45-65Hz with and without bandpass filter 90
7.45 Time-frequency plot for excitation at 0.06 V from 45-65 Hz. 90

8 Structural model update **91**
8.1 Nodes of the blocked DOF 92
8.2 Simulated and experimental results for *LPylon:2* and *RPylon:2* at *sweep1* with the excitation level of 0.01 V and with $\zeta_1 = 1.07\%$ and $\zeta_2 = 0.46\%$ 93
8.3 Modal answers at *sweep1* for the excitation level of 0.01 V and with $\zeta_1 = 1.07\%$ and $\zeta_2 = 0.46\%$ 94
8.4 Simulated and experimental results for *LPylon:2* at *sweep1* with the excitation level of 0.01 V and with $\zeta_1 = 0.46\%$ and $\zeta_2 = 0.46\%$ 94
8.5 Simulated and experimental results for *RPylon:2* at *sweep1* the excitation level of 0.01 V and with $\zeta_1 = 0.46\%$ and $\zeta_2 = 0.46\%$ 95
8.6 Simulated and experimental results for *LPylon:2* at *sweep1* with the excitation level of 0.01 V and with $\zeta_1 = 0.50\%$ and $\zeta_2 = 1.30\%$ 95

8.7 Simulated and experimental results for *RPylon:2* at *sweep1* with the excitation level of 0.01 V and with $\zeta_1 = 0.50\%$ and $\zeta_2 = 1.30\%$ 96
8.8 Simulated and experimental stiffness curves for *RPylon:2* and *LPylon:2* at *sweep1* with the excitation level of 0.01 V and with $\zeta_1 = 0.50\%$ and $\zeta_2 = 1.30\%$ 96
8.9 Simulated and experimental results for *LPylon:2* at *sweep1* with the excitation level of 0.02 V and with $\zeta_1 = 0.50\%$ and $\zeta_2 = 1.30\%$ 97
8.10 Simulated and experimental results for *RPylon:2* at *sweep1* with the excitation level of 0.02 V and with $\zeta_1 = 0.46\%$ and $\zeta_2 = 0.46\%$ 97
8.11 Simulated and experimental stiffness curves for *RPylon:2* and *LPylon:2* at *sweep1* with the excitation level of 0.02 V and with $\zeta_1 = 0.50\%$ and $\zeta_2 = 1.30\%$ 98
8.12 Simulated and experimental results for *LPylon:2* and *RPylon:2* at *sweep2* with the excitation level of 0.01 V and with $\zeta_1 = 0.50\%$ and $\zeta_2 = 1.30\%$ 98
8.13 Simulated and experimental stiffness curves for *RPylon:2* and *LPylon:2* at *sweep2* with the excitation level of 0.01 V and with $\zeta_1 = 0.50\%$ and $\zeta_2 = 1.30\%$ 99
8.14 Simulated and experimental results for *LPylon:2* at *sweep2* with the excitation level of 0.02 V and with $\zeta_1 = 0.50\%$ and $\zeta_2 = 1.30\%$ 99
8.15 Simulated and experimental results for *RPylon:2* at *sweep2* with the excitation level of 0.02 V and with $\zeta_1 = 0.46\%$ and $\zeta_2 = 0.46\%$ 100
8.16 Simulated and experimental stiffness curves for *RPylon:2* and *LPylon:2* at *sweep2* with the excitation level of 0.02 V and with $\zeta_1 = 0.50\%$ and $\zeta_2 = 1.30\%$ 100
8.17 Simulated and experimental results for *LPylon:2* and *RPylon:2* at *sweep2* with the excitation level of 0.02 V and with $\zeta_1 = 0.50\%$ and $\zeta_2 = 0.50\%$ 101
8.18 Simulated and experimental results for *LPylon:2* and *RPylon:2* at *sweep1* with the excitation level of 0.06 V and with $\zeta_1 = 0.50\%$ and $\zeta_2 = 1.30\%$ without considering the nonlinear behaviour 102
8.19 Simulated and experimental stiffness curves for *RPylon:2* and *LPylon:2* at *sweep2* with the excitation level of 0.06 V and with $\zeta_1 = 0.50\%$ and $\zeta_2 = 1.30\%$ without considering the nonlinear behaviour 102
8.20 Simulated and experimental results for *LPylon:2* and *RPylon:2* at *sweep1* with the excitation level of 0.04 V and with $\zeta_1 = 0.50\%$ and $\zeta_2 = 1.30\%$ using a cubic stiffness 104
8.21 Simulated and experimental stiffness curves for *RPylon:2* and *LPylon:2* at *sweep1* with the excitation level of 0.04 V and with $\zeta_1 = 0.50\%$ and $\zeta_2 = 1.30\%$ using a cubic stiffness 105
8.22 Simulated and experimental results for *LPylon:2* and *RPylon:2* at *sweep2* with the excitation level of 0.04 V and with $\zeta_1 = 0.50\%$ and $\zeta_2 = 1.30\%$ using a cubic stiffness 105
8.23 Simulated and experimental results for *LPylon:2* at *sweep1* with the excitation level of 0.06 V and with $\zeta_1 = 0.50\%$ and $\zeta_2 = 1.30\%$ using a cubic stiffness . . . 106
8.24 Simulated and experimental results for *RPylon:2* at *sweep1* with the excitation level of 0.06 V and with $\zeta_1 = 0.50\%$ and $\zeta_2 = 1.30\%$ using a cubic stiffness . . . 106
8.25 Simulated and experimental stiffness curves for *RPylon:2* and *LPylon:2* at *sweep1* with the excitation level of 0.06 V and with $\zeta_1 = 0.50\%$ and $\zeta_2 = 1.30\%$ using a cubic stiffness 107
8.26 Accelerance curves *LPylon:2-LWing:5_force* for the different excitation levels using a cubic stiffness 107
8.27 Simulated and experimental results for *LPylon:2* at *sweep1* with the excitation level of 0.04 V and with $\zeta_1 = 0.52\%$ and $\zeta_2 = 5.00\%$ using a cubic stiffness . . . 108

8.28 Simulated and experimental results for *RPylon:2* at *sweep1* with the excitation level of 0.04 V and with $\zeta_1 = 0.52\%$ and $\zeta_2 = 5.00\%$ using a cubic stiffness . . . 108
8.29 Simulated and experimental stiffness curves for *RPylon:2* and *LPylon:2* at *sweep1* with the excitation level of 0.04 V and with $\zeta_1 = 0.52\%$ and $\zeta_2 = 5.00\%$ using a cubic stiffness . . . 109
8.30 Simulated and experimental results for *LPylon:2* at *sweep1* with the excitation level of 0.06 V and with $\zeta_1 = 0.73\%$ and $\zeta_2 = 7.00\%$ using a cubic stiffness . . . 109
8.31 Simulated and experimental results for *RPylon:2* at *sweep1* with the excitation level of 0.06 V and with $\zeta_1 = 0.73\%$ and $\zeta_2 = 6.00\%$ using a cubic stiffness . . . 110
8.32 Simulated and experimental stiffness curves for *RPylon:2* and *LPylon:2* at *sweep1* with the excitation level of 0.06 V and with $\zeta_1 = 0.73\%$ and $\zeta_2 = 6.00\%$ using a cubic stiffness . . . 110
8.33 Simulated and experimental results for *LPylon:2* at *sweep1* with the excitation level of 0.07 V and with $\zeta_1 = 0.73\%$ and $\zeta_2 = 6.00\%$ using a cubic stiffness . . . 111
8.34 Simulated and experimental results for *RPylon:2* at *sweep1* with the excitation level of 0.07 V and with $\zeta_1 = 0.73\%$ and $\zeta_2 = 6.00\%$ using a cubic stiffness . . . 111
8.35 Simulated and experimental stiffness curves for *RPylon:2* and *LPylon:2* at *sweep1* with the excitation level of 0.07 V and with $\zeta_1 = 0.73\%$ and $\zeta_2 = 6.00\%$ using a cubic stiffness . . . 112
8.36 Simulated and experimental results for *LPylon:2* at *sweep1* with the excitation level of 0.08 V and with $\zeta_1 = 0.83\%$ and $\zeta_2 = 6.40\%$ using a cubic stiffness . . . 112
8.37 Simulated and experimental results for *RPylon:2* at *sweep1* with the excitation level of 0.08 V and with $\zeta_1 = 0.83\%$ and $\zeta_2 = 6.40\%$ using a cubic stiffness . . . 113
8.38 Simulated and experimental stiffness curves for *RPylon:2* and *LPylon:2* at *sweep1* with the excitation level of 0.08 V and with $\zeta_1 = 0.83\%$ and $\zeta_2 = 6.40\%$ using a cubic stiffness . . . 113
8.39 Simulated and experimental results for *LPylon:2* at *sweep1* with the excitation level of 0.09 V and with $\zeta_1 = 0.93\%$ and $\zeta_2 = 6.30\%$ using a cubic stiffness . . . 114
8.40 Simulated and experimental results for *RPylon:2* at *sweep1* with the excitation level of 0.09 V and with $\zeta_1 = 0.93\%$ and $\zeta_2 = 6.30\%$ using a cubic stiffness . . . 114
8.41 Simulated and experimental stiffness curves for *RPylon:2* and *LPylon:2* at *sweep1* with the excitation level of 0.09 V and with $\zeta_1 = 0.93\%$ and $\zeta_2 = 6.30\%$ using a cubic stiffness . . . 115
8.42 Simulated and experimental results for *LPylon:2* at *sweep2* with the excitation level of 0.04 V and with $\zeta_1 = 0.52\%$ and $\zeta_2 = 5.00\%$ using a cubic stiffness . . . 115
8.43 Simulated and experimental results for *RPylon:2* at *sweep2* with the excitation level of 0.04 V and with $\zeta_1 = 0.52\%$ and $\zeta_2 = 5.00\%$ using a cubic stiffness . . . 116
8.44 Simulated and experimental stiffness curves for *RPylon:2* and *LPylon:2* at *sweep2* with the excitation level of 0.04 V and with $\zeta_1 = 0.52\%$ and $\zeta_2 = 5.00\%$ using a cubic stiffness . . . 116
8.45 Simulated and experimental results for *LPylon:2* and *RPylon:2* at *sweep2* with the excitation level of 0.06 V and with $\zeta_1 = 0.73\%$ and $\zeta_2 = 7.00\%$ using a cubic stiffness . . . 117
8.46 Simulated and experimental stiffness curves for *RPylon:2* and *LPylon:2* at *sweep2* with the excitation level of 0.06 V and with $\zeta_1 = 0.73\%$ and $\zeta_2 = 6.00\%$ using a cubic stiffness . . . 117

8.47 Simulated and experimental results for *LPylon:2* and *RPylon:2* at *sweep2* with the excitation level of 0.07 V and with $\zeta_1 = 0.73\%$ and $\zeta_2 = 6.00\%$ using a cubic stiffness . . . 118
8.48 Simulated and experimental stiffness curves for *RPylon:2* and *LPylon:2* at *sweep2* with the excitation level of 0.07 V and with $\zeta_1 = 0.73\%$ and $\zeta_2 = 6.00\%$ using a cubic stiffness . . . 118
8.49 Simulated and experimental results for *LPylon:2* at *sweep2* with the excitation level of 0.08 V and with $\zeta_1 = 0.83\%$ and $\zeta_2 = 6.40\%$ using a cubic stiffness . . . 119
8.50 Simulated and experimental results for *RPylon:2* at *sweep2* with the excitation level of 0.08 V and with $\zeta_1 = 0.83\%$ and $\zeta_2 = 6.40\%$ using a cubic stiffness . . . 119
8.51 Simulated and experimental stiffness curves for *RPylon:2* and *LPylon:2* at *sweep2* with the excitation level of 0.08 V and with $\zeta_1 = 0.83\%$ and $\zeta_2 = 6.40\%$ using a cubic stiffness . . . 120
8.52 Simulated and experimental results for *LPylon:2* at *sweep2* with the excitation level of 0.09 V and with $\zeta_1 = 0.93\%$ and $\zeta_2 = 6.30\%$ using a cubic stiffness . . . 120
8.53 Simulated and experimental results for *RPylon:2* at *sweep2* with the excitation level of 0.09 V and with $\zeta_1 = 0.93\%$ and $\zeta_2 = 6.30\%$ using a cubic stiffness . . . 121
8.54 Simulated and experimental stiffness curves for *RPylon:2* and *LPylon:2* at *sweep2* with the excitation level of 0.09 V and with $\zeta_1 = 0.93\%$ and $\zeta_2 = 6.30\%$ using a cubic stiffness . . . 121
8.55 Simulated and experimental results for *LPylon:2 RPylon:2* at *sweep1* with the excitation level of 0.06 V and with $\zeta_1 = 0.73\%$ and $\zeta_2 = 0.73\%$ using a cubic stiffness . . . 122
8.56 Simulated and experimental stiffness curves for *RPylon:2* and *LPylon:2* at *sweep1* with the excitation level of 0.06 V and with $\zeta_1 = 0.73\%$ and $\zeta_2 = 0.73\%$ using a cubic stiffness . . . 122
8.57 Simulated and experimental results for *LPylon:2 RPylon:2* at *sweep2* with the excitation level of 0.06 V and with $\zeta_1 = 0.73\%$ and $\zeta_2 = 4.00\%$ using a cubic stiffness . . . 123
8.58 Simulated and experimental results for *LPylon:2* and *RPylon:2* at *sweep1* with the excitation level of 0.02 V and with $\zeta_1 = 0.50\%$ and $\zeta_2 = 1.30\%$ using a polynomial stiffness . . . 125
8.59 Simulated and experimental stiffness curves for *RPylon:2* and *LPylon:2* at *sweep1* with the excitation level of 0.02 V and with $\zeta_1 = 0.50\%$ and $\zeta_2 = 1.30\%$ using a polynomial stiffness . . . 125
8.60 Simulated and experimental results for *LPylon:2* and *RPylon:2* at *sweep2* with the excitation level of 0.01 V and with $\zeta_1 = 0.50\%$ and $\zeta_2 = 1.30\%$ using a polynomial stiffness . . . 126
8.61 Simulated and experimental stiffness curves for *RPylon:2* and *LPylon:2* at *sweep2* with the excitation level of 0.01 V and with $\zeta_1 = 0.50\%$ and $\zeta_2 = 1.30\%$ using a polynomial stiffness . . . 126
8.62 Simulated and experimental results for *LPylon:2* and *RPylon:2* at *sweep2* with the excitation level of 0.02 V and with $\zeta_1 = 0.50\%$ and $\zeta_2 = 1.30\%$ using a polynomial stiffness . . . 127
8.63 Simulated and experimental stiffness curves for *RPylon:2* and *LPylon:2* at *sweep2* with the excitation level of 0.02 V and with $\zeta_1 = 0.50\%$ and $\zeta_2 = 1.30\%$ using a polynomial stiffness . . . 127

8.64 Simulated and experimental results for *LPylon:2* and *RPylon:2* at *sweep1* with the excitation level of 0.04 V and with $\zeta_1 = 0.52\%$ and $\zeta_2 = 5.00\%$ using a polynomial stiffness 128
8.65 Simulated and experimental stiffness curves for *RPylon:2* and *LPylon:2* at *sweep1* with the excitation level of 0.04 V and with $\zeta_1 = 0.52\%$ and $\zeta_2 = 5.00\%$ using a polynomial stiffness 128
8.66 Simulated and experimental results for *LPylon:2* at *sweep1* with the excitation level of 0.04 V and with $\zeta_1 = 0.46\%$ and $\zeta_2 = 4.50\%$ using a polynomial stiffness 129
8.67 Simulated and experimental results for *RPylon:2* at *sweep1* with the excitation level of 0.04 V and with $\zeta_1 = 0.46\%$ and $\zeta_2 = 4.50\%$ using a polynomial stiffness 129
8.68 Simulated and experimental stiffness curves for *RPylon:2* and *LPylon:2* at *sweep1* with the excitation level of 0.04 V and with $\zeta_1 = 0.46\%$ and $\zeta_2 = 4.50\%$ using a polynomial stiffness 130
8.69 Simulated and experimental results for *LPylon:2* at *sweep1* with the excitation level of 0.06 V and with $\zeta_1 = 0.65\%$ and $\zeta_2 = 5.90\%$ using a polynomial stiffness 130
8.70 Simulated and experimental results for *RPylon:2* at *sweep1* with the excitation level of 0.06 V and with $\zeta_1 = 0.65\%$ and $\zeta_2 = 5.90\%$ using a polynomial stiffness 131
8.71 Simulated and experimental stiffness curves for *RPylon:2* and *LPylon:2* at *sweep1* with the excitation level of 0.06 V and with $\zeta_1 = 0.65\%$ and $\zeta_2 = 5.90\%$ using a polynomial stiffness 131
8.72 Simulated and experimental results for *LPylon:2* at *sweep1* with the excitation level of 0.07 V and with $\zeta_1 = 0.65\%$ and $\zeta_2 = 5.90\%$ using a polynomial stiffness 132
8.73 Simulated and experimental results for *RPylon:2* at *sweep1* with the excitation level of 0.07 V and with $\zeta_1 = 0.65\%$ and $\zeta_2 = 5.90\%$ using a polynomial stiffness 132
8.74 Simulated and experimental stiffness curves for *RPylon:2* and *LPylon:2* at *sweep1* with the excitation level of 0.07 V and with $\zeta_1 = 0.65\%$ and $\zeta_2 = 5.90\%$ using a polynomial stiffness 133
8.75 Simulated and experimental results for *LPylon:2* at *sweep1* with the excitation level of 0.08 V and with $\zeta_1 = 0.75\%$ and $\zeta_2 = 6.90\%$ using a polynomial stiffness 133
8.76 Simulated and experimental results for *RPylon:2* at *sweep1* with the excitation level of 0.08 V and with $\zeta_1 = 0.75\%$ and $\zeta_2 = 6.90\%$ using a polynomial stiffness 134
8.77 Simulated and experimental stiffness curves for *RPylon:2* and *LPylon:2* at *sweep1* with the excitation level of 0.08 V and with $\zeta_1 = 0.75\%$ and $\zeta_2 = 6.90\%$ using a polynomial stiffness 134
8.78 Simulated and experimental results for *LPylon:2* at *sweep1* with the excitation level of 0.09 V and with $\zeta_1 = 0.80\%$ and $\zeta_2 = 7.70\%$ using a polynomial stiffness 135
8.79 Simulated and experimental results for *RPylon:2* at *sweep1* with the excitation level of 0.09 V and with $\zeta_1 = 0.80\%$ and $\zeta_2 = 7.70\%$ using a polynomial stiffness 135
8.80 Simulated and experimental stiffness curves for *RPylon:2* and *LPylon:2* at *sweep1* with the excitation level of 0.09 V and with $\zeta_1 = 0.80\%$ and $\zeta_2 = 7.70\%$ using a polynomial stiffness 136
8.81 Simulated and experimental results for *LPylon:2* at *sweep2* with the excitation level of 0.04 V and with $\zeta_1 = 0.46\%$ and $\zeta_2 = 4.50\%$ using a polynomial stiffness 136
8.82 Simulated and experimental results for *RPylon:2* at *sweep2* with the excitation level of 0.04 V and with $\zeta_1 = 0.46\%$ and $\zeta_2 = 4.50\%$ using a polynomial stiffness 137
8.83 Simulated and experimental stiffness curves for *RPylon:2* and *LPylon:2* at *sweep2* with the excitation level of 0.04 V and with $\zeta_1 = 0.46\%$ and $\zeta_2 = 4.50\%$ using a polynomial stiffness 137

8.84 Simulated and experimental results for *LPylon:2* at *sweep2* with the excitation level of 0.06 V and with $\zeta_1 = 0.65\%$ and $\zeta_2 = 5.90\%$ using a polynomial stiffness 138
8.85 Simulated and experimental results for *RPylon:2* at *sweep2* with the excitation level of 0.06 V and with $\zeta_1 = 0.65\%$ and $\zeta_2 = 5.90\%$ using a polynomial stiffness 138
8.86 Simulated and experimental stiffness curves for *RPylon:2* and *LPylon:2* at *sweep2* with the excitation level of 0.06 V and with $\zeta_1 = 0.65\%$ and $\zeta_2 = 5.90\%$ using a polynomial stiffness 139
8.87 Simulated and experimental results for *LPylon:2* at *sweep2* with the excitation level of 0.07 V and with $\zeta_1 = 0.65\%$ and $\zeta_2 = 5.90\%$ using a polynomial stiffness 139
8.88 Simulated and experimental results for *RPylon:2* at *sweep2* with the excitation level of 0.07 V and with $\zeta_1 = 0.65\%$ and $\zeta_2 = 5.90\%$ using a polynomial stiffness 140
8.89 Simulated and experimental stiffness curves for *RPylon:2* and *LPylon:2* at *sweep2* with the excitation level of 0.07 V and with $\zeta_1 = 0.65\%$ and $\zeta_2 = 5.90\%$ using a polynomial stiffness 140
8.90 Simulated and experimental results for *LPylon:2* at *sweep2* with the excitation level of 0.08 V and with $\zeta_1 = 0.75\%$ and $\zeta_2 = 6.90\%$ using a polynomial stiffness 141
8.91 Simulated and experimental results for *RPylon:2* at *sweep2* with the excitation level of 0.08 V and with $\zeta_1 = 0.75\%$ and $\zeta_2 = 6.90\%$ using a polynomial stiffness 141
8.92 Simulated and experimental stiffness curves for *RPylon:2* and *LPylon:2* at *sweep2* with the excitation level of 0.08 V and with $\zeta_1 = 0.75\%$ and $\zeta_2 = 6.90\%$ using a polynomial stiffness 142
8.93 Simulated and experimental results for *LPylon:2* at *sweep2* with the excitation level of 0.09 V and with $\zeta_1 = 0.80\%$ and $\zeta_2 = 7.70\%$ using a polynomial stiffness 142
8.94 Simulated and experimental results for *RPylon:2* at *sweep2* with the excitation level of 0.09 V and with $\zeta_1 = 0.80\%$ and $\zeta_2 = 7.70\%$ using a polynomial stiffness 143
8.95 Simulated and experimental stiffness curves for *RPylon:2* and *LPylon:2* at *sweep2* with the excitation level of 0.09 V and with $\zeta_1 = 0.80\%$ and $\zeta_2 = 7.70\%$ using a polynomial stiffness 143
8.96 Simulated and experimental results for *LPylon:2* and *RPylon:2* at *sweep1* with the excitation level of 0.06 V and with $\zeta_1 = 0.73\%$ and $\zeta_2 = 5.50\%$ using a piecewise stiffness 144
8.97 Simulated and experimental stiffness curves for *RPylon:2* and *LPylon:2* at *sweep1* with the excitation level of 0.06 V and with $\zeta_1 = 0.73\%$ and $\zeta_2 = 5.50\%$ using a piecewise stiffness 144

9 Conclusion **147**
9.1 Exterior factors: a) holes misalignment; b) fatigue fracture 148

List of Tables

6 Structural modelling and experimental measurements **47**
6.1 Parameters utilized in the different measurements 58

7 Linear model validation and nonlinear characterization **61**
7.1 Modal synthesis error 63
7.2 Correlation MAC values and frequency error values 67
7.3 Cubic function fitting coefficients and performance values 87
7.4 Polynomial function fitting coefficient values 87
7.5 Polynomial function performance values 87
7.6 Piecewise function coefficients and performance values 87

8 Structural model update **91**
8.1 Damping values extracted from Testlab® 92

Notation

Abbreviations

ASM	Acceleration Surface Method
CRP	Conditioned Reverse Path
CWT	Continuous Wavelet Transform
DFT	Discrete Fourier Transform
DWT	Discrete Wavelet Transform
EMD	Empirical Mode Decomposition
FFT	Fast Fourier Transform
FRF	Frequency Response Function
FS	Sampling Frequency
FT	Fourier Transform
IRR	Infinite Impulse Response
MAC	Model Assurance Criteria
MDOF	Multiple Degrees of Freedom
MOR	Model Order Reduction
MRA	Multi-Resolution Analysis
NMN	Nonlinear Normal Modes
RFS	Restoring Force Surface
ROM	Reduced Order Model
RP	Reverse Path
SDOF	Single Degree of Freedom
STFT	Short Time Fourier Transform
WFT	Windowed Fourier Transform
WT	Wavelet Transform

Symbols

$\{x\}$	Displacements vector
$\{\dot{x}\}$	Velocity vector
$\{\ddot{x}\}$	Acceleration vector
$\{F\}$	Force vector
$[M]$	Mass matrix

$[K]$	Stiffness matrix
$[C]$	Damping matrix
F_{nl}	Nonlinear force
k_{nl}	Nonlinear stiffness
n	Stiffness order
$f(x, \dot{x})$	Restoring force
m	mass
k	stiffness
c	damping
u	displacement
$\dot{u}$	velocity
$\ddot{u}$	acceleration
t	time
ω	Frequency
ω_1	Main harmonic
Δt	time-step
α	Newmark parameter
β	Newmark parameter
$\{r\}$	Residual vector
$\{\eta\}$	Reduced coordinates
λ^2	Square of the natural frequency
$[\Phi]$	Transformation matrix
$[\Phi_i]$	Fixed interface modes
$R_b b$	Reactions at the boundary degrees of freedom
ψ_{ib}	Non-unitary displacements of the constraint modes
$\{\Psi_b\}$	Constraint modes
$[\Phi_k]$	Selected or kept modes
$\{\Phi_a\}$	Attachment modes
$\{\Phi_{rira}\}$	Residual attachment modes
$\{\lambda_k^2\}$	Square of the natural frequency of the kept modes
$\{\lambda_k^2\}$	Square of the natural frequency of the attachment modes
$\{\lambda_{rira}^2\}$	Square of the natural frequency of the residual attachment modes
$[\Phi_r]$	Rigid body modes
$[\Phi_f]$	Flexible modes
$\{\eta_r\}$	Rigid reduced coordinates
$\{\eta_f\}$	Flexible reduced coordinates
$\{x_r\}$	Rigid body displacements
$\{x_f\}$	Flexible displacements
$\{F_r\}$	Rigid body force
$\{F_f\}$	Flexible body force
$[G_c]$	Flexibility matrix
A	Accelerance
$\bar{S}_x$	Spectrum of the input signal
$\bar{S}_f$	Spectrum of the output signal
$\bar{S}_{xx}$	Autopower spectrum of the input signal
$\bar{S}_{ff}$	Autopower spectrum of the output signal
$\bar{S}_{xf}$	Crosspower spectrum between the input and output signal
H_1	Estimator H_1

H_2	Estimator H_2
N_f	Normalized frequency
FT	Fourier Transform
TF	Transfer Function
N_{sweeps}	Number of sweeps
N_{inputs}	Number of input forces

CHAPTER 1

Introduction

1.1 Context

This work was developed in the context of the MSc dissertation in "Projecto e Construção Mecânica" at Faculdade de Engenharia da Universidade do Porto (FEUP), during an internship at Siemens Digital Industry Software, at Leuven, Belgium. Among the different divisions of the company, this thesis was developed in the Test and Research division, whose goal is the research and development of new numerical tools and technologies to be incorporated in the commercial software's sold by Siemens like Siemens Simcenter 3D® or Siemens Testlab® for example.

1.2 Motivation

Probably the most used simplification in the field of engineering is the approximation of many behaviours by linear functions, not just because it is what really happens in many systems, where they operate within a limited range and for that reason a linear approximation is sufficient to understand, predict and control their behaviour, but also because it allows a huge simplification in terms of mathematical development. For example, at the field of vibrations and dynamics, that consideration allows the utilization of principles like the superposition principle where a answer of a system excited by multiple forces can be calculated as the sum of the answers of each force applied individually, or the modal analysis which allows engineers to study a multiple degree of freedom (MDOF) as group of multiple single degree of freedom (SDOF) systems. These are just two "big tools" that many times cannot be used in the context of nonlinear dynamics [1, 2]. About modal analysis, it is true that it can be used in nonlinear dynamics via Nonlinear normal modes, but it has two very important limitations, which are the superposition principle and the lack of orthogonality relations, that prevents its utilization as a basis for order reduction. It is important to have in mind that the orthogonality relations between the modes in a linear analysis is what makes the decoupling of the DOF become reality. A complete decoupling is not possible in nonlinear systems [3].

But even in the conception of linear numerical models there are big challenges, and a good example of that are the vibration ground tests that are performed by airplane manufacturers to assure the accuracy of their models. In this thesis, in a mock-up airplane, similar analysis

will be done, and even the same software that is used in these tests by Airbus® will be utilized. With the realization of these experimental tests it will be possible to evaluate the evolution from linear to nonlinear behaviour and compare the differences between the answers.

Despite of the advantages of using a linear model, they present their limitations, as it will be seen when comparing simulated answers without considering the nonlinear effects, with the experimental nonlinear answers. To obtain better results is necessary to consider the nonlinearities in the numerical models, but at the same time their consideration also represents a big increase in computational cost, and that represents an obstacle for its easy implementation. Overcoming this inconvenient represents one of the big challenges of this thesis, and for that goal a process of model order reduction for linear systems is applied, and posteriorly the model is coupled with a local nonlinear data-driven model of the nonlinearities, which results in a hybrid nonlinear model, with an incredibly low computational weight! Everything in order to have the same "computational comfort".

1.3 Goals

The main goal of this work is to obtain a numerical model that is able to simulate and predict a dynamic transient answer of a system with sparse nonlinearities, and posteriorly compare the simulated answer with the experimental one. Due to the high computational cost associated to nonlinear simulations the second goal is the obtention of a nonlinear hybrid reduced model, and to achieve those two goals, the first step is to get a validated linear model, from which a reduced order model will be generated.

The structure to be studied is an airplane mock-up with two localized nonlinearities connected to its wings, simulating the presence of the engines. Besides the goal of obtaining the numerical model, another objective is to understand and distinguish the differences between a linear and a nonlinear behaviour, to see how the nonlinear behaviour evolves with different excitation levels, identify the particularities of this type of answer like the "jumps" or the hardening effect, for example, and finally to characterize the nonlinear properties of the system.

It is important to note that, despite of its importance in the study of nonlinear dynamics, the thesis will not present any kind of study about the mathematical theory developed around nonlinear oscillations, like the theory of stabilization and other theories related with the resolution of differential equations, because the aim of this study is about nonlinear identification.

1.4 Outline

In this section the content of the remaining chapters is summarised:

- **Chapter 2** - Brief introduction to nonlinear dynamics and nonlinear identification. In the first part there is the presentation of the common sources of nonlinearity and characteristics of nonlinear resonances, and at the second part the different concepts associated to nonlinear identification are presented, with a more detailed study on structural model updating;

- **Chapter 3** - Presentation and study of the nonlinear time integration procedure and time transformation technique to be used on this thesis;

- **Chapter 4** - The nonlinear characterization technique to be used on this thesis is studied by presenting its foundations, limitations and disadvantages, with the application of some practical examples;
- **Chapter 5** - The fundamentals of model order reduction are presented, with the presentation of the two different approaches. At the end of the chapter the chosen model order reduction technique is applied to a cantilever beam, and then on the generated model is applied the Acceleration Surface Method. On that example it is also explained the incorporation of the reduced model at the Newmark algorithm;
- **Chapter 6** - The finite element model of the airplane is presented and the different steps associated to the experimental procedure are explored. At the final part of the chapter the theoretical background and the procedure associated to the processing of the data obtained experimentally is presented;
- **Chapter 7** - The experimental modal model is extracted, and then correlated with the finite element model of the previous chapter. After validation of the linear model, it is done a analysis to the evolution of the answer of the system with the applied force and the nonlinearity of the system is characterized;
- **Chapter 8** - The structural model update is realized. Different ways of characterizing the nonlinearity are tested and analysed by comparison with the experimental results;
- **Chapter 9** - The conclusions of this thesis are presented.

CHAPTER 2

Brief literature review

2.1 Nonlinear dynamics

In nature most of the phenomena are nonlinear, and "straight lines" are just a mathematical abstraction. Like it is stated at [1] "Nature does not recognize straight lines" and like it was said on section 1.1, nonlinear dynamics doesn't allow the utilisation of different concepts associated to linear dynamics, like modal analysis or superposition principle, and for these reasons it is important to do brief introduction to this theme by presenting its causes and its "special particularities".

2.1.1 Causes

There are many different factors that can induce a nonlinear behaviour, but in general terms, they can be grouped in the following sources [1, 2]:

- Geometrical nonlinearities – characterized by the occurrence of large displacements or rotations. A very typical example, which is presented in almost all literature is the pendulum movement, which can be described by the following equation:

$$\ddot{\theta} + \frac{g}{l}\sin(\theta) = 0$$

  If only small oscillations occur the term $\sin(\theta)$ can be approximated by θ, and the equation of movement is linear. If large oscillations happen ($\theta > 20°$) that simplification cannot be done and the equation is nonlinear.

- Inertia nonlinearity – characterized by the presence of nonlinear terms containing velocities or accelerations in the equations of motion. An example of that, is the Coriolis acceleration in bodies moving relatively to rotating frames.

- Material nonlinearities – it occurs when the constitutive law of the material relating stress and strain is not linear.

- Damping dissipation – damping is essentially a nonlinear phenomenon and the modal damping approximation is many times not an appropriate approximation. An example of nonlinear damping are the dry friction forces between two bodies in contact.

- Nonlinear boundary conditions - Can be associated with the presence of clearances, loose joints or external nonlinear body forces like magnetic forces, for example. A typical example of this last case, in the motion of a beam subjected to a magnetic field.

Besides those causes, nonlinearities can be originated by damage in the structure like the appearance of fatigue cracks or rivets and bolts that subsequently open and close under dynamic loading or internal parts impacting each other.

2.1.2 Nonlinear oscillations and resonance

After presenting the concept of a nonlinear response and its causes, it is important to see some characteristics of their oscillations and specially in the resonance area, because it is probably where the most interesting "peculiarities" can be found.

When analyzing a nonlinear response of a dynamical system, a characteristic that can quickly be identified is the frequency in which the response occurs. While in a linear system the frequency of the response is equal to the frequency of excitation, in a nonlinear system that doesn't occur. In a nonlinear system, besides the main harmonic component (frequency of the excitation) two other groups of harmonics can appear, the superharmonics which have a frequency equal to an integer number of the main harmonic (2ω, 3ω...) and the subharmonics which have a frequency equal to a fraction of an integer number ($1/2\omega$,...) of the main harmonic (in some cases the response in a nonlinear system to a harmonic excitation may not even be periodic). Relatively to the generation of the harmonics it is known that the even order nonlinearities generate even harmonics and odd nonlinearities tend to order odd harmonics. The phenomena of superharmonic frequencies will be viewed in the next chapters, via time-frequency plot [4].

Considering the existence of superharmonics and subharmonics components, instinctively it is possible to "imagine" the occurrence of resonance without exciting the resonance frequency, because, for example, if the excitation force is at $1/2\omega_r$, the harmonic 2ω will be at the resonance frequency of the system. These phenomena are called superharmonic and subharmonic resonance and in some cases can be a modal interaction. The term modal interaction is due to the fact that one excitation force can be applied to a certain modal frequency, but due to the presence of the other harmonics, other modes can undergo in large-amplitude oscillations [4, 5]. Let´s now consider the following picture:

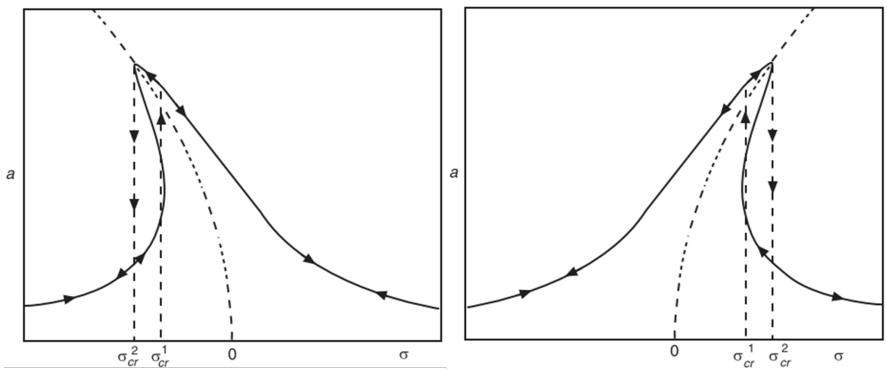


Figure 2.1: Response curves for a resonantly excited and damped SDOF nonlinear system with softening behaviour (left) and hardening behaviour (right) [4]

In the figure, where a is the amplitude and σ is the frequency, others very typical behaviours can be observed. One of them are the "jumps", which consists in a "vertical" or "abrupt" variation of the system amplitude answer. Associated to the jumps, there is a second phenomenon that can be seen, designated as "hysteresis". This "hysteresis" is not the one associated with hysterical springs, but yes, the difference between the paths followed by the system answers when subjected to forward and backward variations in the excitation frequency. The last features that are displayed are the hardening and softening effects, which reflects the frequency dependence on the amplitude vibration. If the frequency where the peak occur is above the linear natural frequency, the nonlinearity causes a hardening effect on the system (increase on stiffness), and if the opposite behaviour happens, there is a softening effect [2, 4].

Besides those characteristics of nonlinear resonance and dynamics, there are other phenomena like resonance capture, bifurcations, chaos, etc. But the focus of this thesis is on nonlinear identification, and for that reason these topics will not be further explored.

2.2 Nonlinear identification

As it is normal in any engineering field, everyday the performance requirements demanded on dynamical structures are getting higher and higher, and for that reason the presumption that a system has a perfectly linear behaviour, sometimes can no longer be used, and the consideration of the nonlinear aspects is necessary to achieve better results. When it is not easy to characterize or predict analytically the performance of a system, the solution is always the same, which is to carry out experimental tests. In that context there is an engineering field denominated as "Nonlinear System Identification" that allows the characterization of the system similarly to what is done in experimental modal analysis. This procedure is constituted by the three following steps [2, 6]:

- Detection – Does the system present any kind of nonlinearity?
- Characterization – Where is the nonlinearity located? What type of nonlinearity is it? What is the functional form of the nonlinearity?
- Parameter estimation – Determination of the nonlinear coefficients.

2.2.1 Detection

The step of detecting the nonlinearity is done by analyzing if the system response violates any of the fundamental's characteristics of linear systems, like the superposition or homogeneity principle, or if one of the characteristics of nonlinear systems appears, like the jumps for example. Considering this last characteristic, one of the ways to see if the system is nonlinear is to analyze its response to a sine-sweep frequency excitation in the plot *"response vs sweep frequency"*. If the system is linear, in the resonance area it is expected to see an approximately symmetric shape, because since there is no "jump" or hardening effect, there will be a gradual evolution of the amplitude in the resonance zone, and the shape of the envelope of the response will be smooth, without any kind of vertices on its shape. Besides that, considering what was exposed on fig. 2.1, an alternative is to plot the sweep-up and sweep-down responses, because if a linear behaviour is present, the shapes will almost perfectly overlay, and not totally due to the transient effect of the answers, while if a nonlinearity is present, the resonance peaks will be clearly separated and reveal hysteresis. Using the same type of plots, an also good

way to detected nonlinearity is to see the symmetry of the oscillations around the equilibrium position, because in some nonlinear cases the system may present bigger displacements in one of the directions. In the next figure, it is possible to see very clearly the jump phenomena at 9.4 Hz, the nonsmoothness of the envelope for negative displacements around 7.5 Hz and the nonsymmetric response around the equilibrium position [2, 6]. These and other characteristics from nonlinear responses will also be shown for the application of this thesis.

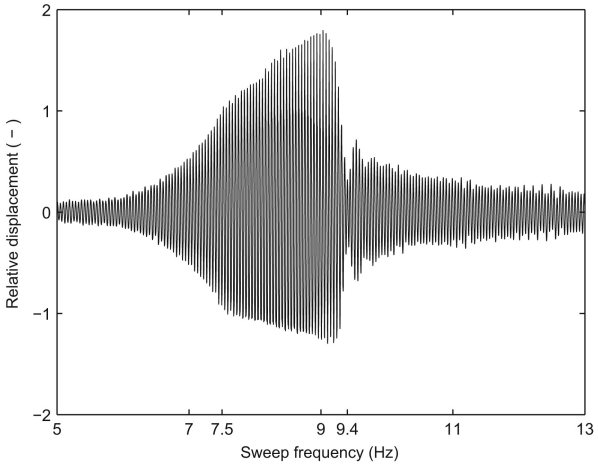


Figure 2.2: Sine-sweep answer example [6]

Besides the ways that were referred previously, at literature other techniques can be found like the utilization of the coherence function, which in a linear system should always be one. But like it is quoted at literature, the problem of this procedure is that it doesn't distinguish the situation where the deviation is caused by noise or by a nonlinear behaviour. Another common technique is the use of the Hilbert transformation which diagnoses the nonlinearity based on the measured FRF [2]. More information about this and other detection tools can be found in the literature listed at the bibliography.

2.2.2 Characterization and parametrization

Like exposed previously, the next step after detection is the characterization, which first step is the localization of the nonlinearity. Unfortunately this is mostly done by engineering judgement, because nonlinearities may often be located easily, at least for simple structures, by seeing which modal shapes are more deformed and corrupted by the nonlinearities or by simply assuming that the nonlinearity is localized where the relative displacement of the modes is bigger [2]. In the application of this thesis, since the location is already known, this topic will not be further explored.

The second goal, is to know what kind of nonlinearity it is, if it comes from stiffness or damping, or both, if it has hardening or softening characteristics, if it is weak or strong, and so on. To answer these questions different techniques like the restoring force surface (RFS) or the reverse path method are used. This step is important to answer the next question, which is "what is the functional form of the nonlinearity?". Only by doing a correct characterization it is possible to choose what kind of mathematical expression should be used to approximate the nonlinearity, like a cubic polynomial function or a piecewise function, etc. This task can be more challenging in situations where a hysteric stiffness is present (do not confuse with the hysteresis described in previous sections; they are different concepts) [2].

The last and final step is the parametrization of the nonlinearity. This step is somehow done almost simultaneously with characterization step, because for example, the RFS method is used to see what type on nonlinearity exists, and it can also be used to parametrize the nonlinearity, because after obtaining the surface, a curve fitting process can be done, and then the nonlinear identification process is complete. So, in short, these two steps are intimately connected to each other, and the big challenge is to choose the most adequate and efficient process to characterize and parametrize the nonlinearity [2, 6].

To perform these steps there are different techniques that can be grouped in the next way [2]:

- By-passing nonlinearity: linearization – as the name indicates this technique has the goal of linearize the nonlinear systems answer, in order to apply the very well-known techniques of linear analysis;
- Time-domain methods – a method is said to be time-domain if the analyzed data is in the form of time-series. A famous method included in this category is the restoring surface force method (RFS), which will be analyzed in a further section;
- Frequency-domain methods – similarly to the previous one, a method belongs to this category, if the data is processed in frequency domain (FRFs or spectra). Example of methods inside of this category are the Voltera and Wiener series, and the reverse path method;
- Modal methods – these methods pretend to characterize the nonlinearity in the modal space. In order to do that, the concept of nonlinear normal modes (NMN) is used;
- Time-frequency analysis – The method uses the data in the time-frequency form, which provides a good inside of the dynamics of the nonlinear systems since it allows the decomposition of the response on its different harmonics. Very well-established methods are the wavelet and Hilbert transforms, but in recent years other methods have appeared like the empirical mode decomposition (EMD) for example;
- Black-box methods – these are methodologies that are applied to the situation where there is no parametric model known previously. This field evolves the use of artificial neural networks, wavelet networks, splines and neuro-fuzzy networks. Examples of methods that included in this category are the NARMAX and NARX models;
- Structural model updating – this procedure consists in the updating of a finite element model according to the realized experimental measurements.

2.2.3 Structural Model Updating

Since this is the central topic of this thesis, a special attention will be given to this subject. As it is known, finite element models are the most used tool in engineering to evaluate/characterize a system, which can for example, evolve studying stress distributions, doing fatigue calculations, and determining the modal modes and frequencies. Only in special occasions, experimental activities are performed. But since these models are numerical and based in some physical assumptions that sometimes may not be accurate, errors will exist, and in some situations may not have the desired correspondence with the real model, and when those situations occur, updates based in experimental data are done to the model to improve its accuracy. Examples of those situations are when a linear finite model is used, and

the system presents nonlinearities, or even when a nonlinear solver is used, like *NASTRAN SOL129*, but the model doesn't predict well the nonlinearity [2, 6].

The structural model updating process is composed by the following steps:

- Experimental measurements and structural modeling – as it obvious, the first steps are to build a numerical model and to perform experimental measurements. The experimental procedure is a critical step, since for example, the location and number of sensors to be used should be carefully considered in order to distinguish situations like the first and second bending modes, or the first and second torsional modes of a generic system. Besides that, precautions should be taken to avoid exterior interferences like the weight of the cables used to connect the sensors to the data collector device. Bad measurements will not certainly contribute to obtain a good model;

- Feature extraction and correlation study – this step consists in processing the experimental data and perform a correlation study to evaluate the accuracy or quality of the numerical model. A correlation study can be for example, the comparison of the experimental modal modes with the numerical modal modes or can be the comparison of time-domain answers. This step will determine if an update of the model is necessary or not;

- Selection of the parameters to update – this is certainly the most critical procedure of the entire process, because if the correct parameters are not select the updating process will not be successful. In case of a nonlinear system update, a good location and characterization of the nonlinearity is critical;

- Minimization of the objective function – after selecting the parameters to update, the final step is to define a criterium for the process. There are different techniques proposed by different authors, and they can be found in [2].

The steps exposed previously will be done in this thesis, with the presentation of the finite element model, analysis of the experimental results, correlation, characterization of the nonlinearity, and by last the numerical update.

CHAPTER 3

Nonlinear integration and time-frequency transformation

3.1 Numerical integration methods

In order to perform the nonlinear simulations it is necessary to choose a methodology to perform the numerical calculations. As it is known, numerical integration methods are methods that allow the direct integration of the differential equation of motion without any manipulation of equations, unlike to what is done in modal analysis. There are different methods, but all they consist in ensure that the equation of motion is verified in some discrete time instants, separated by a time-step Δt. And the difference between the different methods, lies in their "variation law", which is a set of equations that allow the calculation of the variation of the different variables from t to $t + \Delta t$. There are different techniques, but probably the most known methods are [7]:

- Central difference method – This method is based in the approximation of the velocity and acceleration by the Taylor series expansion for the displacements at $t-\Delta t$ and $t+\Delta t$. After some algebraic manipulation, the following recurrence equation is obtained:

$$\left(\frac{1}{(\Delta t)^2}[M] + \frac{1}{2\Delta t}[C]\right)\{x\}^{t+\Delta t} = \{F\}^t - \left([K] - \frac{2}{(\Delta t)^2}[M]\right)\{x\}^t - \left(\frac{1}{(\Delta t)^2}[M] - \frac{1}{2\Delta t}[C]\right)\{x\}^{t-\Delta t}$$

  The previous expression is obtained from the equilibrium equation at the time instant t, and for that reason this is an explicit integration method. Besides that, since it is necessary to know the response at $t - \Delta t$ it is necessary an auxiliary start mechanism, and the integration procedure is not unconditionally stable;

- Wilson-θ – this method is an extension of the linear acceleration procedure, where the integration step is multiplied by a constant θ. This method presents the following

recurrence expression:

$$\left[[K]+\frac{6}{(\theta\Delta t)^2}[M]+\frac{3}{\theta\Delta t}[C]\right]\{x\}^{t+\theta\Delta t}=\{F\}^t+\theta\left(\{F\}^{t+\Delta t}-\{F\}^t\right)$$
$$+[M]\left(\frac{6}{(\theta\Delta t)^2}\{x\}^t+\frac{6}{\theta\Delta t}\{\dot{x}\}^t+2\{\ddot{x}\}\right)+[C]\left(\frac{3}{\theta\Delta t}\{x\}^t+2\{\dot{x}\}^t+\frac{\theta\Delta t}{2}\{\ddot{x}\}^t\right)$$

This expression is obtained from the equilibrium equation at time instant $t+\Delta t$ and for that reason this is an implicit integration method. Unlike the previous method, it doesn't require any start auxiliary mechanism and is unconditionally stable (independently of time-step value) for $\theta > 1.37$;

- Newmark method – similarly to the Wilson-θ method, this procedure is also an extension of the linear acceleration method, with the difference that in this method two new parameters are inserted, α and β. This method has the next recurrence law:

$$\left[\frac{1}{\beta(\Delta t)^2}[M]+\frac{\alpha}{\beta\Delta t}[C]+[K]\right]\{x\}^{t+\Delta t}=\{F\}^{t+\Delta t}+[M]\left(\frac{1}{\beta(\Delta t)^2}\{x\}^t+\frac{1}{\beta\Delta t}\{\dot{x}\}^t+\right.$$
$$\left.\left(\frac{1}{2\beta}-1\right)\{\ddot{x}\}^t\right)+[C]\left(\frac{\alpha}{\beta(\Delta t)^2}\{x\}^t+\left(\frac{\alpha}{\beta}-1\right)\{\dot{x}\}^t+\frac{\Delta t}{2}\left(\frac{\alpha}{\beta}-2\right)\{\ddot{x}\}^t\right)$$

According to what was stated for the previous methods, this is an implicit integration method, and the variables β and α are parameters related with the precision and stability of the integration, and for the Newmark procedure they assume the values of 1/4 and 1/2, respectively, and with these values the method is unconditionally stable. Beside that, the method doesn't need any kind of auxiliary start mechanism.

As it was seen previously, the first method presents the disadvantages of not being unconditionally stable and of needing an auxiliary start mechanism, presenting also a higher computational cost. Between the two remaining methods, the Wilson-θ procedure presents the disadvantage of having numerical damping [7], which induces extra damping to the system, and for those reasons, combined with the fact that is the most used procedure in literature, the Newmark method was chosen.

3.1.1 Newmark - nonlinear systems

In nonlinear systems the governing equation of motion can be defined as:

$$[M]\{\ddot{x}\}+[C]\{\dot{x}\}+[K]\{x\}+\{F_{nl}(\{\dot{x}\},\{x\})\}=\{F(t)\} \tag{3.1}$$

where $\{F_{nl}\}$ represents the contribution from the nonlinear damping and stiffness. For linear systems, the Newmark method is based in the following governing system of equations, which are in the base of the recurrence expression presented previously [7, 8, 9]:

$$\begin{cases}\{\dot{x}\}^{t+\Delta t}=\{\dot{x}\}^t+\Delta t\left((1-\alpha)\{\ddot{x}\}^t+\alpha\{\ddot{x}\}^{t+\Delta t}\right)\\ \{x\}^{t+\Delta t}=\{x\}^t+\{\dot{x}\}\Delta t+(\Delta t)^2\left(\left(\frac{1}{2}-\beta\right)\{\ddot{x}\}^t+\beta\{\ddot{x}\}^{t+\Delta t}\right)\end{cases} \tag{3.2}$$

In order to apply this set of equations to nonlinear systems it is necessary to use a mechanism to solve nonlinear equations. The most famous and efficient way to solve those problems is by using the Newton-Raphson algorithm, which works according to the next equations [8]:

$$[K]_{n+1}^{j-1}\{\Delta U\}_{n+1}^{j} = \{r\}_{n+1}^{j-1} \tag{3.3}$$

$$\{U\}_{n+1}^{j} = \{U\}_{n+a}^{j-1} + \{\Delta U\}_{n+1}^{j}\{r\}_{n+1}^{j} = \{f\}_{n+1}^{ext} - \{f\}_{n+1}^{int}\left(\{U\}_{n+1}^{j}\right) \tag{3.4}$$

$$\text{If} \quad \left|\left|\{r\}_{n+1}^{j}\right|\right| > \varepsilon_{tol} \quad \text{and} \quad j < N_{max.iter} \Rightarrow j = j+1 \tag{3.5}$$

where, $[K]_{n+1}^{j-1}$ is the tangent stiffness matrix, U_{n+1}^{j} is the variable to be incremented, $\{\Delta U\}_{n+1}^{j}$ is the increment and $\{r\}_{n+1}^{j-1}$ is the residue, which is given by the difference between the external and internal forces.

In order to incorporate the Newmark procedure in that algorithmic it is necessary to proceed to the linearization of its governing equation. The linearization will be done in order to $\{\ddot{x}\}^{t+\Delta t}$, that will consequently lead to an iterative procedure based on acceleration increments. Considering the previously exposed governing equation of motion for nonlinear system, eq. 3.3 can be written as [10, 8, 9]:

$$\frac{\partial}{\partial\{\ddot{x}\}_{t+\Delta t}^{j-1}}\Big([M]\{\ddot{x}\}_{t+\Delta t}^{j-1} + [C]\{\dot{x}\}_{t+\Delta t}^{j-1} + [K]\{x\}_{t+\Delta t}^{j-1} + \{F_{nl}(\{\dot{x}\}_{t+\Delta t}^{j-1}, \{x\}_{t+\Delta t}^{j-1})\}\Big)\{\Delta\ddot{x}\}_{t+\Delta t}^{j} = \{r\}_{n+1}^{j-1} \tag{3.6}$$

Now, considering the equations 3.2 and calculating the derivative in order to $\{\ddot{x}\}^{t+\Delta t}$:

$$\left([M] + \alpha\Delta t[C] + \beta(\Delta t)^2[K] + \frac{\partial}{\partial\{\ddot{x}\}^{t+\Delta t}}\{F_{nl}(\{\dot{x}\},\{x\})\}\right)\{\Delta\ddot{x}\}_{t+\Delta t}^{j} = \{r\}_{t+\Delta t}^{j-1} \tag{3.7}$$

The derivative of the last term of the equation will depend on the type of nonlinearity that system possesses. To simplify the understanding of this procedure, let´s consider that the kind of nonlinearity that will be treated is a spring nonlinearity of type $K_{nl} \times x^n$. Considering that, the previous equation can be rewritten as:

$$\left([M] + \alpha\Delta t[C] + \beta(\Delta t)^2[K] + \beta\,(\Delta t)^2\left(\frac{\partial\{F_{nl}\}}{\partial\{x\}_{t+\Delta t}^{j-1}}\right)\right) = \{r\}_{t+\Delta t}^{j-1} \tag{3.8}$$

The term $\frac{\partial\{F\}_{nl}}{\partial\{x\}_{t+\Delta t}^{j-1}}$ is commonly known as the Jacobian matrix. So, that means, that the term has the following structure [9]:

$$\frac{\partial\{F_{nl}\}}{\partial\{x\}_{t+\Delta t}^{j-1}} = \begin{bmatrix} \frac{\partial f_1}{\partial x_1} & \cdots & \frac{\partial f_1}{\partial x_n} \\ \vdots & \ddots & \vdots \\ \frac{\partial f_n}{\partial x_1} & \cdots & \frac{\partial f_n}{\partial x_n} \end{bmatrix} \tag{3.9}$$

Considering that the system contains only one nonlinear spring between the DOF i and j, for example, the matrix will have the next shape:

$$\frac{\partial\{F_{nl}\}}{\partial\{x\}_{t+\Delta t}^{j-1}} = nK_{nl}\cdot\begin{bmatrix} 0 & \cdots & 0 & \cdots & 0 & \cdots & 0 \\ \vdots & \ddots & \vdots & \ddots & \vdots & \ddots & \vdots \\ 0 & \cdots & (x_j-x_i)^{n-1} & \cdots & -(x_j-x_i)^{n-1} & \cdots & 0 \\ \vdots & \ddots & \vdots & \ddots & \vdots & \ddots & \vdots \\ 0 & \cdots & -(x_j-x_i)^{n-1} & \cdots & (x_j-x_i)^{n-1} & \cdots & 0 \\ \vdots & \ddots & \vdots & \ddots & \vdots & \ddots & \vdots \\ 0 & \cdots & 0 & \cdots & 0 & \cdots & 0 \end{bmatrix} \tag{3.10}$$

So, considering the previous equations, the Newmark algorithm for nonlinear systems can be summarised in the following steps:

1. Mechanical properties: $[M]$, $[C]$, $[K]$ and nonlinearity;
2. Initial conditions: $\{x_0\}$ and $\{\dot{x}_0\}$;
3. Calculation of acceleration at instant $t = 0$:

$$\{\ddot{x}\} = \left(\{F\}_0 - [C]\{\dot{x}\}_0 - [K]\{x\}_0 - \{F_{nl}(\{\dot{x}\}_0, \{x\}_0)\}\right)[M]^{-1}$$

4. Determination of $\{\ddot{x}\}$, $\{\dot{x}\}$, $\{x\}$ and $\{r\}$ for $j = 0$:
   (a) $\{\ddot{x}\}_{t+\Delta t}^{j=0} = 0$;
   (b) $\{\dot{x}\}_{t+\Delta t}^{j=0} = \{\dot{x}\}^t + \Delta t\left((1-\alpha)\{\ddot{x}\}^t + \alpha\{\ddot{x}\}^{t+\Delta t}\right)$
   (c) $\{x\}_{t+\Delta t}^{j=0} = \{x\}^t + \{\dot{x}\}\Delta t + (\Delta T)^2\left(\left(\frac{1}{2}-\beta\right)\{\ddot{x}\}^t + \beta\{\ddot{x}\}^{t+\Delta t}\right)$
   (d) $\{r\}^{j=0} = \{F\}_{t+\Delta t} - \left([M]\{\ddot{x}\}_{t+\Delta t}^{j=0} + [C]\{\dot{x}\}_{t+\Delta t}^{j=0} + [K]\{x\}_{t+\Delta t}^{j=0} + \{F_{nl}(\{x\}_{t+\Delta t}^{j=0})\}\right)$;
5. Newton-Raphson procedure. While $||\{r\}|| > \varepsilon_{tol}$ and $j < N_{max.iter}$ do:
   (a) $\{\Delta\ddot{x}\}^j = \{r\}^{j-1}\left([M] + \alpha\Delta t[C] + \beta(\Delta t)^2[K] + \beta\left(\Delta t\right)^2\left(\frac{\partial\{F_{nl}\}}{\partial\{x\}_{t+\Delta t}^{j-1}}\right)\right)^{-1}$;
   (b) $\{\ddot{x}\}_{t+\Delta t}^{j} = \{\ddot{x}\}_{t+\Delta t}^{j-1} + \{\Delta\ddot{x}\}^j$;
   (c) $\{\dot{x}\}_{t+\Delta t}^{j} = \{\dot{x}\}_{t+\Delta t}^{j-1} + \alpha\Delta t\{\Delta\ddot{x}\}^j$;
   (d) $\{x\}_{t+\Delta t}^{j} = \{x\}_{t+\Delta t}^{j-1} + \beta\left(\Delta t\right)^2\{\Delta\ddot{x}\}^j$;
   (e) $\{r\}^{j+1} = \{F\}_{t+\Delta t} - \left([M]\{\{\ddot{x}\}_{t+\Delta t}^{j} + [C]\{\dot{x}\}_{t+\Delta t}^{j} + [K]\{x\}_{t+\Delta t}^{j} + \{F_{nl}(\{x\}_{t+\Delta t}^{j})\}\right)$;

If nonlinear damping was also considered, the procedure would be identical, but instead of multiplying by $\beta(\Delta t)^2$, it would be by $\alpha\Delta t$, and instead of the difference between the displacements, the difference between the velocities would be considered.

3.2 Time-frequency transformation

Besides the numerical integration tools that are needed to perform the simulations in this thesis, another tool is intended to be used, which is the decomposition of the signal on its different harmonics, in order to detect the presence of superharmonics and subharmonics, which will allow to understand if the system is in a linear or nonlinear regime, and to evaluate the nature of the nonlinearity. To do that there are essentially two different methods, the Fast Fourier Transform (FFT) and its associated Matlab® function, *instfreq* and by last, the Wavelet transform.

3.2.1 Fourier Transform

The traditional Fourier Transform introduced by Joseph Fourier, can be written in the following way:

$$X(\omega) = \int_{-\infty}^{\infty} x(t) e^{-i\omega t}\, dt \tag{3.11}$$

That equation is made for continuous systems and in order to overcome the limitations associated to that, it was developed the Discrete Fourier Transform (DFT), and after that, was developed the Fast Fourier Transform (FFT) which is, shortly speaking, a faster way of the DFT. In practical terms, this method decomposes the signal into its sine functions of various frequencies, amplitude and phases, as it is exposed in the next figure [11, 12].

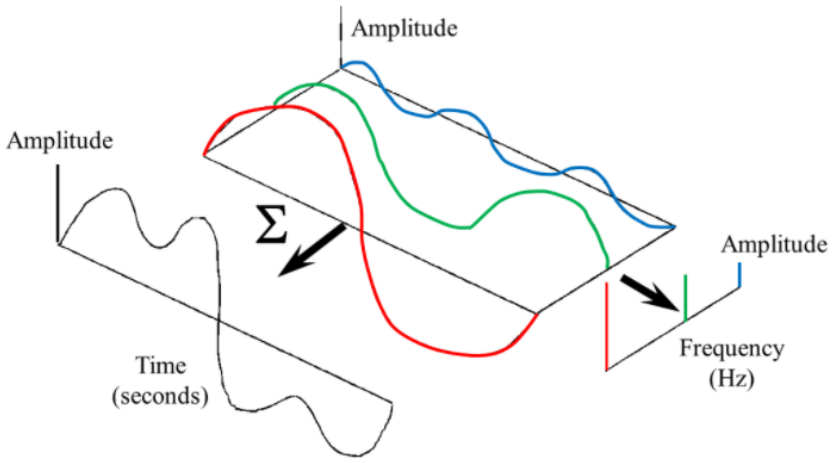


Figure 3.1: Working principle of the Fourier Transform [12]

This method has the big advantage of ensure full precision in the frequency content, but with zero precision in the time domain. This means that it is known for sure, that the signal has that frequency content but it is not known the time instant where that frequency was measured. This problem in signal processing is similar to the famous principle of Heisenberg on nuclear physics, because it is not possible to characterize simultaneously, with precision, the answer in the time domain and frequency domain. What happens, is that when using the FFT, a local signal information becomes a global information of the transformed. So basically, the information that is obtained, is the average amplitude of the individual frequencies over the entire signal, without any kind of information about its location or duration, but with full precision in frequency domain. And besides this disadvantage, there is also the disadvantage

related with the fact that the FFT cannot capture nonstationary signals since a FFT is the decomposition of a signal in a sum of sines, and consequently signals in which their properties (coefficients) change during time cannot be characterized [11, 12, 13].

To overcome the problem related with the time domain, there is a methodology called "Windowed Fourier Transform" (WFT) or "Short Time Fourier Transform" (STFT). This technique as the name indicates, consists in splitting the time domain in time-intervals and then apply the FFT to that domain. But, according to the principle of the uncertainty, there is an inverse relationship between time and frequency resolution, so consequently the frequency resolution will be lower. In Matlab® there is a function called "*instfreq*" that finds a compromise between these two quantities, allowing the user to get a good balance between the time and frequency resolution. Relatively to the nonstationary signals, this solves partially the problem, because in one hand can detect some local non stationarity, but at the same time since this is a FT, it still has the same limitation. But the main limitation of this technique is related with the fact that the FFT has a fixed relationship between time and frequency, unlike the Wavelet Transform that will be presented in the next section [11, 14, 15].

3.2.2 Wavelet transform

On this transform, the signal is decomposed in Wavelets instead of sine-waves. A wavelet is a function that rapidly increases, oscillates about a zero mean, and rapidly decays, this is, while a sine wave oscillates from $-\infty$ to ∞, a wavelet oscillates for a short time duration. The difference between these two signals is illustrated in the next figure [12]:

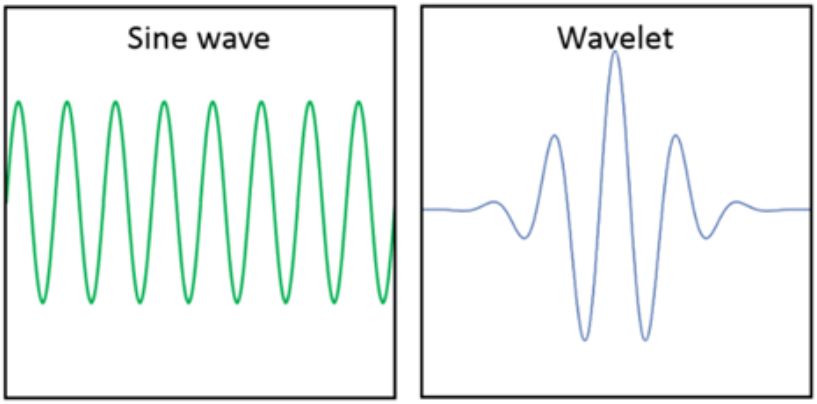


Figure 3.2: Difference between a sine and a wavelet wave [12]

The analyses of the signal using the Wavelet function is done by scaling and shifting the signal. The scaling process, is the one responsible by capture the frequency component, and its mechanism is straightforward, this means, the Wavelet is compressed and uncompressed, like it is presented at fig. 3.3. The stretched wavelets will capture the lower frequencies, while the compressed wavelets will capture the higher frequencies [12]. The shifting process is basically the process where the Wavelet passes through the signal, and during that process the wavelet is simultaneously scaled in order to better approximate the shape of the signal. So, what is the advantage comparatively with the STFT? The advantage is that with the WT a multi-resolution analysis is done, this is, it does not have a fixed relationship between time and frequency, as it can be observed in fig. 3.4. In the figure, CWT is WT. In literature the term continuous is omitted, similarly to what happens with the Continuous Fourier Transform that is mostly referred as Fourier Transform [12, 11, 14].

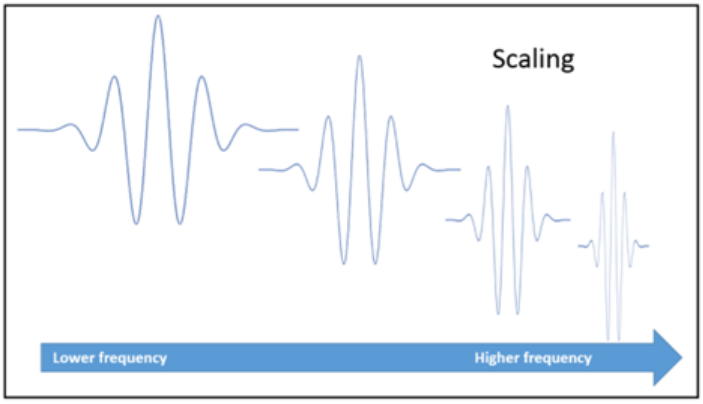


Figure 3.3: Scaling process in the Wavelet Transform [12]

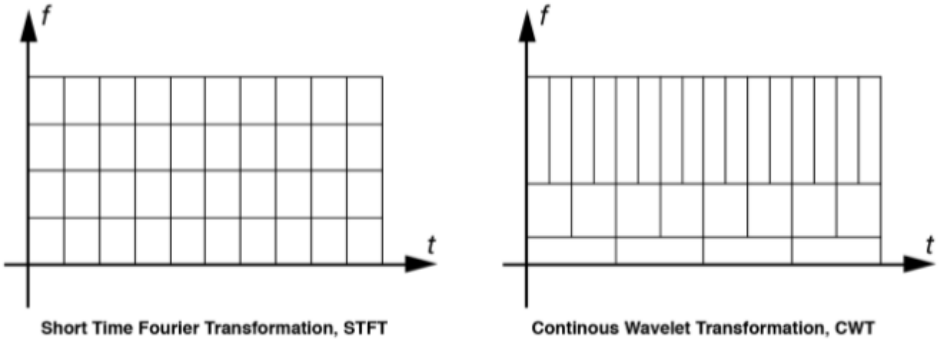


Figure 3.4: Resolution in a STFT and a in a WT [16]

This property represents the big advantage of WT, because in high frequencies the signal changes much faster, so in order to capture better those changes a higher resolution should be used, while in lower frequencies a larger resolution can be used. So, in short, the WT can use a higher or lower frequency resolution along the signal as it is needed. But, this approach presented previously, like it was already explained, is the "Continuous Wavelet Transform" (CWT), and despite of its advantages, has a high computational cost that restricts its use. An alternative to that method is the "Discrete Wavelet Transform" and associated to this one there is the "Multi-Resolution Analysis" (MRA), which is a "multi-level" version of the DWT. On Matlab® both functions are available - *dwt* and *wavedec* - and they require choosing a reference curve from the different wavelet family types that are available [11, 14].

Relatively to the nonstationary signals, there is a similar situation to SFTF. The approach is better, specially for long-range dependent data, but theoretically speaking, the problem still exists.

3.2.3 Final remarks

The Wavelet Transform is indeed better than STFT, but its application is not as straightforward as STFT, and would also require a deeper research. But since, the application of STFT has fulfilled its goals as it will be seen, which is the detection of other harmonics in the nonlinear response, the time-frequency plots presented in this work are all obtained by using the STFT.

CHAPTER 4

Nonlinear characterization

According to what was stated in chapter 2, at Model Structural Update one of its phases consists in characterizing the nonlinearities of the system. In that chapter different procedures were referred to do that, including the Restoring Force Surface (RFS) method, the Reverse Path (RP) method, the Conditioned Reverse Path (CRP) method or the Hilbert Transformation method, for example. Among those different techniques, the RFS and its variation, the Acceleration Surface Method (ASM), were chosen due to their simplicity and because they allow to visually see the shape of the nonlinearity, unlike the other methods.

4.1 Restoring force surface (RFS) method

This method as the name indicates is based in the restoring force concept. This concept is extracted through the Newton's second law:

$$m\ddot{x} + f(\dot{x}, x) = F(t) \tag{4.1}$$

where $f(\dot{x}, x)$ is the so called restoring force, m is the mass, $\ddot{x}$ is the acceleration, and *F(t)* is the excitation. Considering the general equation of motion from a nonlinear single degree of freedom system, the restoring force will be:

$$f(\dot{x}, x) = kx + c\dot{x} + F_{nl}(\dot{x}, x) \tag{4.2}$$

This shows that if the mass, acceleration and excitation are known it is possible to obtain a surface with the remaining properties of the system - damping and stiffness (linear and nonlinear). To extract only the stiffness or the damping properties, there is a very simple procedure that should be made: when the velocity tends to zero the RF will only be composed by its component relative to the stiffness and if the displacement tends to zero, the RF will only be composed by its component relative to the damping. By this way two 2D plots are obtained, and the stiffness and damping are extracted through a curve fitting procedure, which is usually done via the mean-square error method [17, 18].

This methodology for a one DOF system raises no doubts and questions about its efficiency, but for a system with MDOF that is not that simple, but in some cases can be applied. For that, let's consider the system from fig. 4.1.

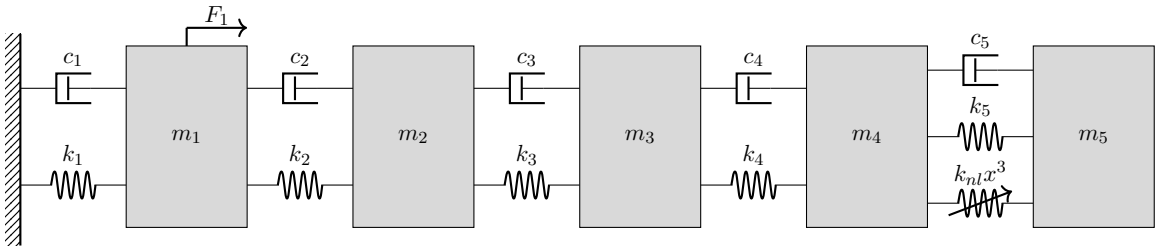


Figure 4.1: Nonlinear 5DOF system

From that system is possible to extract the next governing equation of motion:

$$\begin{bmatrix} m_1 & 0 & 0 & 0 & 0 \\ 0 & m_2 & 0 & 0 & 0 \\ 0 & 0 & m_3 & 0 & 0 \\ 0 & 0 & 0 & m_4 & 0 \\ 0 & 0 & 0 & 0 & m_5 \end{bmatrix} \begin{Bmatrix} \ddot{u}_1 \\ \ddot{u}_2 \\ \ddot{u}_3 \\ \ddot{u}_4 \\ \ddot{u}_5 \end{Bmatrix} + \begin{bmatrix} k_1+k_2 & -k_2 & 0 & 0 & 0 \\ -k_2 & k_2+k_3 & -k_3 & 0 & 0 \\ 0 & -k_3 & k_3+k_4 & -k_4 & 0 \\ 0 & 0 & -k_4 & k_4+k_5 & -k_5 \\ 0 & 0 & 0 & -k_5 & k_5 \end{bmatrix} \begin{Bmatrix} u_1 \\ u_2 \\ u_3 \\ u_4 \\ u_5 \end{Bmatrix}$$
$$+ \begin{bmatrix} c_1+c_2 & -c_2 & 0 & 0 & 0 \\ -c_2 & c_2+c_3 & -c_3 & 0 & 0 \\ 0 & -c_3 & c_3+c_4 & -c_4 & 0 \\ 0 & 0 & -c_4 & c_4+c_5 & -c_5 \\ 0 & 0 & 0 & -c_5 & c_5 \end{bmatrix} \begin{Bmatrix} \dot{u}_1 \\ \dot{u}_2 \\ \dot{u}_3 \\ \dot{u}_4 \\ \dot{u}_5 \end{Bmatrix} + k_{nl} \begin{Bmatrix} 0 \\ 0 \\ 0 \\ -(u_5-u_4)^3 \\ (u_5-u_4)^3 \end{Bmatrix} = \{F(t)\} \quad (4.3)$$

As expected for a MDOF system, the equations are coupled, and consequently it is not possible to just use the acceleration from one of the DOF and its excitation force if it exists, and then extract a surface. But, since this is a simple case, by just applying Newton's second law it is possible to extract stiffness and damping properties related with the DOF number 5:

$$m_5\ddot{u}_5 = -k_{nl}(u_5-u_4)^3 - k_5(u_5-u_4) - c_5(\dot{u}_5-\dot{u}_4) \quad (4.4)$$

From this equation it can be observed that the properties k_5, c_5 and k_{nl} can be known by considering the relative displacement and velocity between the DOF 5 and 4. This can somehow be interpreted as a "transformation of a MDOF equation in a SDOF equation", where in this case the single degree of freedom is the relative displacement.

Also, at the previous equation there is a detail, that distinguishes this situation from the SDOF case, which is the fact that no excitation force is applied. This is one of the conditions that is behind the Acceleration Surface Method (ASM). This method is characterized by the next equation [19]:

$$\ddot{x} \approx -f(\dot{x}, x) \quad (4.5)$$

At this expression an important detail is the non consideration of the mass, which in some situations may be unknown. Despite of that, it remains possible to observe the nature of the nonlinearity and the shape of the surface, which is exactly the same that is obtained considering the mass, but on other hand, there is a disadvantage, because by not considering the mass, it is not possible to quantify and characterize the nonlinearity, except obviously, in the situations where the mass is 1kg [19].

Considering again the system from fig. 4.1, besides the limitation relatively to the SDOF condition there are another limitations related with the "nonlinear connection". If the nonlinear connection is dependent upon more than two DOF, the method is obviously no longer valid and if the nonlinear connection is for instance between DOF 3 and 5, it will also be no longer valid, although in some cases it may be possible to see the shape or nature of the nonlinearity at the plot. This is explained in following equation:

$$m_5\ddot{u}_5 = -k_5(u_5 - u_4) - c_5(\dot{u}_5 - \dot{u}_4) - k_{nl}(u_5 - u_3)^3 \tag{4.6}$$

As it can be seen, two different relative displacements are involved, and for that reason it is not possible to just consider u_3 and u_5 to determine the nonlinear stiffness. This is basically a violation of the single degree of freedom hypothesis. Despite of that, in the application example it will be possible to see the nonlinear cubic shape, although, some points will be located outside the plane. But, if the remaining elements of the equation are considered, obviously a perfect cubic shape plane is obtained.

But the previous analysis was made for discrete systems. In a continuous system like the airplane to be treated on this thesis or a beam, the SDOF hypothesis is related with the natural coordinates, and that for its turn is related with the number of modes that are excited, and each mode has its own plane at the 3D plot, which slope is the square of the natural frequency. So, if more than one mode is excited, or if the remaining modes contribution is not negligible, a surface will not be obtained, although if the natural frequencies are close to each other it will be obtained an "approximate plane". This particularity will be further explored when applying this case to a beam and when analysing the experimental results.

So, in short there are three rules to apply the acceleration surface method:

- The excitation force in the considered DOF must be zero;
- The single degree of freedom hypothesis;
- Single nonlinear connection.

4.1.1 RFS - application example

For the application of this method the following system will be considered :

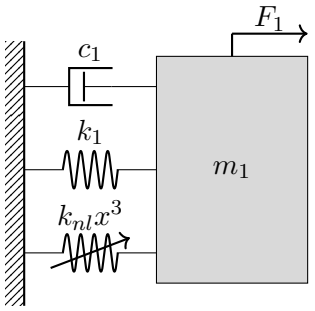


Figure 4.2: Nonlinear 1DOF system

This system presents the following properties:

- $m = 0.100\,\text{kg}$;

- $k = 500\,\mathrm{N/m}$;
- $c = 5\,\mathrm{Ns/m}$;
- $k_{nl} = 100\,000\,\mathrm{Nm}^{-3}$;
- $|F_1| = 50\,\mathrm{N}$.

For the excitation the application of a logarithmic sine-sweep will be considered, from 0-25 Hz during 40s, with a sampling frequency (Fs) of 400 Hz, and with the amplitude indicated previously. Since it is good to present the "simplest situation" to check the theory, at fig. 4.3 and 4.4 the RFS surface and stiffness and damping curves for the linear system are presented. In those plots is possible to visualize a perfect ellipse and at the 2D plots it can be verified that the slope is coincident with the stiffness and damping properties of the system. Then if the nonlinear stiffness is considered, according to what was previously exposed, a plane will also be obtained, but at this time with a cubic shape, and that is what was obtained in fig. 4.5, and in fig. 4.6. At the damping curve, since no nonlinear damping is considered, a curve equal to the linear case is obtained, as expected.

Since this may have some importance, it is good to see the difference in the obtained results when using a linear sweep. At the results exposed in fig. 4.7 and 4.8, it can be seen that at the 3D plots there are some differences, but the differences that are really important to note are the ones at the 2D plots, since it is from those plots that the properties of the system will be extracted. And comparing the two situations, in the logarithmic case there is a bigger concentration of points around zero, while for the linear case there are almost no points in that region, revealing in this way that it is preferable to use logarithmic sweeps. For that reason, in the experimental work all the plots were obtained using a logarithmic sine-sweep, although in some theoretical examples that will be shown on this work, the plots will be obtained through a linear sweep, because since they are theoretical cases, the points will always fit perfectly the curves. At the same time, it will be seen that this is not a "pure rule", this is, in some cases as it will be seen, a linear sweep also allows a good point distribution around zero.

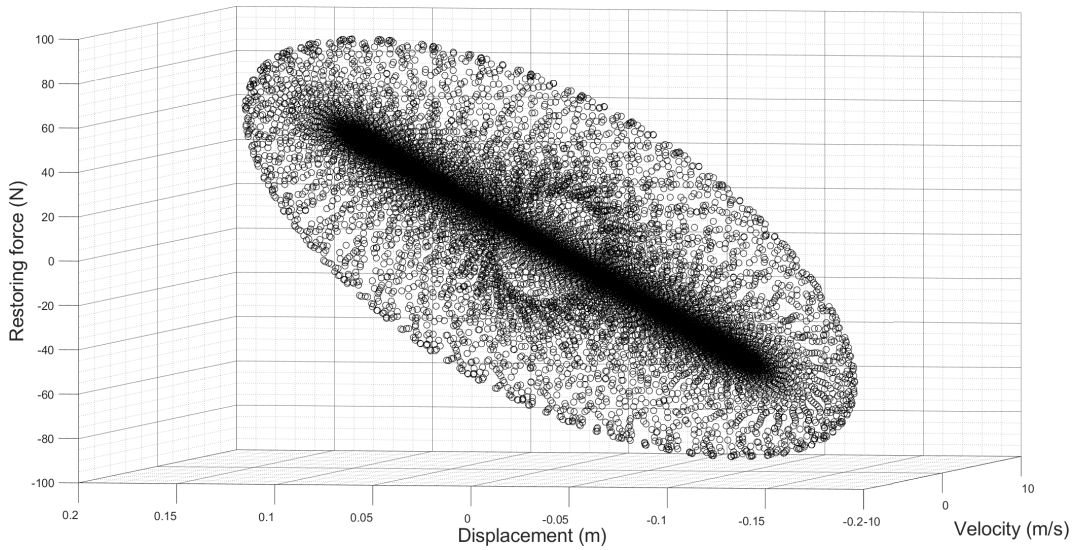


Figure 4.3: Restoring force surface - linear case

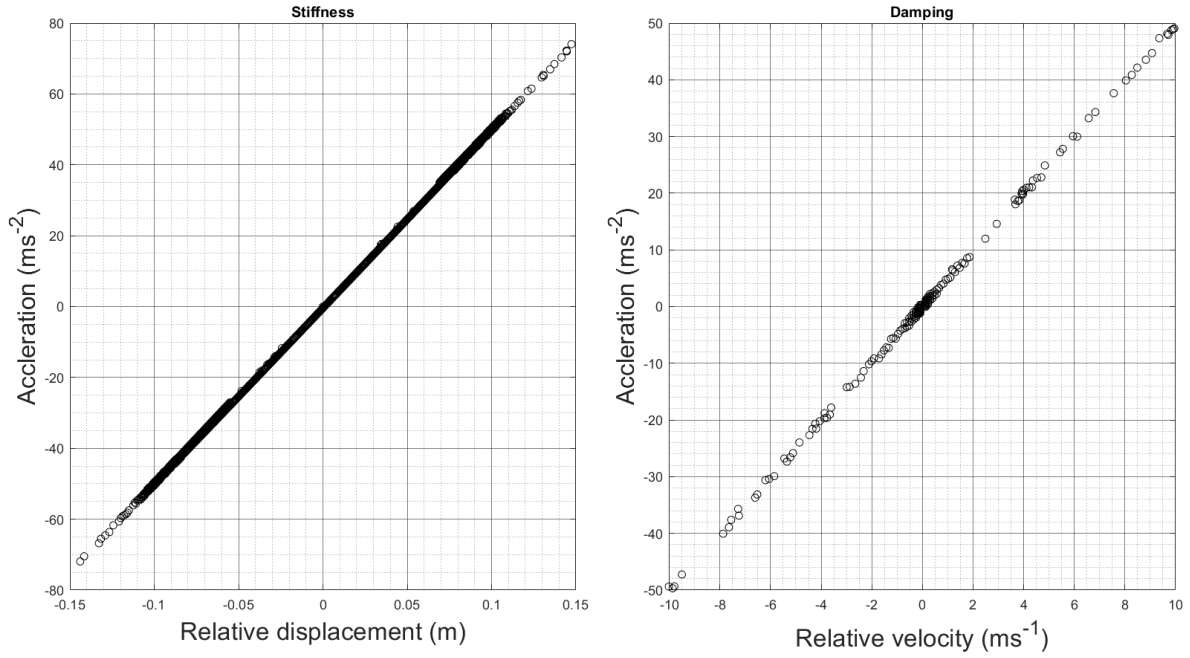


Figure 4.4: Stiffness and damping curves - linear case

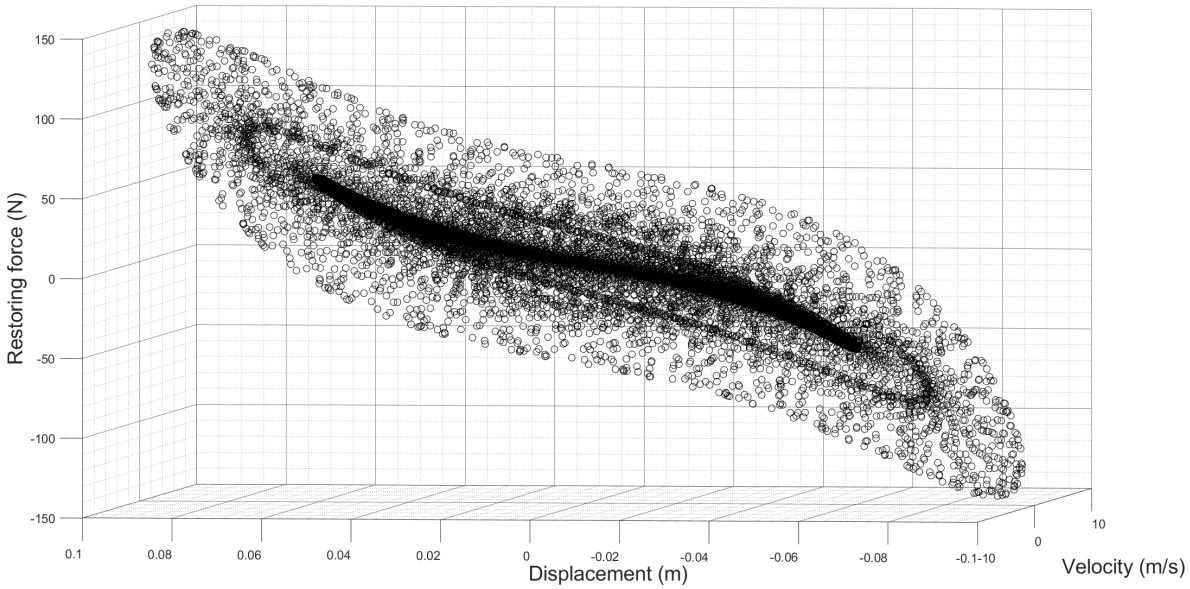


Figure 4.5: Restoring force surface - nonlinear case

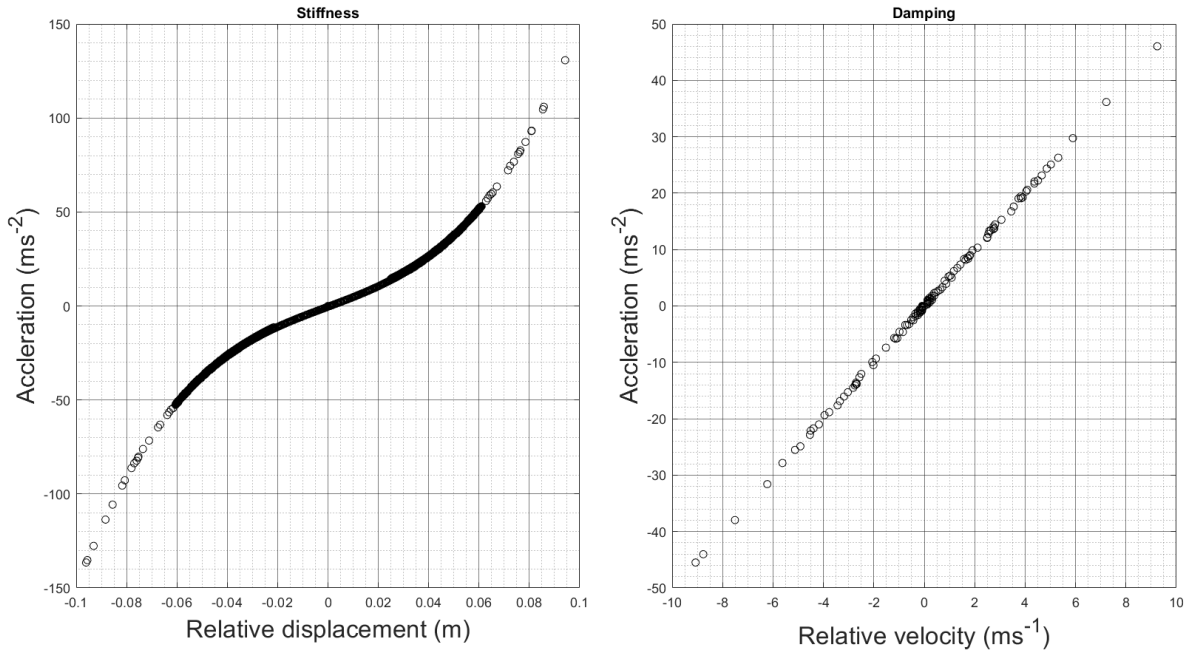


Figure 4.6: Stiffness and damping curves - nonlinear case

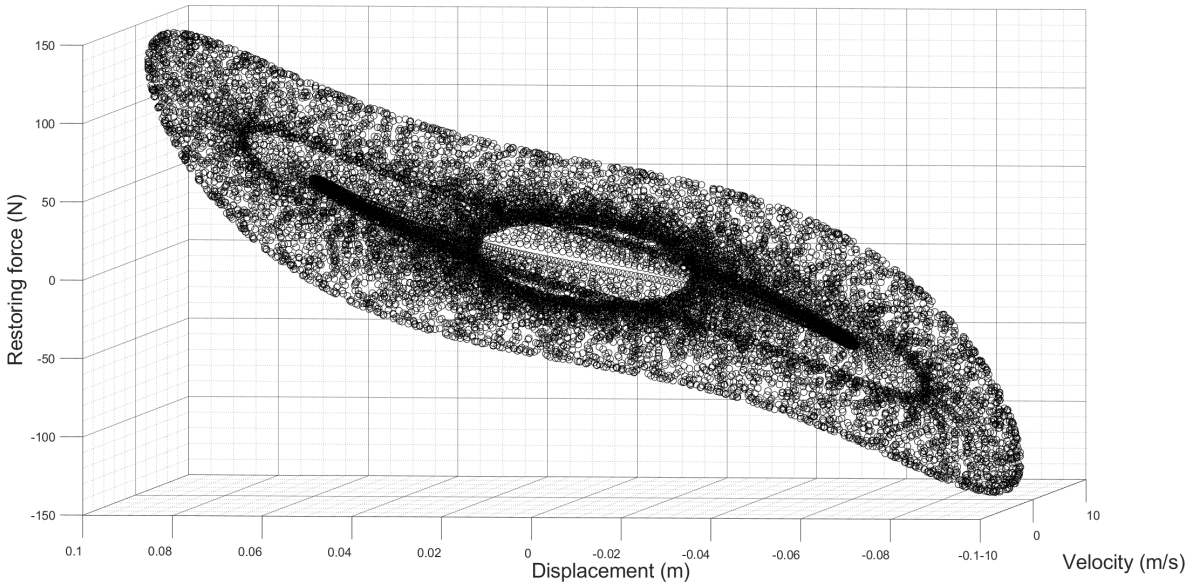


Figure 4.7: Restoring force surface - nonlinear case with linear sine-sweep

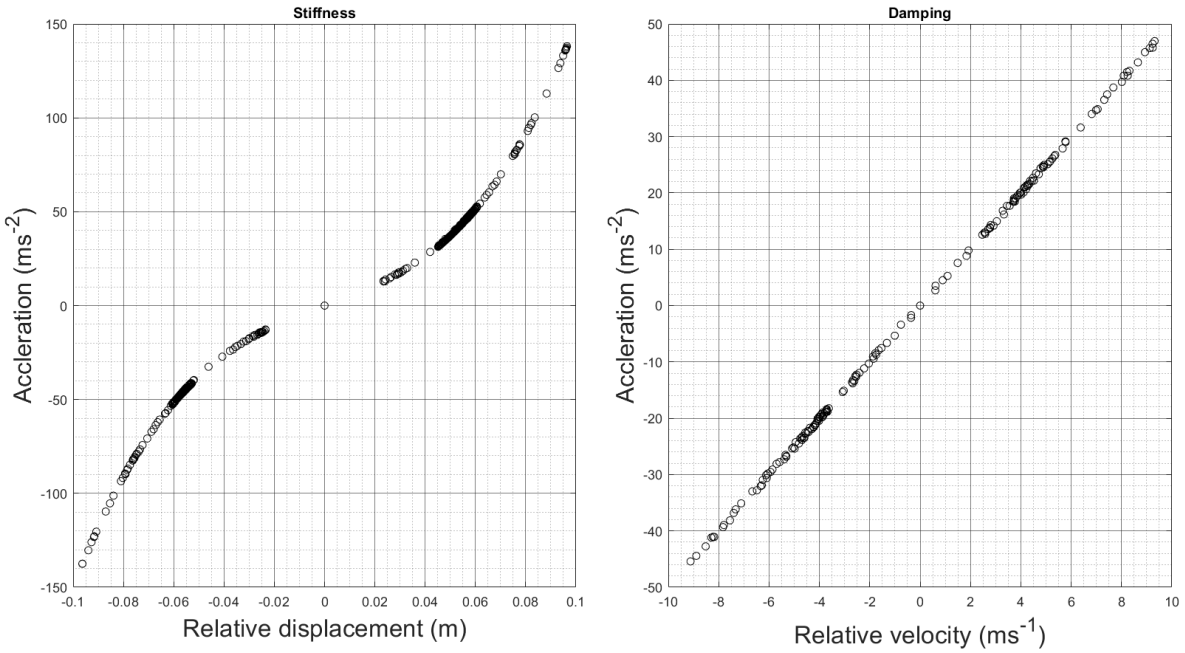


Figure 4.8: Stiffness and damping curves - nonlinear case - linear sweep

4.1.2 ASM - application example

Before presenting the example itself, let's consider again the previous example and instead of using the restoring force, only the acceleration is used. At the plots from fig. 4.9 and 4.10 it can be seen that when the condition of zero excitation is not fulfilled, is not possible to obtain a surface or characterize the properties of the system.

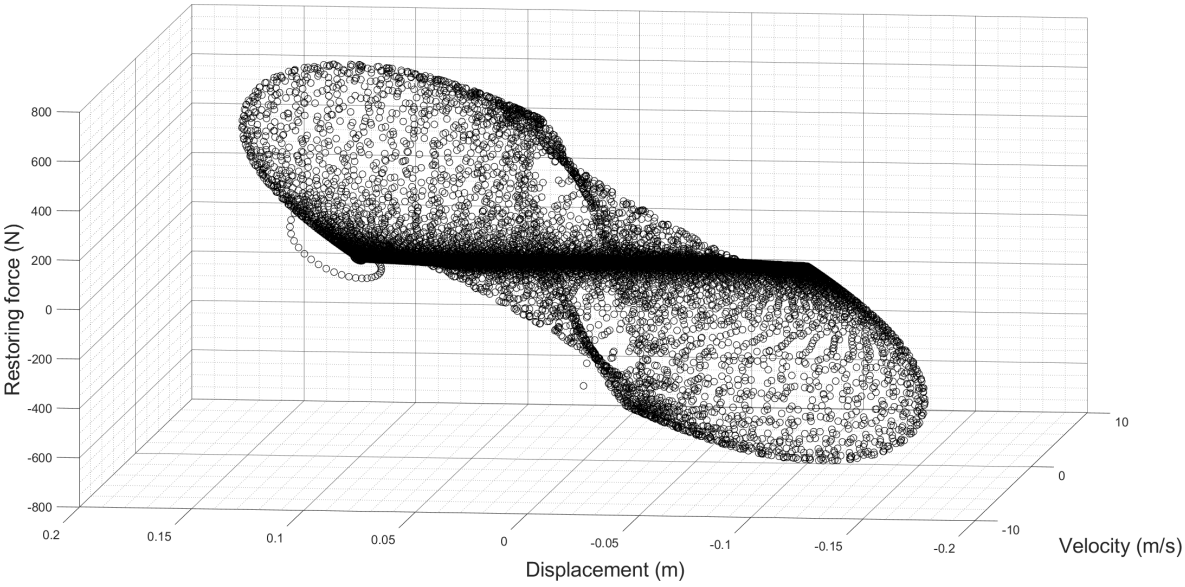


Figure 4.9: Acceleration surface for the SDOF system

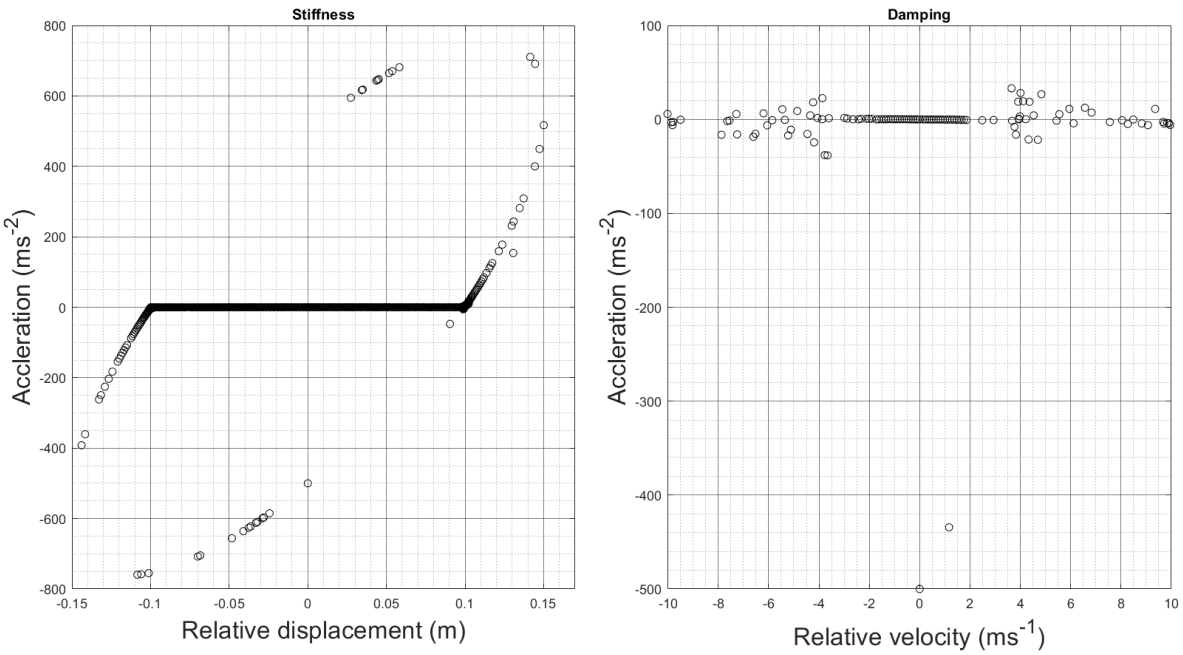


Figure 4.10: Stiffness and damping curves for the SDOF system using ASM

But, like it was stated at the first section of this chapter, the ASM is a method to be mostly applied to MDOF systems. So for this method, let's consider the system from fig. 4.1 and the next properties:

- $m_1 = m_2 = m_3 = m_4 = m_5 = 0.2\,\mathrm{kg}$;
- $k_1 = k_2 = k_3 = k_4 = k_5 = 5000\,\mathrm{N/m}$;
- $c_1 = c_2 = c_3 = c_4 = c_5 = 10\,\mathrm{Ns/m}$;
- $k_{nl} = 500\,000\,\mathrm{Nm}^{-3}$;
- $|F_1| = 1000\,\mathrm{N}$

Again, by considering a logarithmic sine-sweep (5-50Hz, 40s, Fs=400Hz), at fig. 4.11 and 4.12 the acceleration surface, and stiffness and damping curves are obtained. As expected, the surface and the stiffness curve have a cubic shape, and the damping curve is a "straight" line. Once again it is important to have in mind that this is not a quantitative method, since the mass is not considered.

Since this is a theoretical example with all variables under control, it is a good moment to check the performance of the STFT presented in the previous chapter, and for that the fig. 4.13 is presented. In that plot it can be visualized the presence of other than the first harmonic. According to what was indicated at section 2.1.2, if an odd stiffness is used, odd harmonics will appear. This can be verified through the vertical line done in plot, where the frequency from the superharmonics are $3\omega_1$, $5\omega_1$ and so on (ω_1 is the frequency of the main harmonic). A question that might be raised by looking at the plot, is the vertical yellow "line" around 5 Hz, and the reason of that line is related with the fact that on that region is located the first resonance frequency of the system, which is the region where the nonlinear behaviour is born. By last, the shape of the lines is not logarithmic because in the X axis

is used the sweep frequency and not the time variable. If time is used a logarithmic shape is obtained, as exposed in fig 4.14. Besides these plots, others could have been made to show the particularities of a nonlinear answer, like the "jump" phenomenon, that will be seen in posterior chapters. But the goal of these plots was mainly to prove that the utilization of STFT is valid and allows perfectly the identification of the other harmonics.

By end, in order to illustrate the topic related with the nonlinear connection from 4.1, it will be considered that the nonlinearity is connected between DOF 3 and 5. Looking to the plots from fig. 4.15 and 4.16 it can be confirmed what was previously stated, this is, it is possible to verify that the nature of the nonlinearity is cubic, but there are points outside the plane, which is obvious considering the equation 4.6. If the other remaining variables of the equation are considered perfect plots are obtained, like it is illustrated on fig. 4.17.

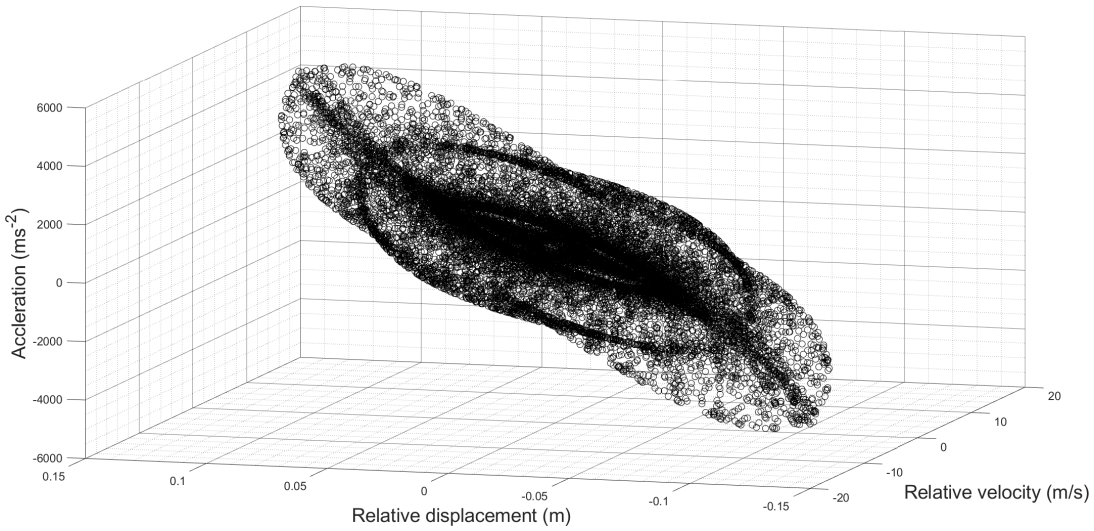


Figure 4.11: Acceleration surface

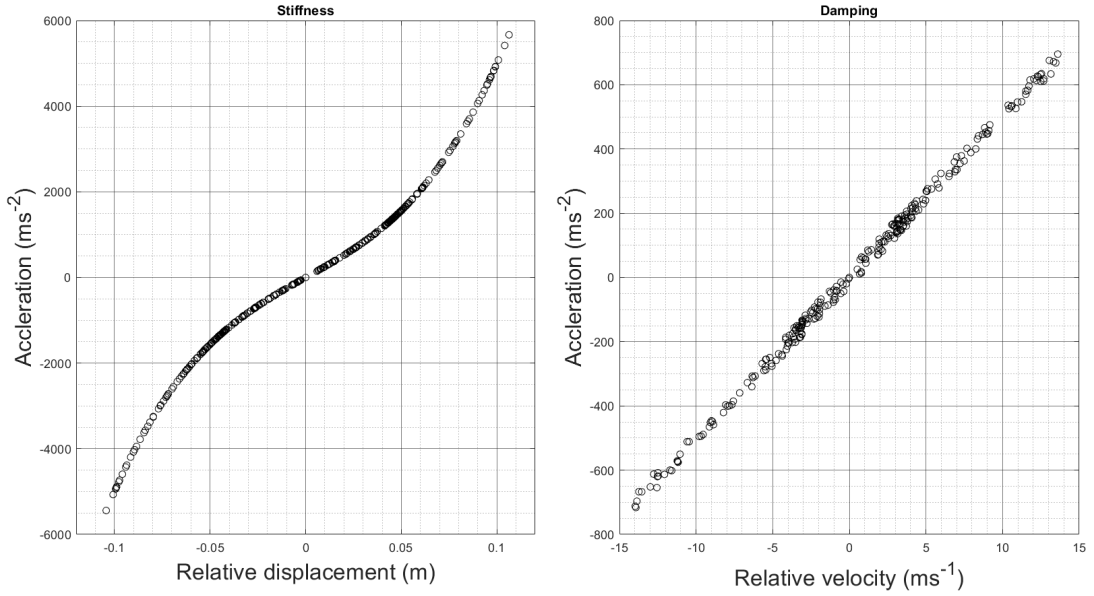


Figure 4.12: Stiffness and damping curves

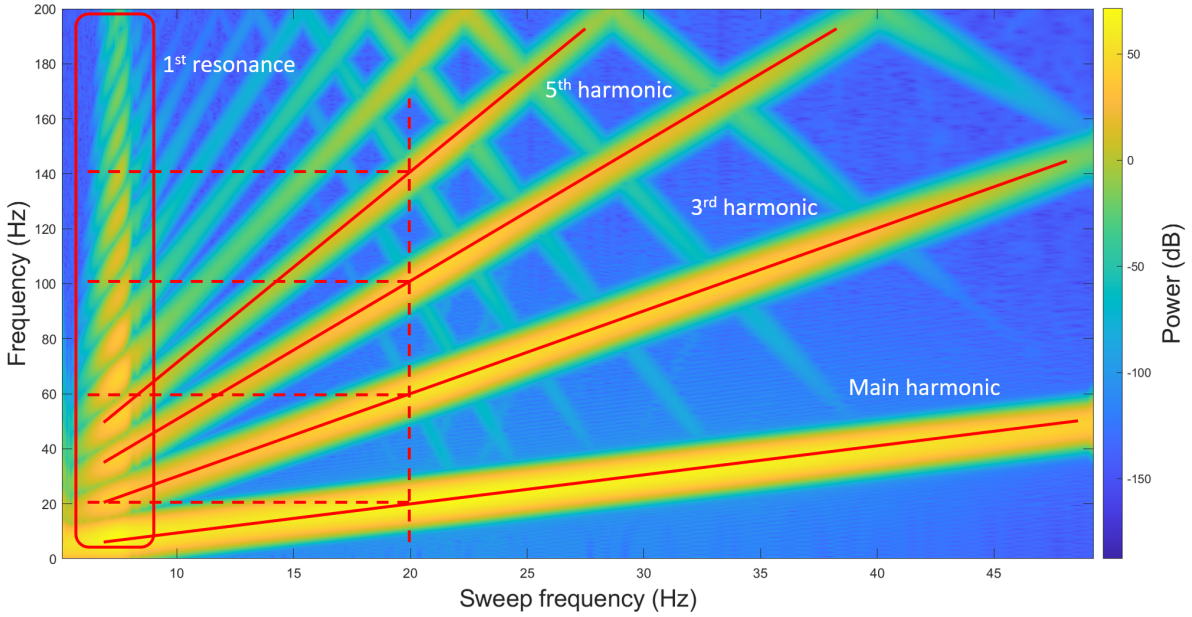


Figure 4.13: Time-frequency plot with the indication of the different harmonics

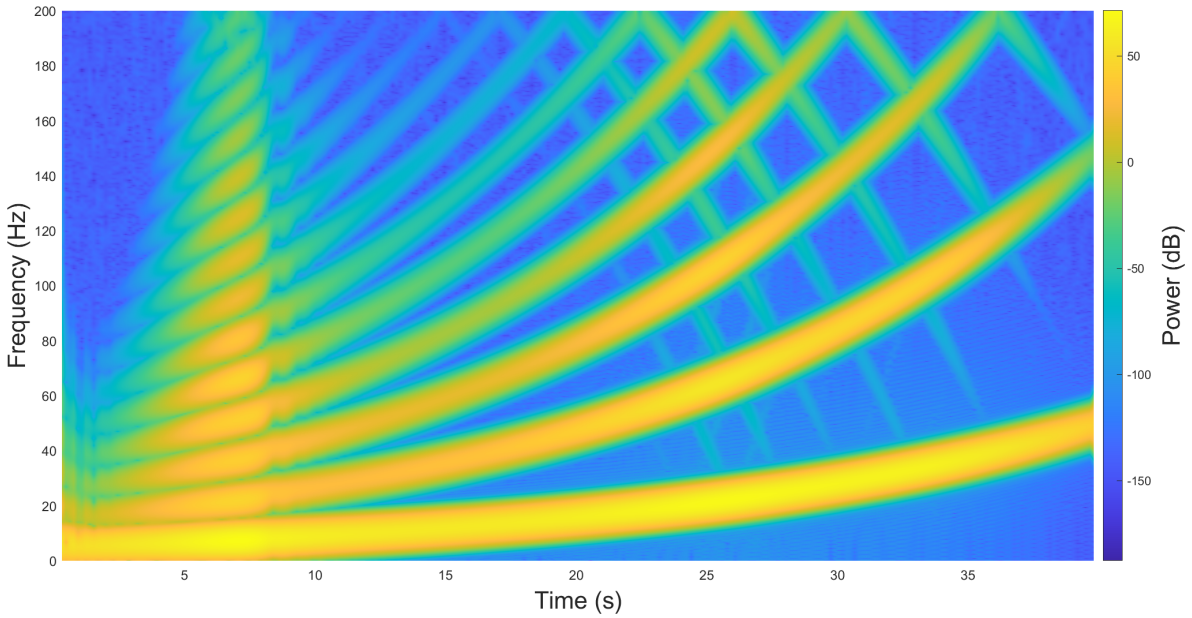


Figure 4.14: Time-frequency plot using time at X axis

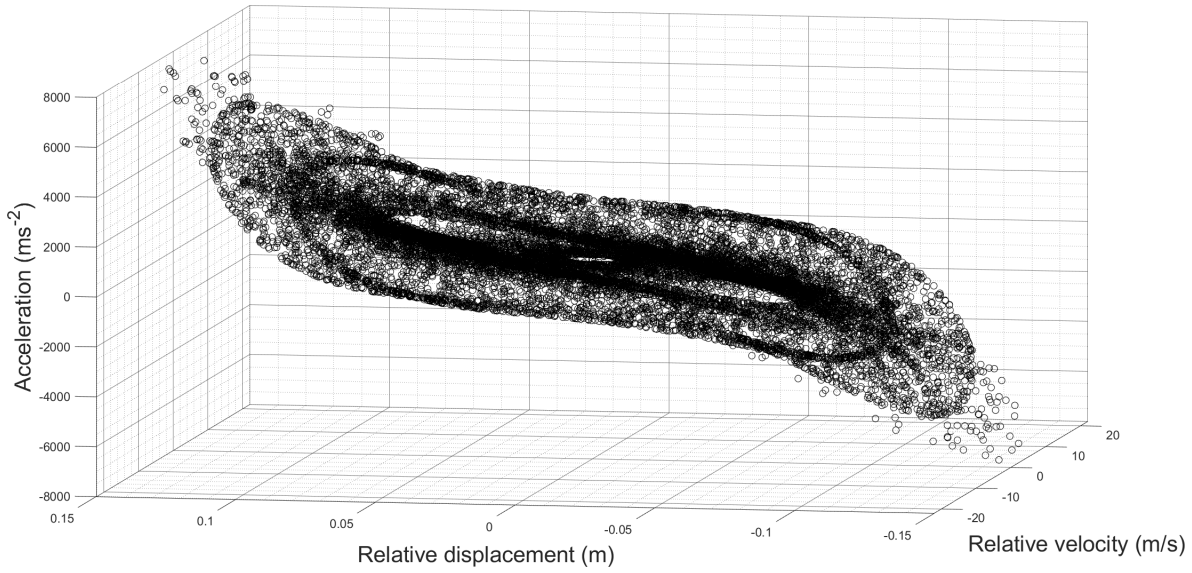


Figure 4.15: Acceleration surface considering the nonlinearity between DOF 3 and 5

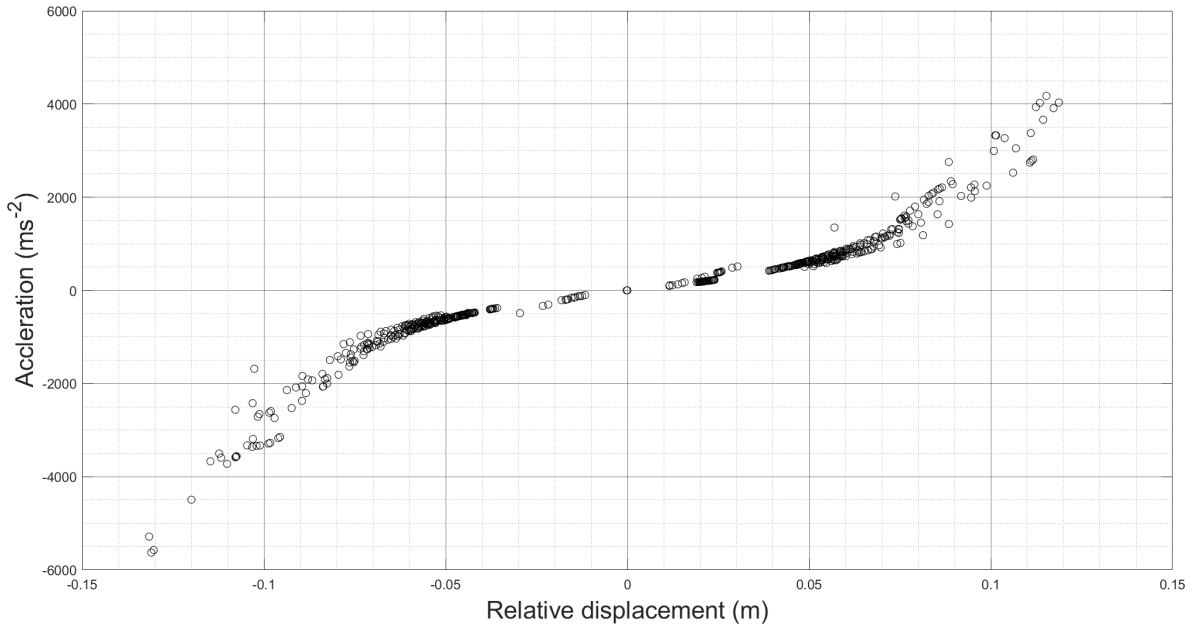


Figure 4.16: Stiffness curve considering the nonlinear connection between DOF 3 and 5

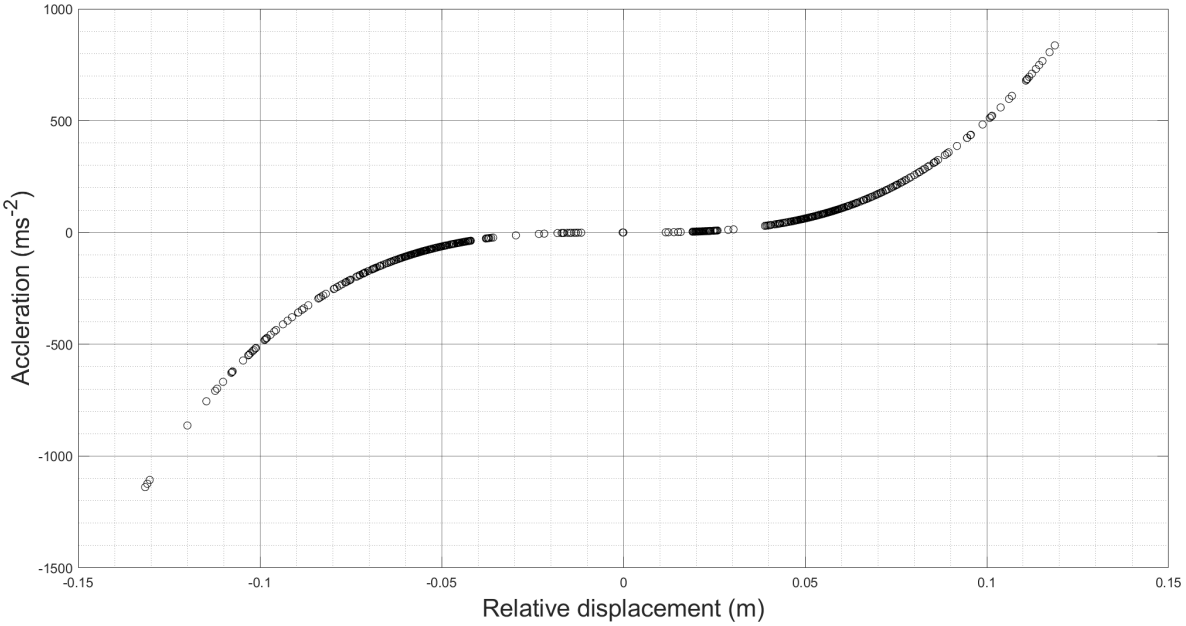


Figure 4.17: Stiffness curve for the nonlinear connection between DOF 3 and 5 considering the full equation

CHAPTER 5

Model order reduction

The full model analysis of some very large structures, like an airplane, are not viable due to its very high computational cost. A solution that started to be created at the end of 60^{th} decade was the division of the structure in different groups of substructures, which nowadays are commonly called "superelements". So basically, the substructuring process, is a process that allows to reduce a large group of finite elements of a certain substructure into a reduced size stiffness, mass, damping, and load matrices. Those reduced size matrices are then "applied" to its boundary degrees of freedom, and will allow in the case of an airplane, for example, to evaluate successive changes of the wing format, considering the overall influence of all other components, but only running a full analysis at the component that is being designed and studied, which in this case is the wing [20, 21].

But the concept of model order reduction is also applied at very simple situations in commercial finite element software, namely in linear dynamics analysis, where systems of thousands of degrees of freedoms, are reduced to a few modal coordinates. In fact, the process of calculating the answer of the system is always preceded by the calculation of the normal modes, in which the user defines the number of normal modes he pretends to obtain, and after obtaining those modes the user can also exclude some modes because of the range frequency that he pretends to simulate, or because the load that he pretends to apply makes the contribution of some mode negligible. For example, in a cantilever beam, if the user is interested in simulating the bending behaviour, he does not need to include the transverse normal modes on its simulation.

In the context of this thesis, the model order reduction will be used to reduce the large computational time work associated to nonlinear analysis, because unlike what happens with the linear analysis, the software does not reduce the model to a couple of modal degrees of freedom, meaning that the software works always with the full model. In the context of this topic, two different techniques are presented, the Craig-Brampton model and the model based on Rubin and MacNeal approximations. In a first phase the concepts common to these two methodologies are presented and then their specifications are explored.

5.1 Introduction

In mathematical terms, the model order reduction operation, consists in a simple coordinate transformation, similarly to what is performed with modal coordinates: [22, 23]

$$\{x\} = [\Phi] \cdot \{\eta\} \tag{5.1}$$

where $[\Phi]$ is the transformation matrix, $\{x\}$ are the generalized coordinates and $\{\eta\}$ are the reduced coordinates. The difference between the different methods, relays on the deduction of $[\Phi]$.

The process of obtaining $[\Phi]$ (model order reduction) for dynamic systems, in these two methods, involves two different phases, the dynamic part, where a procedure denominated as "component mode synthesis" is done, and a second phase where a statical reduction is performed, and has the goal of complementing the dynamic reduction. This procedure is exposed at the next figure [21, 23]:

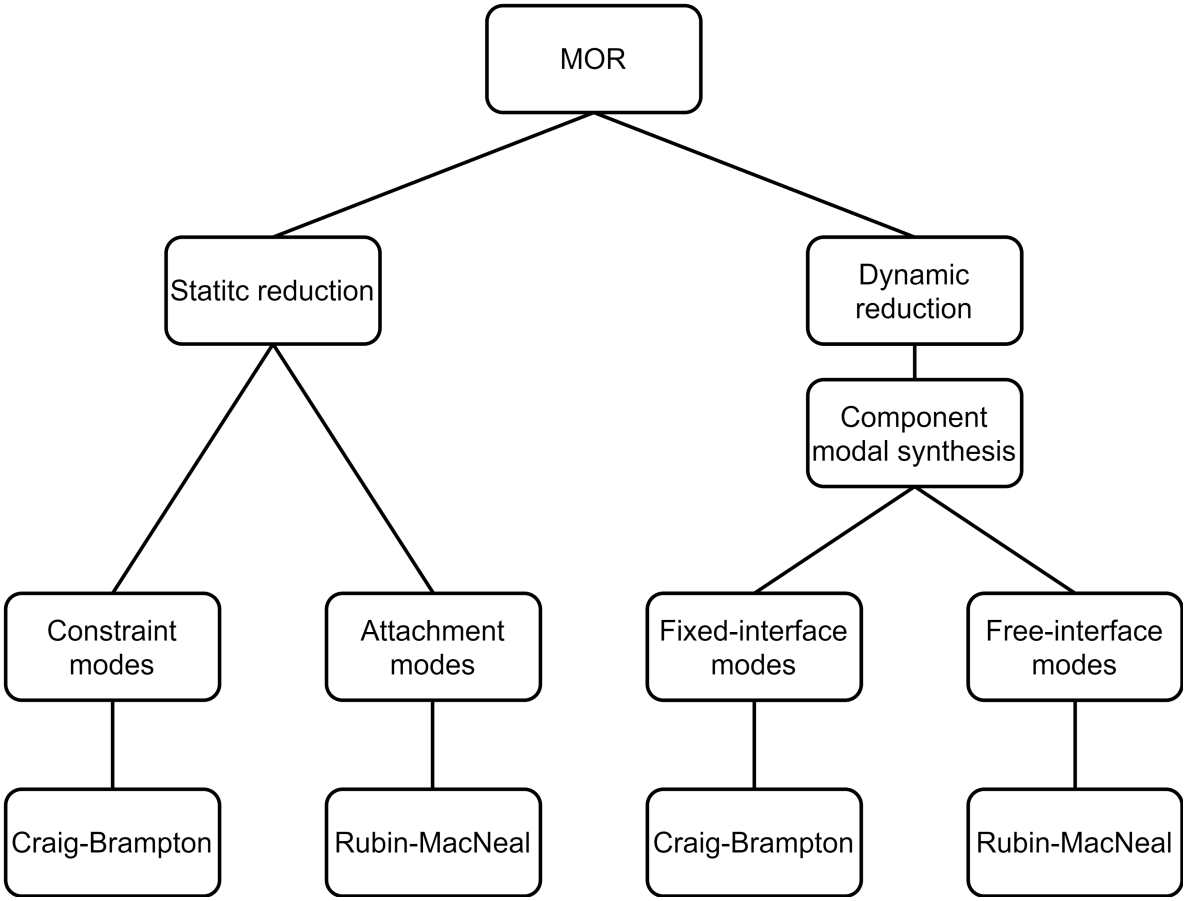


Figure 5.1: Model order reduction procedure and its particularities for Craig-Brampton and Rubin-MacNeal

The different concepts exposed at the previous scheme will be more explored in the posterior sections. To conclude, it is important to indicate that in terms of notation, at the literature different terms can be found, like "master" and "slave" coordinates, "interior" and "boundary"/"junction" coordinates. In this thesis, it will be followed the notation usually used at commercials software – "interior" and "boundary" degrees of freedom.

5.2 Craig-Brampton model

For this formulation let's start by considering a simple undamped system, similar to what is done in literature, where the subscripts i and b represent respectively the interior and boundary degrees of freedom:

$$\begin{bmatrix} m_{ii} & m_{ib} \\ m_{bi} & m_{bb} \end{bmatrix} \begin{Bmatrix} \ddot{u}_i \\ \ddot{u}_b \end{Bmatrix} + \begin{bmatrix} k_{ii} & k_{ib} \\ k_{bi} & k_{bb} \end{bmatrix} \begin{Bmatrix} u_i \\ u_b \end{Bmatrix} = \begin{Bmatrix} 0 \\ f_b \end{Bmatrix} \tag{5.2}$$

According to what was exposed in the fig. 5.1, in this method the dynamic reduction is performed by using the fixed-interface modes, where the interface or boundary degrees of freedom are constrained. This concept is illustrated at fig. 5.2, for a cantilever beam, where besides its "natural" constrain, the tip of the beam, which in this case corresponds to the boundary degree of freedom, is also constrained. The mathematical formulation of these modes is similar to what is done in the calculation of natural frequencies and modal shapes of the system. The difference relies in the fact that only the interior degrees of freedom are considered [20, 21, 24]:

$$\left[[k_{ii}] + \lambda^2 [m_{ii}] \right] \{u_i\} = \{0\} \tag{5.3}$$

The statical reduction component of this method is done via constraint modes, $\{\Psi_b\}$. Constraint modes by definition, as exposed at the fig. 5.2, are calculated by imposing one unit displacement on one of the boundary coordinates of the system and zero displacement at the remaining boundary coordinates. Those modes are calculated according to the next equation [20, 21]:

$$\begin{bmatrix} k_{ii} & k_{ib} \\ k_{bi} & k_{bb} \end{bmatrix} \cdot \begin{Bmatrix} \psi_{ib} \\ I_{bb} \end{Bmatrix} = \begin{Bmatrix} 0 \\ R_{bb} \end{Bmatrix} \Rightarrow \Psi_b = \begin{Bmatrix} \psi_{ib} \\ I_{bb} \end{Bmatrix} = \begin{Bmatrix} -k_{ii}^{-1} k_{ib} \\ I_{bb} \end{Bmatrix} \tag{5.4}$$

In this equation, similarly to what is done at the statical condensation method of Guyan, the inertia of the system is not considered, and that's the reason for the constraint modes being defined in some literature as a application of Guyan reduction method to the interior degrees of freedom [21].

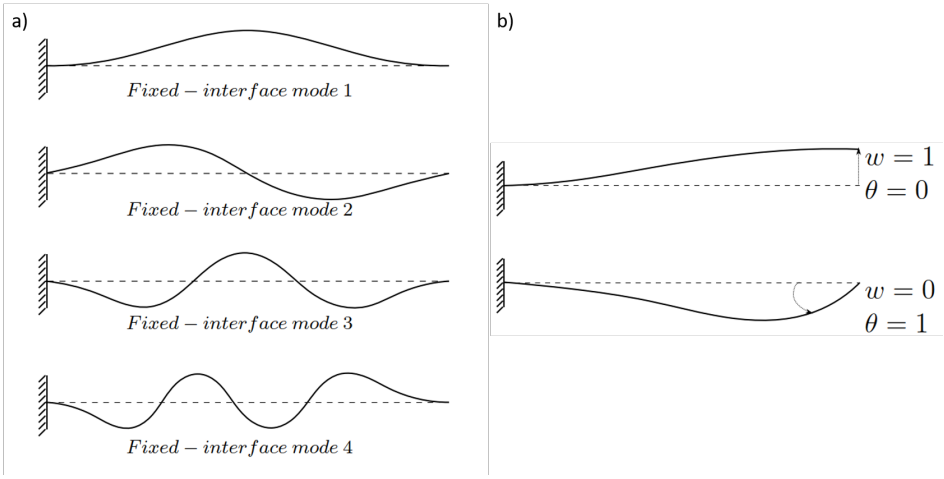


Figure 5.2: a) Fixed-interface modes for a cantilever beam; b) Constraint modes for a cantilever beam [24]

After performing the calculation of the fixed-interface and constraint modes the transformation matrix $[\Phi]$ can be built [20]:

$$[\Phi] = \begin{bmatrix} \Phi_i & \Psi_b \end{bmatrix} = \begin{bmatrix} \Phi_{ii} & \psi_{ib} \\ 0 & I_{bb} \end{bmatrix} \tag{5.5}$$

Finally, the reduced mass and stiffness matrices, but also the reduced damping matrix, if proportional damping is used, can finally be calculated:

$$[M]_{red} = [\Phi]^T \cdot [M] \cdot [\Phi] \qquad [K]_{red} = [\Phi]^T \cdot [K] \cdot [\Phi] \qquad [C]_{red} = [\Phi]^T \cdot [C] \cdot [\Phi] \tag{5.6}$$

A disadvantage of this method lies in the fact that it cannot be used on free-free boundary conditions systems because as it was seen, in all steps constraints were used. The next method that is going to be present is applicable to free-free systems [25].

5.3 Rubin and MacNeal approximations

As it was exposed at fig. 5.1, this method unlike Craig-Brampton uses the free-interface modes. These modes correspond to typical natural modes that are calculated in dynamic analysis [25, 21]:

$$\left[[K] + \lambda^2 [M] \right] \{x\} = \{0\} \tag{5.7}$$

And for the statical part the residual attachment modes, $\{\Phi_{rira}\}$ are used. In order to understand this concept, it is important to first understand the concept of attachment modes, $\{\Phi_a\}$. These modes, are calculated by applying a unit force displacement on one of the boundary coordinates and zero at the remaining ones [22, 21]:

$$\begin{bmatrix} k_{ii} & k_{ib} \\ k_{bi} & k_{bb} \end{bmatrix} \cdot \begin{Bmatrix} u_{ib} \\ u_{bb} \end{Bmatrix} = \begin{Bmatrix} 0 \\ I_{bb} \end{Bmatrix} \Rightarrow \{\Phi_a\} = \begin{bmatrix} k_{ii} & k_{ib} \\ k_{bi} & k_{bb} \end{bmatrix}^{-1} \cdot \begin{Bmatrix} 0 \\ I_{bb} \end{Bmatrix} \tag{5.8}$$

These modes have the particularity of being able to be represented by a linear combination of all natural modes of the system. Consequently, as the name "residual" suggests, the residual modes will be the attachment modes without the contribution of the kept or selected modes calculated previously. In order to understand the reason for the residual modes being represented by a statical approximation, lets consider the definition of the answer of the system using the concept of receptance [21, 25]:

$$\{x\} = [\alpha(\omega)]\{F\} \quad \text{with} \quad \alpha_{jk}(\omega) = \sum_{r=1}^{n} \frac{\phi_{jr}\phi_{kr}}{\lambda_r^2 - \omega^2} \tag{5.9}$$

With this equation it can be observed that the terms where $\lambda_n \gg \omega$, can be approximated by the static effects only, this is, by not considering the contribution of ω. This approximation corresponds to the concept of "residual flexibility" and justifies the use of a static approximation for the high frequency modes, because as Rubin stated, "those modes don't need to be obtained explicitly". With this simplification the receptance can be rewritten as [25]:

$$\alpha_{jk}(\omega) = \left(\sum_{r=1}^{S} \frac{\phi_{jr}\phi_{kr}}{\lambda_r^2 - \omega^2} \right) + \left(\sum_{r=S+1}^{n} \frac{\phi_{jr}\phi_{kr}}{\lambda_r^2} \right) \tag{5.10}$$

After explaining the reason of the name "residual", it is important now to understand how these modes can be extracted or how the removal of the selected modes can be performed. For that, let's consider that the transformation matrix, $[\Phi]$ has a similar structure to the one that was presented for the Craig-Brampton model:

$$[\Phi] = \begin{bmatrix} \Phi_k & \Phi_{rira} \end{bmatrix} \tag{5.11}$$

Considering the eq. 5.8, where it is exposed that the attachment modes are a displacement, and considering the previous equation and eq. 5.1, eq. 5.8 can be rewritten as: [25]

$$\{\Phi_a\} = [\Phi_k]\{\eta_k\} + \{\Phi_{rira}\} \tag{5.12}$$

Now, neglecting the dynamic component from eq. 5.2, because these are statical modes, and multiplying it by eq. 5.11, the next expression is obtained: [25]

$$\begin{bmatrix} \Phi_k^T \\ \Phi_{rira}^T \end{bmatrix} [K] \begin{bmatrix} \Phi_k & \Phi_{rira} \end{bmatrix} \begin{Bmatrix} \eta_k \\ \eta_{rira} \end{Bmatrix} = \begin{bmatrix} \Phi_k^T \\ \Phi_{rira}^T \end{bmatrix} \{F\} \tag{5.13}$$

Since those modes present the same properties of natural modes:

$$[\Phi_k]^T[K]\{\Phi_{rira}\} = \{\Phi_{rira}\}^T[K][\Phi_k] = 0 \tag{5.14}$$

$$[\Phi_k]^T[K][\Phi_k] = [\lambda_k^2] \tag{5.15}$$

$$\{\Phi_{rira}\}^T[K]\{\Phi_{rira}\} = \lambda_{rira}^2 \tag{5.16}$$

From eq. 5.13, it can be concluded that:

$$[\lambda_k^2]\{\eta_k\} = [\Phi_k]^T\{F\} \Rightarrow \{\eta_k\} = [\lambda_k^2]^{-1}[\Phi_k]^T\{F\} \tag{5.17}$$

Returning to eq. 5.12, it can be concluded that residual attachment modes are given by [25]:

$$\{\Phi_{rira}\} = \{\Phi_a\} - [\Phi_k][\lambda_k^2]^{-1}[\Phi_k]^T\{F\} \tag{5.18}$$

By observing all the deduction process that was made, the problem referred at the previous section, about the free-free systems remains, because if rigid-body modes exist, the $[K]$ matrix will be singular, and for that reason it is not possible to calculate the attachment modes. In order to process these systems, it is necessary to determinate and remove the inertia relief modes. For that, considering that the displacement can be given as [25]:

$$x = x_r + x_f \tag{5.19}$$

where x_r represents the rigid body motion and x_f represents the (relative) flexible motion. Considering now that:

$$[\Phi] = \begin{bmatrix} \Phi_r & \Phi_f \end{bmatrix} \tag{5.20}$$

equation 5.19 can be rewritten as:

$$\{x\} = [\Phi_r]\{\eta_r\} + [\Phi_f]\{\eta_f\} \tag{5.21}$$

Now, multiplying both members of eq. 5.2 by eq. 5.20:

$$\begin{bmatrix} \Phi_r^T \\ \Phi_f^T \end{bmatrix} [M] \begin{bmatrix} \Phi_r & \Phi_f \end{bmatrix} \begin{Bmatrix} \ddot{\eta}_r \\ \ddot{\eta}_f \end{Bmatrix} + \begin{bmatrix} \Phi_r^T \\ \Phi_f^T \end{bmatrix} [K] \begin{bmatrix} \Phi_r & \Phi_f \end{bmatrix} \begin{Bmatrix} \eta_r \\ \eta_f \end{Bmatrix} = \begin{bmatrix} \Phi_r^T \\ \Phi_f^T \end{bmatrix} \{F\} \tag{5.22}$$

If it is now considered again the properties of normal modes exposed on eq. 5.14-5.17, and that the rigid body modes have a corresponding natural frequency equal to zero, the governing equation of motion can be rewritten in the two following expressions:

$$\begin{cases} \{\ddot{\eta}_r\} = [\Phi_r]^T\{F\} \\ \{\ddot{\eta}_f\} + [\lambda_f^2]\{\eta_f\} = [\Phi_f]^T\{F\} \end{cases} \tag{5.23}$$

By looking to the first expression of the previous equation, the acceleration can be interpreted as an opposite reaction force. Consequently, and considering that $\{x_r\} = [\Phi_r]\{\eta_r\}$:

$$\{F_r\} = [M]\{\ddot{x}_r\} = [M][\Phi_r][\Phi_r]^T\{F\} \tag{5.24}$$

And since the total applied force is equal to the sum of the inertia forces plus the flexible forces, the flexible forces are given by:

$$\{F\} = \{F_f\} + \{F_r\} \Rightarrow \{F_f\} = \{F\} - [M][\Phi_r][\Phi_r]^T\{F\} \tag{5.25}$$

By last, in order to have any kind of flexible-body motion it is necessary to impose temporary constraints on that structure. That is logical, since if it is imagined a rigid body in space where it doesn't exist any kind of exterior forces, if a force is applied, a rigid body motion will happen and the body will not vibrate. So, to impose those temporary constraints, the rows and columns corresponding to the constraint degree of freedoms are removed in order to invert the matrix. After inverting the matrix, the previous columns and rows are filled with zeros, and a matrix denominated as augmented flexibility matrix, $[G_c]$ is obtained. By this way, the motion of the body will be [25, 21]:

$$\{x\} = [G_c]\{F_f\} \tag{5.26}$$

To obtain the flexible body motion, it is now necessary to remove the rigid-body motion component, which will be done considering the following property [25]:

$$[\phi_r]^T[M][\phi_f] = \{0\} \Rightarrow [\phi_r]^T[M]\{x_f\} = \{0\} \tag{5.27}$$

And as it was shown previously:

$$\{x_f\} = \{x\} - \{x_r\} = \{x\} - [\phi_r]\{\eta_r\} \tag{5.28}$$

By replacing this expression at eq. 5.27:

$$\begin{gathered} [\phi_r]^T[M]\left(\{x\} - [\phi_r]\{\eta_r\}\right) = \{0\} \Rightarrow [\Phi_r]^T[M][\Phi_r]\{\eta_r\} = [\Phi_r]^T[M]\{x\} \\ \Rightarrow \{\eta_r\} = [\Phi_r]^T[M]\{x\} \end{gathered} \tag{5.29}$$

And now returning to eq. 5.28, it is finally obtained the expression for the flexible displacement:

$$\{x_f\} = \{x\} - [\Phi_r][\Phi_r]^T[M]\{x\} \tag{5.30}$$

This displacement it is what is denominated as "inertia-relief attachment mode". By end, it is necessary to repeat the same process of getting the residual attachment modes or in this case the residual inertial-relief attachment modes:

$$\{\Phi_{rira}\} = \{x_f\} - [\Phi_k][\lambda_k^2]^{-1}[\Phi_k]^T\{F\} \tag{5.31}$$

In the previous topics, referring the calculation of the attachment modes, is important to keep in mind that $\{F\}$ is a unitary force. By last, after performing all these steps the transformation matrix $[\Phi]$ is finally obtained:

$$[\Phi] = \begin{bmatrix} \Phi_k & \Phi_{rira} \end{bmatrix} \tag{5.32}$$

5.4 Conclusion

Since the model to be tested in on free-free regime, the model order reduction technique that will be used is the one based on Rubin and MacNeal approximations. As it is stated at diverse literature, the previous technique was developed with the main goal of using it for these kind of situations. By end, it is important to refer, in what substructuring concerns, no study will be done about the equally important theme of substructure coupling, since the main goal was to only reduce the size of the system of equations to be processed, when simulating the nonlinear model. By last, it is exposed the algorithmic structure used at this thesis:

1. Data processing – Importation of $[K]$, $[M]$ and $[\Phi]$ from Simcenter3D® to Matlab®;
2. Input data:
   - Number of modes to keep;
   - Degree of freedom of the applied force or forces ("node"+"force direction") – for the calculation of the attachment modes;
   - If rigid body modes exist: indication of the degrees of freedom to be constrained, for the determination of $\{\Phi_{rira}\}$
3. Data simplification – removal of the *RBE's* elements and other clamped degrees of freedom;
4. Model order reduction
   (a) Check if rigid body mode exists:
      - If not – Calculation of attachment modes;
      - If yes – Calculation of inertia relief attachment modes;
   (b) Calculation of residual modes;
   (c) Calculation of the reduced matrices: $[K]$, $[M]$ and $[C]$, if it exists;

5.5 Implementation in Newmark algorithm

At chapter 3 it was seen that the steps of Newmark's algorithm related with the nonlinear component, this is, the calculation of the force applied by the nonlinearity at steps 4 d) and 5 e), and the calculation of the tangent stiffness matrix at step 5 a), are done in physical coordinates. But, with the utilization of the ROM (reduced order model) all components of the algorithm are going to be in reduced coordinates. So, this means that it is necessary to calculate the tangent stiffness matrix associated to the nonlinear stiffness, and the nonlinear force in physical coordinates, and then transform them to reduced coordinates. However, since the coordinates that need to be transformed are known, it is possible to minimize the

calculation time by only using the necessary lines and rows of the $[\Phi]$ matrix. Besides those aspects related with the nonlinearity, it is also necessary to calculate the excitation force in reduced coordinates, but once again, since the DOF where the force is applied is known the calculation time can be reduced.

After explaining the overall changes to the code, it matters now to explicitly indicate how a reduced time calculation is obtained despite of all these coordinate changes. So for the excitation force the next calculation is done:

$$[\Phi]^T \cdot \{F\} \Rightarrow [\Phi]^T \cdot \begin{Bmatrix} 0 \\ \vdots \\ F \\ \vdots \\ 0 \end{Bmatrix} \Rightarrow [\Phi]^T \cdot \{F\} = \Phi(DOF_f, :)^T \cdot F \tag{5.33}$$

where DOF_f represents the degree of freedom where the force is applied. About the simplification on the calculation of the force applied by the nonlinearity the procedure is very similar. Considering a nonlinear spring between the DOF i and j:

$$\begin{aligned} [\Phi]^T \cdot \{F_{nl}\} &\Rightarrow [\Phi]^T \cdot k_{nl} \begin{Bmatrix} 0 \\ \vdots \\ -(xdofj - xdofi)^n \\ \vdots \\ (xdofj - xdofi)^n \\ \vdots \\ 0 \end{Bmatrix} \\ &= k_{nl} \left(\Phi(DOF_i, :)^T \cdot -(xdofj - xdofi)^n + \Phi(DOF_j, :)^T \cdot (xdofj - xdofi)^n \right) \end{aligned} \tag{5.34}$$

where *xdof* represents the displacement in physical coordinates. The difference from this step to the previous one is that it is necessary to calculate the physical displacements:

$$\{x\} = [\Phi]\{\eta\} \Rightarrow xdof_i = \Phi(DOF_i, :) \cdot \{\eta\} \tag{5.35}$$

By last, there is the calculation of the tangent stiffness matrix:

$$\begin{aligned} \frac{\partial \{F_{nl}\}}{\partial \{x\}_{t+\Delta t}^{j-1}} &= nK_{nl}[\Phi]^T \cdot \begin{bmatrix} 0 & \cdots & 0 & \cdots & 0 & \cdots & 0 \\ \vdots & \ddots & \vdots & \ddots & \vdots & \ddots & \vdots \\ 0 & \cdots & (x_j - x_i)^{n-1} & \cdots & -(x_j - x_i)^{n-1} & \cdots & 0 \\ \vdots & \ddots & \vdots & \ddots & \vdots & \ddots & \vdots \\ 0 & \cdots & -(x_j - x_i)^{n-1} & \cdots & (x_j - x_i)^{n-1} & \cdots & 0 \\ \vdots & \ddots & \vdots & \ddots & \vdots & \ddots & \vdots \\ 0 & \cdots & 0 & \cdots & 0 & \cdots & 0 \end{bmatrix} [\Phi] \\ &\text{If} \quad val1 = (x_j - x_i)^{n-1} \quad \text{and} \quad val2 = -val1 \\ &= \begin{bmatrix} \Phi(DOF_i, :)^T \cdot val1 + \Phi(DOF_j, :)^T \cdot val2 & \Phi(DOF_i, :)^T \cdot val2 + \Phi(DOF_j, :) \cdot val1 \end{bmatrix} \\ &\quad \cdot \begin{bmatrix} \Phi(DOF_i, :) \\ \Phi(DPF_j, :) \end{bmatrix} \cdot nK_{nl} \end{aligned} \tag{5.36}$$

To finalise is important to say, that despite of those coordinate changes, as it will be seen in the final chapters of this thesis the calculation time is very low.

5.6 Application example - cantilever beam

In order to check if the MOR and Newmark algorithmic are working, it was decided to test a cantilever beam made of aluminium with a 20x20 mm cross section, and 1 m length. In the next figure the simulated model in Simcenter3D® can be found. In the generation of the mesh, since this is a beam, a 2D mesh was used, although a 1D mesh could have also been used. That was not done, because in the airplane model, which is the central work of this thesis, a 2D mesh is used, and with this example, it was also intended to verify that the 2D mesh is well processed.

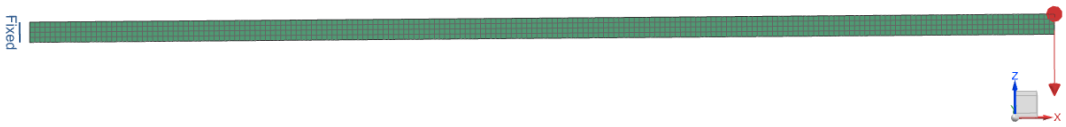


Figure 5.3: Simcenter3D® model.

In the previous figure, a coarser mesh could have been used, but since the model to simulate is a reduced model, the use of a mesh finer than necessary is simply irrelevant. Considering the range frequency from 0 to 105 Hz, the software generates the first and second bending modes of the beam, whose frequencies are at 16.529 Hz and 103.389 Hz:

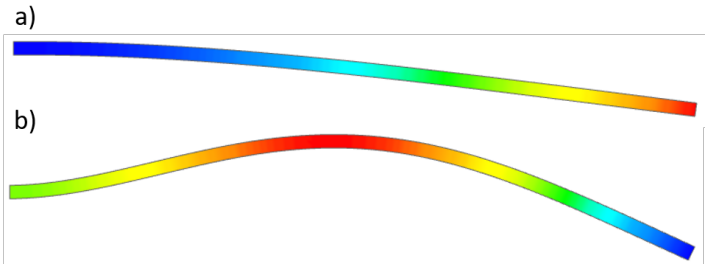


Figure 5.4: Natural modes of the beam: a) first natural mode; b) second natural mode.

For the simulation, let's consider that a sine-sweep with a magnitude of 20 N is applied from 10 to 50 Hz, during 20 seconds with a sampling frequency of 400 Hz. In fig. 5.5 and 5.6 it is shown that the modal answers of the 1^{st} and 2^{nd} modes obtained via Matlab® and Simcenter3D® are identical, proving that the model order reduction process is working. The shape of the answer is a "little strange" because no damping was considered, and consequently it doesn't follow the normal shape where the amplitude reaches the peak at resonance and then decays. What happens, as it can be seen by the time-frequency plot from fig. 5.7, is that when the answer reaches the natural frequency, the amplitude stays constant at that level, as it should be since there is no damping. But if a little bit of damping is added ($\zeta = 0.012$), a more normal time-frequency plot is obtained as it can be seen at fig. 5.8. By last, to complete the comparison between the reduced order model (ROM) and the Simcenter3D®, at fig. 5.9, 5.10 and 5.11 the acceleration surface, stiffness and damping curves, respectively, are presented, considering the middle node of the tip of the beam. On those plots a perfect match is also obtained.

To test the reduced order model with a nonlinearity, it will be considered that the beam possesses a cubic stiffness between the previous node and the middle node of the constraint. This nonlinear stiffness will have a value of $80\,000\,\mathrm{Nm}^{-3}$. Considering the same force applied previously, but at this time adding a little bit of damping ($\zeta = 0.012$), the plots from fig. 5.12 and 5.13 are obtained, and as it can be seen, the code is imposing the nonlinearity as it should be. In order to illustrate the importance of damping, in fig. 5.14 the case with no damping is shown.

Finally, to justify what was told in chapter 4 about continuous system, in fig. 5.15 it is showed the case where the sine-sweep is done until 100 Hz. In that plot it is perfectly visible the appearance of a second plane due to the presence of the second mode, justifying in this way that the presence of more than one mode in continuous systems violates the rule of the single degree of freedom.

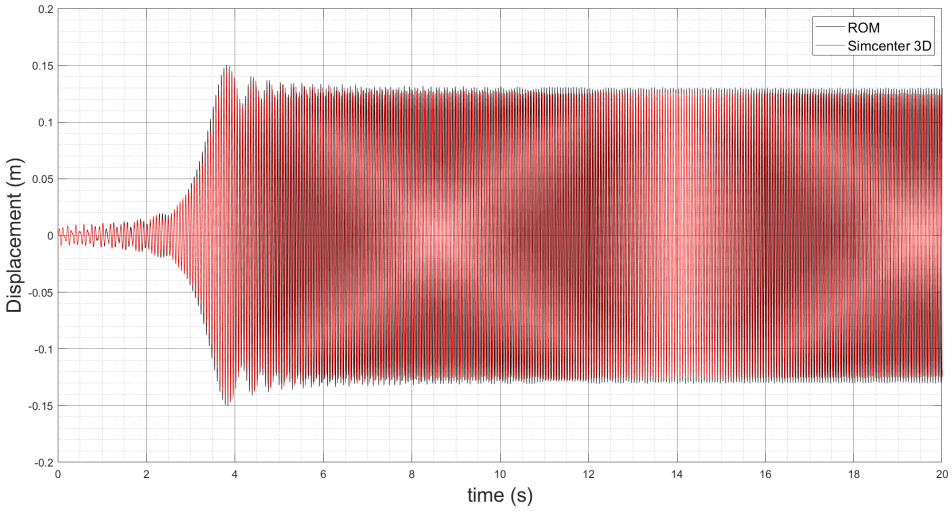


Figure 5.5: 1st modal answer of the beam

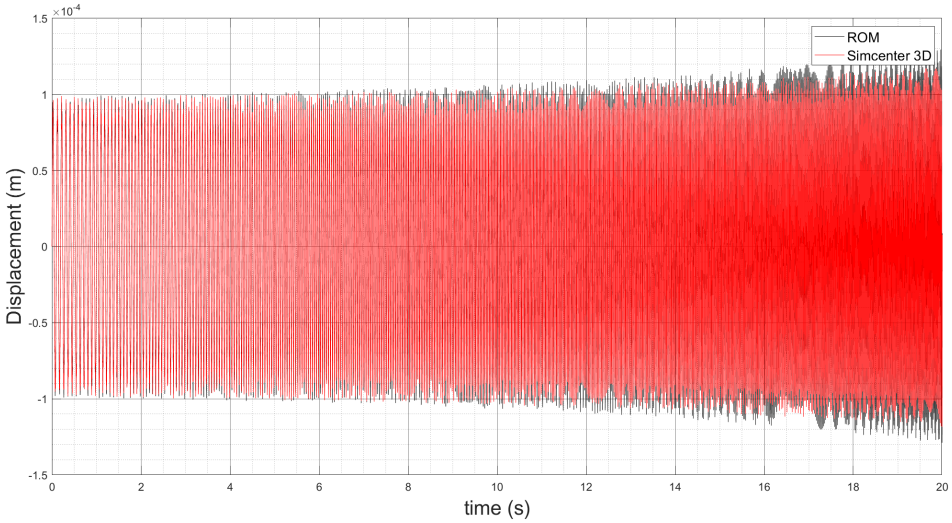


Figure 5.6: 2nd modal answer of the beam

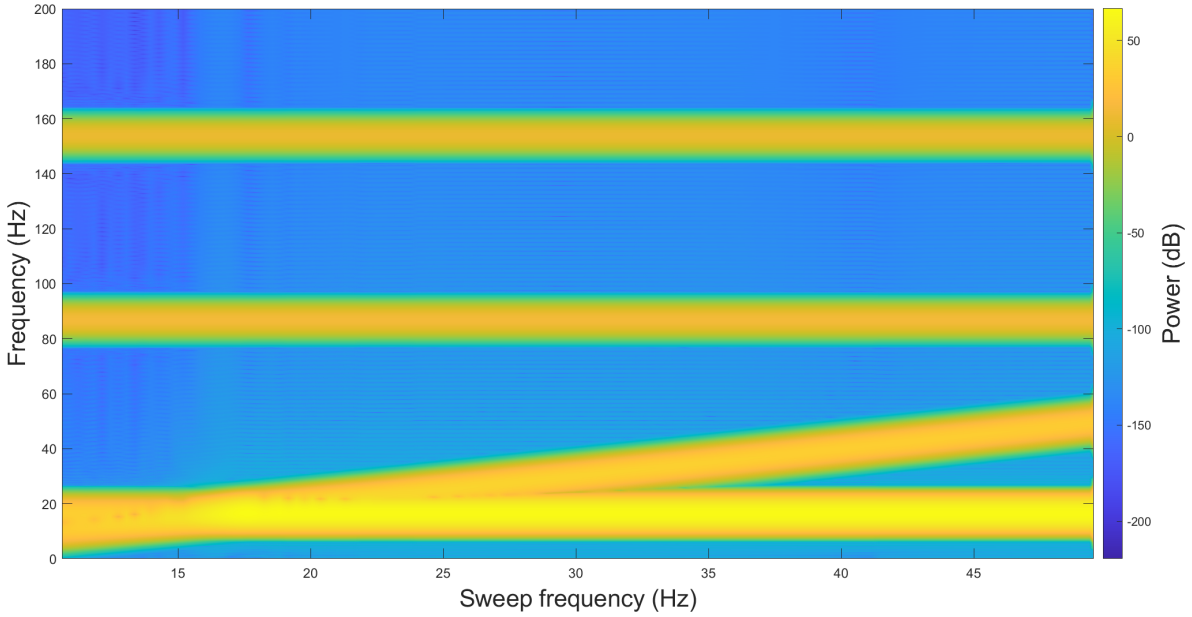


Figure 5.7: Time-frequency plot of the undamped answer

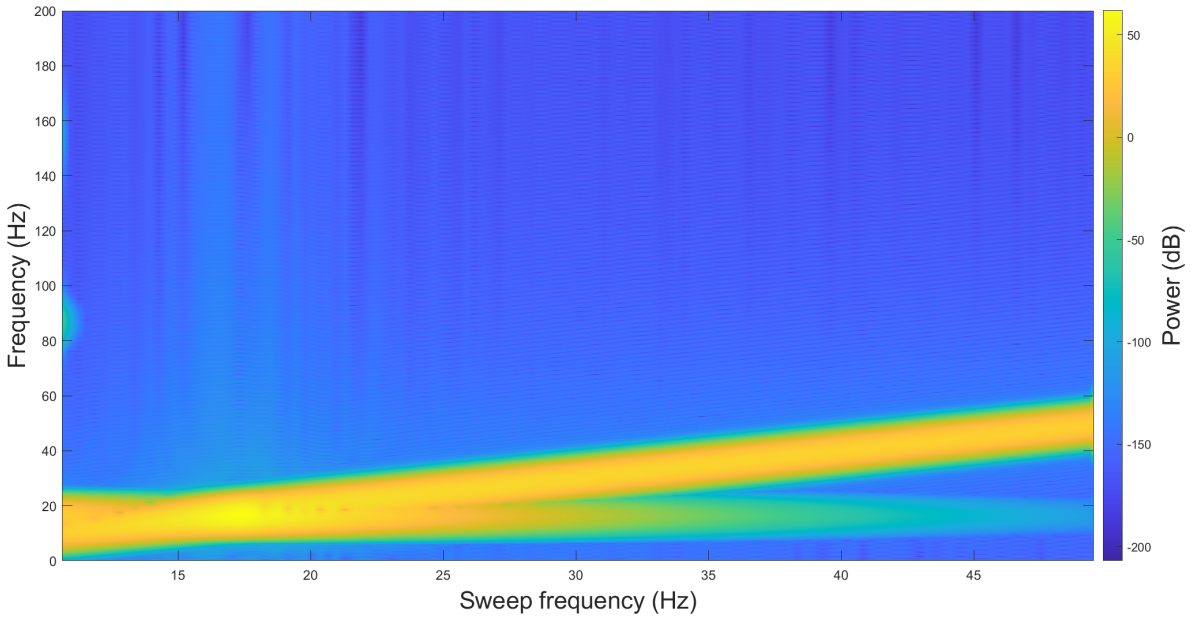


Figure 5.8: Time-frequency plot of the damped answer

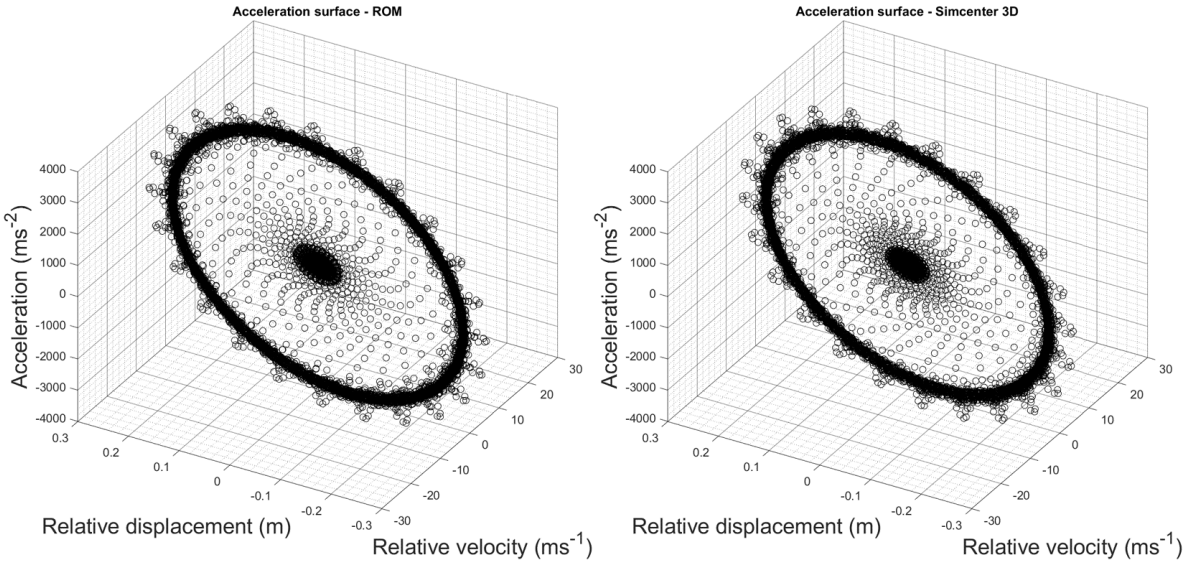


Figure 5.9: Accelerations surface obtained with the reduced order model and Simcenter3D®

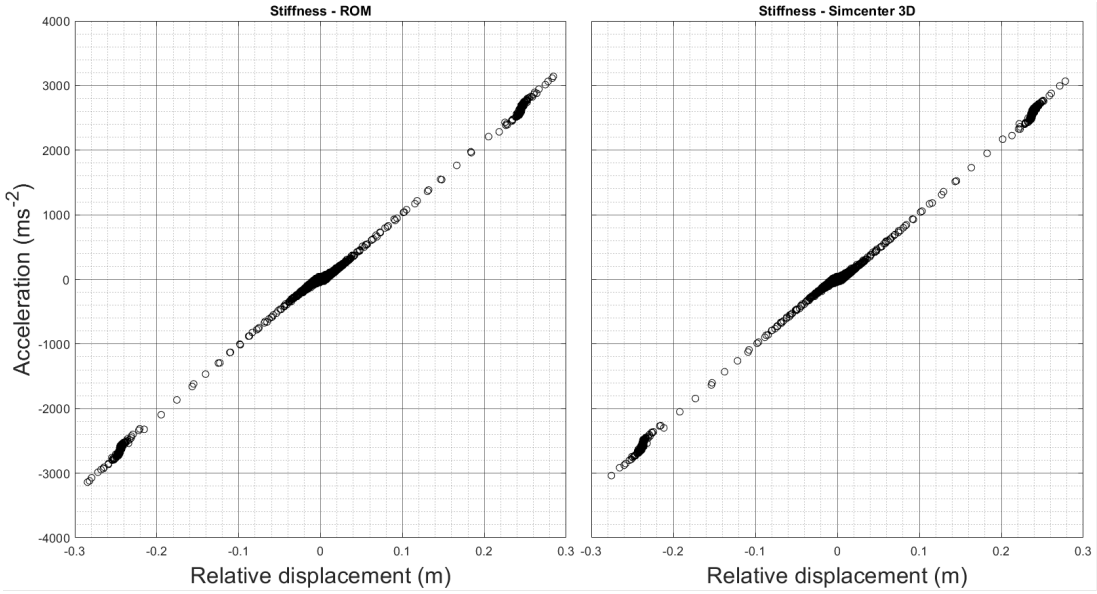


Figure 5.10: Stiffness curves obtained with the reduced order model and Simcenter3D®.

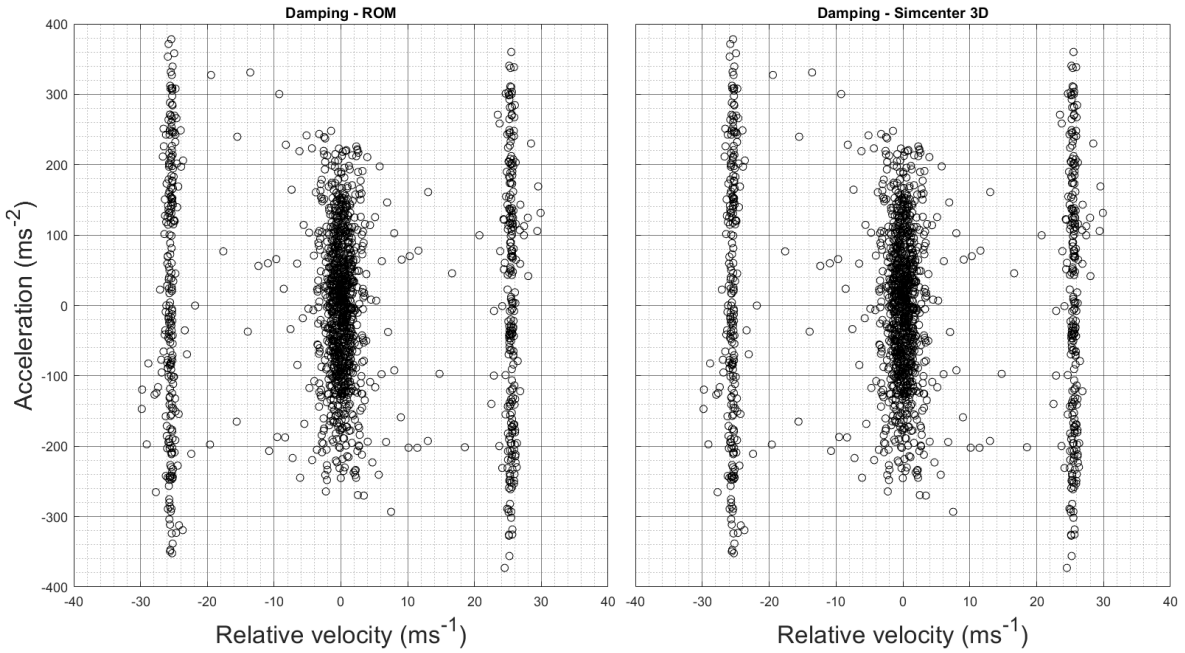


Figure 5.11: Damping curves obtained with the reduced order model and Simcenter3D®.

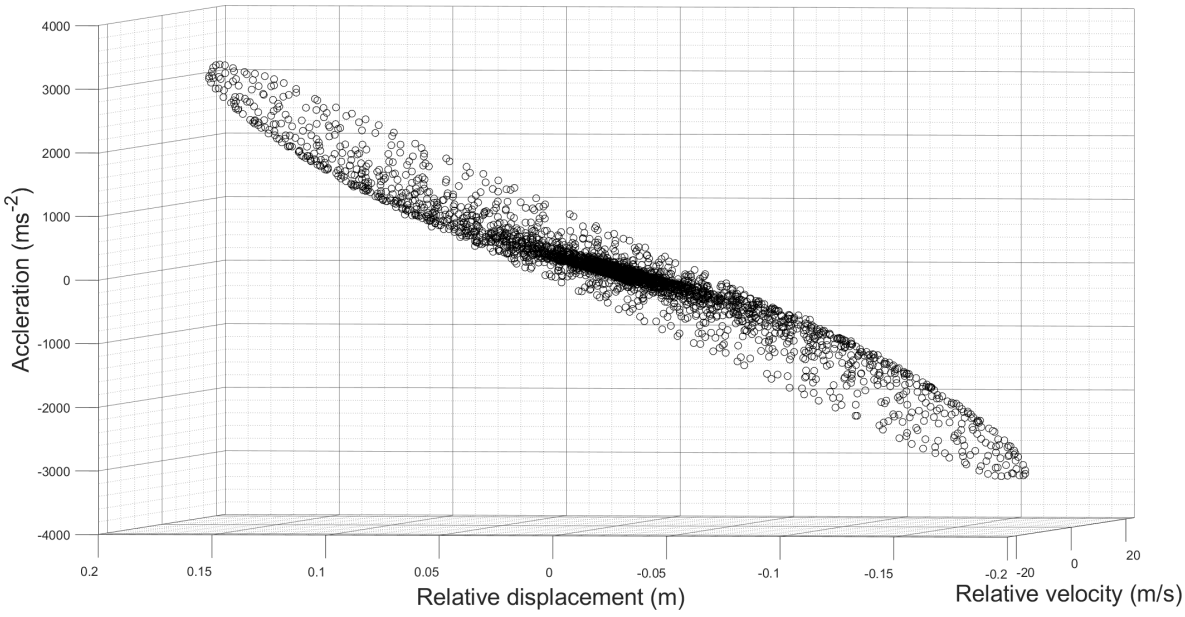


Figure 5.12: Acceleration surface - nonlinear case

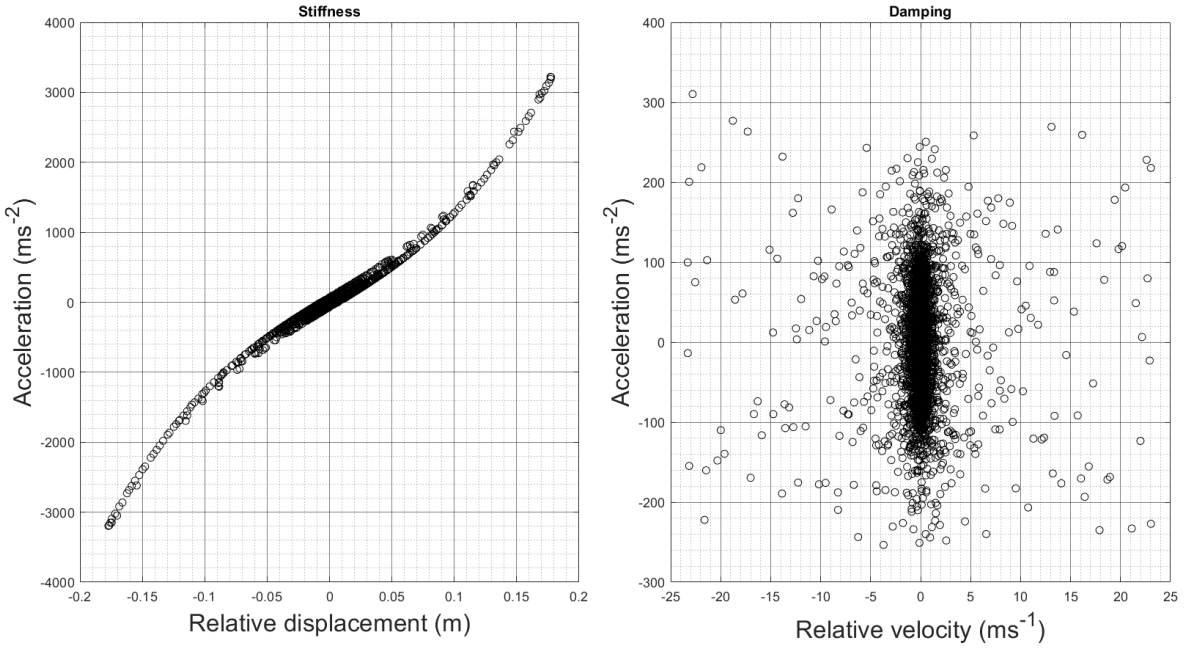


Figure 5.13: Stiffness and damping curves - nonlinear case

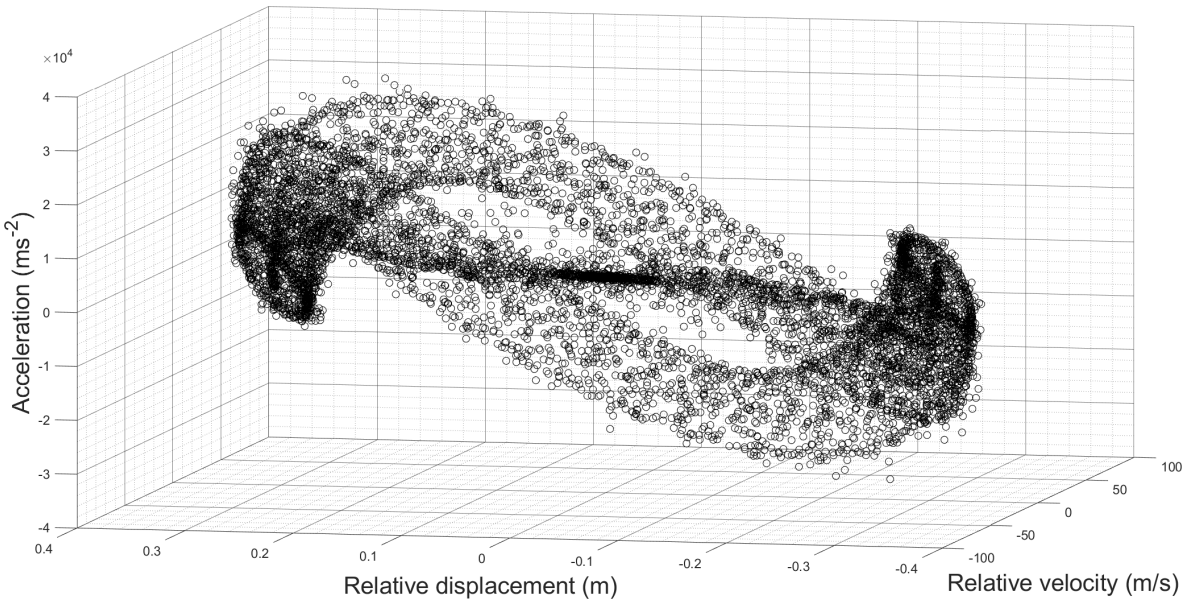


Figure 5.14: Acceleration surface - nonlinear undamped case

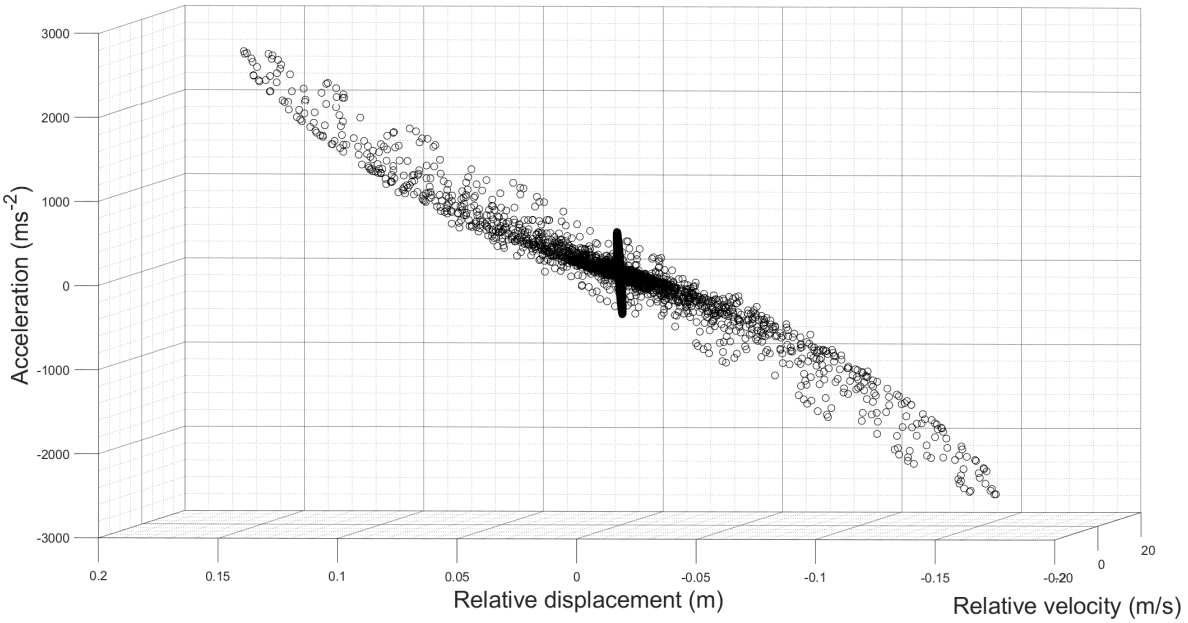


Figure 5.15: Acceleration surface - nonlinear case from 5-100Hz

CHAPTER 6

Structural modelling and experimental measurements

According to what was exposed at the topic 2.2.3, the first step of the Structural Model Updating method is the building of the structural model and the realization of the experimental measurements. In that sense, in this chapter the finite element model and experimental procedure will be presented.

6.1 Finite element model

The technical drawings of the airplane and of the pylons are presented in the following figures:

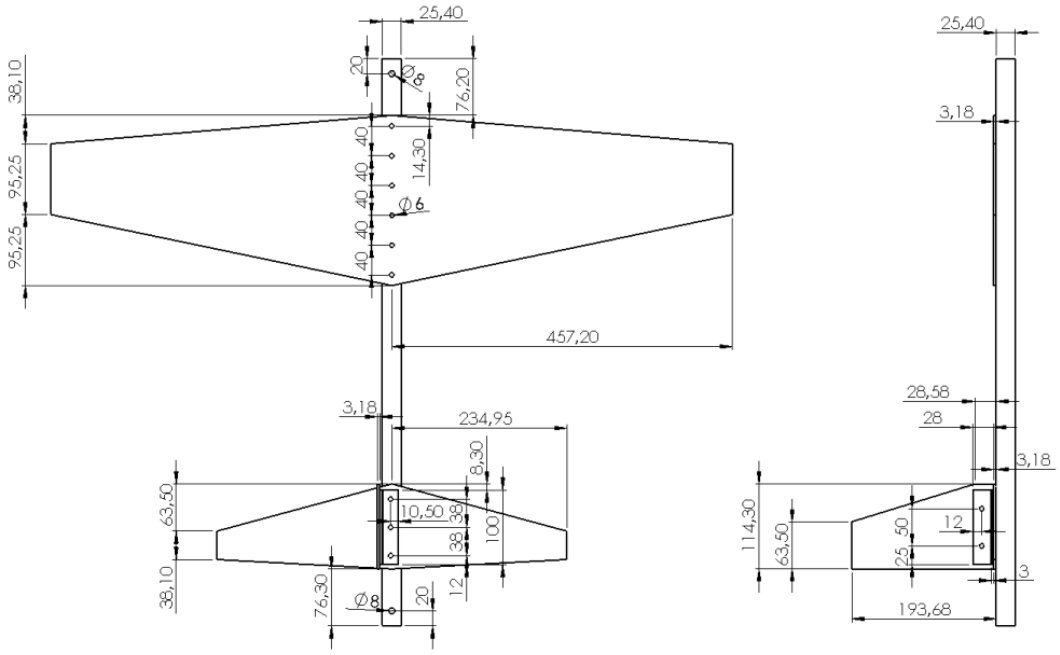


Figure 6.1: Airplane technical drawing [26]

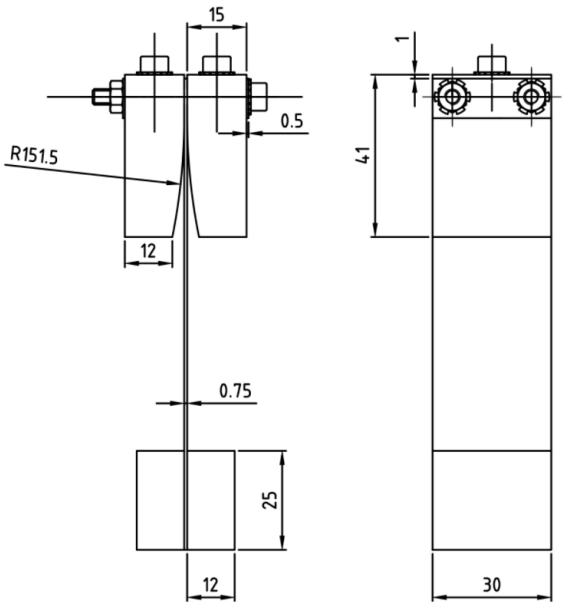


Figure 6.2: Pylon technical drawing

An already experimentally validated finite element model of the airplane was provided by Siemens® from a previous work done by a student in 2018. The model is constituted by the following elements:

- Wings, tail and fin - quadrangular shell elements of 8 nodes;
- Fuselage - tetrahedral solid elements of 10 nodes;
- Connection tips – 1d bar elements.

In order to obtain better results, to the mesh, clamped masses were added to consider the additional mass of the accelerometers used during the experimental activity. Relatively to the finite element model of the pylon, at the geometry the following simplifications were made:

- Removal of the bolts, nut and washer;
- Fill of the holes, that were used to do the connection between the upper blocks of the pylon and between the pylon and the airplane;
- Simplification of the plate to a 2D middle surface.

Relatively to the used elements, on the 2D plane, quadrangular shell elements of 4 nodes were used and at the remaining components tetrahedral solid elements of 4 nodes were used. On the connections between the plate and pylons, *RBE2* elements were used. These elements have the advantage of allowing the two bodies to behave as "separated" bodies from each other, but at same time with a constraint that imposes equal displacements at the selected DOFs. To make this connection perfect, at the plate and top pylon's block, auxiliary lines were made in order to ensure that the nodes between the surfaces were coincident, as it can be seen at fig. 6.3. Besides that, on the blocks 2D auxiliary meshes were made in order to sure an equally distributed mesh along the surface, and to warranty coincident nodes at the

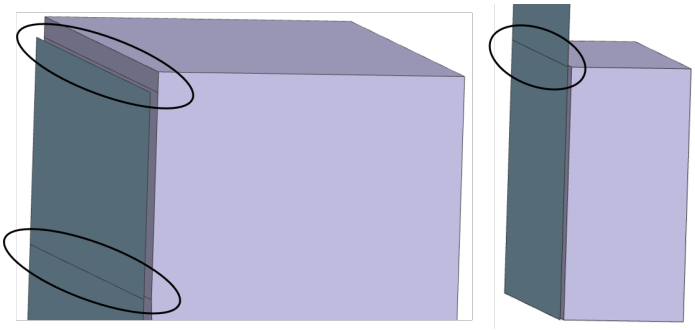


Figure 6.3: Geometrical simplifications done at the pylon

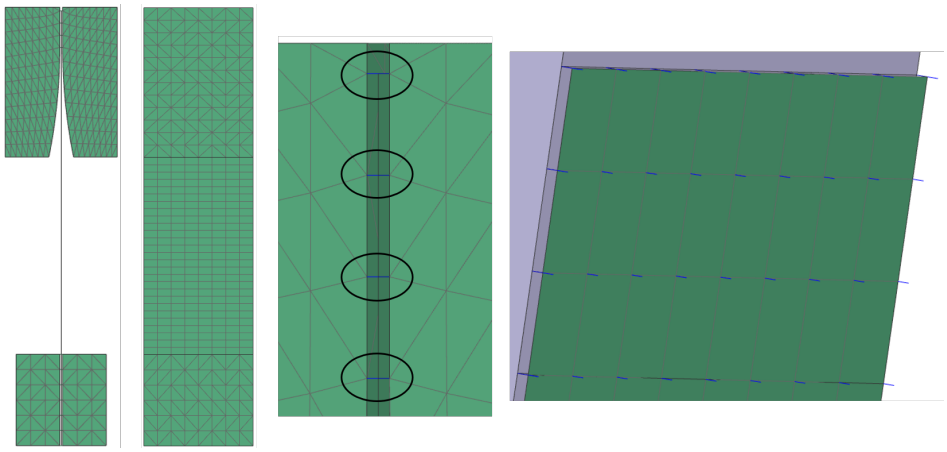


Figure 6.4: Pylon finite element model

contact zones. At the plate, in the region between the blocks a finer mesh was used. The final result is exposed at fig. 6.4.

At the connection between the pylons and the airplane initially *RBE2* elements were used to simulate the bolted connections but their utilization didn't avoid the penetration of the of the pylons at the wings which by its turn induced errors. The best solution that was found was the utilization of a tool called "face gluing", which basically allows the merge of the surface of the contact elements. When using this tool, the surfaces become as if they were only one. This tool could indeed, have been used at the connection between the blocks and plate of the pylons. However, their utilization revealed slightly worse results, (less 5% in MAC plot) revealing that the processing of the different parts as separated bodies with imposed constraints at the nodes is a better option. The final model with the indication of the location of the sensors is exposed at fig. 6.5.

Some critics can be made to the finite element model, namely the size of the mesh at the pylons and the utilization of *RBE2* elements instead of "face gluing" in the connection between the blocks and plate at the pylon. About the size of the mesh of the pylons, it is important to keep in mind that this model is only used for the obtention of a validated linear model, and lastly to the generation of the reduced order model that will be used to perform the nonlinear simulations. And like it was already stated the use of a mesh finer than necessary is irrelevant after the generation of the ROM. Relatively to the use of *RBE2* elements, like it was said before, allowed the achievement of slightly better results. Theoretically they should have generated the same results but there is a small difference, because if the same results

were obtained, obviously the final choice would have been the utilization of "face gluing" at the pylons, for a matter of consistency. But, despite of those things, as it will be seen in the next chapter a "really good" MAC plot was obtained.

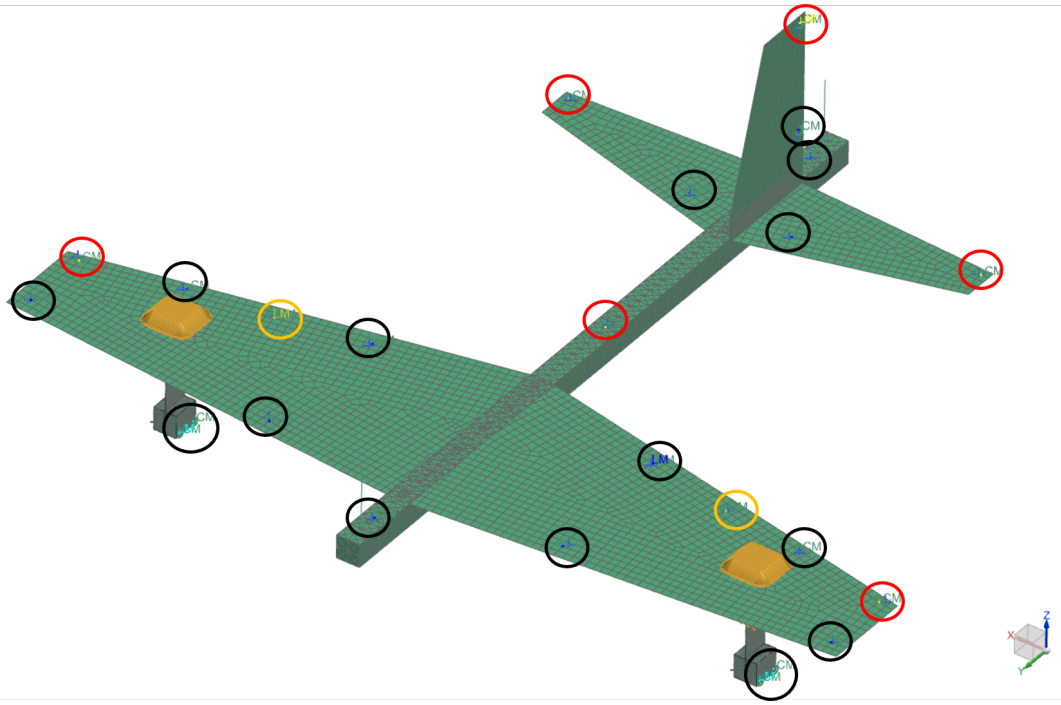


Figure 6.5: Finite element model of the airplane with wings with indication of the sensor locations

6.2 Experimental procedure

Like it was already said in section 2.2.3 a good experimental procedure is essential to get good results, and one of the first steps in the planning of this activity is the disposition of the sensors. And to make a good decision in that parameter is important to see the natural modes shapes of the airplane with the pylons. As initial goal it was established the obtention of a validated model until 300 Hz and for that reason, in fig. 6.6 the natural modes of the airplane until 300 Hz can be visualized. The modes can be described in the following way:

1. 6.60 Hz - Pylon 1st bending mode with symmetric disposition;
2. 7.04 Hz - Pylon 2nd bending mode with asymmetric disposition;
3. 14.93 Hz - Wings first bending mode;
4. 35.03 Hz - Wings second bending mode;
5. 43.51 Hz - Wing 1st torsional mode with the pylons orientated in the opposite sense;
6. 44.14 Hz - Wing 1st torsional mode with the pylons orientated in the same direction;
7. 46.28 Hz - Pylon 2nd natural mode (torsional mode) in the left pylon;

8. 46.30 Hz - Pylon 2nd natural mode (torsional mode) in the right pylon;
9. 64.83 Hz - Tail bending;
10. 66.95 Hz - Tail bending and wing bending;
11. 78.64 Hz - Finn bending;
12. 81.57 Hz - Wings third bending mode;
13. 93.43 Hz - Pylon 3rd natural mode (2nd bending mode) with a symmetric disposition;
14. 93.73 Hz - Pylon 3rd natural mode (2nd bending mode) with a asymmetric disposition;
15. 99.24 Hz - Fuse bending with wing torsion, fin and tail bending;
16. 146.82 Hz - Wing, fin and tail bending;
17. 180.99 Hz - Fuse bending in the Z direction with wing bending+torsion;
18. 190.46 Hz - Fuse bending in the Z direction with wing 4th bending mode;
19. 216.68 Hz - Wing second torsional mode with the pylons in the opposite sense;
20. 228.06 Hz - Wing second torsional mode with the pylons in the same sense;
21. 237.02 Hz - Tail and fin second bending modes;

Looking at the modes, in the sensors configuration some details need to be considered in order to distinguish the previous modal modes:

- Two sensors, unidirectional oriented in X direction, in one of the inferior blocks of the pylon in order to detect the pylon torsional mode;
- One sensor, also unidirectional according to X direction in the superior block of the pylon. This one is mostly necessary in order to measure the relative displacement between the blocks, in order to then characterize the nonlinearity of the pylon;
- At least four sensors aligned in each of the wings to distinguish the different bending modes. Those four sensors were inserted at the back of the wing. To identify the torsional modes and also to get the geometrical shape of the wing two sensors were inserted at the front of the wing. All the sensors are unidirectional in the Z direction except the one in back tip of the wing that is triaxial. The triaxial sensor will allow a better identification of the torsional movements and also a better "spatial description" of the modes;
- Two sensors at each of the tails (right and left) and fin to measure the bending. The sensors at the tips of those components are also triaxial for the second reason described previously. The unidirectional sensor at the fin is obviously pointed in the X direction;
- Three sensors in the fuselage – one in the middle and two at the tips. The sensor in the middle is triaxial for the same reason of the previous one;

The configuration is in fig. 6.5, where the sensors with black circles represent the unidirectional sensors and the ones in a red circles represent the triaxial ones. The orange circles besides indicating the position of two unidirectional sensors, it also represents the excitation points of the structure. To measure the applied force, force sensors were also added.

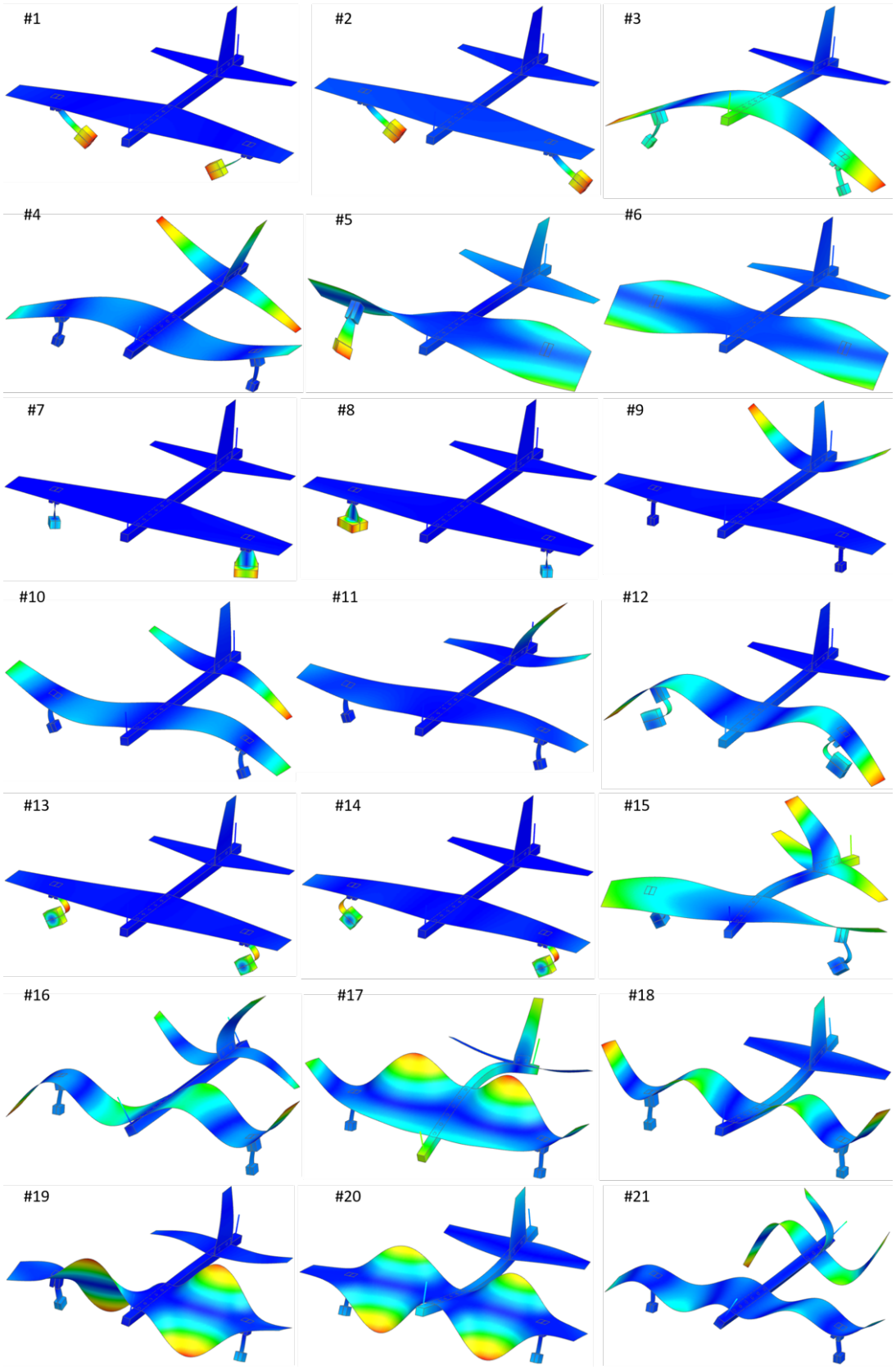


Figure 6.6: Natural shapes of the airplane with the pylons

The sensors by their turn are connected by cables to the SCADAS, which is a data collector device, and this one is connected to a laptop. Concerning the cables, it is important to avoid their interference with the mechanical system, and for that reason they were rolled up around the bar and joined as it is pointed by the arrows at fig. 6.7. In the figure it can be seen that a tape was also used beneath the sensors in order to eliminate any electrical interference between the different sensors, that the connection between the shakers and the airplane was done with stingers and that like in any ground vibration test the structure is suspended.

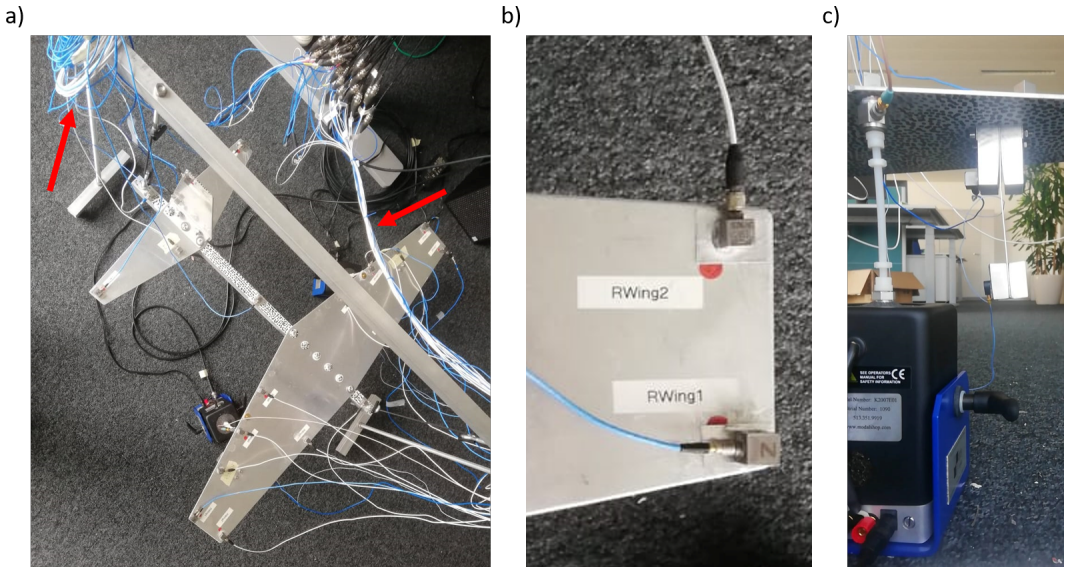


Figure 6.7: Experimental setup - a) Overall setup b) Tape beneath the sensors c) Connection between the shaker and the airplane

All the processing work is done at the software Testlab®. When performing the experiments in the software, these different input variables need to be defined:

- The choice of the estimators - H_1 or H_2. It is known that the FRF is calculated based in the autopower and crosspower spectra, as it can be seen at the next equation: [27]

$$A = \frac{\bar{S}_x(\omega)}{\bar{S}_F(\omega)} \Rightarrow \begin{cases} A = \frac{\bar{S}_x(\omega)\bar{S}_f^*(\omega)}{\bar{S}_f(\omega)\bar{S}_f^*(\omega} \Rightarrow A = \frac{\bar{S}_{xf}(\omega)}{\bar{S}_{ff}(\omega)} = H_1 \\ A = \frac{\bar{S}_x(\omega)\bar{S}_x^*(\omega)}{\bar{S}_f(\omega)\bar{S}_x^*(\omega} \Rightarrow A = \frac{S_{xx}(\omega)}{\bar{S}_{xf}(\omega)} = H_2 \end{cases} \tag{6.1}$$

  where S_{xx} and S_{ff} are the autopower spectrum of the output and input signals, respectively and S_{xf} is the crosspower spectrum between the output and input signal. The H_1 estimator is characterized by assuming no noise in the input and some uncorrelated noise in the response, while the H_2 estimator assumes no noise in the output and uncorrelated noise in the input. In systems where multiple inputs and multiple outputs exists (MIMO measurements), only the H_1 estimator can be used, because as it is stated in [27], the use of the estimator H_2 in MIMO tests is limited to the cases where the number of inputs is equal to the number of outputs, and that "constraint limits the use of the H_2 technique in practice to the single input cases where each response is considered separately". For this reasons H_1 was used, and H_2 option was blocked by the software.

- The voltage to be applied to the shakers – the amplitude force (10.5 N/V);

- The frequency range to be excited;
- The number of sweeps to be performed and the phase of the applied forces. To obtain the FRF matrix, considering the previous equation, the autopower spectrum matrix must be non-singular, and for that the following conditions must be respected: [28]
  - $N_{sweeps} \geq N_{inputs}$ – the number of performed sweeps must be at least equal to the number of input forces applied to the system;
  - The forces belonging to the different performed sweeps must not be correlated, this is, the excitation configuration needs to change from one sweep to another;

  So, since two forces are applied, one in each wing, two sweeps must be done, and to satisfy the second condition in the second sweep the forces are applied with a phase difference of 180°. In short, the first sweep is symmetric and second one is antisymmetric;
- The sweep rate - octave/min. This term defines the evolution of the excitation frequency. About the units used, an octave is a frequency width, and two frequencies are at one octave distance when a frequency is the double of the other. For example, 10 and 20 Hz are 1 octave apart, 10 and 40 Hz are 2 octaves apart and so on;
- The sampling frequency (FS) – this parameter defines the rate at which the measurements are made. This value, according to the Nyquist-Shannon theorem, should be at least two times higher than the maximum frequency intended to measure. This means, that if the excitation is applied from 5-100 Hz, for example, the sample-frequency should be at least of 200 Hz. But since this is a nonlinear system, this condition needs to be applied in terms of the superharmonics that are intended to measure, and not only in terms of the main harmonic. By last, as it will be seen in the next topic of this chapter these values should also be decided considering the integration procedure that will be applied to the measured accelerations;

Besides all those input variables, it is also necessary to indicate to the software the sensitivity of the used sensors, the direction in which they are measuring and also the location of the sensors. The location of the sensors allows the construction of the geometry and the visualisation of the identified modal shapes.

6.3 Data processing phase

After obtaining the accelerations measured by the sensors it is necessary to process all the values to obtain the natural mode shapes and the displacement values. The obtainment of these two quantities will be discussed in the next two topics.

6.3.1 Natural modes - Polymax®

The modal fitting process is similar to what is done at curve fitting. The curve fitting is a process where different polynomial orders are tested and then the coefficients of the polynomial are calculated in order to minimize the difference (or error) between the curve and the data points. In modal curve fitting a similar procedure is done, where different number of modes are considered, and then the modal shapes, natural frequencies and modal damping values are calculated in order to best fit the measured FRFs. This fitting process is done via LMSE

– least mean square error. About the procedure that is done at Testlab® it is constituted by the following steps: [29]

- FRF and frequency range selection – this first step consists in selecting the FRFs (already calculated by the software) and the frequency range to be considered in the stabilization diagram. Not all FRFs need to be displayed, only the needed ones to help selecting the modes. Another option is the utilization of the "sum" option which is basically an average FRF off all FRFs. This is not the selection of the FRFs that are used in the calculation of the modes. All measured FRFs are used in the calculation of the modes;

- Maximum model order - this last input for the generation of the stabilization diagram is to indicate the maximum number of modes to be considered in the calculation of the modal modes. This value should be high enough to allow the identification of all modes;

- Stabilization diagram – in this step the modal modes are selected. These modal modes, as it can be seen in fig. 6.8, are represented by "columns of letters". The number of rows represent the number of modes that were considered in obtention of that potential mode. The letters have the following modes:

  - s – stable – this is the letter that should be selected, because it means that the modal solution is completely stabilized in frequency, damping and modal participation vector;
  - v – vector – frequency and modal participation vector are both stabilized;
  - d – damping – frequency and damping values are stabilized;
  - f – frequency – only the frequency value is stabilized;
  - o – the pole is not stable;

  So, in short, only "s" modes should be selected, and they should be from the last row, considering that the user only used the necessary number of modes to obtain the required modes. Sometimes, a higher number of modes is considered because some natural frequencies are close to each other and for that reason they are not "easy to catch", and the software may consider one of the peaks as "noise" instead of a modal mode. It is important to keep in mind that the consideration of for example 100 modes in the calculation does not mean that software generates 100 modes. At the fig. 6.8, 40 modes were considered and only 15 different modes were given to choose.

- Calculation of the modal shapes – at this step the modal shapes and the upper and downer residuals are calculated;

- Modal validation – the modal validation step is done by two ways: via Modal Synthesis and via Modal Assurance Criterion (MAC). Modal synthesis is a step where the experimental FRFs are compared with the synthetized FRFs obtained with the determined modes, and the quality of that comparison is done via two quantities, the correlation, that should be higher than 95% and the error that should be lower than 5%. The MAC is a colormap (see next chapter) and a very important procedure because it ensures that the selected modes are indeed modes of the system, this is, that they are not repeated. A good MAC has all its terms in the diagonal at 100%, which always happens by definition, and the terms outside of the diagonal should be close to zero. When that doesn't

happen, it is necessary to justify the reason for why the values are different from zero, outside the diagonal;

Inside Testlab® there are two main procedures of calculating the modes: Time MDOF® and Polymax®. The previous steps are common to both methods and the difference between them lies in the way the modes and stabilization diagrams are obtained. It was decided to use Polymax®, because it is "better" and the most used procedure.

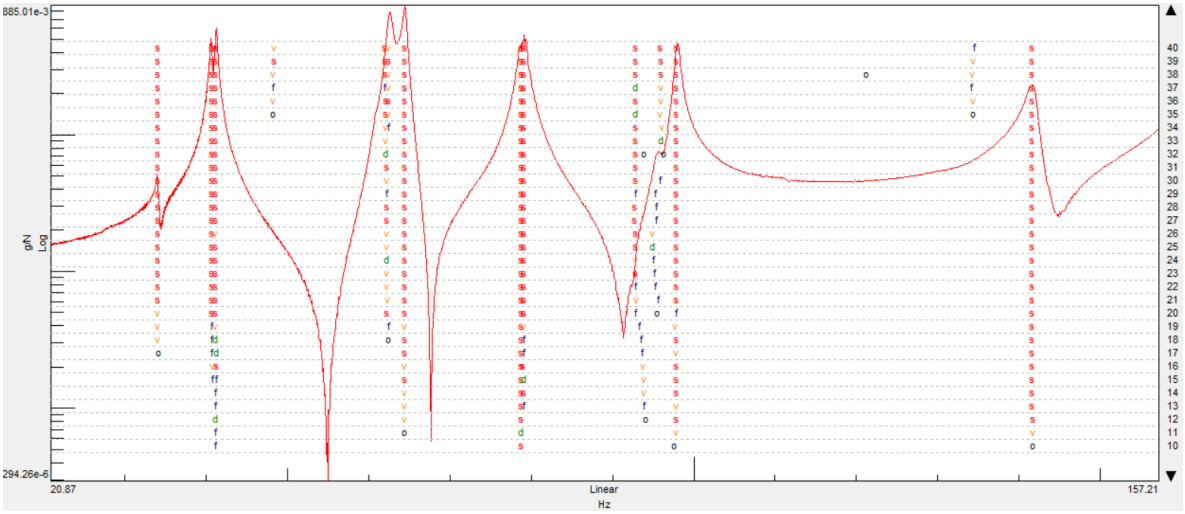


Figure 6.8: Example of a stabilisation diagram

6.3.2 Acceleration integration procedure

The measured data is composed by accelerations so in order to apply the Acceleration Surface Method is necessary to obtain the velocities and the displacements, which means it is necessary to integrate the data. To do that there are several procedures like the trapezium rule, the Simpson's rule, the integration in the frequency domain, etc, and among those different procedures the trapezium rule, is the simplest one, the less computationally expansive and is an effective procedure. The transfer function of the trapezium rule is [30]:

$$TF(Nf) = \frac{FT(estimatedresults)}{FT(trueresults)} = \cos(Nf/2)\frac{Nf/2}{\sin(Nf/2)} \tag{6.2}$$

where Nf is the normalized frequency, this is, is the frequency of interest divided by the sampling frequency and FT is the Fourier Transform. This shows that if the sampling frequency is only two times higher than the maximum frequency of interest to measure, the accuracy of the integration is about 98%. In literature authors recommend that the sampling frequency should be 10 to 20 times higher than the highest frequency of interest [30].

As it is known, with any integration procedure a trend is generated, which in practical terms means that the integrated answers will not oscillate around zero. This trend is also known as low frequency trend and can be easily eliminated by using a highpass filter [31]. But to avoid any kind of distortions in terms of phase a zero-phase digital filtering should be done, and the assigned tool at Matlab® that allows that is the function *filtfilt*. To use that function is also necessary do define a digital filter, that should be sharp as possible. And the filters that satisfy better that condition are the *IIR* (infinite impulse response) filters, and

inside of that group the Butterworth filter was chosen for not having ripples, and for having the smoothest curve. In the definition of a Butterworth filter some parameters need to be defined, and as an example, a case of a highpass filter will be considered. The parameters are listed bellow [32] and for a better understanding at the fig. 6.9 a Butterwoth highpass filter with a passband and stopband frequencies equal to 3 Hz and 5 Hz, passband ripple equal to 10 dB and a stopband attenuation of 60 dB is presented. The value of the passband ripple is high in order to make the image clearer and the concept more understandable for the reader.

- Passband and Stopband frequency – these are the frequencies where the "transition" from the filtered to non-filtered frequencies happens;
- Passband ripple – Is the maximum gain that the signals with a frequency higher than the passband frequency can get. This value ideally should be zero, and for that reason in this thesis a gain of 1 dB was used;
- Stopband attenuation – Is the attenuation that is imposed to the signals, with a frequency lower than the stopband frequency. This value should be high as possible. At this thesis was used the value of 60 dB;

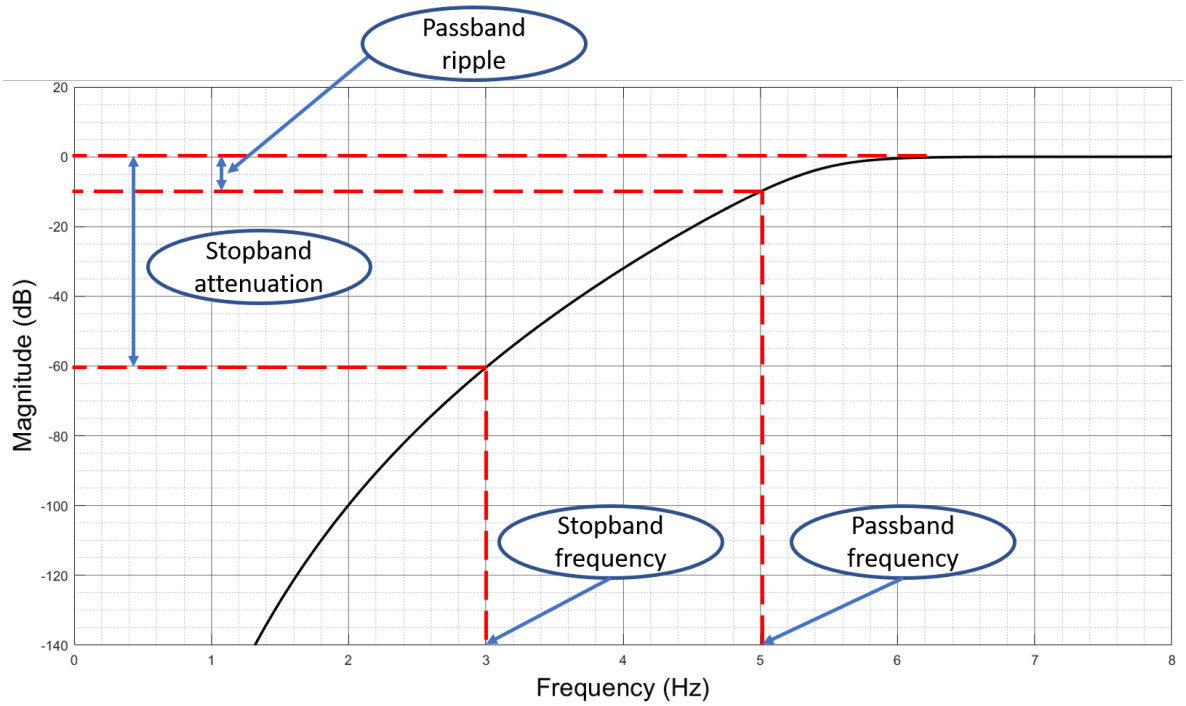


Figure 6.9: Butterworth highpass filter parameters

Like it was already indicated, the main source of the nonlinear behaviour on the airplane is located at the pylons, and consequently the nonlinearities will be more visible at the pylon natural modes, especially in the pylon first natural mode, that on the airplane corresponds to the first and second natural modes (see fig. 6.6), and for that reason the characterization of the nonlinearities will be done in the frequency range from 6.3-8 Hz. To study that frequency range, there are two different options: or the excitation frequency is known and the corresponded points to that frequency are selected, or a bandpass filter can applied. This filter

is essentially a lowpass+highpass filter, and its use requires the definition of the equivalent parameters related with the lowpass filter. But when using a bandpass filter there is the removal of other harmonics of the answer, and this fact is important to keep in mind when processing nonlinear answers. And since the goal of utilising the bandpass filter is to select a specific frequency range it also needs to be applied to the acceleration, and besides that it wouldn't make sense to use the ASM with the accelerations containing higher harmonics and displacements and velocities not containing them. In short the overall procedure to be followed in the obtention of the displacements and velocities is exposed at fig. 6.10.

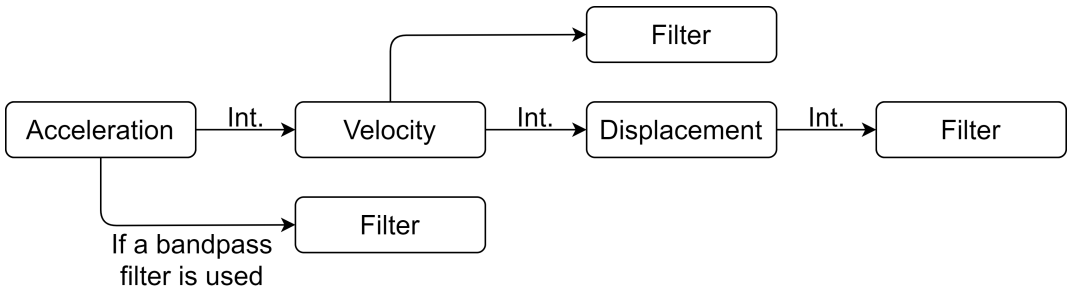


Figure 6.10: Acceleration integration procedure

The integration of the displacements is not from the filtered velocity because filtering generates a very small gain, since there are no perfect filters. And the "zero-phase digital filtering" removes all trends including the ones that come from the integration of the acceleration.

6.4 Performed experiments

After presenting the finite element model, exposing the setup, the experimental procedure and how the data processing works, it is necessary to indicate the measurements that were realised in this experience. They are listed in the following table:

Tension (V)	Freq. range (Hz)	Sweep-rate (oct/min)	Samp. freq. (Hz)	No. sweeps
0.005	5-300	0.4	3200	2
0.01	5-100	0.4	1600	2
0.02	5-100	0.4	1600	2
0.02	5-100	1	1600	2
0.02	5-100 (down)	1	1600	2
0.04	5-100	0.4	1600	2
0.06	6-100	0.4	1600	2
0.06	40-60	0.4	1600	1 (0-90°)
0.07	6.3-10	0.4	400	2
0.08	6.3-10	0.4	400	2
0.09	6.3-10	0.4	400	2

Table 6.1: Parameters utilized in the different measurements

The first sweep with 0.005 V was done with the goal of validating the linear model, since like it was indicated in the first chapter for small displacements the nonlinear models can be treated as linear models. This experiment also has a characteristic that the others don't have

which is related with the gain of the sensors. During the experiments, one of the problems that was found was the occurrence of overloads due to the lack of damping in the system, and the overloads obligated the use of a higher range value, that for regions where the accelerations are lower is not good, because the utilisation of high range values comparatively with the values that are measured, will make the measurements more susceptible to noise. To solve that problem, in the first measurement was used a tool in the software that allows the automatic adjustment of the range values when a overload occurs. The advantage of that is that it allows the obtention of a less noisy FRF plot, but on the other hand doesn't allow the obtention of a continuous response in time and frequency domain. This is, when a overload happens the software doesn't continue the normal evolution, i.e., the experiment "stops literally" and then there is a phase where the system is excited to get to the same point where it was before. For this reason, the scope tool was not used for higher tension values, and the range was fixed to a conservative value of 10 V, to avoid overloads. Since for 0.005 V there is not a continue response, it will not receive the same treatment of the other responses.

CHAPTER 7

Linear model validation and nonlinear characterization

7.1 Linear model validation

7.1.1 Experimental modal model

The first step in the process of linear model validation is the extraction of the mode shapes from the experimental data. According to the previous chapter, the first step in that process is the selection of the FRFs plots, and the next curves were chosen:

- LWing5:Z-Lwing:5_forceZ – this is one of the direct FRFs available. Direct FRFs have special characteristics, like the presence of an antiresonance between resonances, that help the user to identify more easily the different modes;
- LWing1:Z-Lwing:5_forceZ – this is an FRF from the sensor that is located at the tip of the left wing. If a careful analysis is made it can be observed that in many modes the tip of the wing is the place where the largest oscillations happen, and for that reason it is a good option to identify the modes;
- LPylon2:X-Lwing:5_forceZ – this was chosen in order to detect the modes associated to the pylons (pylon bending and pylon torsion);
- RPylon2:X-Lwing:5_forceZ – the FRF from the other pylon was also chosen because the peak of the torsional mode in right pylon is not visible in the left pylon FRF due to the phenomenon of the vibration nodes;
- Tail4:Z-Lwing:5_forceZ – one of the modes consist essentially in the bending of the tail, so the consideration of this sensor is important to capture that mode;
- Fin1:X-Lwing:5_forceZ – one of the modes consist simply in the fin bending, so the aim of its utilization to capture better that mode;

All resonances are visible in all FRFs, except when due to the presence of vibration nodes, the peak does not exist or it is difficult to distinguish it from noise. With the previously

indicated curves the different peaks are perfectly visualized and it is possible to distinguish the physical modes from the numerical poles. After that, the stabilization plot is generated, and it is now exposed in the next figure:

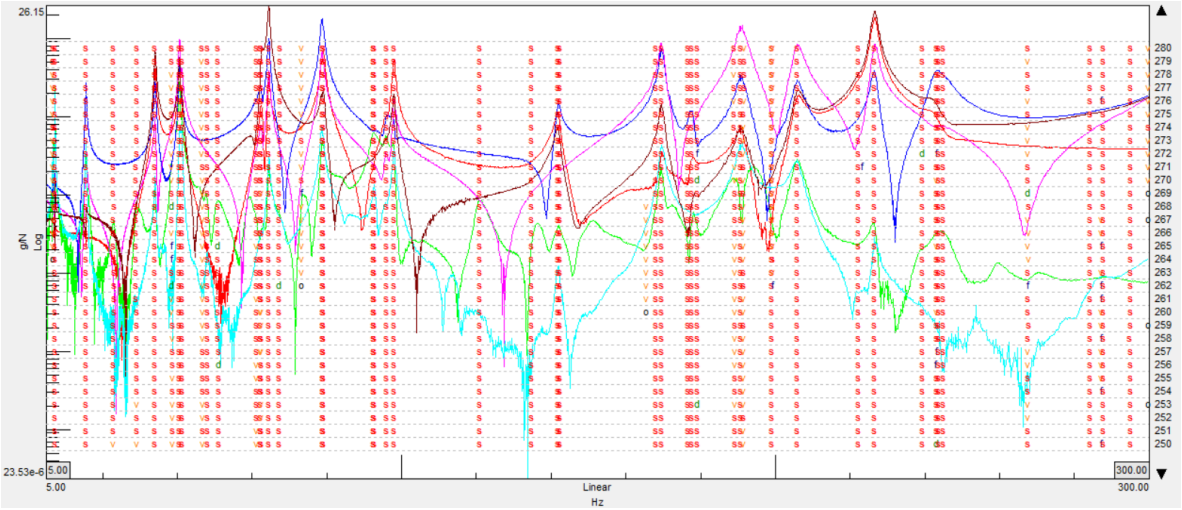


Figure 7.1: Stabilization diagram

After obtaining the stabilization plots, the next steps are to choose the poles and generate the modes. After doing that, the validation procedure can be done. In table 7.1, the errors associated to modal synthesis are presented, and the Auto-MAC plot is presented at fig. 7.2.

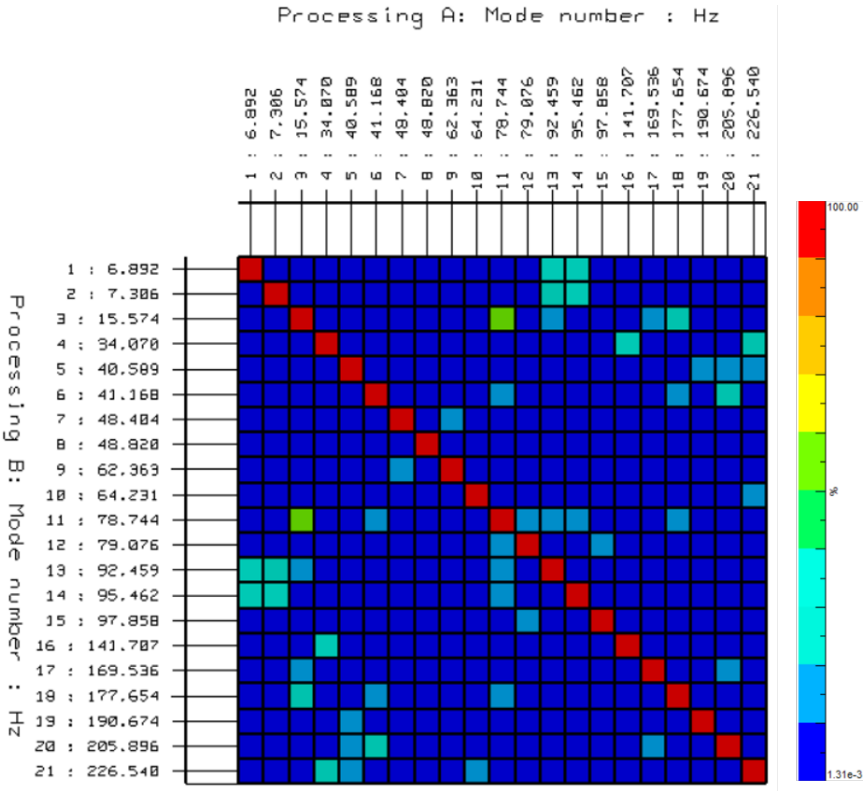


Figure 7.2: MAC for the modal modes generated by Testlab®

Point	Direction	Lwing:5_forceZ		Rwing:5_forceZ	
		Correlation (%)	Error (%)	Correlation (%)	Error (%)
	X	98.36	1.65	97.69	2.34
Fin:1	Y	98.56	1.45	98.66	1.34
	Z	98.21	1.80	97.43	2.61
Fin:2	X	98.81	1.2	97.53	2.51
Fuse:1	Z	98.59	1.43	98.75	1.27
	X	98.41	1.59	97.59	2.42
Fuse:2	Y	98.5	1.50	98.93	1.07
	Z	98.51	1.50	98.59	1.41
Fuse:3	Z	97.82	2.21	97.84	2.17
LPyl:1	X	92.31	7.84	92.98	7.40
LPyl:2	X	71.5	37.32	89.93	11.48
LPyl:3	X	88.84	13.60	96.48	3.55
	X	93.26	7.00	94.59	5.58
LWing:1	Y	96.33	3.67	95.70	4.31
	Z	89.59	10.85	90.67	9.76
LWing:2	Z	94.65	5.49	93.40	6.72
LWing:3	Z	94.25	5.77	93.99	6.04
LWing:4	Z	97.01	3.00	95.34	4.72
LWing:5	Z	94.88	5.13	95.03	5.01
LWing:6	Z	95.28	4.72	95.13	4.87
RPyl:1	X	93.14	7.55	93.35	6.87
RPyl:2	X	90.98	9.03	91.32	9.28
RPyl:3	X	78.25	24.32	85.23	15.76
	X	94.12	6.06	93.42	6.69
RWing:1	Y	95.67	4.34	96.30	3.71
	Z	92.95	7.62	91.57	8.72
RWing:2	Z	93.87	6.49	92.57	7.61
RWing:3	Z	93.89	6.15	95.00	5.02
RWing:4	Z	97.56	2.45	97.73	2.27
RWing:5	Z	94.64	5.46	95.80	4.23
RWing:6	Z	94.81	5.25	96.34	3.69
	X	98.43	1.57	97.7	2.31
Tail:1	Y	97.46	2.54	97.79	2.23
	Z	97.77	2.25	95.34	4.97
Tail:2	Z	99.28	0.72	98.56	1.46
Tail:3	Z	99.24	0.77	98.57	1.44
	X	98.42	1.58	98.39	1.63
Tail:4	Y	96.85	3.18	95.87	4.28
	Z	86.33	19.07	85.12	24.24

Table 7.1: Modal synthesis error

Like it was told previously about the MAC plot, when some values outside of the diagonal are not close to zero, they need to be justified. When analysing the previous description, it is important to have in mind that the 11^{th} and 12^{th} modes in Testlab® are the 12^{th} and $11th^{th}$ modes in fig. 6.6. This can be confirmed at the fig. 7.4.

- 1^{st} and 3^{rd} pylon modes – the sensor configuration doesn't allow to distinguish between the 1^{st} and 2^{nd} bending modes of the pylon. So, it is normal the presence of nonzero values, between the modes evolving these pylon modes (1-13, 1-14, 2-13 and 2-14);

- Bending modes – the utilization of the 4 sensors at back of the wing are more than enough to distinguish the different bending situations, but at the front of the wing only 2 sensors are used and consequently, the line defined by these two sensors will have an equal movement in some of the bending modes. This is the cause of the majority of the "light blue squares" - 3-18, 4-16, 11-18, 10-21 and 4-21. Inside of this category it is also the worst case which is the "green square" between the 3^{rd} and 11^{th} modes. Since this is the worst case, and to clarify the reader, this situation is illustrated in fig. 7.3;

- Torsional modes – once again this is a problem caused by the utilization of only two sensors in the front of the wing. This is what happens with the modes 5-19, 5-20 and 6-20;

- Bending and torsional modes – there are other squares with a "light blue" color and they are caused by different reasons. Since most of the sensors measure the movement in the Z direction, the torsional movement is measured like a bending movement this is, an "up and down" movement of those sensors. In the back of the wing where there are 4 sensors is difficult for those "up and down" movements to be coincident between the torsional and bending modes, but at the front of the wing where there are only 2 sensors, is easier for that happen. Besides that, at the back of the wing there is one triaxial sensor while at the front there is none. That is the case of the 6-18, 5-21 and 6-11 situations. In this category there are two special situations that are the 3-17 and 17-20 modes cases. They are special because the 17^{th} mode is not a pure torsional mode, it also has bending in the front of the wing as it can be seen at fig. 6.6.

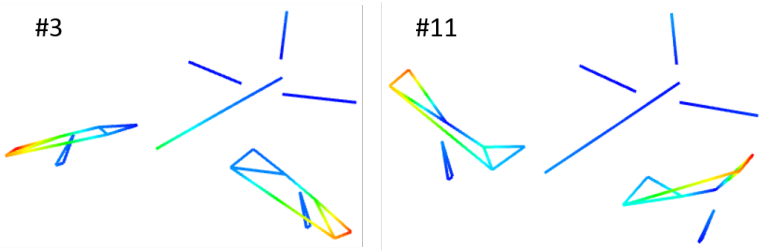


Figure 7.3: 3^{rd} and 11^{th} modes obtained by Testlab®

In short, the previous comments show that it is the spatial resolution of the accelerometers that is responsible for non-perfectly orthogonal modes, i.e., some non-null values outside the diagonal and that the utilization of more sensors in the front of the wing would have contributed for better results. But at the same time, the existence of some points higher than zero is perfectly normal, so it can be affirmed that MAC results are good. At the second criterion which is the modal synthesis, the results are generally good, but at LPyl:2-Lwing:5_forceZ

and RPyl:3-Lwing:5_forceZ the results are very bad considering the error values of 37.32% and 24.32%. But that doesn't mean necessarily that the modes are badly identified, because on one hand looking to other values concerning the sensors at the inferior block of the pylons (LPyl:2, LPyl:3, RPyl:2 and RPyl:3) errors of 3.55% and 9.03% can be found, and on the other hand if the modes were badly identified it would have been impossible to have correlation values of 98.81% or 99.28%. In conclusion the identified modeset is validated and can be used as good reference for the experimental results.

7.1.2 Linear model correlation

The model correlation process is done via Modal Assurance Criteria (MAC), and the difference from the previous MAC is that in the Y axis the numerical modes from Simcenter3D® are represented. The correlation between the modes is done by considering the nodes in the numerical model that are coincident with the position of the sensors used during the experiments. The obtained MAC is shown in the following figure:

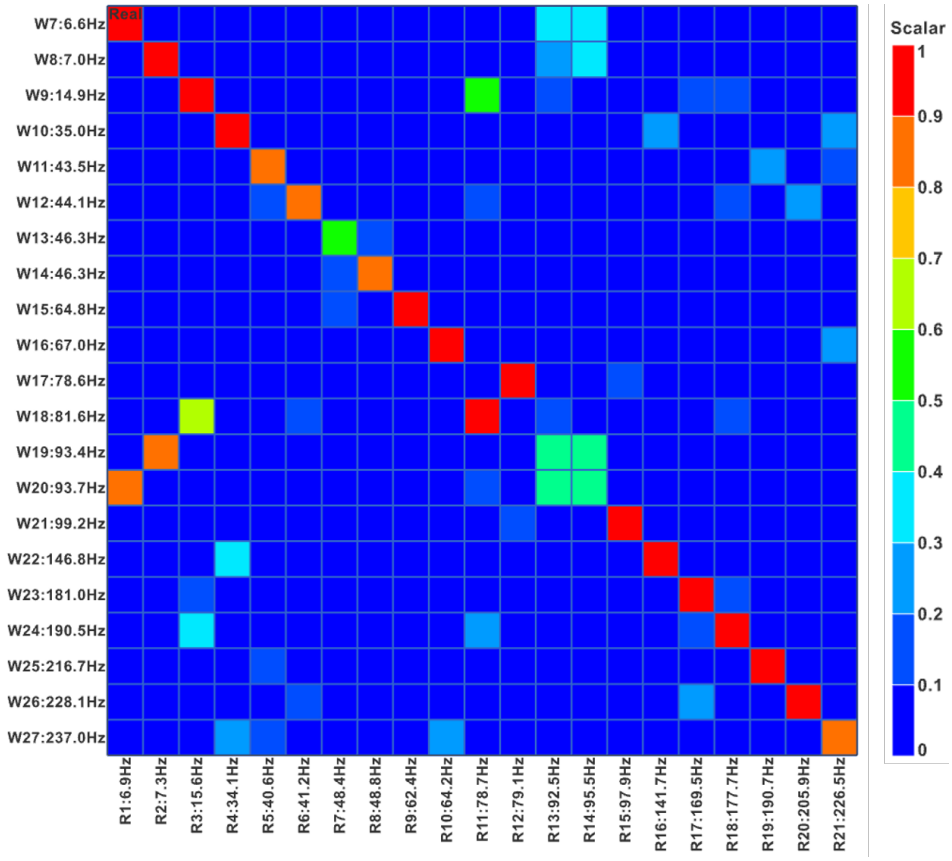


Figure 7.4: MAC between the numerical and experimental modesets

From the plot, it can be concluded that the results are quite good. But there are two main problems:

- In one of the pylon torsional modes the MAC value is not high as it would be good to be. That happens because the captured mode is not "perfect", this is, it also presents some bending in the tail and fin. If those sensors are not considered, the MAC value increases to 0.79, showing in this way that the mode is valid.

- The modes associated to the 3rd pylon mode are not valid. This happens because, as it can be seen at fig. 7.5 and 7.6, the resonance in the real mode behaves differently, this is, while in the numerical mode there is firstly the symmetric and then the asymmetric disposition, in the experimental model, there is a behaviour similar to the torsional modes, this is, first there is the 3rd mode in the right pylon and then in the left. Somehow, since these modes are not easy to extract, it could exist the possibility of the modes have not being well extracted, but looking to the FRF plot from fig. 7.7, it can be clearly seen that the resonance at the right and left pylon are at different frequencies.

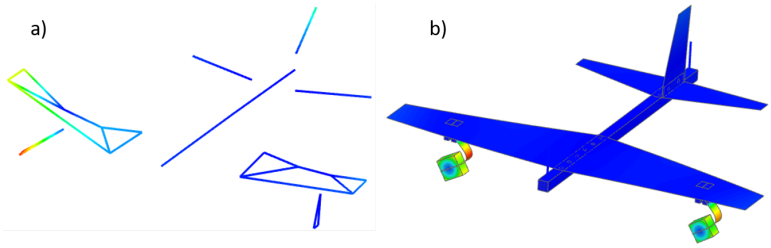


Figure 7.5: Comparison between the 13th modes on Testlab® - a) - and Simcenter3D® - b)

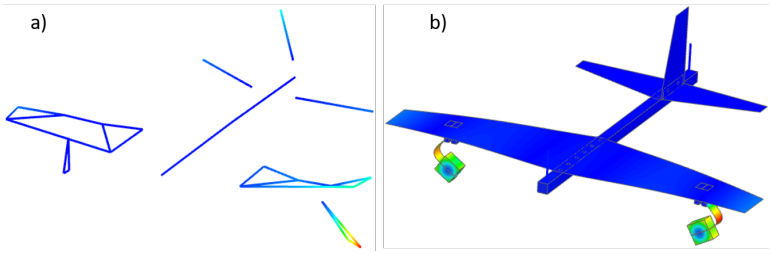


Figure 7.6: Comparison between the 14th modes on Testlab® - a) - and Simcenter3D® - b)

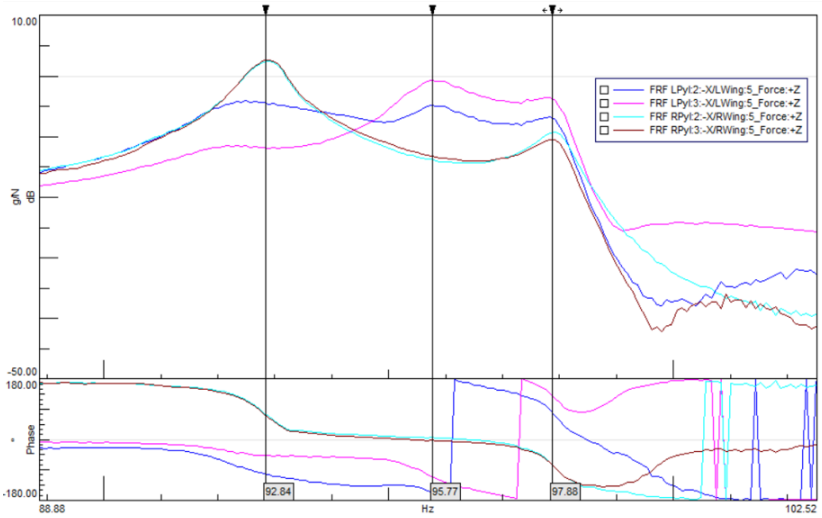


Figure 7.7: FRF curves from left and right pylon

Besides the MAC criterion, there is a last one that is the frequency error, that should be

lower than 5% and the results in that parameter are presented in fig. 7.8. To allow a better analysis, the MAC values and frequencies errors are also presented in table 7.2.

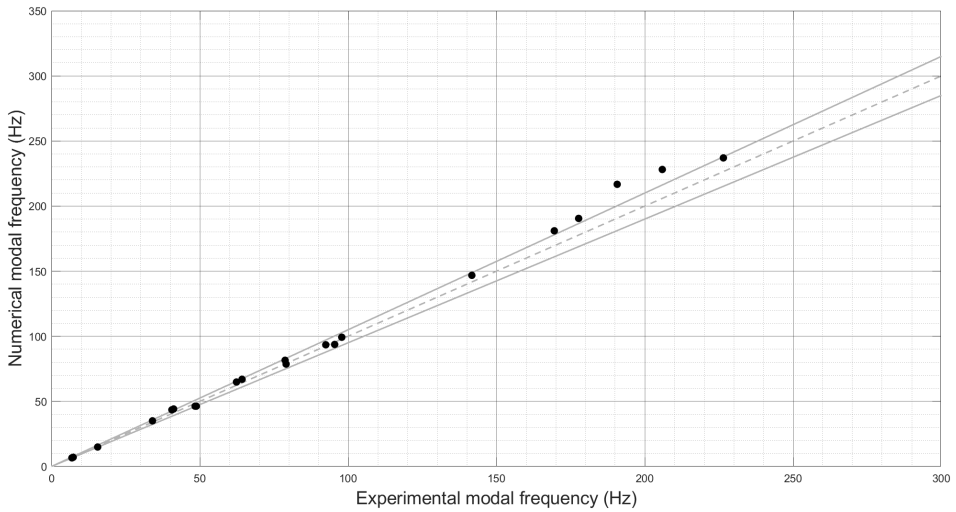


Figure 7.8: Frequency error between the experimental and the numerical model

Pair	Freq. exp. model (Hz)	Freq. num. model (Hz)	Freq. error (%)	MAC (%)
#1	6.89	6.60	-4.17	96.66
#2	7.31	7.04	-3.62	95.50
#3	15.57	14.93	-4.16	98.93
#4	34.07	35.03	2.81	99.25
#5	40.59	43.51	7.20	82.11
#6	41.17	44.14	7.22	85.31
#7	48.41	46.28	-4.39	57.66
#8	48.82	46.30	-5.17	82.35
#9	62.36	64.83	3.96	95.07
#10	64.23	66.95	4.23	95.13
#11	79.08	78.64	-0.56	96.58
#12	78.74	81.57	3.58	96.92
#13	92.46	93.43	1.05	48.38
#14	95.46	93.72	-1.82	49.49
#15	97.86	99.24	1.41	98.14
#16	141.71	146.81	3.60	97.79
#17	169.54	180.99	6.75	95.07
#18	177.66	190.46	7.20	93.89
#19	190.68	216.68	13.64	95.14
#20	205.90	228.06	10.76	90.13
#21	226.54	237.02	4.62	88.49

Table 7.2: Correlation MAC values and frequency error values

Concluding if the goal is to simulate a continuous sine-sweep starting around 5Hz like it was done in the experimental measurements, the model is only valid until 93 Hz. Concerning

the modes bellow that frequency error, the frequency error criterion is respected in all modes except at the torsional modes of the airplane (modes 5 and 6), but at the same time is only an addition of more 2%, which is something acceptable. To finalize, in the modes bellow 93 Hz the frequency errors have an expected behaviour this is, they are not always positive or negative, which means that the error cannot be related with an excess of mass or damping, and for those reasons it can be declared that the numerical model is valid until 93 Hz. For simulations regarding frequencies higher than 93 Hz, the model is not "totally valid" because the frequencies errors on modes 19 and 20 are too high.

7.2 Nonlinear characterization

After the validation of the linear model, the next step is the characterization of the nonlinearity, that will be done from 6.3-8 Hz, like it was explained in section 6.3.2. But before doing that step, it is a good to see the evolution of the response for the different levels of excitation, and for that let's consider the fig. 7.9, 7.10, 7.11, 7.12, 7.13, 7.14, 7.15 and 7.16 where the answers measured in the left pylon at *sweep1* and *sweep2* for different levels of excitation are exposed. Starting by analysing the *sweep1* it can be seen that at 0.01 V and 0.02 V there is linear behaviour because, according to what was indicated in the first chapter, there is a smooth evolution before and after the resonance peak, and the resonance peak presents also a "symmetric" shape. If the applied force is increased for 0.04 V a nonlinear answer can already be detected, because there is clearly a nonsymmetric shape in the resonance zone, and the evolution of the answer is not smooth, as it can be confirmed at 6.95 Hz and 7.05 Hz by the changes in the slope of the answer, and by last the answer is nonsymmetric, this is, the accelerations in the positive sense are larger than in the negative sense, which reinforces the nonlinear nature of the answer. After that voltage the remaining answers are also nonlinear, but the jump becomes more abrupt and starts to happen at higher frequencies, showing that the pylon also presents a hardening behaviour. At 0.07 V a second peak starts to appear at lower frequencies, around 6.7 Hz, revealing in that way an even greater nonlinear behaviour, comparatively with the lower excitation levels. For the plots related with *sweep2*, comparatively with *sweep1* a difference that can immediately be spotted is that while at *sweep1* only one mode is excited, at *sweep2* two modes are excited, as it can be confirmed at 0.01 V. At 0.02 V it already seems to exist a nonlinear behaviour because the shape is completely different from the one at 0.01 V and it is known that in a linear system the shape of the answer remains always the same. Passing for 0.04 V, the shape is even more different, and seems to exist a jump at 7.35 Hz, but with 0.06 V a more similar shape to *sweep1* is obtained, and with 0.07 V there starts to exist a "standard" shape for *sweep2*, with two jumps, around the first and second resonance frequencies of the airplane, and in both cases a hardening behaviour exists.

In fig. 7.17, it is shown an example of what happens when the sweep rate frequency is increased, using as example the *sweep2* at 0.02 V. It is possible to see that with the increase of the sweep-rate, the answer appears to be more nonlinear. The explanation for that resides in the fact that when using a lower sweep rate the answer of the system approaches a more steady-state behaviour, while with a higher sweep-rate there is bigger influence of the transient nonlinear answers which means that the nonlinear effect propagates to higher frequencies. That propagation creates a "accumulation" of transient nonlinear answers that causes the effect of increasing the nonlinear behaviour, and for that reason it is commonly said that a higher sweep rate accentuates the nonlinear phenomenon. This propagation of nonlinear

effects for higher frequencies is very visible in this case because the “jump” happens in a frequency higher than the “jump” at 0.07 V when using a sweep-rate of 0.4 oct/min.

Another thing that was mentioned about the detection of the nonlinearity was the realization of a sweep-up and a sweep-down to check the existence of nonlinearity. In fig. 7.18 for a sweep-rate of 1 oct/min for *sweep2* at 0.02 V, it can be visualized that with the sweep down the ”jump” no longer exists and that the shapes are quite different. It is not a good example, comparatively with what was found on literature (ref. [6]), where the shapes where similar and the hysteresis could be seen, but it stands for the point that in nonlinear systems the answer in a sweep-up and sweep-down are different. Unfortunately, a sweep-down was not made for 0.01 V to see the coincidence of the shapes that happens in linear systems.

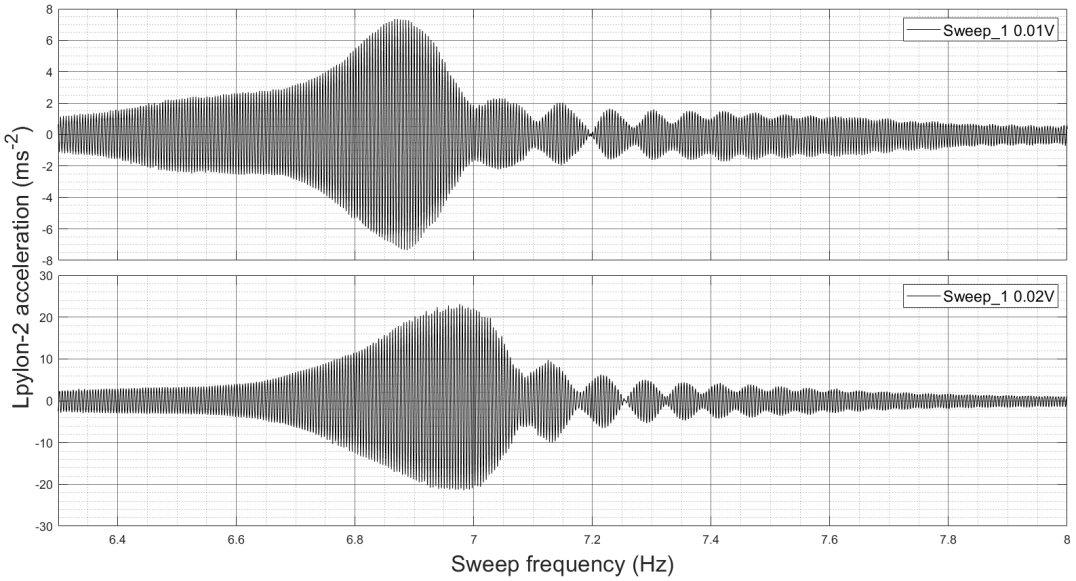


Figure 7.9: Sweep 1 answers for 0.01V and 0.02V at LPylon:2

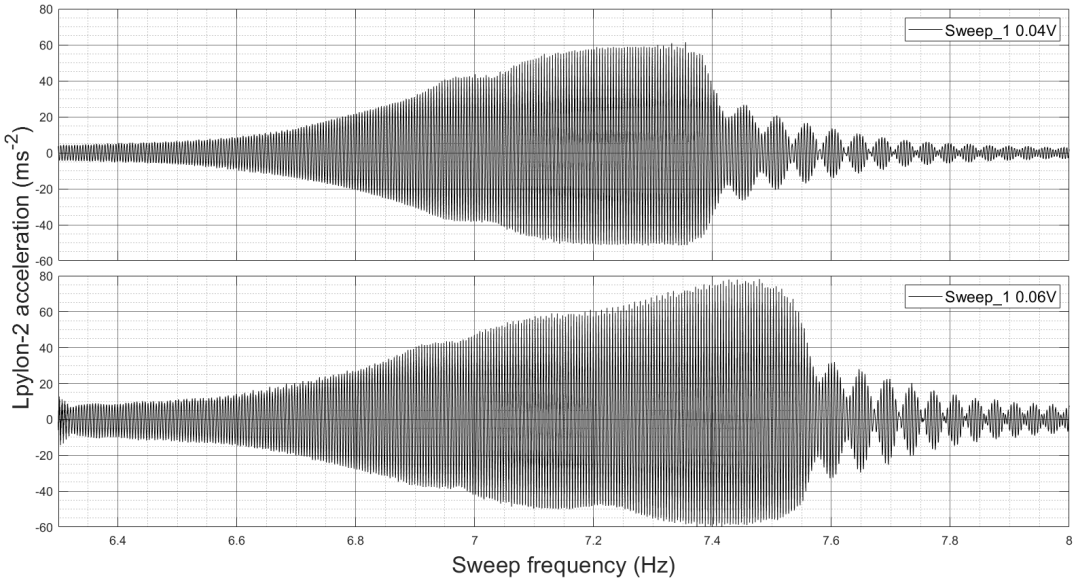


Figure 7.10: Sweep 1 answers for 0.04V and 0.06V at LPylon:2

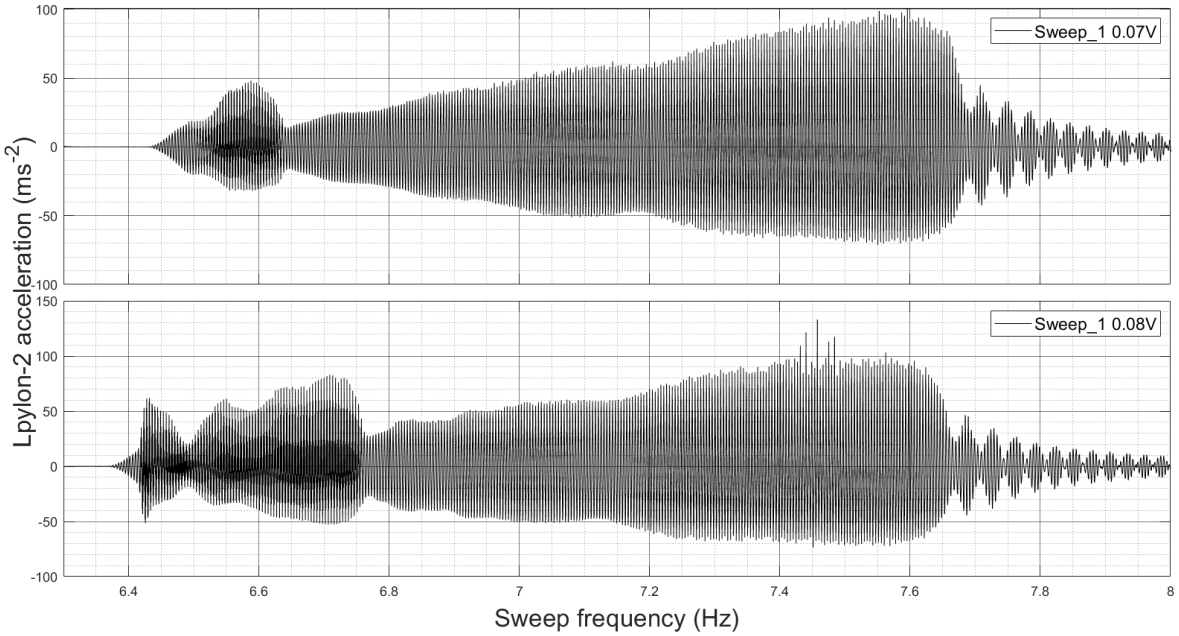


Figure 7.11: Sweep 1 answers for 0.07V and 0.08V at LPylon:2

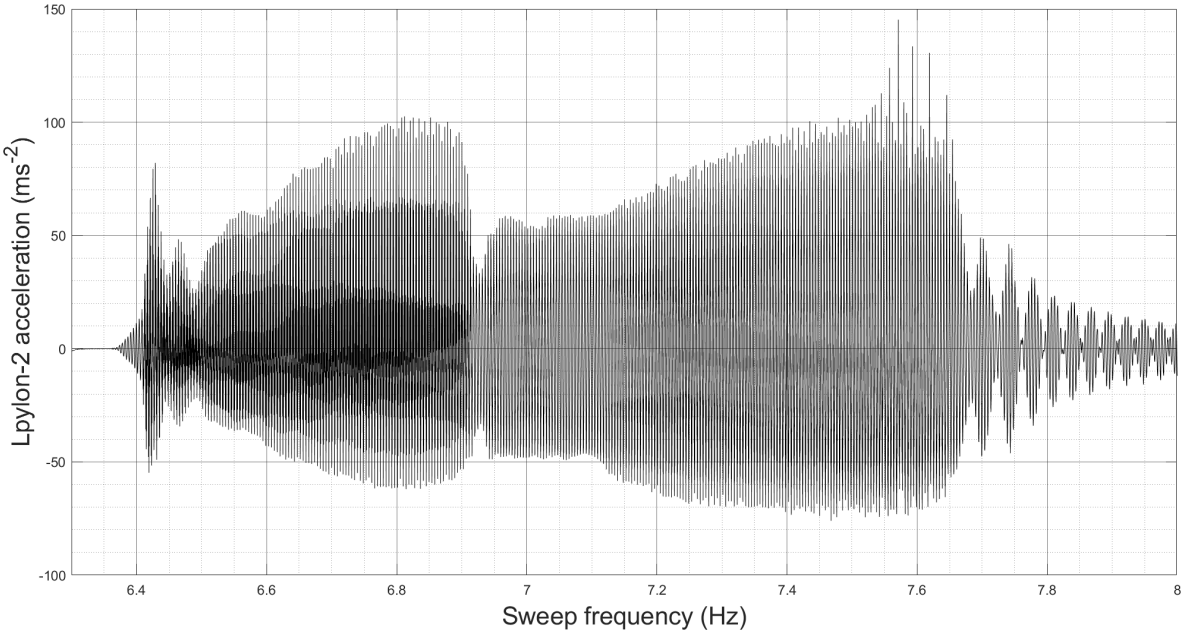


Figure 7.12: Sweep 1 answer for 0.09V at LPylon:2

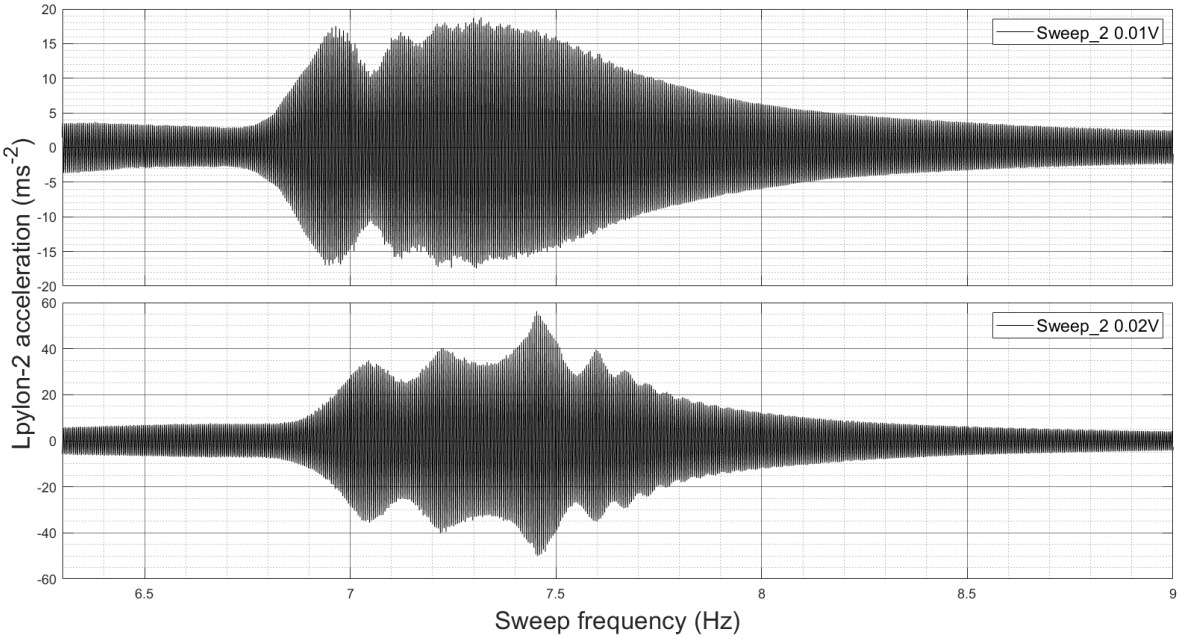


Figure 7.13: Sweep 2 answers for 0.01V and 0.02V at LPylon:2

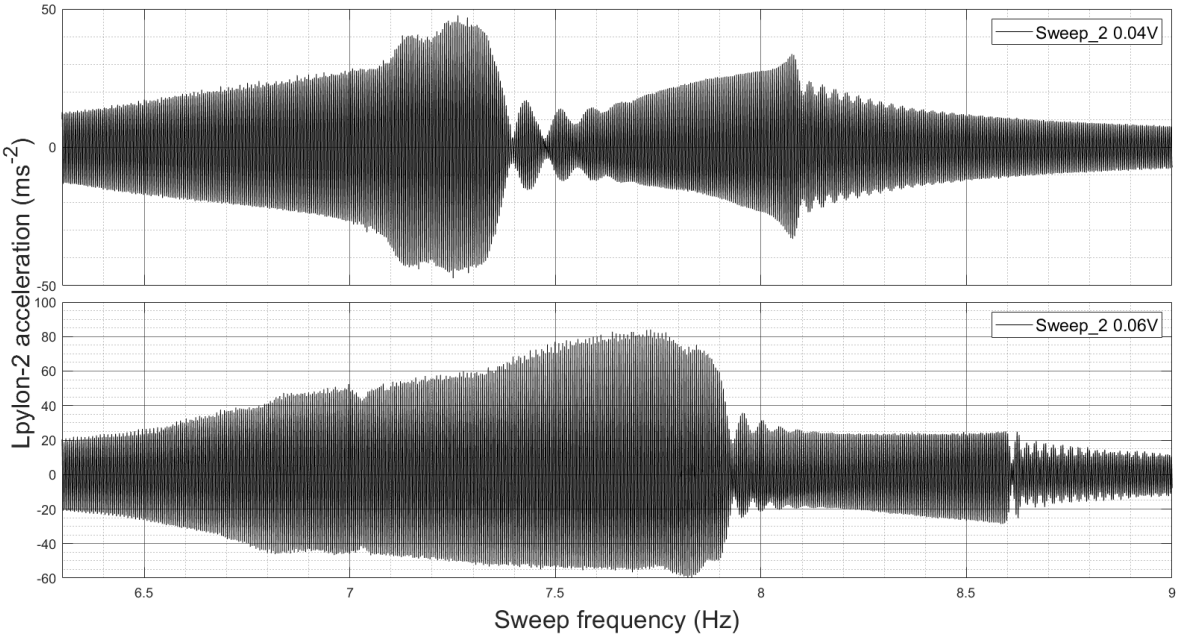


Figure 7.14: Sweep 2 answers for 0.04V and 0.06V at LPylon:2

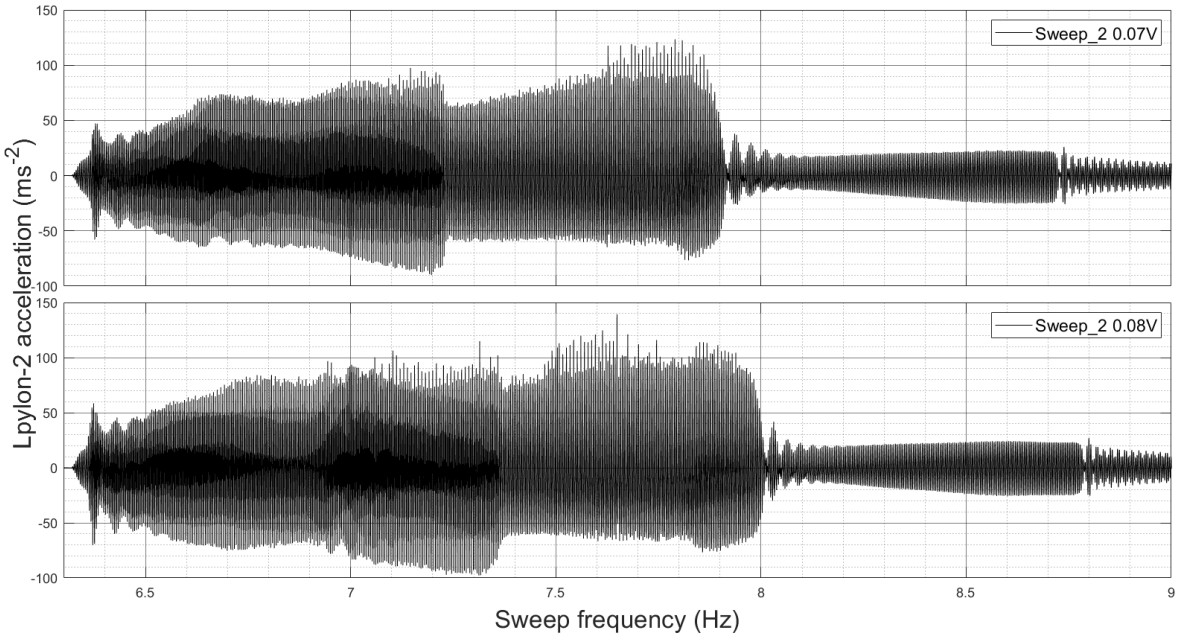


Figure 7.15: Sweep 2 answers for 0.07V and 0.08V at LPylon:2

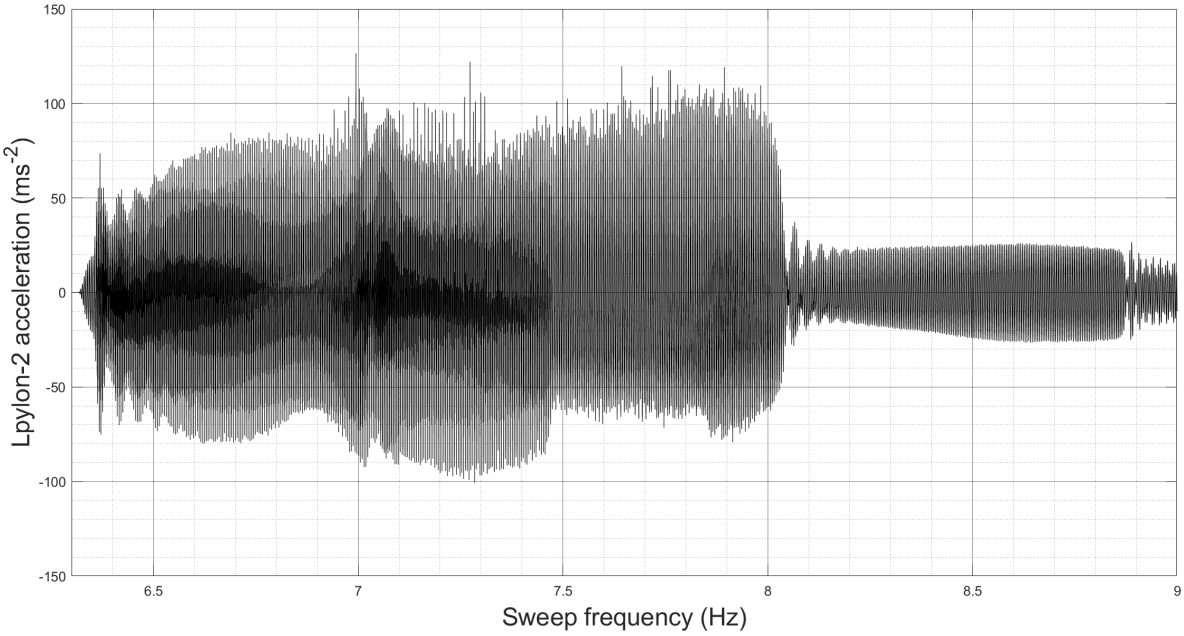


Figure 7.16: Sweep 2 answers for 0.09V at LPylon:2

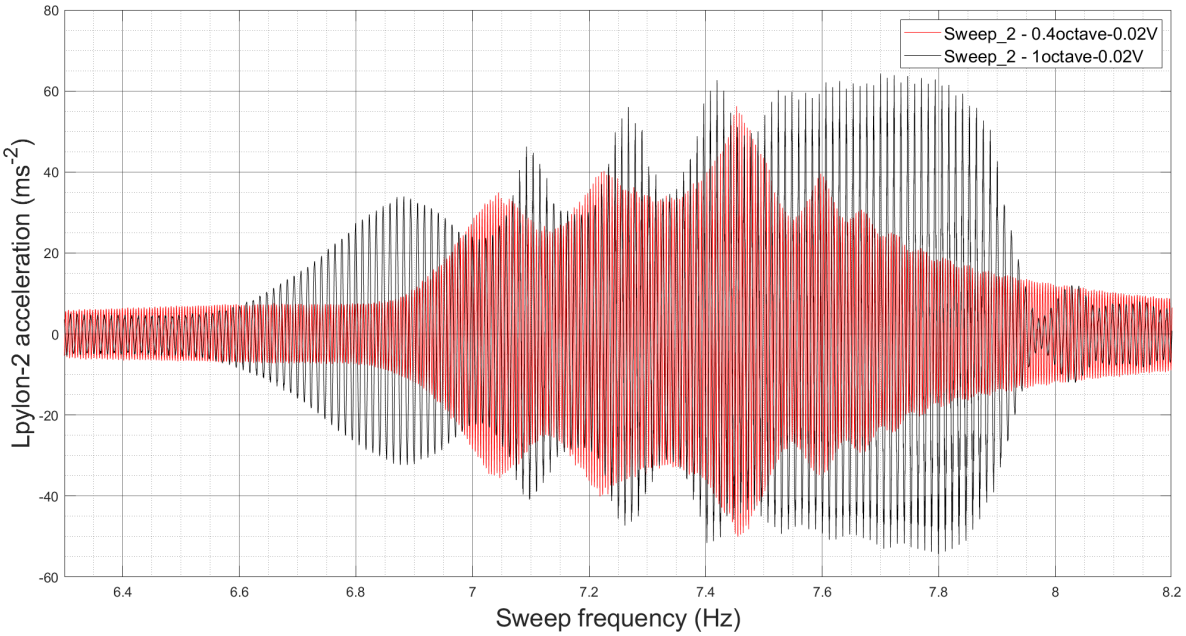


Figure 7.17: Sweep 2 answers for 0.02V with sweep-rates of 0.4 oct/min and 1.0 oct/min

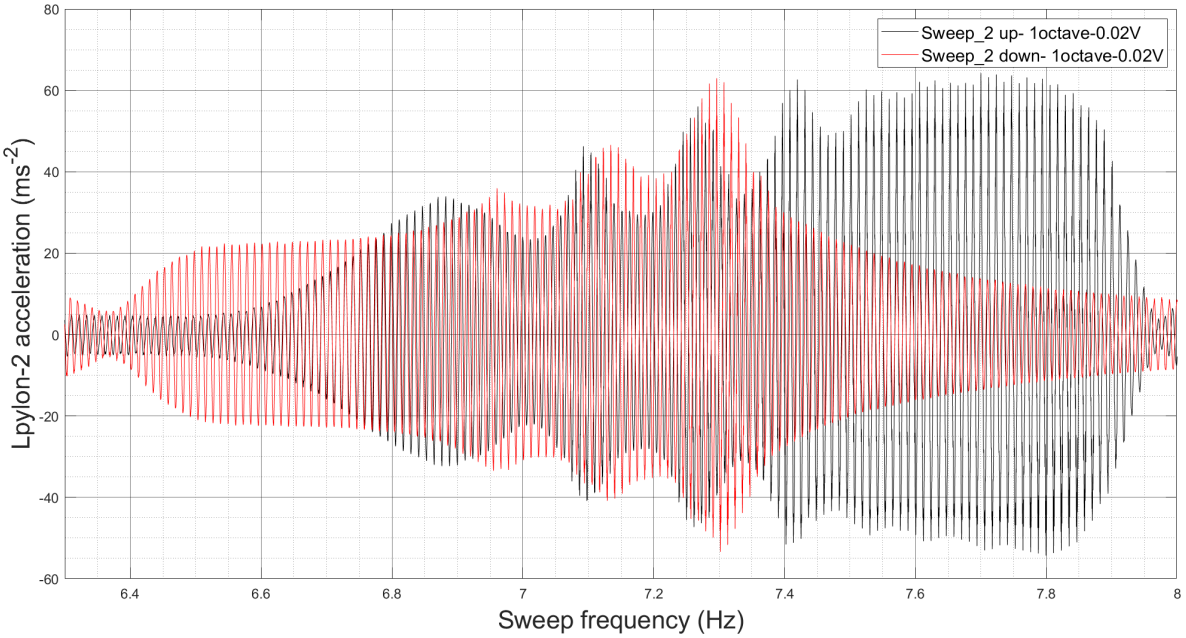


Figure 7.18: Sweep-up and sweep-down for 0.02V with sweep-rates of 0.4 oct/min

After this brief evaluation of the nonlinear system answer, the next topic is the characterization of the nonlinearity using the Acceleration Surface Method. According to what was indicated in section 6.3.2, the data can be processed in two different ways:

- By doing a selection of the points, based on the known frequency of the applied force ("filter at force"). Like explained, the points are from the range of 6.3-8 Hz and the selection is done without using any kind of digital filtering;
- By applying a bandpass filter, in the considered range, (6.3 to 8 Hz) to the displacements, velocity and acceleration ("filter at answer");

By showing the data on those ways it will be possible to evaluate what happens when the higher harmonics are removed and to see what's their contribution to the answer. About the data that will be exposed, according to the accelerations plots exposed previously the *sweep1* is the one where only mode is dominant, this is, where the single degree of freedom condition is respected, so all the characterization and exposed plots are based on *sweep1*.

In the examples that were presented at this thesis the 3D plot was always presented, but in this chapter the 3D plots will not be presented, with exception of the excitations at 0.07 V and 0.08 V, because as it was seen in the previous sections the characterization of the system was done via 2D plots (stiffness and damping curves), so there is no reason to present all 3D plots. The 3D plots are presented at fig. 7.19 and 7.20. Relatively to the damping curves they will also not be presented because there is no nonlinear damping and the damping itself possess low values as it can be seen at the fig. 7.21 and 7.22 again for 0.07 V and 0.08 V. When doing "filter at the force" the points are all around X axis, evidencing that the damping is reduced, and when applying a bandpass filter some points are removed and only the points for lower accelerations are kept, and the shape of the plot is similar to the one that was obtained at fig. 5.13 where a low damping value was used ($\zeta = 0.012$). It is true that in the situation where a bandpass filter is not used, the damping seems to somehow increase in the regions where higher accelerations exist, but if that was the case it would be visible at the filtered plot as it happens with the stiffness curves. To avoid any eventual speculations, in fig. 7.23 it can be seen that the most of the points are coincident between the two plots. They are not all coincident because the filters are never perfect, this is, there is always gain, specially in the part of the lowpass filter of the bandpass filter, because while in the highpass part, as a consequence of the answer starting at 5Hz the filter can be somehow adjusted to have no gain at 5Hz, and in that way to not affect any value, but at the lowpass filter the same thing cannot be done, so there will always exist some points that will be affected. Before moving to the stiffness curves, a last comment needs to be done about the 3D plots, because the case where the answer is filtered seems to be a linear plane, and it is not as will be verified in the presentation of the stiffness curves, and the first plot is a plane, despite of not looking exactly like one. When using a larger plot in a slightly different perspective, that can be verified (fig. 7.24).

According to the accelerations plots exposed previously, the *sweep1* is the one where only one mode is excited, this is, where the single degree of freedom condition is respected. So, on fig. 7.25, 7.26, 7.27, 7.28, 7.29, 7.30 and 7.31 the stiffness curves for the different levels of excitation at *sweep1* are presented, with the filtered and nonfiltered curves displayed side by side. At the different figures it can be seen the evolution of the stiffness curve, where for 0.01 and 0.02 V there is a linear behaviour and then as the excitation force increases, the curve grows on its extremities and assumes a higher nonlinear shape. Besides that, since the nonlinear stiffness is a characteristic of the system, the different curves must all be the

same, and consequently coincident as it is exposed on fig. 7.32 and 7.33 for the filtered and nonfiltered answers. Among the different curves it was also possible to see that the filter has the effect of making the plot "cleaner" specially for the higher voltages, where there is some dispersion of points outside the main curve. But the filtered curve is also coincident with the nonfiltered curve, as it can be seen on fig. 7.34 and 7.35 for the cases of 0.07 V and 0.08 V.

After the presentation of the previous plots it matters now to see what happens with *sweep2*. At fig. 7.36 for 0.06 V, through the stiffness curve it can be concluded that for *sweep2* the acceleration surface is not a plane, and that the condition of one degree of freedom is violated. This means that the characterization of the nonlinearity cannot be made through sweep 2. Also about that topic, something that could be done is to try to isolate one of the pylon modes, through the application of a bandpass filter around their natural frequency, but when that is done a straight line is obtained without isolating perfectly one degree of freedom, as it can be confirmed through figure 7.37. The same thing could be done at the frequency where the "jump" occurs but similar results were obtained. To finalize, it is important to check if the right pylon has an equal behaviour comparatively with the left pylon, and for that porpoise it is presented the fig. 7.38 and 7.39, where it can be seen that the pylons present slightly different curves, so in order to obtain a better match between the simulated and experimental results a curve fitting will be done for each pylon.

Before passing to the next phase which is the curve fitting process, it is interesting to present the time-frequency plot of one of the different curves that were showed previously. So, on fig. 7.40 it is presented the time-frequency plot for an excitation level of 0.08 V for *sweep1* from which it can be observed that the appearance of superharmonics starts at approximately at 6.42 Hz and ends at 7.6 Hz. Looking to the plots of fig. 7.11, the first frequency is where a sudden increase ("jump") in amplitude happens, and the second one corresponds to the "main jump" that appeared in all nonlinear previous plots. The disappearing of the harmonics "makes sense" because that shape of the answer in that region is equal for all excitation levels. An important detail from that plot is that although the shape of the different stiffness curves suggests the existence of a cubic stiffness, the order of the superharmonics is not only even like in fig. 4.13, which means that maybe the stiffness is not cubic. With the realization of the simulations it will be possible to clarify the existence of a cubic stiffness.

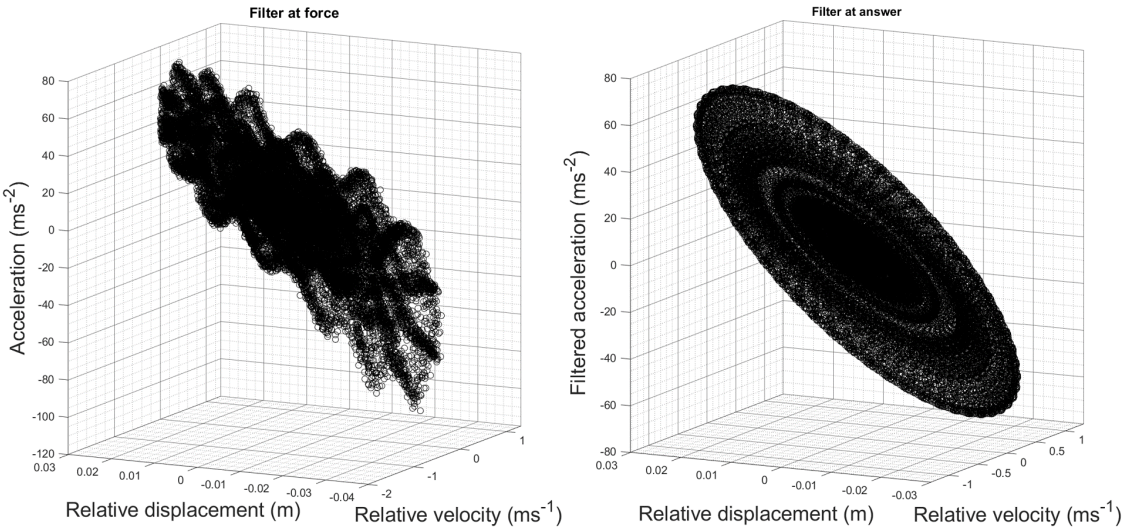


Figure 7.19: Acceleration surface for 0.07 V when filtering the force and the answer for LPylon:2

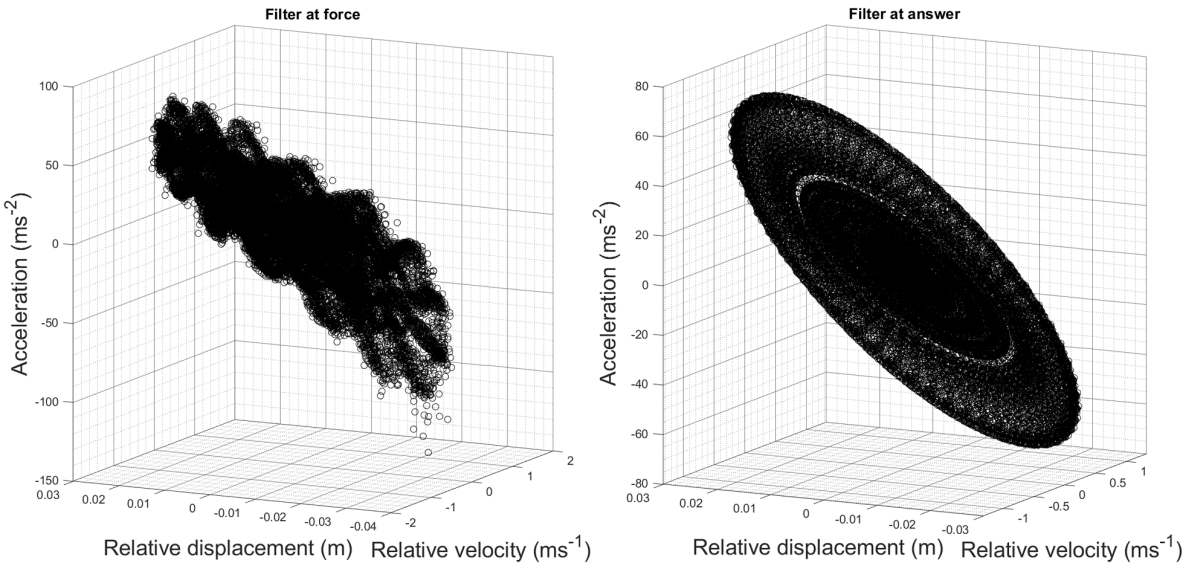


Figure 7.20: Acceleration surface for 0.08 V when filtering the force and the answer for LPylon:2

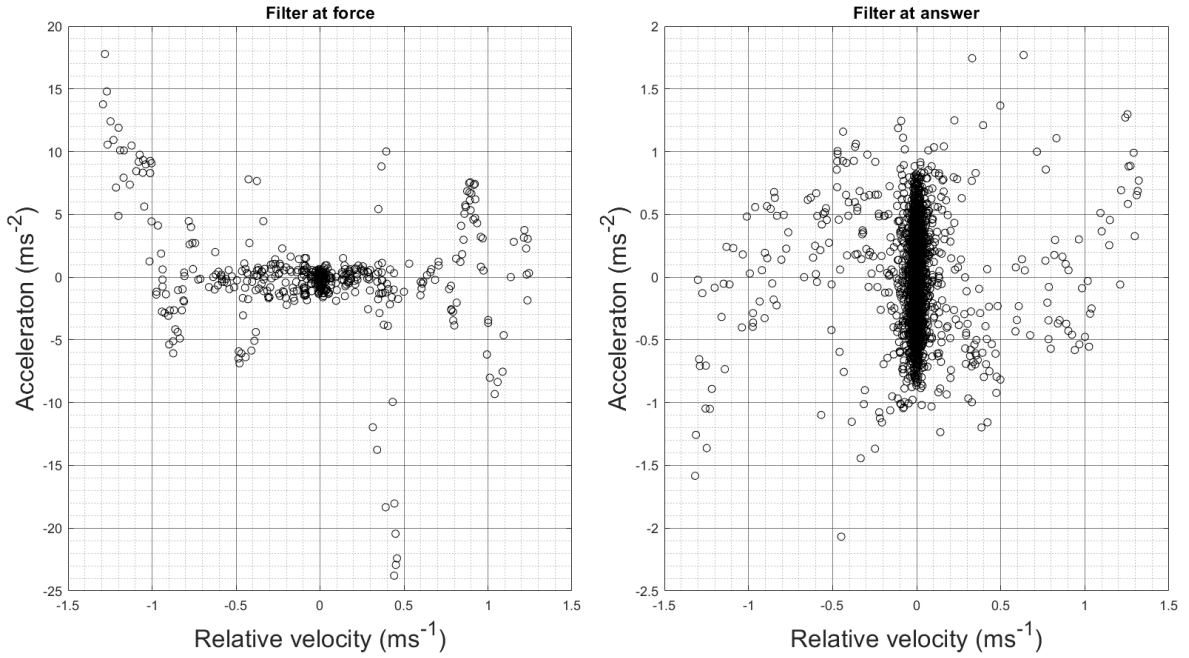


Figure 7.21: Damping curves for 0.07 V when filtering the force and the answer for LPylon:2

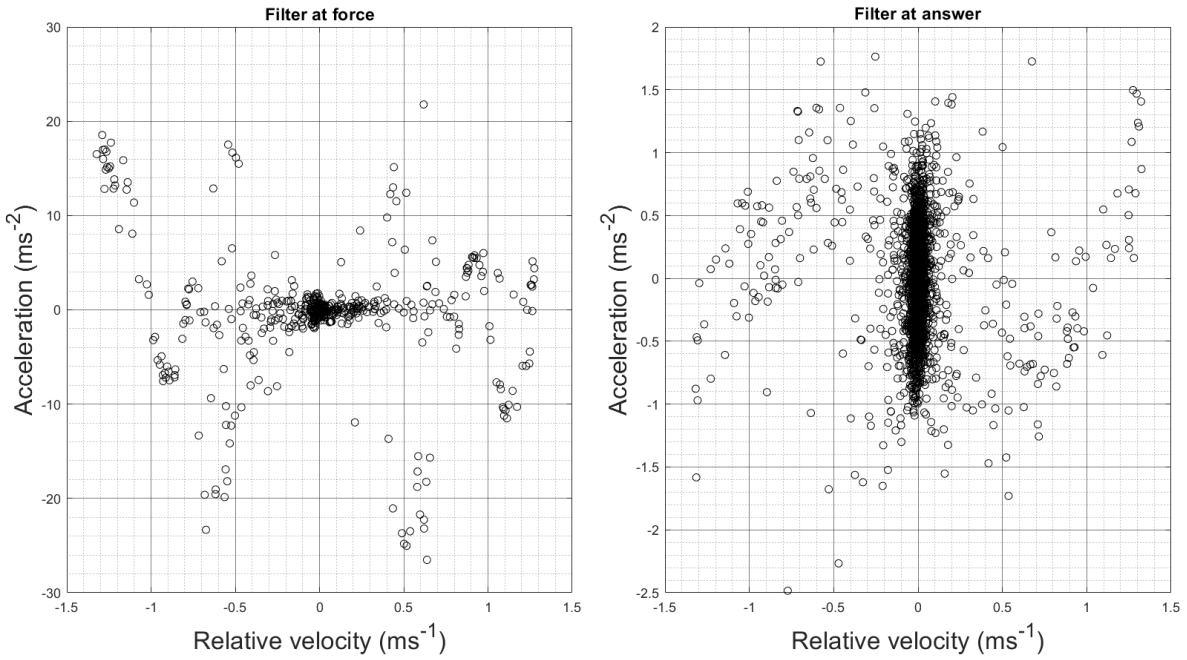


Figure 7.22: Damping curves for 0.08 V when filtering the force and the answer for for LPylon:2

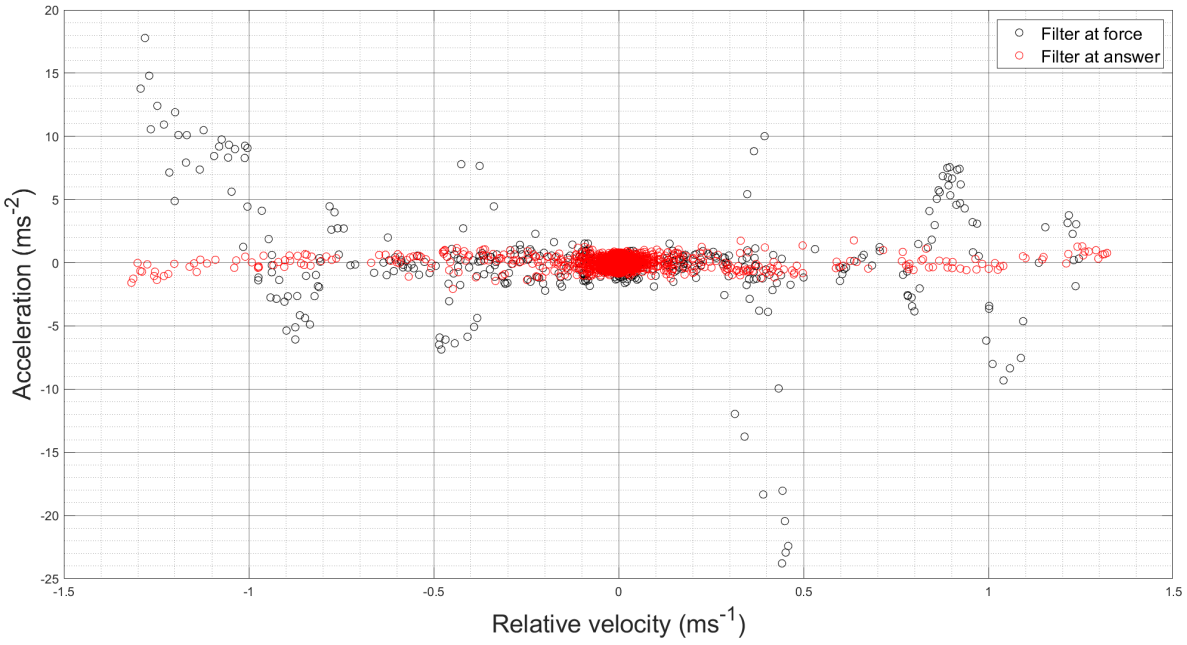


Figure 7.23: Overlaid damping curves when using filtering the force and the answer for 0.07 V for LPylon:2

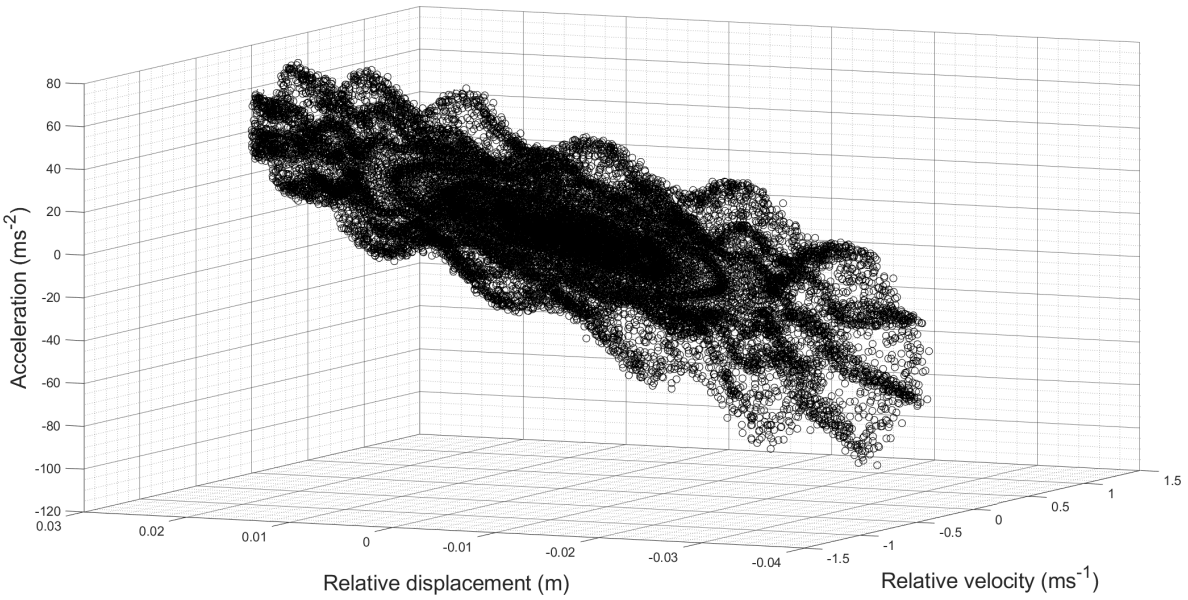


Figure 7.24: Acceleration surface for 0.07 V when "filtering the force" for LPylon:2

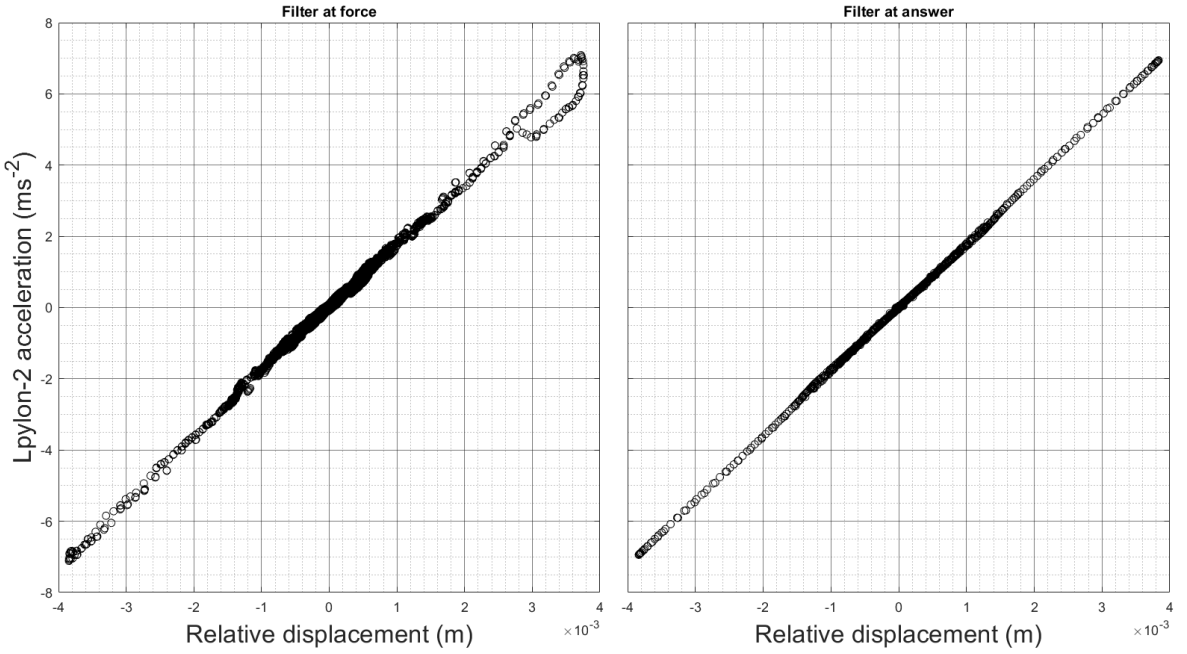


Figure 7.25: Stiffness curve for 0.01 V when filtering the force and the answer

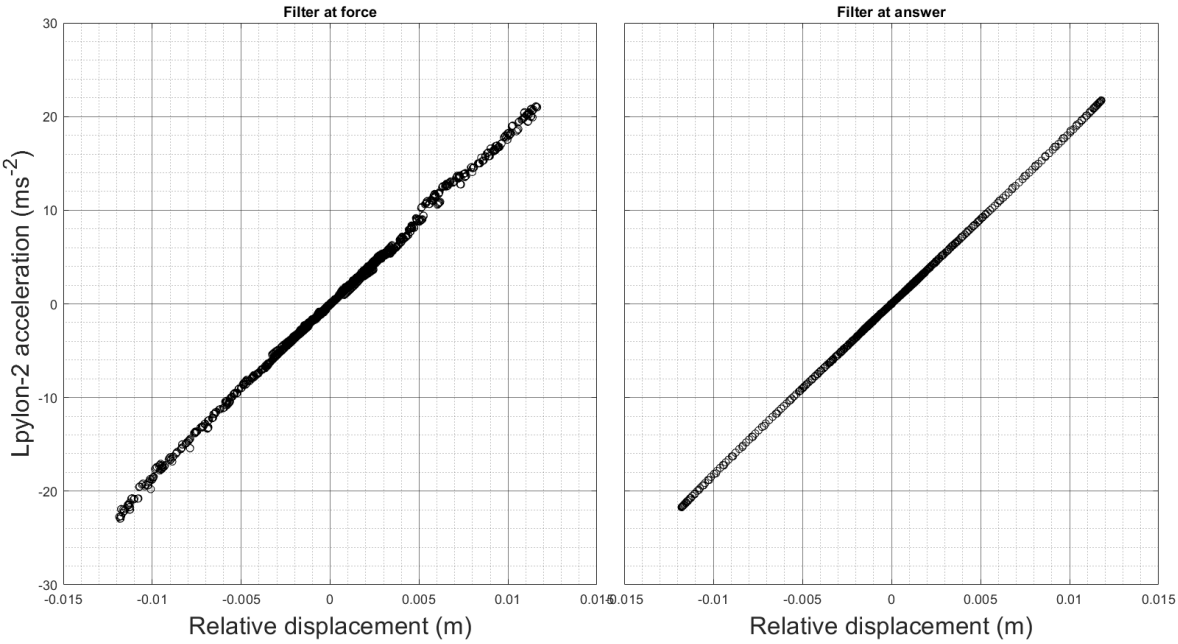


Figure 7.26: Stiffness curve for 0.02 V when filtering the force and the answer

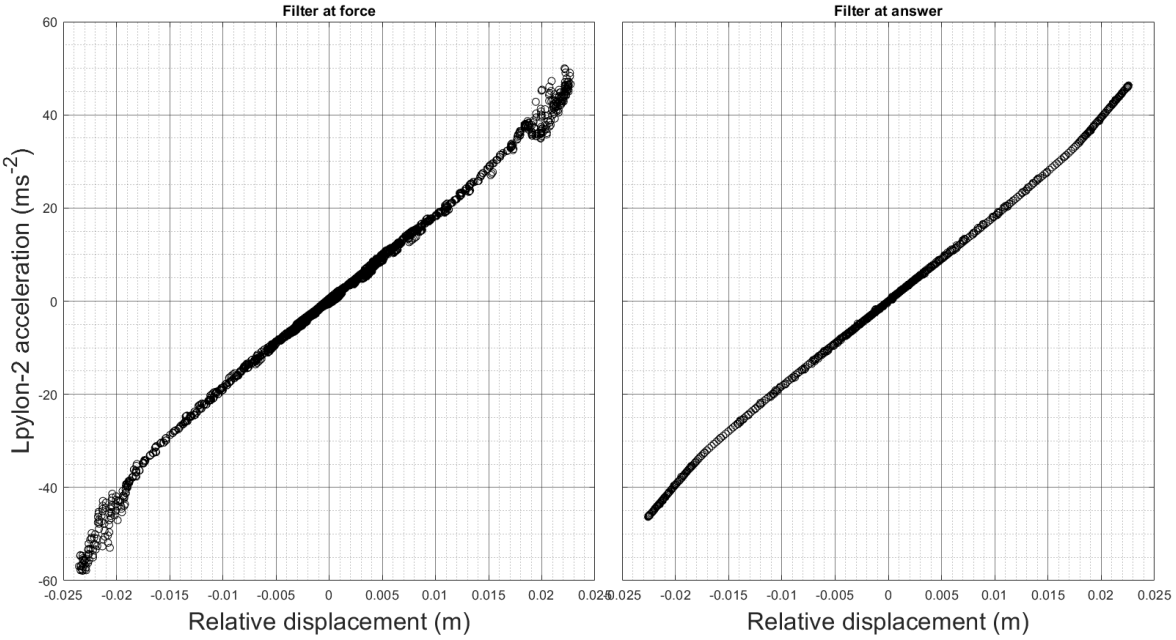


Figure 7.27: Stiffness curve for 0.04 V when filtering the force and the answer

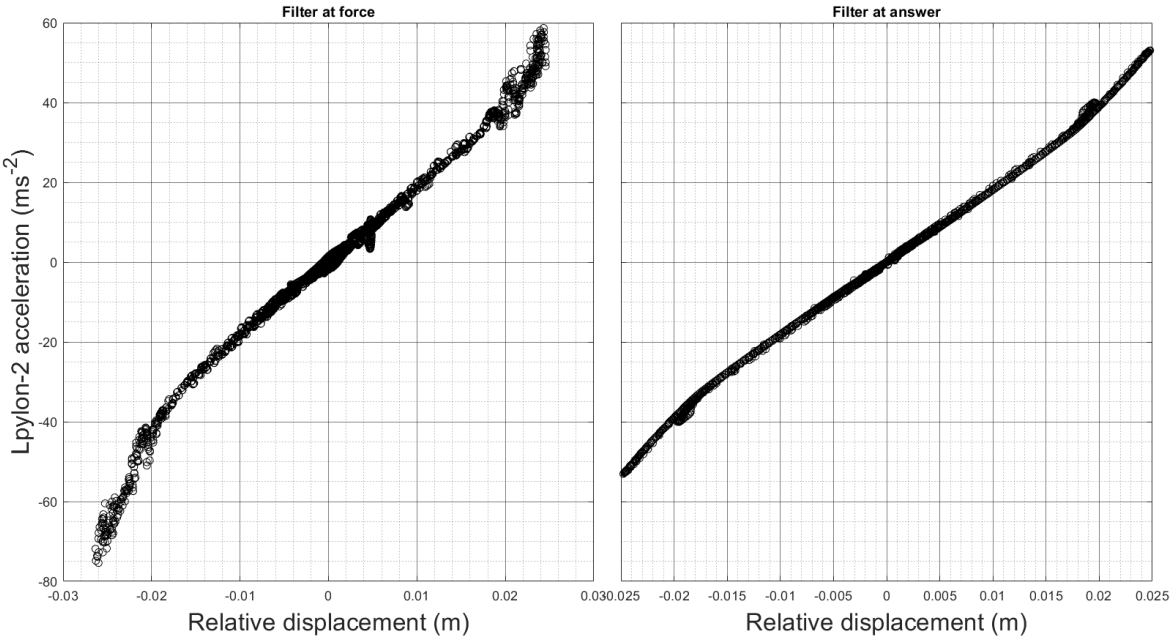


Figure 7.28: Stiffness curve for 0.06 V when filtering the force and the answer

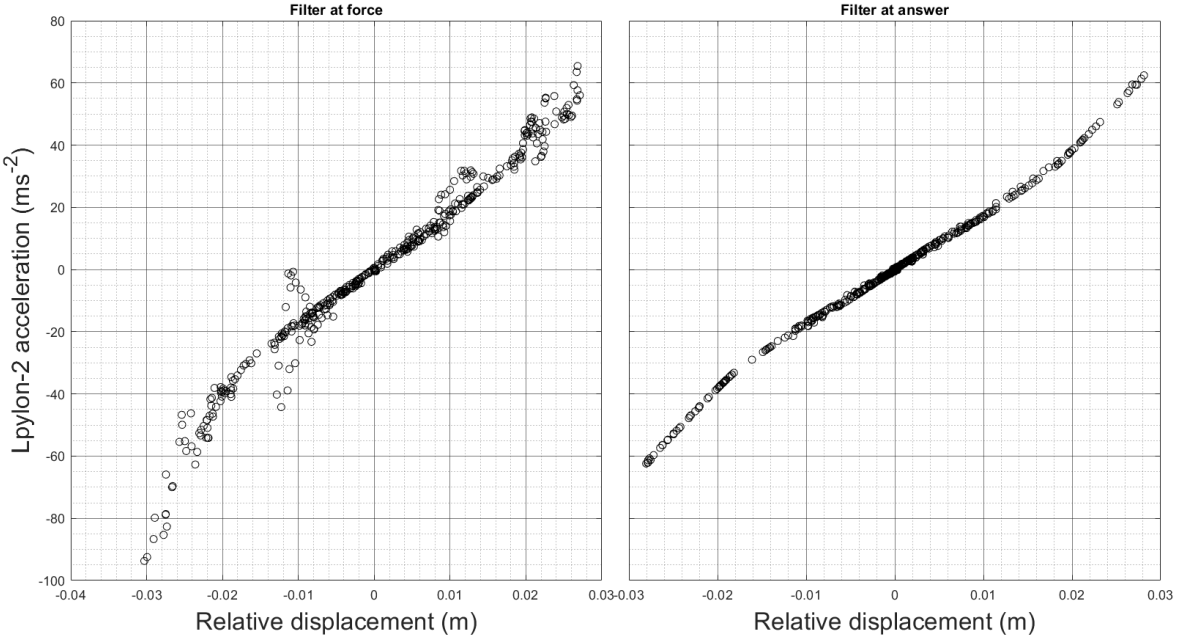


Figure 7.29: Stiffness curve for 0.07 V when filtering the force and the answer

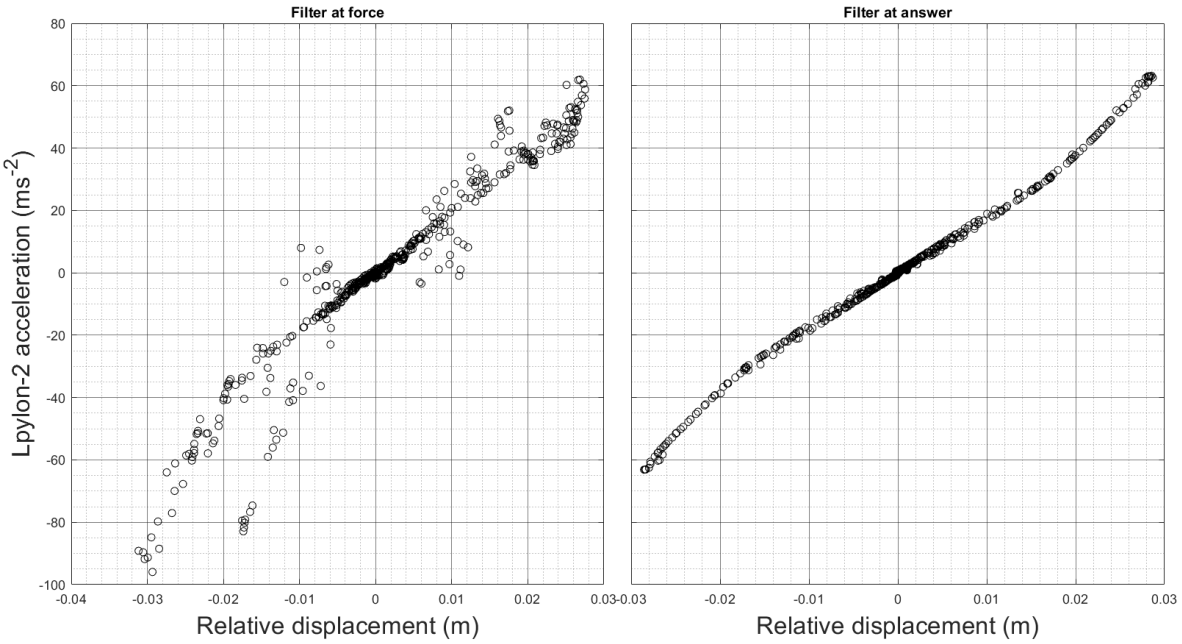


Figure 7.30: Stiffness curve for 0.08 V when filtering the force and the answer

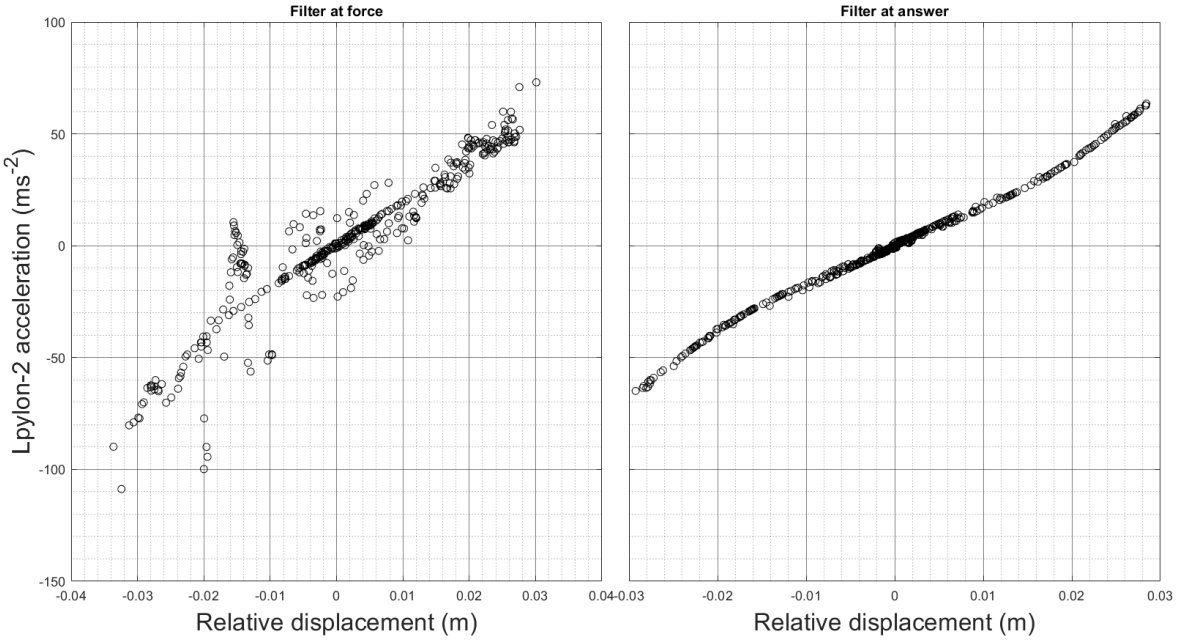


Figure 7.31: Stiffness curve for 0.09 V when filtering the force and the answer

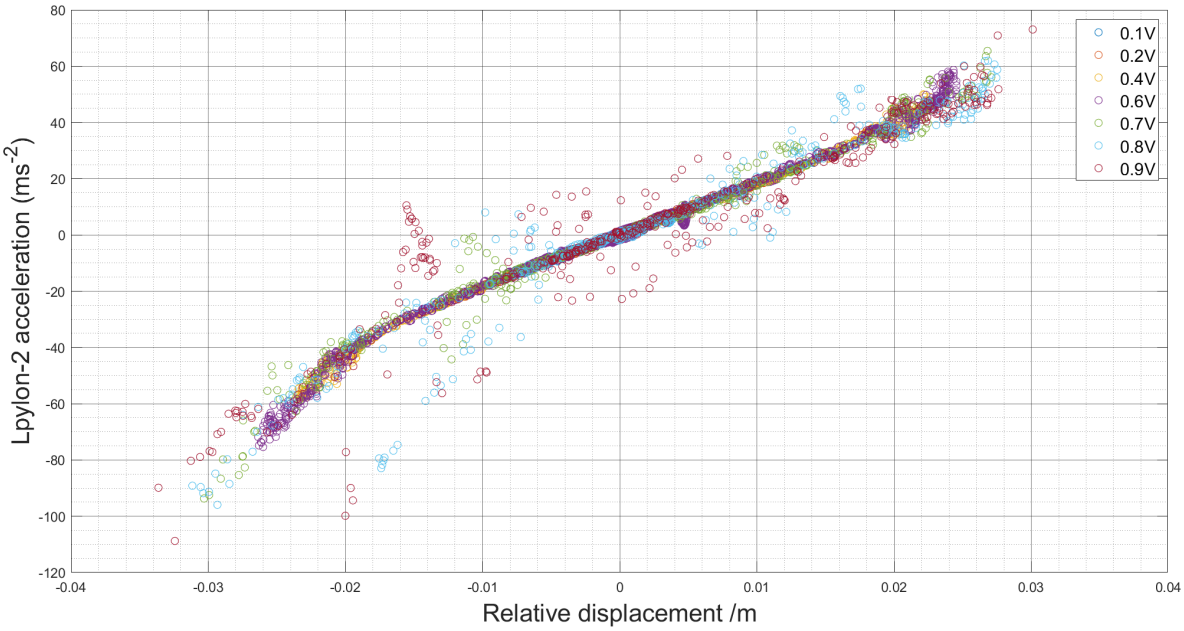


Figure 7.32: Overlaid stiffness curves when "filtering the force"

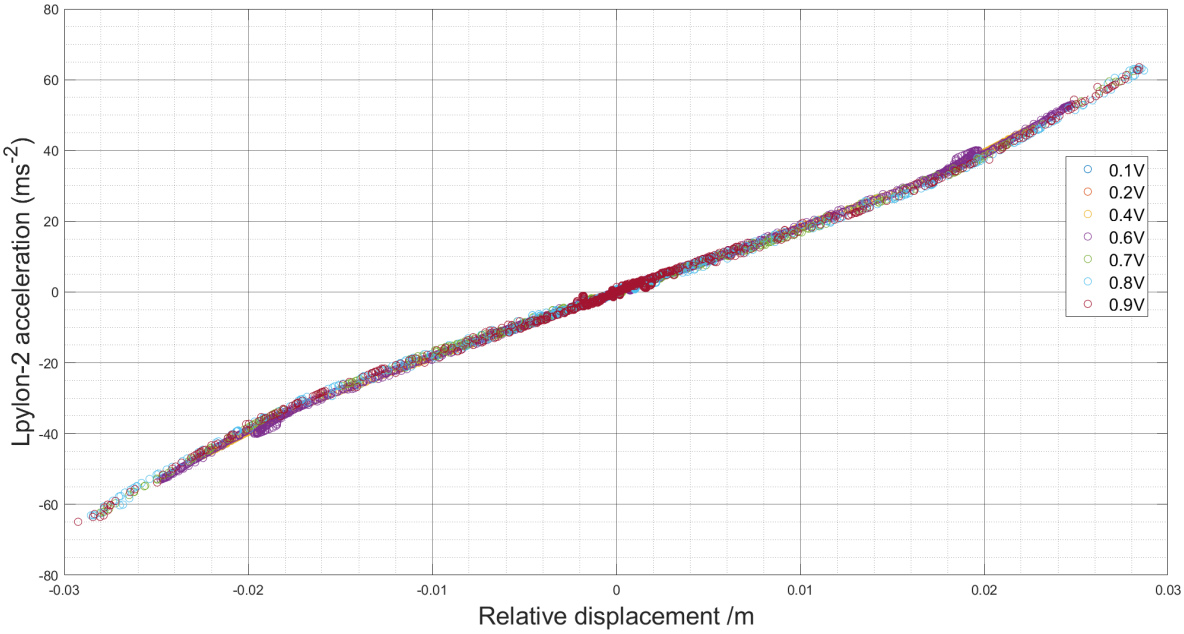


Figure 7.33: Overlaid stiffness curves when filtering the answer

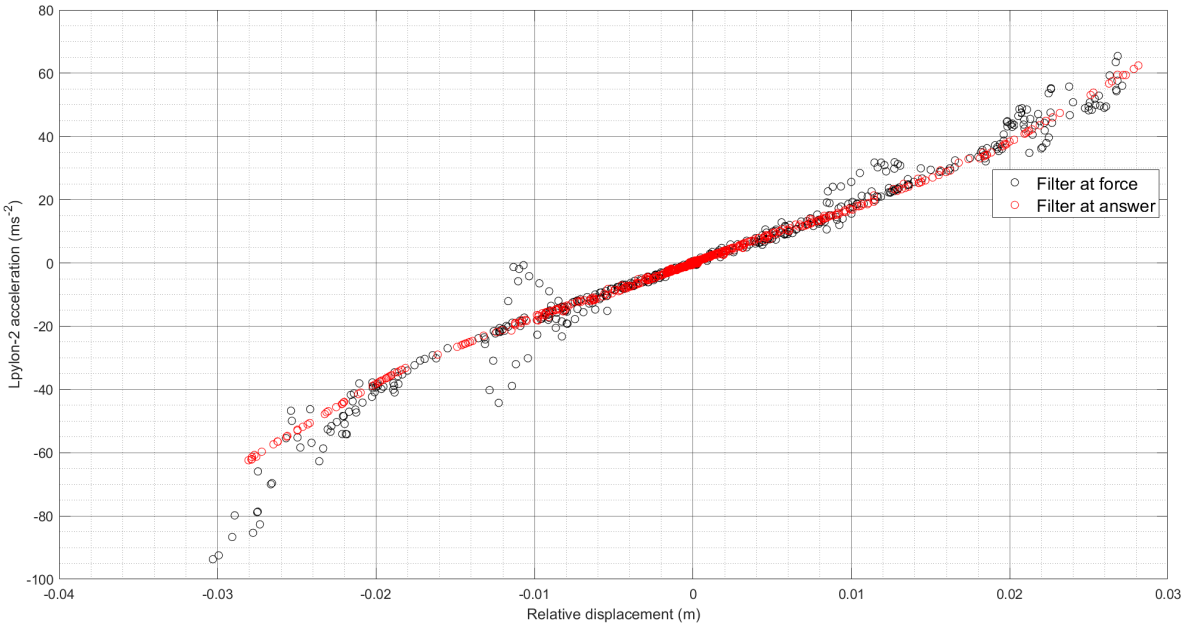


Figure 7.34: Overlaid stiffness curve for 0.07 V when filtering the force and the answer

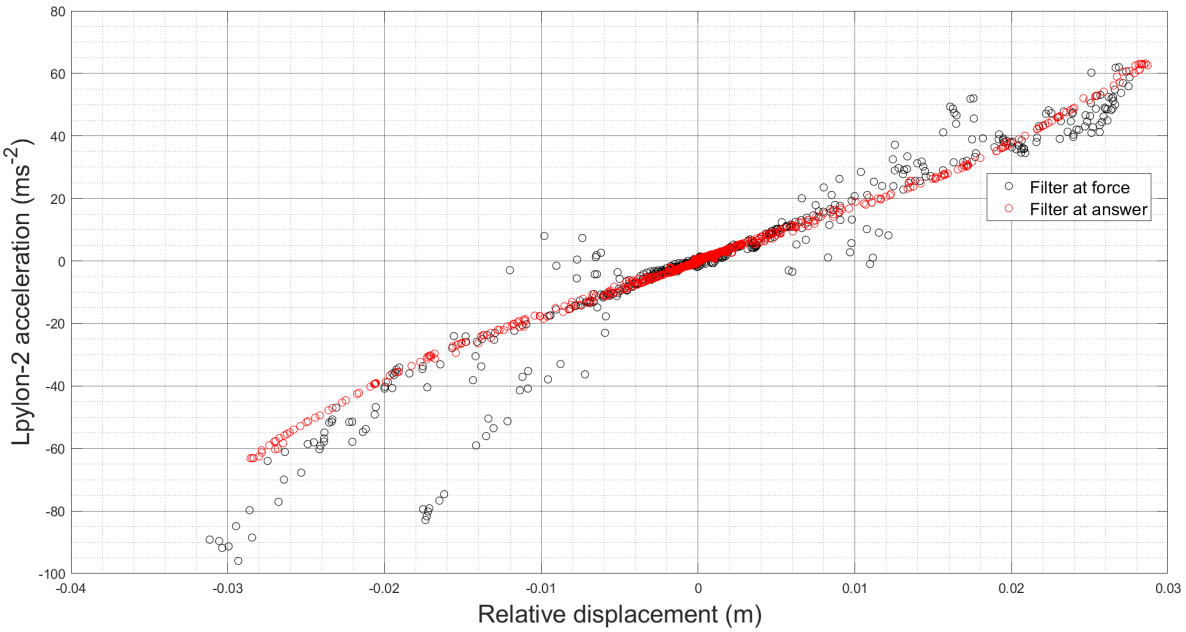


Figure 7.35: Overlaid stiffness curve for 0.08 V when filtering the force and the answer

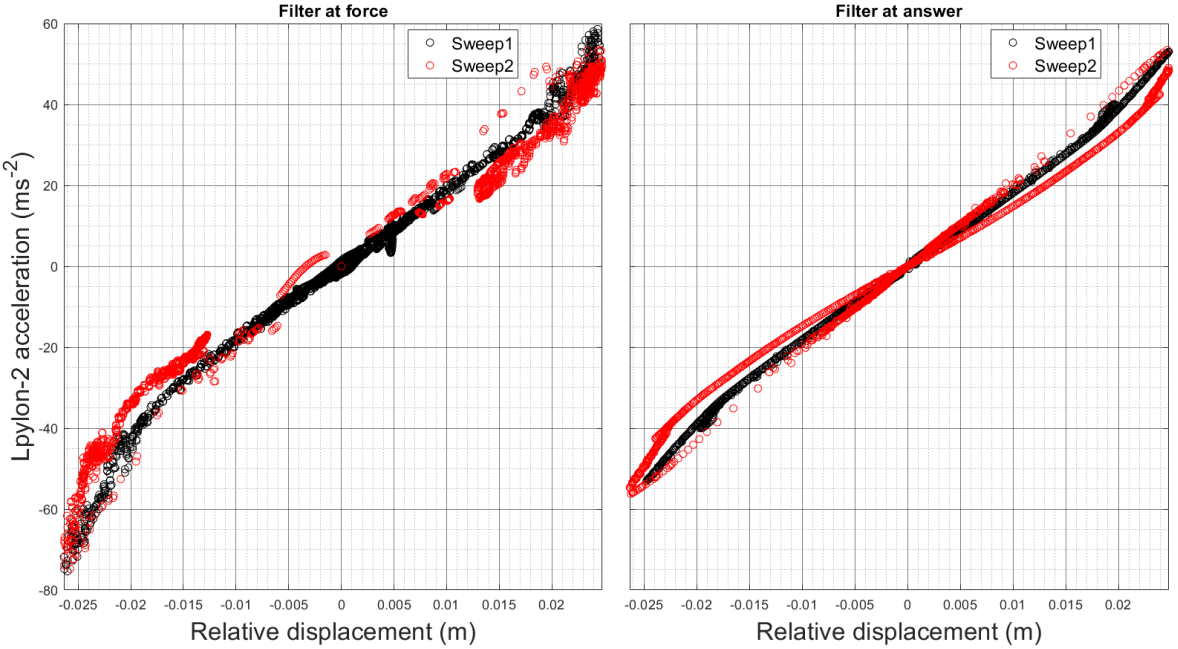


Figure 7.36: Stiffness curve for 0.06 V for *sweep1* and *sweep2* when filtering the force and the answer

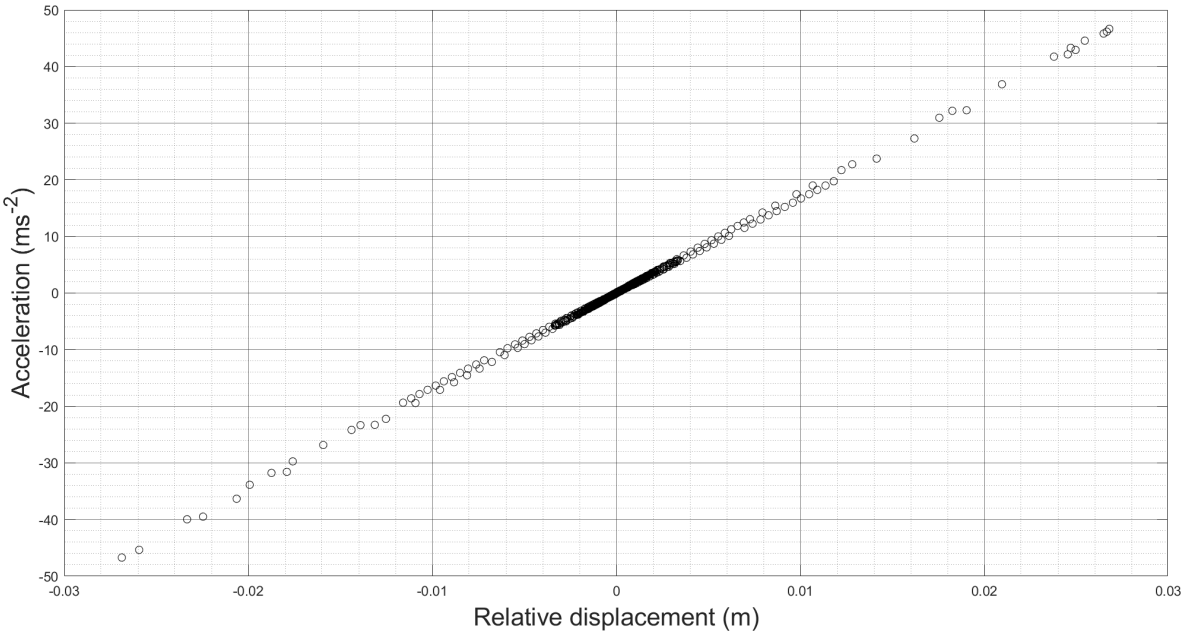


Figure 7.37: Stiffness curve when isolating the first mode through a bandpass filter

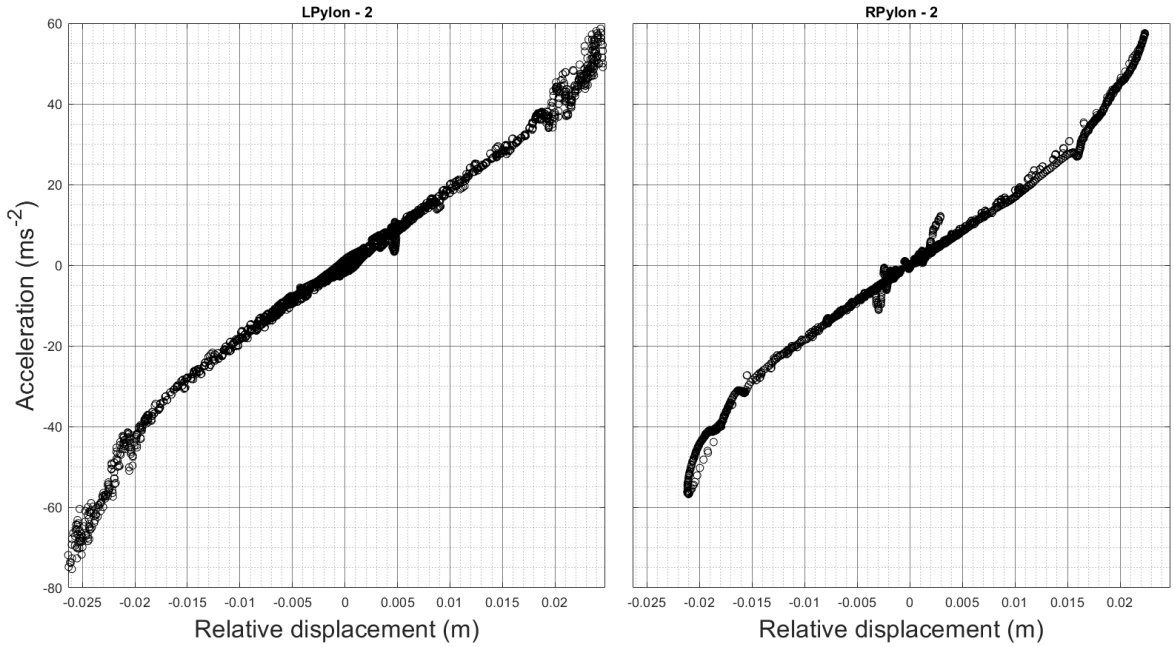


Figure 7.38: Stiffness curve for right and left pylon when "filtering the force"

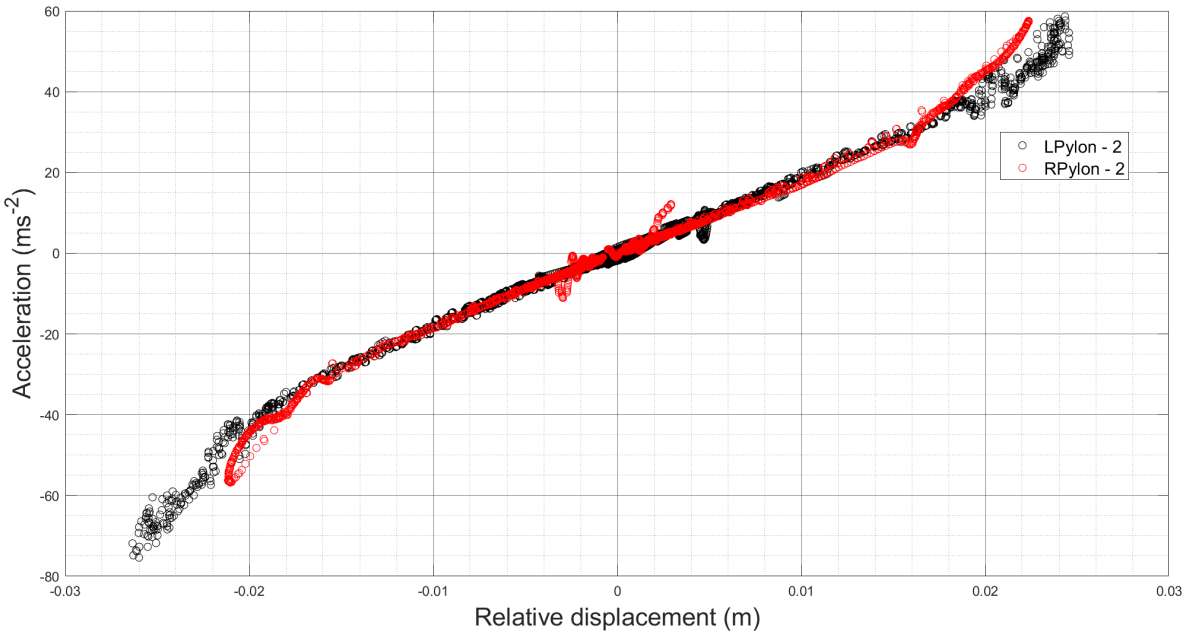


Figure 7.39: Overlaid stiffness curve for right and left pylon when "filtering the force"

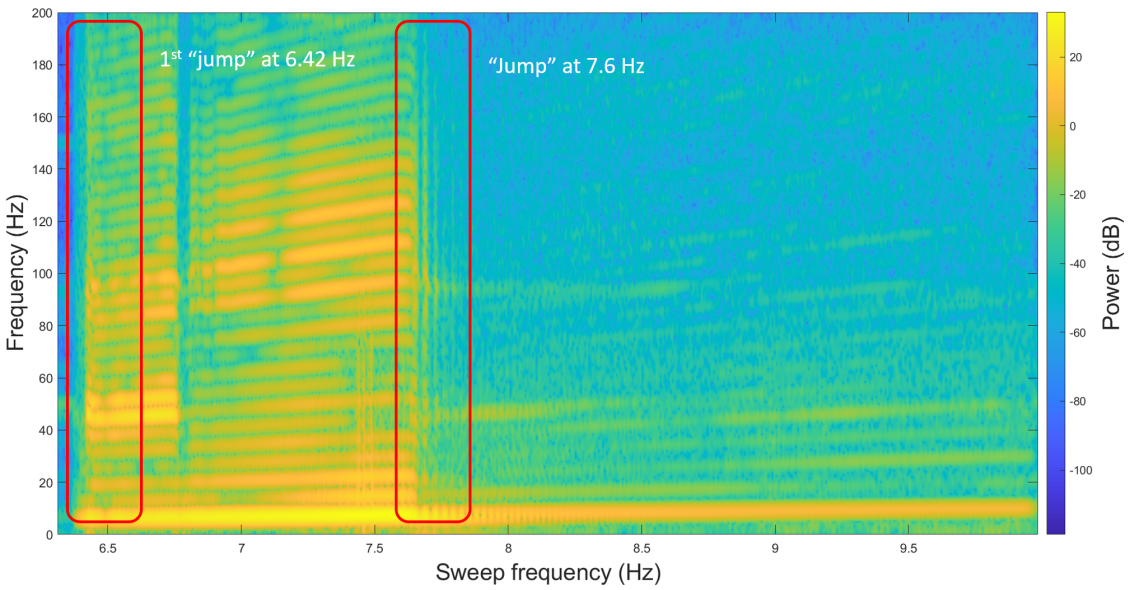


Figure 7.40: Time-frequency plot for *sweep1* excitation at 0.08 V from 6.3-10 Hz.

After showing those different plots, the next step is the realization of the curve fitting process. On this process there are three different alternatives: the first is using a cubic stiffness, which considering only the stiffness curves, it is what makes physically sense, the second is the use of a polynomial function that will allow a better curve fitting but also the insertion of new nonlinear terms and the third is the utilization of a piecewise function. It is important to point out that in curve fitting process with the polynomial function, that the value of the linear term must be equal to the value of the linear stiffness of the model. The same thing could have been said for the cubic stiffness but in the next topic it will been seen why it wasn't said.

For the realization of the curve fitting process it will be considered the answer at 0.06 V. The different variables that resulted from the curve fitting process are illustrated in tables 7.3, 7.4, 7.5 and 7.6. Looking to the curve fitting results for the cubic stiffness it is interesting to observe that the first linear term corresponds approximately to the modal stiffness of the first mode, specially in the numerical model. If the inverse calculation is done, through the slope the values of 6.5 Hz and 6.4 Hz are extracted, which is really close to 6.6 Hz. This fact might be somehow a "surprise" because as it was already commented the time-frequency plot indicated that the stiffness of the system may not be cubic. So these results confirm that only after performing the simulations and testing different versions, can more comments be done about the nature of the nonlinearity. That coincidence in the slope happened because the slope in the ASM is k/m, which corresponds to the square of the natural frequency or modal stiffness and, eventually if the stiffness is intended to be extracted, it needs naturally to be multiplied by the mass.

For the piecewise function the fitting for the linear term was not presented because the fitting from other terms is not dependent of the linear region, unlike the cubic and the polynomial fitting, but also because the linear part is not manipulated in the code, like in the other curve fittings. Only the nonlinear coefficients will be added to the code. In terms of algorithmic, the piecewise function is introduced as increase in stiffness if those relative displacements limits are passed, which corresponds to an extra calculation work because it is necessary to calculate the relative displacement in all iterations and verify the conditions.

Cubic function ($ax + bx^3$)				
Pylon	a	b	R-squared	RMSE
Left	1680	1.12E+06	0.9917	1.893
Right	1623	1.16E+06	0.9958	1.079

Table 7.3: Cubic function fitting coefficients and performance values

Polynomial function ($ax + bx^2 + cx^3 + dx^4 + ex^5 + fx^6 + gx^7$)								
Pylon	a	b	c	d	e	f	g	No.
	1680	5636	1.10E+06	-2.45E+07	4.56E+05	9.59E-01	5.47E-01	#1
	1680	-5635	1.13E+06	-8.40E+05	9373	0.9593	-	#2
Left	1680	4939	7.80E+05	-2.24E+07	6.29E+08	-	-	#3
	1680	5633	1.10E+06	-2.45E+07	-	-	-	#4
	1680	-6035	1.13E+06	-	-	-	-	#5
	1623	-3852	1.65E+06	6.40E+06	8.65E+05	0.8143	0.2435	#6
	1623	-2083	1.65E+06	1.46E+06	1.27E+05	8.14E-01	-	#7
Right	1623	-2095	1.65E+06	1.50E+06	1.28E+05	-	-	#8
	1623	-3818	1.65E+06	6.31E+06	-	-	-	#9
	1623	-1559	1.66E+06	-	-	-	-	#10

Table 7.4: Polynomial function fitting coefficient values

Pylon	Criterium	#1	#2	#3	#4	#5
Right	R-squared	0.9956	0.9947	0.9957	0.9956	0.9946
	RMSE	1.382	1.515	1.355	1.382	1.523
Pylon	Criterium	#6	#7	#8	#9	#10
Left	R-squared	0.9959	0.9959	0.9959	0.9959	0.9959
	RMSE	1.057	1.059	1.059	1.056	1.06

Table 7.5: Polynomial function performance values

Negative displacements ($ax + b$)					
Criterion	a	b	R-squared	RMSE	Lim (m)
Left Pylon	4599	49	0.9498	2.586	-0.018
Right Pylon	4143	35.77	0.9289	2.104	-0.015
Positive displacements ($ax + b$)					
Criterion	a	b	R-squared	RMSE	Lim (m)
Left Pylon	3314	-27.45	0.7645	2.915	0.018
Right Pylon	4144	-37.16	0.9861	1.079	0.015

Table 7.6: Piecewise function coefficients and performance values

7.2.1 Subharmonic resonance

During the experiments it was observed that for higher voltages around 53 Hz, the pylons seem to start shaking with the same frequency that they did in the 1st modal mode, which means that could have been a subharmonic resonance, and since it is not common, it will be treated in a special section.

To better analyse the phenomena, some tests were realized from 45 to 65 Hz, and on this work the results for 0.06 V are shown. The stiffness curve is in fig. 7.41, from which it can be concluded that a surface is not obtained, and that is due to the presence of the pylon torsional modes on that frequency range. But, focusing in the specific region (53-63 Hz) the fig. 7.42 is generated and it also not resembles a surface because although this is a subharmonic resonance, is not a pure main resonance, so it will always exist points outside the plane. Alternatively if a filter is applied by considering the frequency range 6.4-8 Hz a curve equal to the one that was obtained at fig 7.28 (where the first pylon mode was indeed excited) is obtained as it can be checked at fig. 7.43. This proves that indeed, it was subharmonic resonance, because otherwise it would not be possible to filter those points from an answer resulted from an excitation from 45 to 65 Hz. To prove that the filtered answer is among the points of 45-65Hz, fig. 7.44 is presented.

To reinforce the existence of a subharmonic resonance, in fig. 7.45 the time-frequency plot is presented. In that plot there is a "strong yellow" stripe at low frequencies that confirms the existence of the subharmonic.

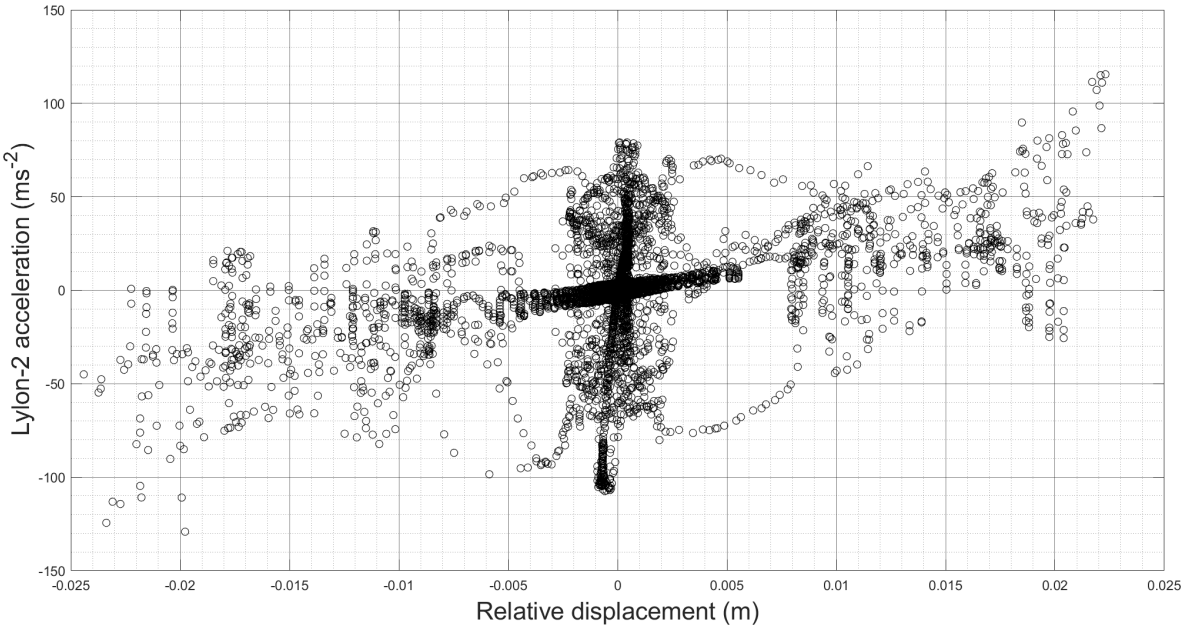


Figure 7.41: Stiffness curve for excitation frequency 45-65 Hz for 0.06 V

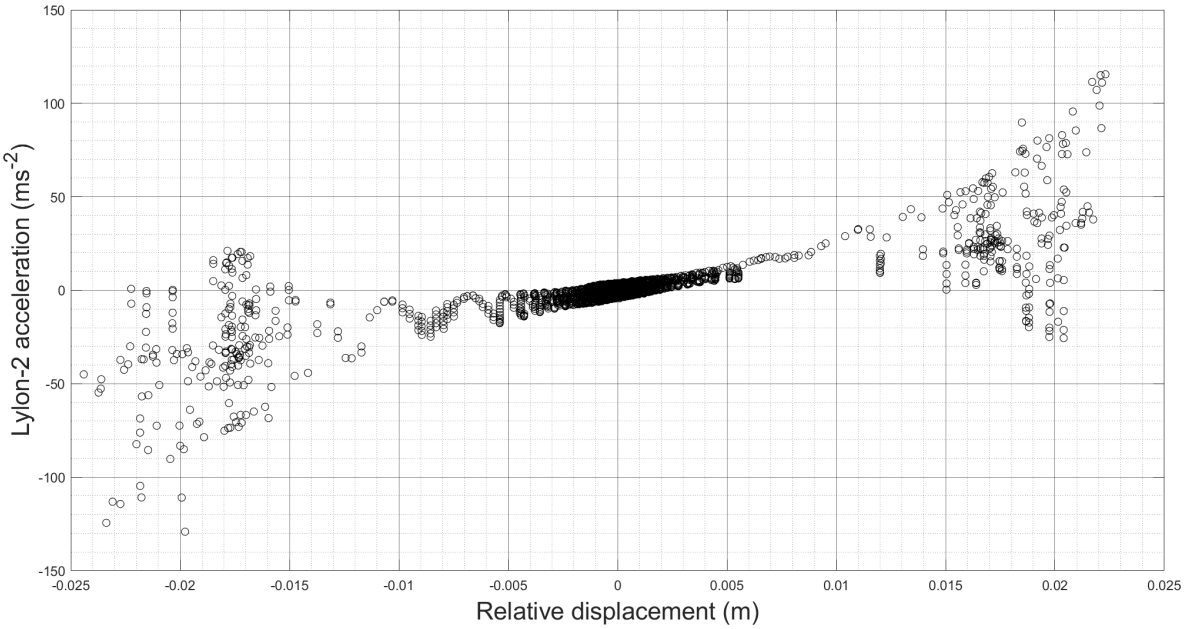


Figure 7.42: Stiffness curve for excitation frequency 53-63 Hz for 0.06 V

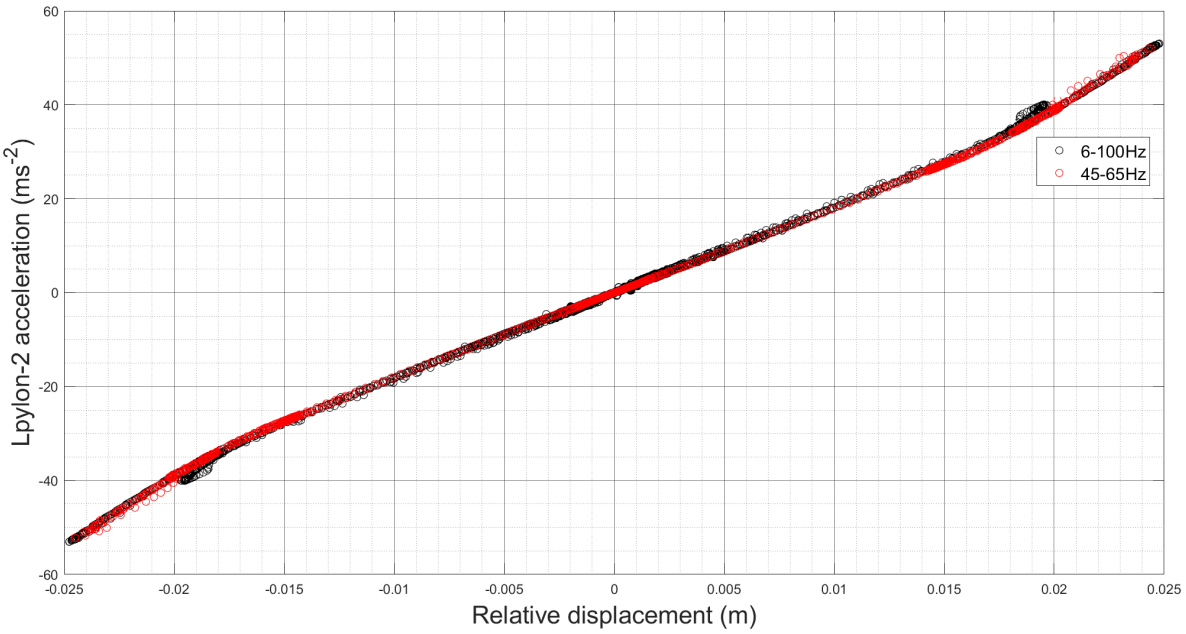


Figure 7.43: Overlaid stiffness curves of the experiments 6-100Hz and 45-65Hz by applying a bandpass filter at 6.4-8Hz

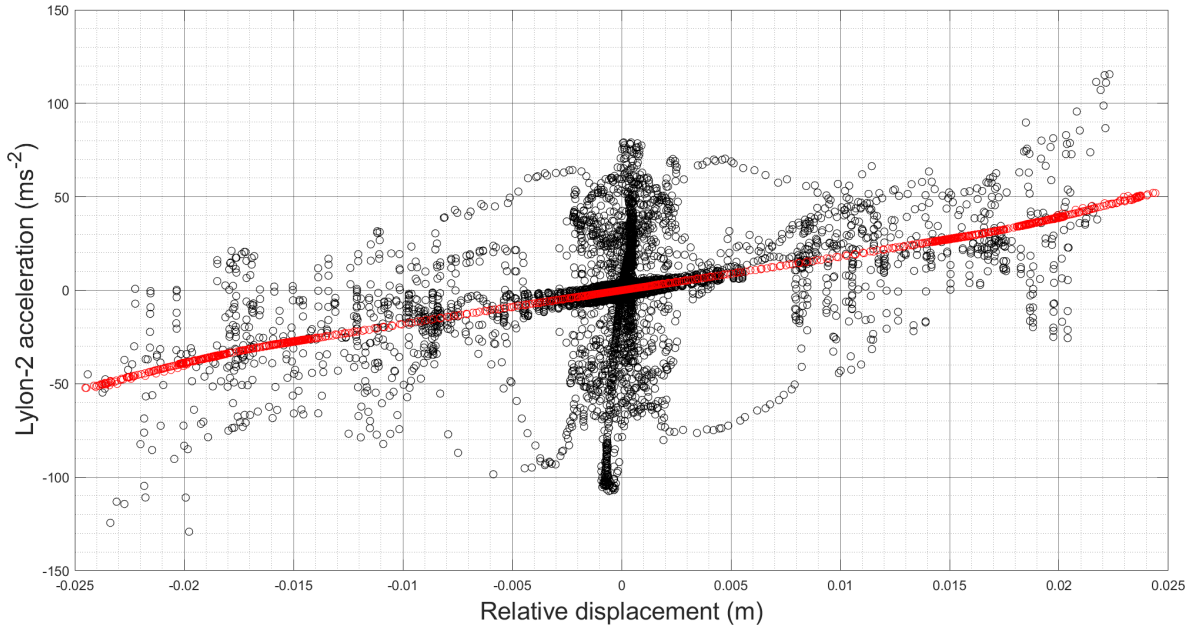


Figure 7.44: Overlaid stiffness curves of 45-65Hz with and without bandpass filter

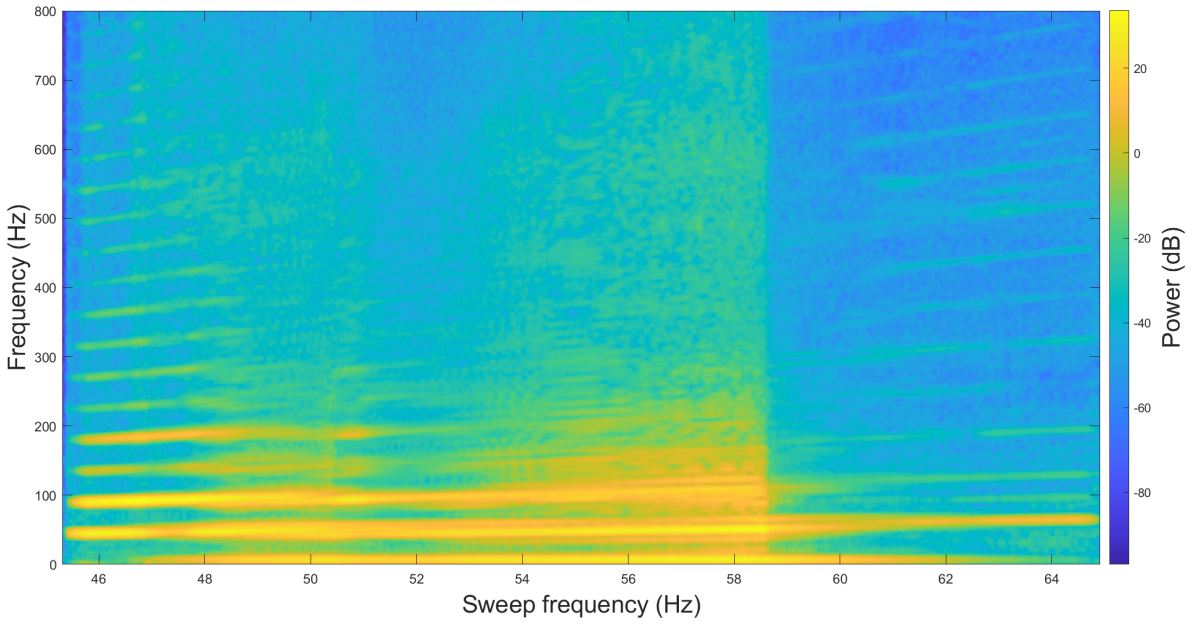


Figure 7.45: Time-frequency plot for excitation at 0.06 V from 45-65 Hz.

CHAPTER 8

Structural model update

After characterising the nonlinearity, the next and final step is the performance of the structural model update itself. In this chapter the simulation results for the linear model will be firstly presented and then the results for the "nonlinear voltages levels" are presented. To evaluate the quality of the simulations the obtained results for *LPylon:2* and *RPylon:2* are compared with the experimental ones (filter at force). The focus of the simulations will be in the frequency range presented in the last chapter, 6.3-8 Hz for being the region of the first resonance of the pylons, where the nonlinear behaviour is more intense. Despite of that, the simulation will always start at the initial frequency of the experiments, not only because the initial state is the steady state, but also because it wouldn't make sense to compare the results at that range without the contribution of the transient answers of the previous frequencies.

Since this is a free-free system, before approaching the simulations themselves, some comments need to be done about the reduced model order, because as it was seen previously in a free-free system some DOF need to be constrained. By engineering judgement, it was decided to select the rotational DOFs of the nodes indicated in figure 8.1. Those nodes belong to the elements that represent the "bolts" used to attach the airplane to "bungees" that suspend the airplane and are flexible enough to represent a free-free condition. Regarding this decision, it is important to keep in mind that it only affects the residual inertia-relief attachment modes, which are at the frequencies of 192.91 Hz and 224.38 Hz. These are high frequencies comparatively with the range that is going to be simulated (6.3-8 Hz) and consequently these modes don't have any influence in the results.

To obtain better results the simulations will be done by using the force measured by the sensors during the experimental activity and not the force that theoretically should have been applied, because the applied force is distorted by the structural resonances. During this process it will be necessary to do tuning of the nonlinear stiffness and linear damping values and the goals of that process are to achieve similar accelerations amplitudes, in order to get a good match on the stiffness curve; and to have a good shape correspondence in the acceleration plots. But the tuning process must respect the next criteria:

- The used nonlinear stiffness must be the same among the different voltages;
- The damping value must at least be the same for *sweep1* and *sweep2*. It can be argued that the damping changes with the applied force, but the same thing can't be said about changing between *sweep1* and *sweep2*;

- The "jump" or peak frequency must increase with the applied force;

About the adjustment of the damping, since the *sweep1* is dominated by the first modal mode, in this sweep the damping of the first mode is adjusted, and at the second sweep the damping of the second mode is adjusted.

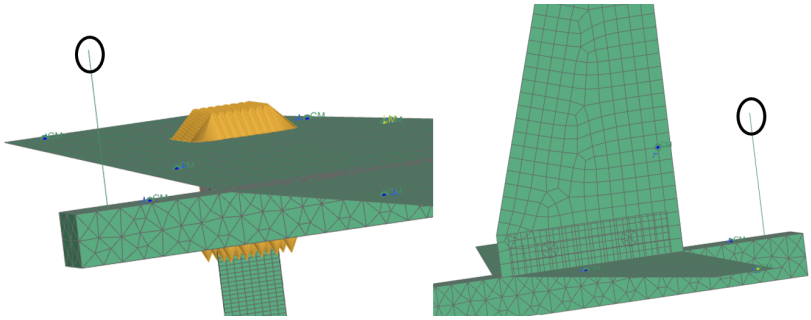


Figure 8.1: Nodes of the blocked DOF

8.1 Linear model

Before presenting the simulation results it is necessary to define the damping values, and those are extracted from Testlab®. But besides the "real modes" there are also the attachment modes, and for them no special criterion was found, and for that reason it was decided to assume the average damping value of the experimental modes. This is definitely not the best way of defining the damping, but like it was said before, due to the high frequency of the attachment modes they have no influence in the results. The damping values are displayed in table 8.1.

Mode	#1	#2	#3	#4	#5	#6	#7
ζ (%)	1.07	0.46	0.85	0.58	0.47	0.47	0.84
Mode	#8	#9	#10	#11	#12	#13 (Att.)	#14 (Att.)
ζ (%)	0.63	0.6	0.5	0.52	0.36	0.61	0.61

Table 8.1: Damping values extracted from Testlab®

Also considering the damping values besides the consideration that in both sweeps the damping needs to be the same, it must also be taken into account that for the linear voltages the damping values must be the same, because while for the excitation levels where the nonlinearity exists it may make sense that the damping values may change with the force level excitation, but in a linear system that doesn't make any sense. To obtain the best possible results the cubic nonlinearity was also considered in the simulations, despite of its low influence for small displacements.

So, in fig. 8.2 the simulation results for *sweep1* at 0.01 V, using the damping values from Testlab® are displayed. Analysing the plot, it can be concluded that something is not correct, because in the previous chapter it was seen that the first mode dominates the answer at *sweep1*.

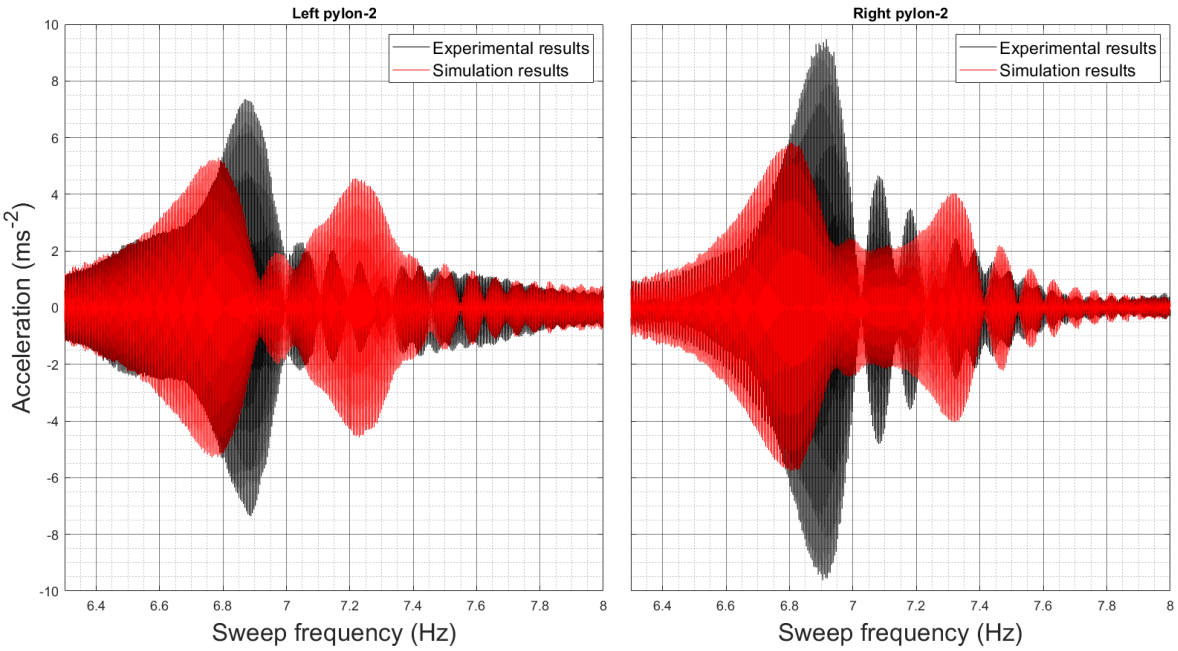


Figure 8.2: Simulated and experimental results for *LPylon:2* and *RPylon:2* at *sweep1* with the excitation level of 0.01 V and with $\zeta_1 = 1.07\%$ and $\zeta_2 = 0.46\%$

When analysing the modal answers at fig. 8.3 the first mode is more excited but not that much comparatively with the second mode, and that is explained by the used damping values, because according to Testlab® the damping value from the first mode is more than two times higher than the damping from the second mode. If the damping from the first mode is reduced to a value equal to the second mode, figs. 8.4 and 8.5 are obtained, where it can be seen that the first mode dominates now the answer.

So, after proving that the problem was not in the ROM but in the damping, at fig. 8.6, 8.7, 8.8 and 8.9, 8.10, 8.11 the final acceleration plots and stiffness curves are presented respectively for 0.01 V and 0.02 V at *sweep1* and at the fig. 8.12, 8.13 and 8.14, 8.15, 8.16 the same for *sweep2*, already with the damping values that allowed to obtain the best results. On those plots for *sweep1* good results are obtained, although for 0.01 V the displacements in the left pylon should be lower (fig. 8.8). About *sweep2*, at 0.01 V the results are bad, despite of all tries and combinations of different damping values to achieve that shape, but at 0.02 V "nice" results were achieved. In some plots like at fig. 8.8 and 8.16 a curious detail that can be seen, is that the experimental displacements in both pylons are different, and in one of the cases it was even possible to simulate that asymmetrical displacement, despite of the fact that in the natural modes the pylons are symmetric and asymmetric. By last, it is possible to confirm that the *sweep2* for 0.02 V presents no longer a linear behaviour, although for the right pylon the stiffness curve is linear.

Considering that the only difference between the two modes is that one has a symmetric and the other one a asymmetric disposition of the pylons, and also the not so good results on *sweep2* for 0.01 V some may ask why the damping values are not equal or closer. To clarify that in fig. 8.17 are shown the results for the acceleration plots for *sweep2* at 0.02 V when using for mode 1 the damping value of 0.5% and for mode 2 the damping value of 0.5%. As it can be seen when the mode 2 has a low damping value the amplitude increases ridiculously for one of the pylons, which exemplifies why the damping value in mode 2 was increased.

In short, the damping value at mode 2 was only used for necessity due to *sweep2*, and most importantly, as already seen, the damping value at mode 2 is not being used to make the mode 1 the dominant one at *sweep1*.

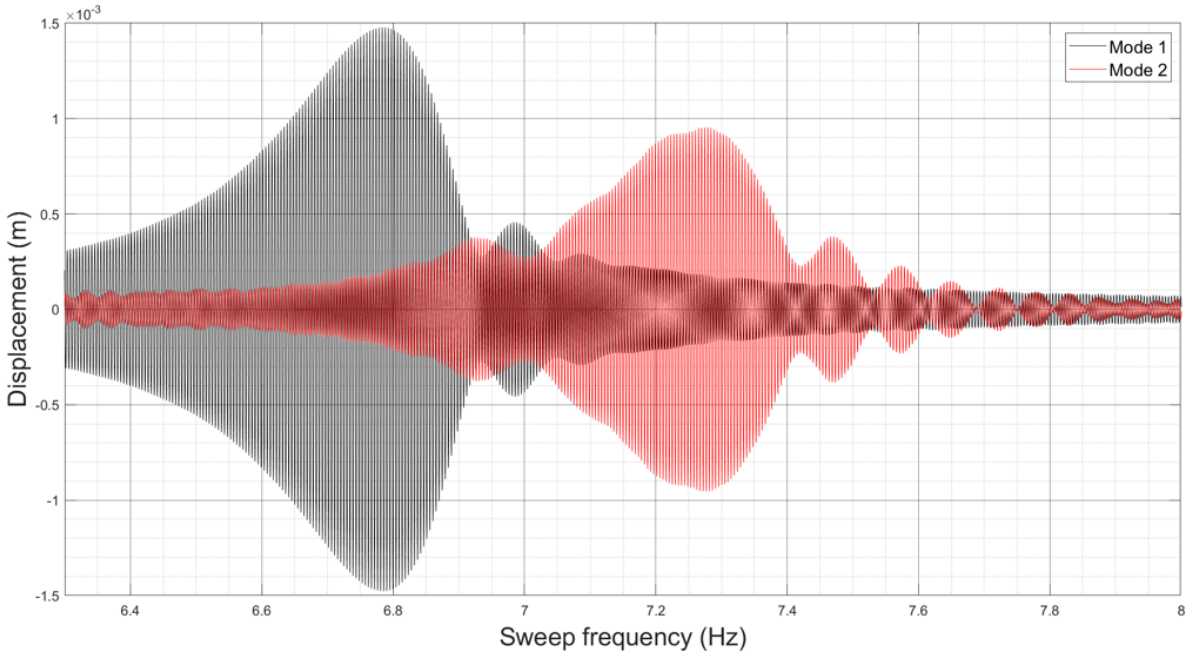


Figure 8.3: Modal answers at *sweep1* for the excitation level of 0.01 V and with $\zeta_1 = 1.07\%$ and $\zeta_2 = 0.46\%$

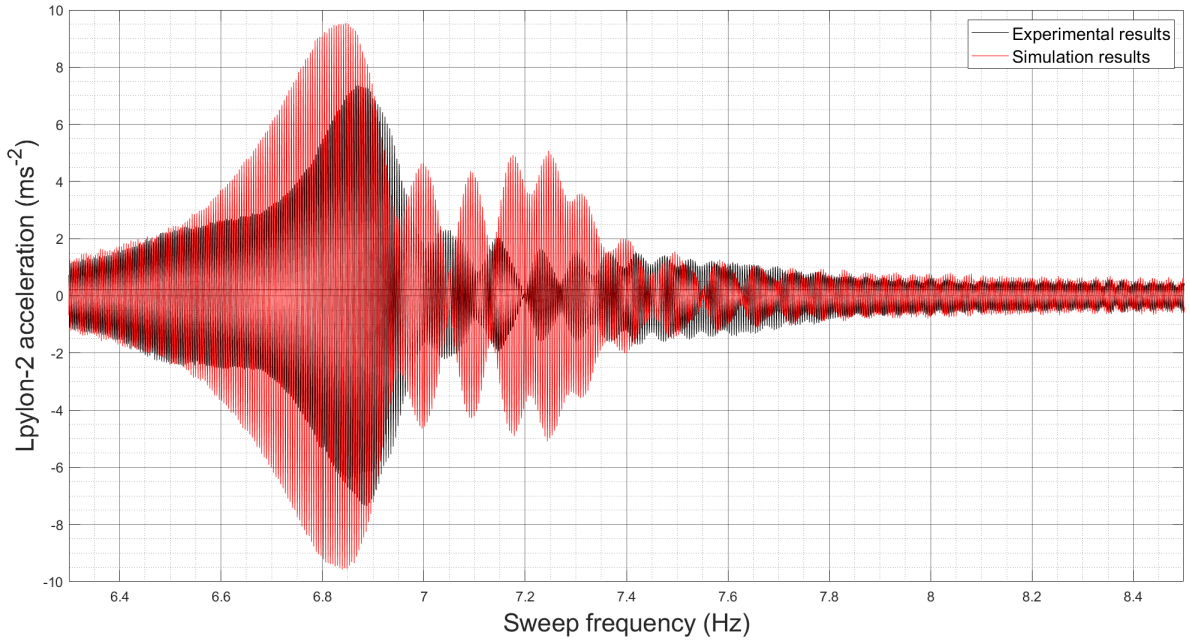


Figure 8.4: Simulated and experimental results for *LPylon:2* at *sweep1* with the excitation level of 0.01 V and with $\zeta_1 = 0.46\%$ and $\zeta_2 = 0.46\%$

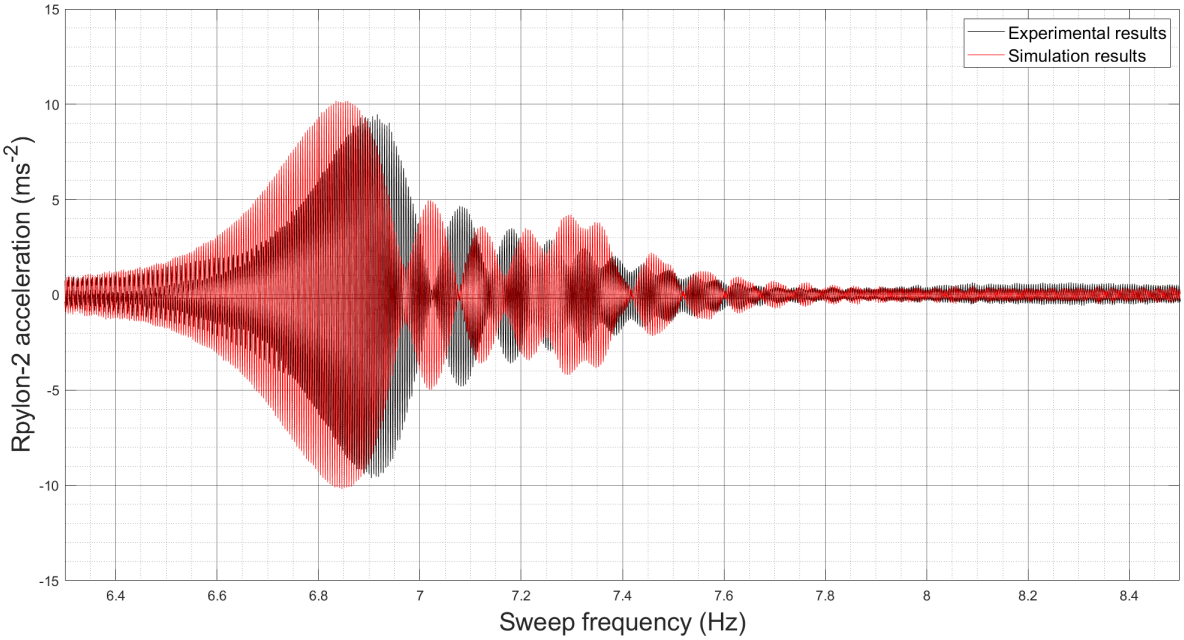


Figure 8.5: Simulated and experimental results for *RPylon:2* at *sweep1* the excitation level of 0.01 V and with $\zeta_1 = 0.46\%$ and $\zeta_2 = 0.46\%$

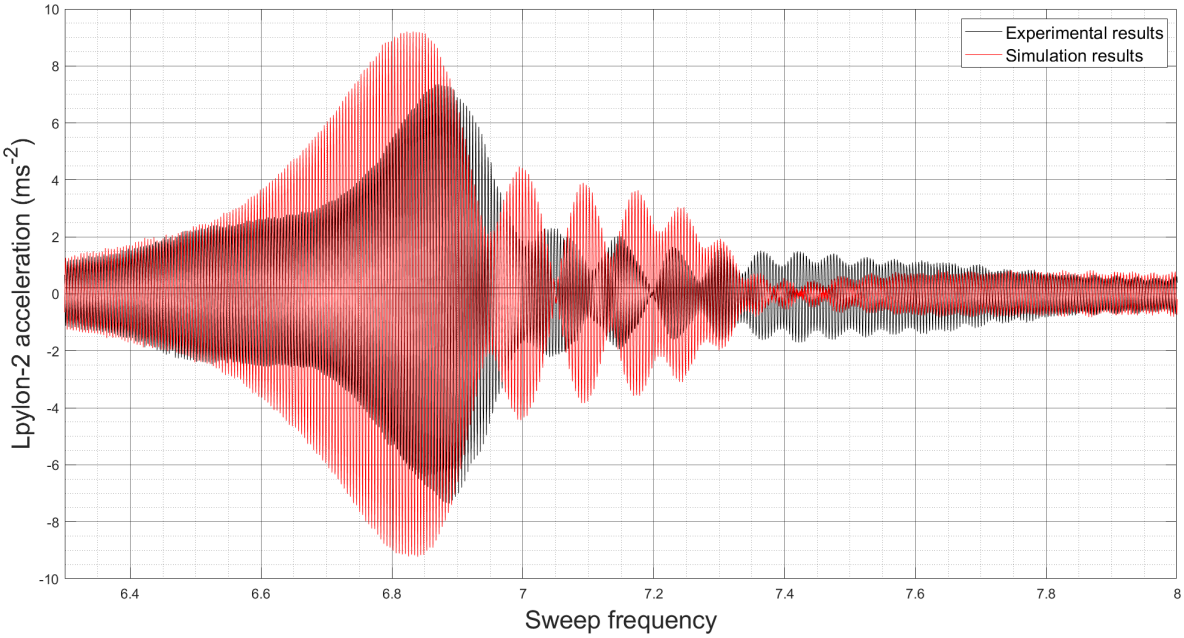


Figure 8.6: Simulated and experimental results for *LPylon:2* at *sweep1* with the excitation level of 0.01 V and with $\zeta_1 = 0.50\%$ and $\zeta_2 = 1.30\%$

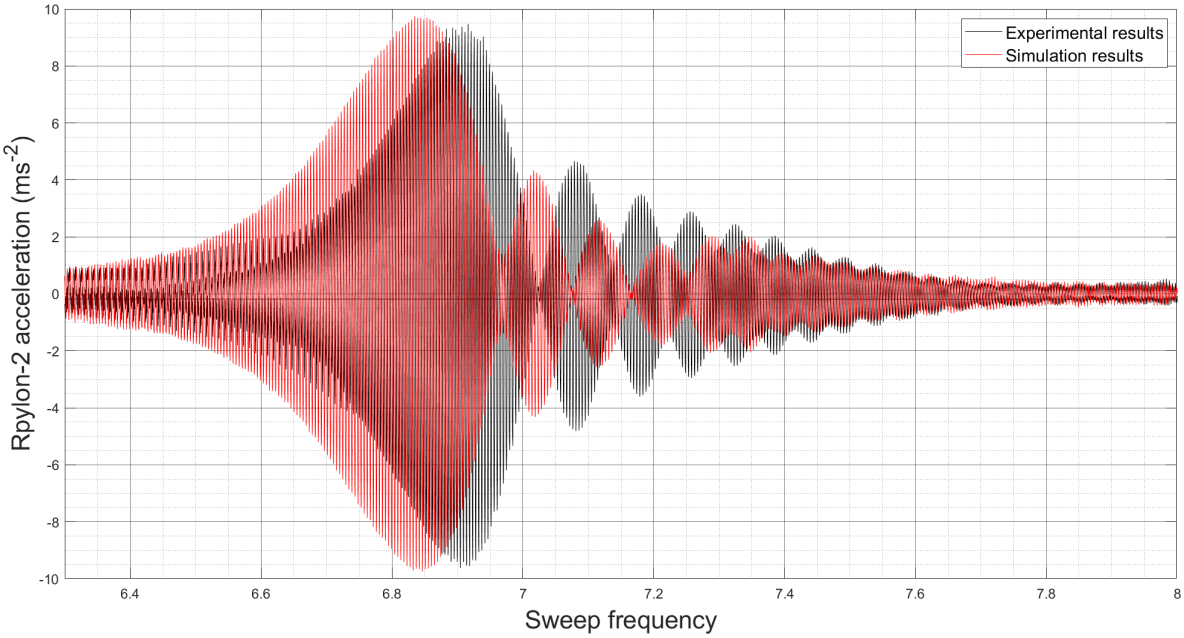


Figure 8.7: Simulated and experimental results for *RPylon:2* at *sweep1* with the excitation level of 0.01 V and with $\zeta_1 = 0.50\%$ and $\zeta_2 = 1.30\%$

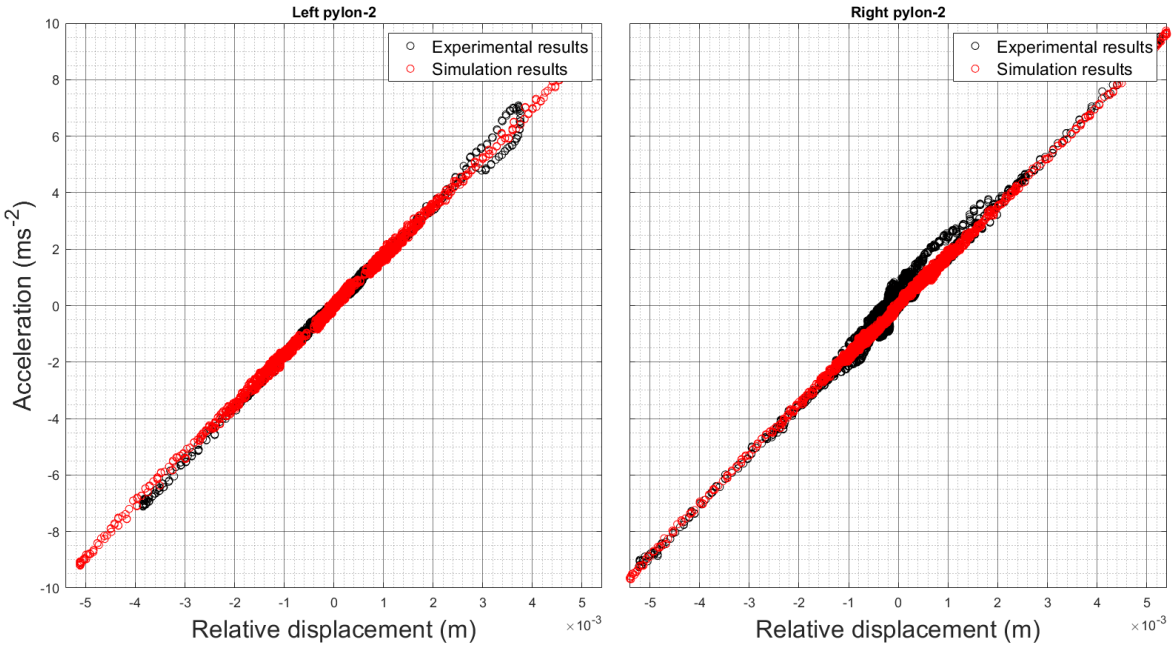


Figure 8.8: Simulated and experimental stiffness curves for *RPylon:2* and *LPylon:2* at *sweep1* with the excitation level of 0.01 V and with $\zeta_1 = 0.50\%$ and $\zeta_2 = 1.30\%$

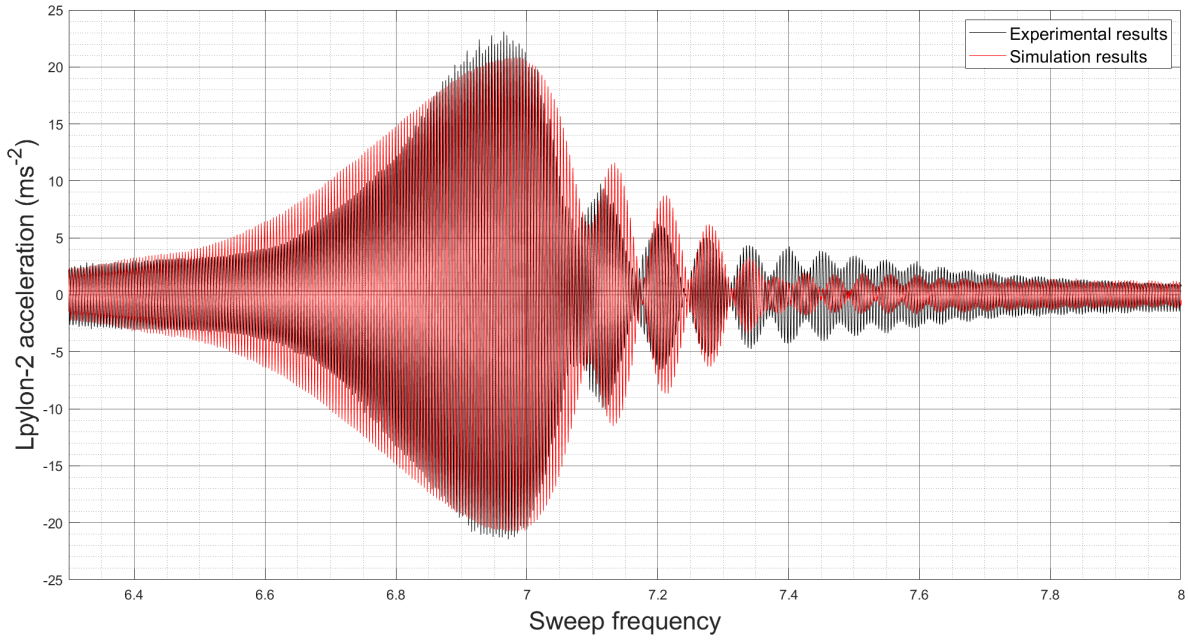


Figure 8.9: Simulated and experimental results for *LPylon:2* at *sweep1* with the excitation level of 0.02 V and with $\zeta_1 = 0.50\%$ and $\zeta_2 = 1.30\%$

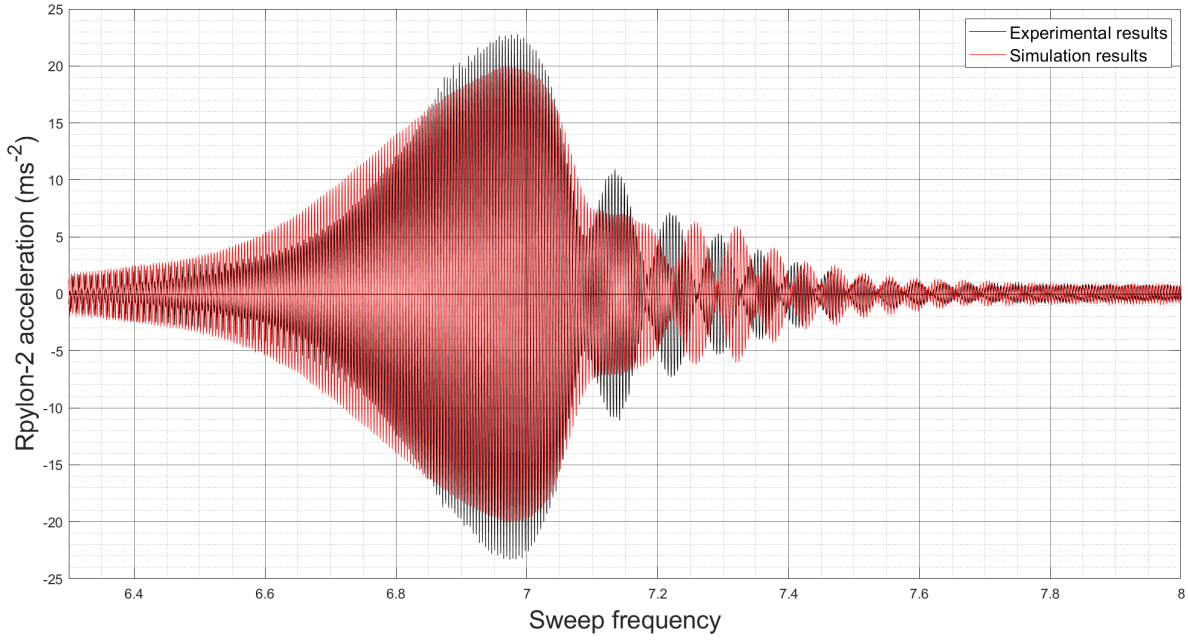


Figure 8.10: Simulated and experimental results for *RPylon:2* at *sweep1* with the excitation level of 0.02 V and with $\zeta_1 = 0.46\%$ and $\zeta_2 = 0.46\%$

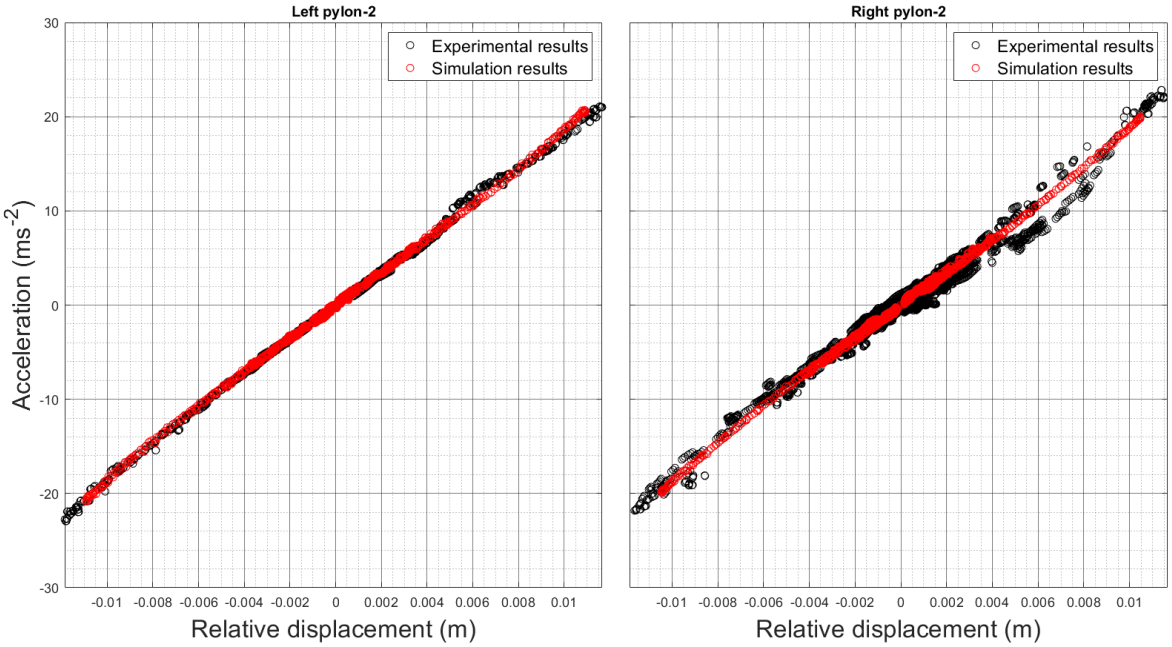


Figure 8.11: Simulated and experimental stiffness curves for *RPylon:2* and *LPylon:2* at *sweep1* with the excitation level of 0.02 V and with $\zeta_1 = 0.50\%$ and $\zeta_2 = 1.30\%$

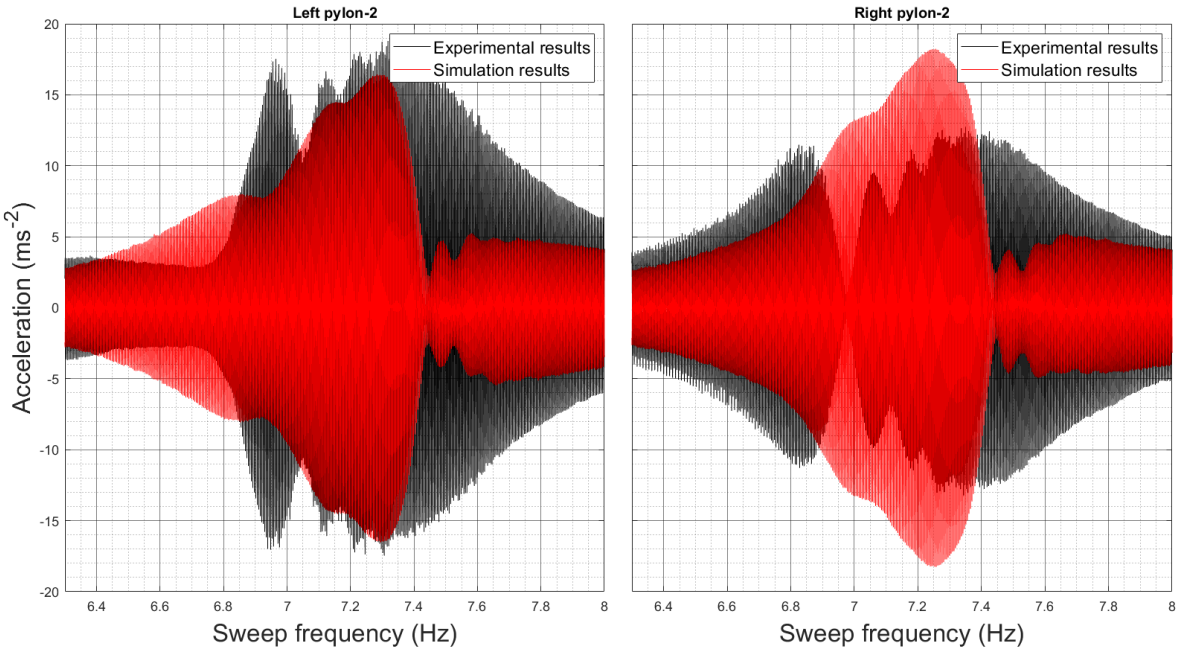


Figure 8.12: Simulated and experimental results for *LPylon:2* and *RPylon:2* at *sweep2* with the excitation level of 0.01 V and with $\zeta_1 = 0.50\%$ and $\zeta_2 = 1.30\%$

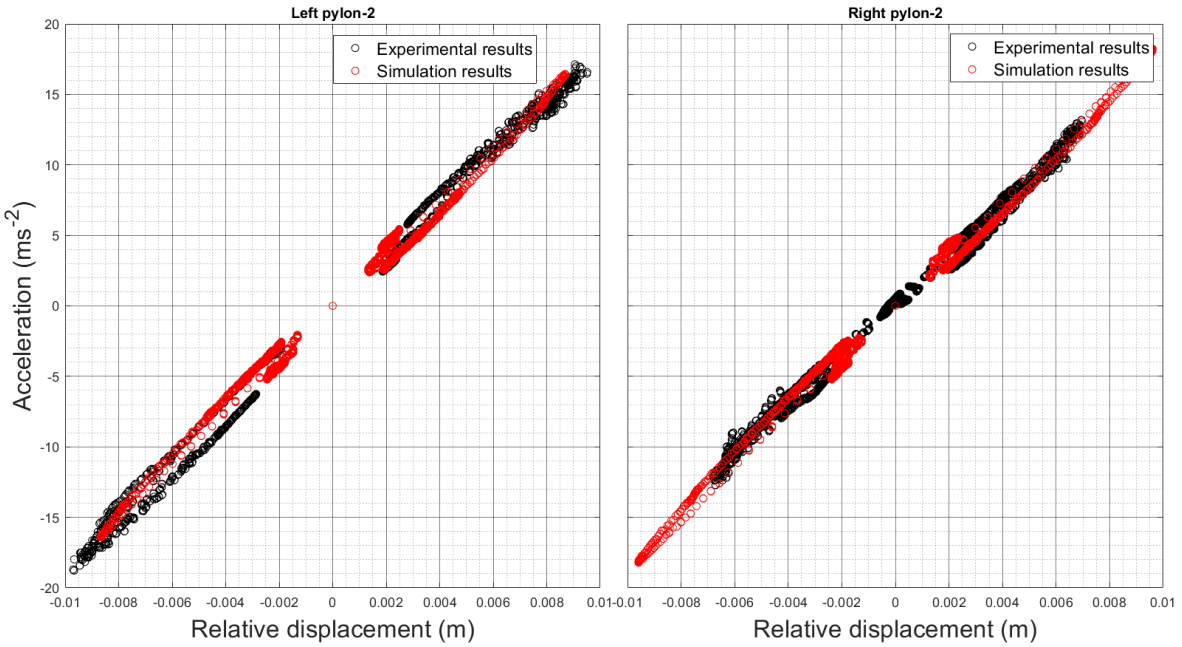


Figure 8.13: Simulated and experimental stiffness curves for *RPylon:2* and *LPylon:2* at *sweep2* with the excitation level of 0.01 V and with $\zeta_1 = 0.50\%$ and $\zeta_2 = 1.30\%$

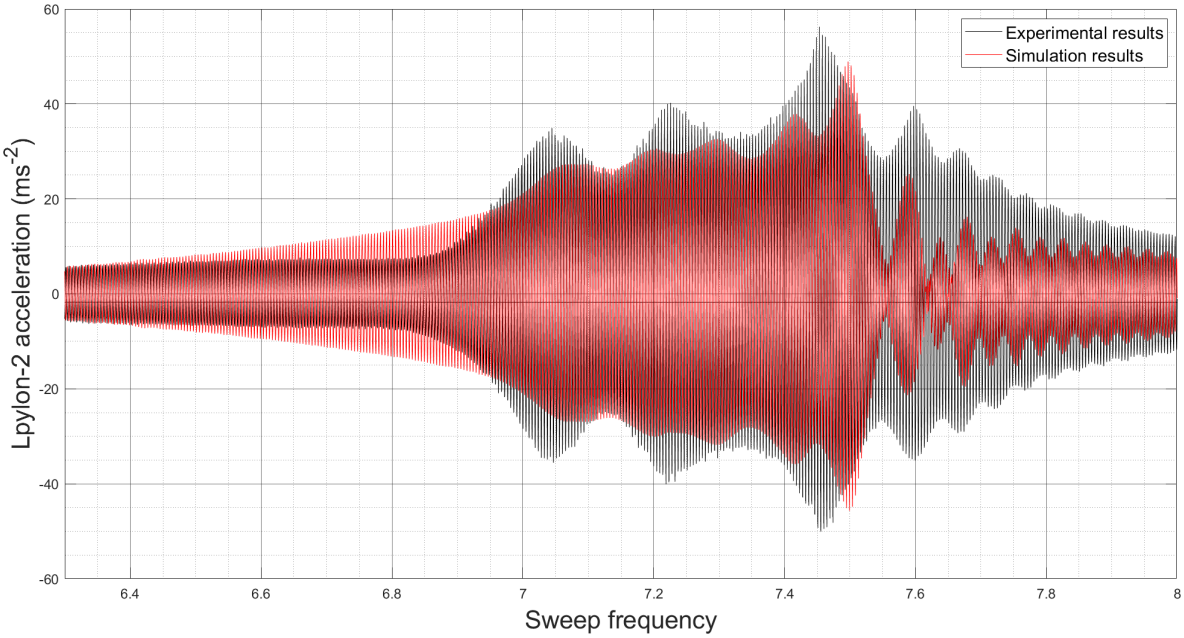


Figure 8.14: Simulated and experimental results for *LPylon:2* at *sweep2* with the excitation level of 0.02 V and with $\zeta_1 = 0.50\%$ and $\zeta_2 = 1.30\%$

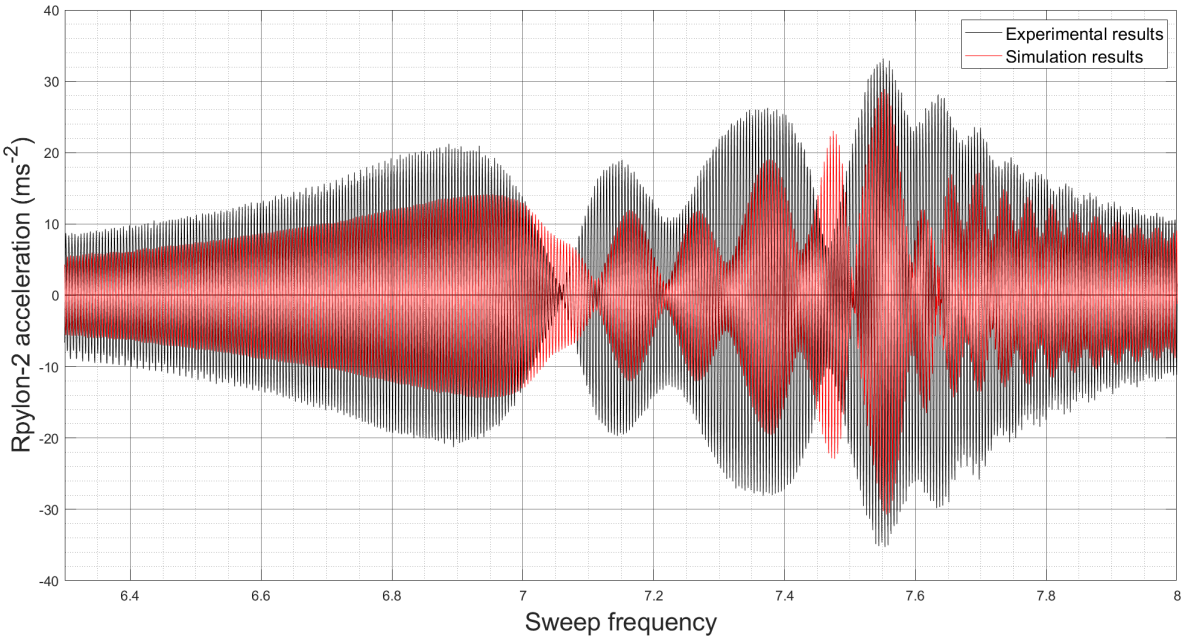


Figure 8.15: Simulated and experimental results for *RPylon:2* at *sweep2* with the excitation level of 0.02 V and with $\zeta_1 = 0.46\%$ and $\zeta_2 = 0.46\%$

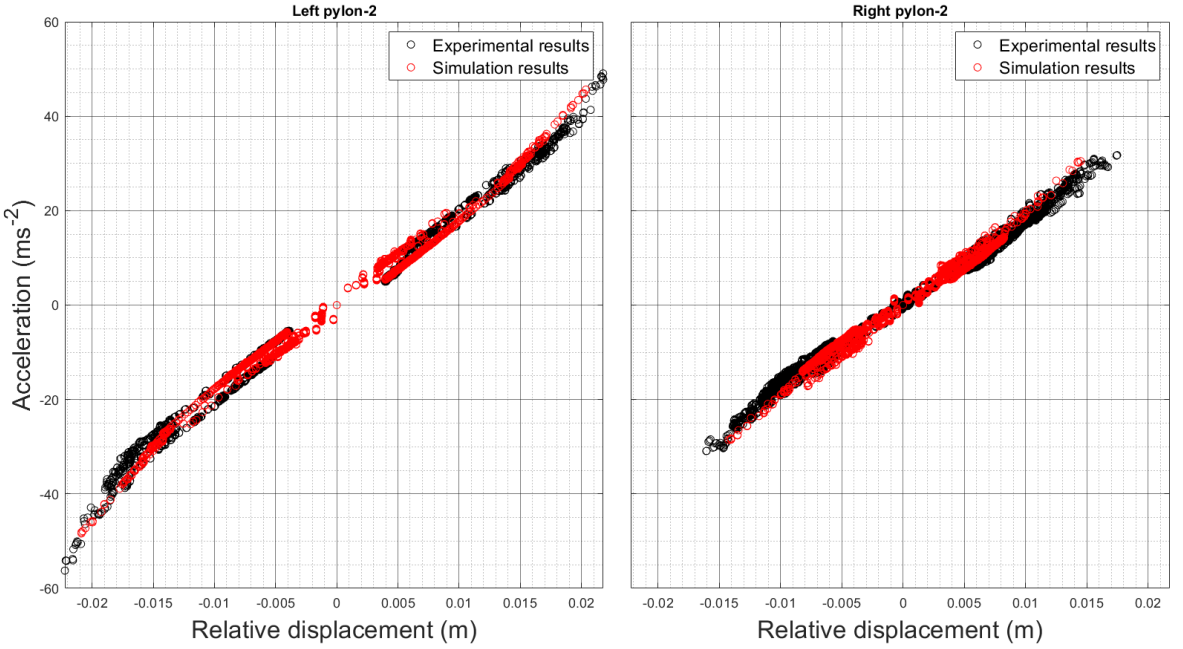


Figure 8.16: Simulated and experimental stiffness curves for *RPylon:2* and *LPylon:2* at *sweep2* with the excitation level of 0.02 V and with $\zeta_1 = 0.50\%$ and $\zeta_2 = 1.30\%$

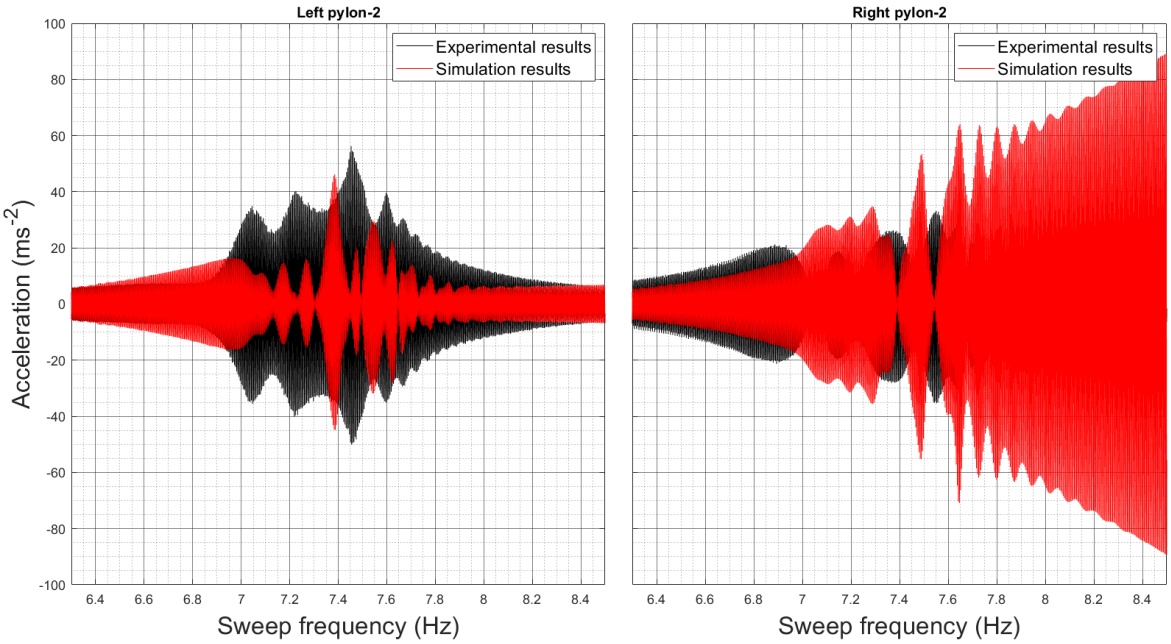


Figure 8.17: Simulated and experimental results for *LPylon:2* and *RPylon:2* at *sweep2* with the excitation level of 0.02 V and with $\zeta_1 = 0.50\%$ and $\zeta_2 = 0.50\%$

To conclude, it matters to say that for *sweep1* in the nonlinear simulations good results are expected, and for *sweep2* the same thing can't be said because of the bad results for 0.01 V, although the results at 0.02 V give some hope. Lastly, the difference between the experimental damping values and the ones used at the simulations are not "absurd" because the initial values were very low, and even with these new values, they continue to be very low. Very low damping values are not easy to measure.

8.2 Nonlinear model

Before presenting the results considering the nonlinearity, as an example, in fig. 8.18 and 8.19 for *sweep1* at 0.06 V are presented the results considering a linear model.

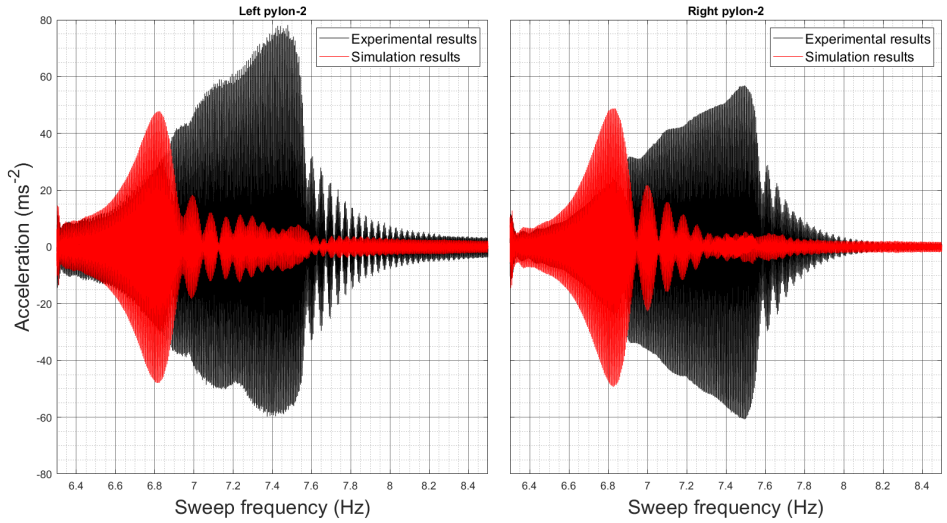


Figure 8.18: Simulated and experimental results for *LPylon:2* and *RPylon:2* at *sweep1* with the excitation level of 0.06 V and with $\zeta_1 = 0.50\%$ and $\zeta_2 = 1.30\%$ without considering the nonlinear behaviour

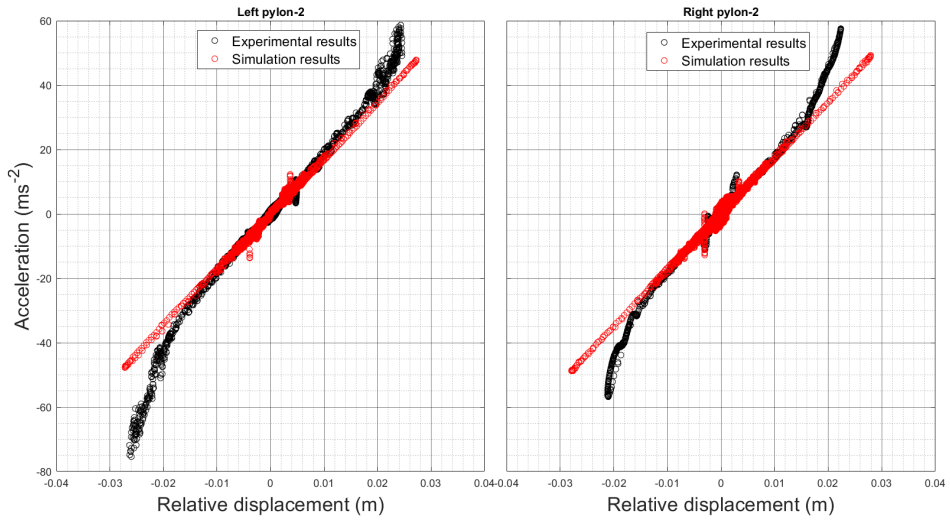


Figure 8.19: Simulated and experimental stiffness curves for *RPylon:2* and *LPylon:2* at *sweep2* with the excitation level of 0.06 V and with $\zeta_1 = 0.50\%$ and $\zeta_2 = 1.30\%$ without considering the nonlinear behaviour

As it can be seen to consider a linear behaviour is definitely not a good idea, and as expected the plots have a similar shape to the ones obtained at 0.01 V. In this section it will be firstly presented the results for the cubic stiffness, then for the "polynomial stiffness" and by last considering a piecewise function.

8.2.1 Cubic stiffness

Firstly, before introducing any changes in the damping values, the results are presented for 0.04 V for *sweep1* and *sweep2* in fig. 8.20, 8.21 and 8.22. In those figures it can be seen that for *sweep1* the results are good, while for *sweep2* the results are bad, and for that reason the stiffness plots are not even presented for *sweep2*. Since in the previous chapter the results were also not that good for *sweep2*, this may be something that was already expected. But to show that the damping values need to be upgraded, the results for 0.06 V are presented in fig. 8.23, 8.24 and 8.25. To find a reason for that, at fig. 8.26, the accelerance curves *LPylon:2-LWing:5_force* for different excitation levels are presented, where it is possible to observe that the resonance peaks associated to the modes move in frequency, displaying a hardening behaviour, but at the same time there is a reduction in amplitude of those same peaks, especially for mode 2. This is certainly caused by the nonlinearity, but at same time it might be eventually explained by an increase in damping.

So, after this clarification regarding the damping values, as a result of diverse iterations, the next results are presented:

- 0.04 V - Fig. 8.27, 8.28 and 8.29 for *sweep1* and fig. 8.42, 8.43 and 8.44 for *sweep2* with $\zeta_1 = 0.52\%$ and $\zeta_2 = 5.00\%$;
- 0.06 V - Fig. 8.30, 8.31 and 8.32 for *sweep1* and fig. 8.45 and 8.46 for *sweep2* with $\zeta_1 = 0.73\%$ and $\zeta_2 = 6.00\%$;
- 0.07 V - Fig. 8.33, 8.34 and 8.35 for *sweep1* and fig. 8.47 and 8.48 for *sweep2* with $\zeta_1 = 0.73\%$ and $\zeta_2 = 6.00\%$;
- 0.08 V - Fig. 8.36, 8.37 and 8.38 for *sweep1* and fig. 8.49, 8.50 and 8.51 for *sweep2* with $\zeta_1 = 0.83\%$ and $\zeta_2 = 6.40\%$;
- 0.09 V - Fig. 8.39, 8.40 and 8.41 for *sweep1* and fig. 8.52, 8.53 and 8.54 for *sweep2* with $\zeta_1 = 0.93\%$ and $\zeta_2 = 6.30\%$;

Looking at the plots relatively to *sweep1* it can be seen that the results are good because there is a good correspondence in terms of displacement, the frequency peak increases with the applied force, but at same time it was not possible to capture the nonsymmetric oscillations around the equilibrium position. That was already predictable because a cubic stiffness is used and nonsymmetric oscillations, generally, only occur if even and odd nonlinearities are present. Another detail that can be stated is the difference of amplitude in the acceleration answers between 6.8-7.6 Hz (before the "jump") which, in the cases of 0.07, 0.08 and 0.09 V for the left pylon are quite visible (fig. 8.33, 8.36 and 8.39). Considering that the "symmetric amplitude" at the "jump" frequency of the experimental and simulated results are equal, that is something expected because the peak frequency of the simulated answer is higher than the experimental one. So, if the answers have a similar evolution, and they have because the slope of the curves are identical, it is simply natural that the amplitude at a same frequency is higher in the experimental case. Secondly, that can also be explained by the existence of nonlinear damping, because to achieve those "jump" amplitudes, higher damping values comparatively with the ones used in the linear model were used, and different damping values were used along the different excitation levels, which indicates the existence of nonlinear damping that was not considered in these simulations. So, this may hypothetically mean that in reality what happens is that when the "jump" frequency approaches, the damping increases. But, as it was seen in the previous chapter no nonlinear damping was detected.

About *sweep2*, the performance can be described in the following points:

- At 0.04 V for the left pylon the results are not bad, but unfortunately the same thing cannot be said about the right pylon;
- At 0.06 V and at 0.07 V the results are bad in the right pylon, although they are not bad for the left pylon;
- At 0.08 V and the shape correspondence is good, but in terms of amplitude of the answer they are not good;
- At 0.09 V the results are similar to 0.08 V, but with a better amplitude correspondence.

There is no much more to say about *sweep2* not only because there are two modes acting, which makes the analysis more difficult, but also because the eventual existence of nonlinear damping is something necessarily transversal to both sweeps. Now, looking at the evolution of the damping among the different excitation levels, it seems to "make sense" according to what was said about the fig. 8.26, because the damping increases with the applied force, especially for the mode 1. For mode 2 the same thing can't be said because the damping in mode 2 for 0.09 V is lower than in 0.08 V. But, just by looking to the damping values it might be said that it is the high damping value in mode 2 that makes mode 1 dominate the answer on *sweep1*. But once again that is not true because as it was exposed in the previous section, when the damping values are equal, the mode 1 dominates the answer (fig. 8.4). And if the reader is still suspicious, at fig. 8.55 and 8.56, for 0.06 V the results for *sweep1* considering equal damping values are exposed.

To finalise, in order to let everything as clear as possible, on fig. 8.57, the results for *sweep2* at 0.06 V considering a lower damping at the mode 2 are exposed. Those damping values at mode 2 were used because they were the ones that provided the best results, and not to hide its contribution in *sweep1*. Multiple iterations were made to achieve those values.

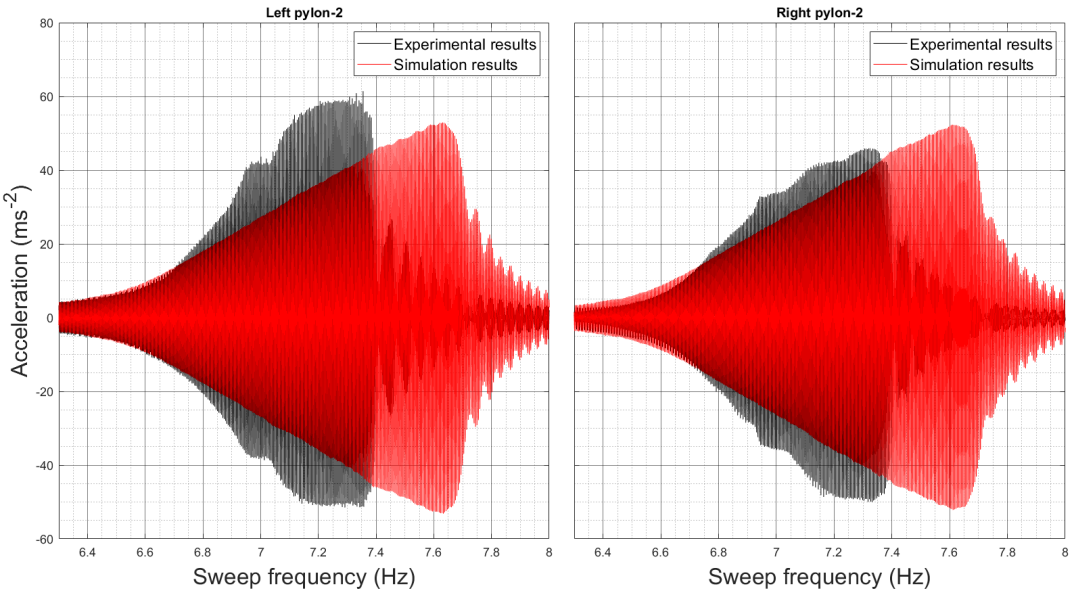


Figure 8.20: Simulated and experimental results for *LPylon:2* and *RPylon:2* at *sweep1* with the excitation level of 0.04 V and with $\zeta_1 = 0.50\%$ and $\zeta_2 = 1.30\%$ using a cubic stiffness

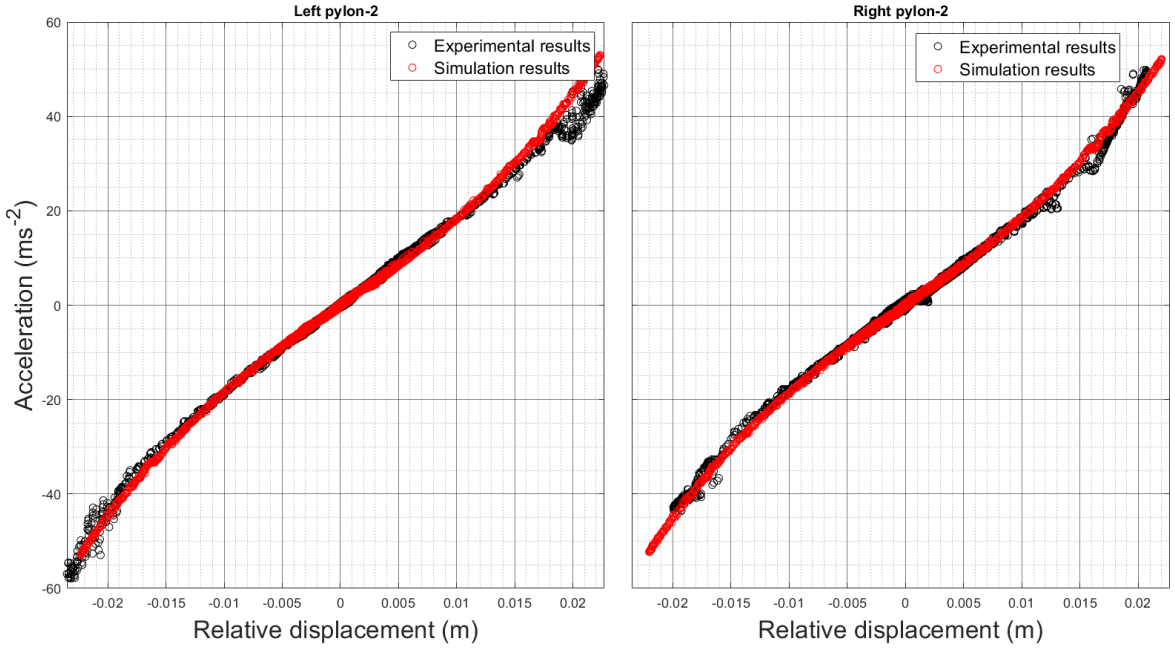


Figure 8.21: Simulated and experimental stiffness curves for *RPylon:2* and *LPylon:2* at *sweep1* with the excitation level of 0.04 V and with $\zeta_1 = 0.50\%$ and $\zeta_2 = 1.30\%$ using a cubic stiffness

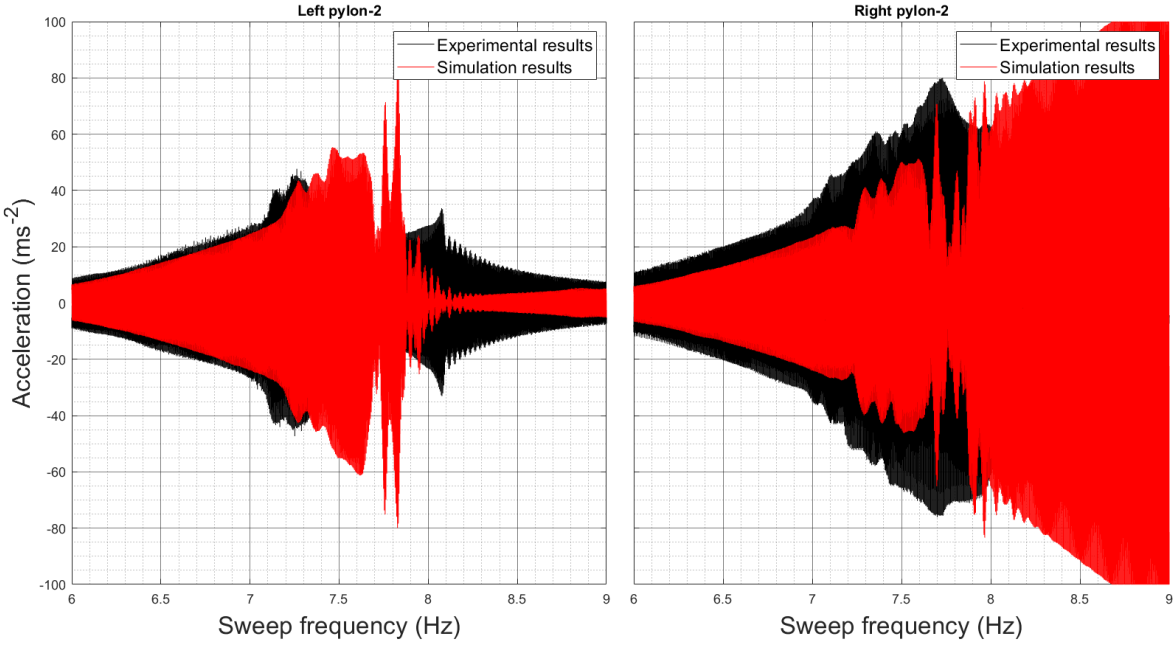


Figure 8.22: Simulated and experimental results for *LPylon:2* and *RPylon:2* at *sweep2* with the excitation level of 0.04 V and with $\zeta_1 = 0.50\%$ and $\zeta_2 = 1.30\%$ using a cubic stiffness

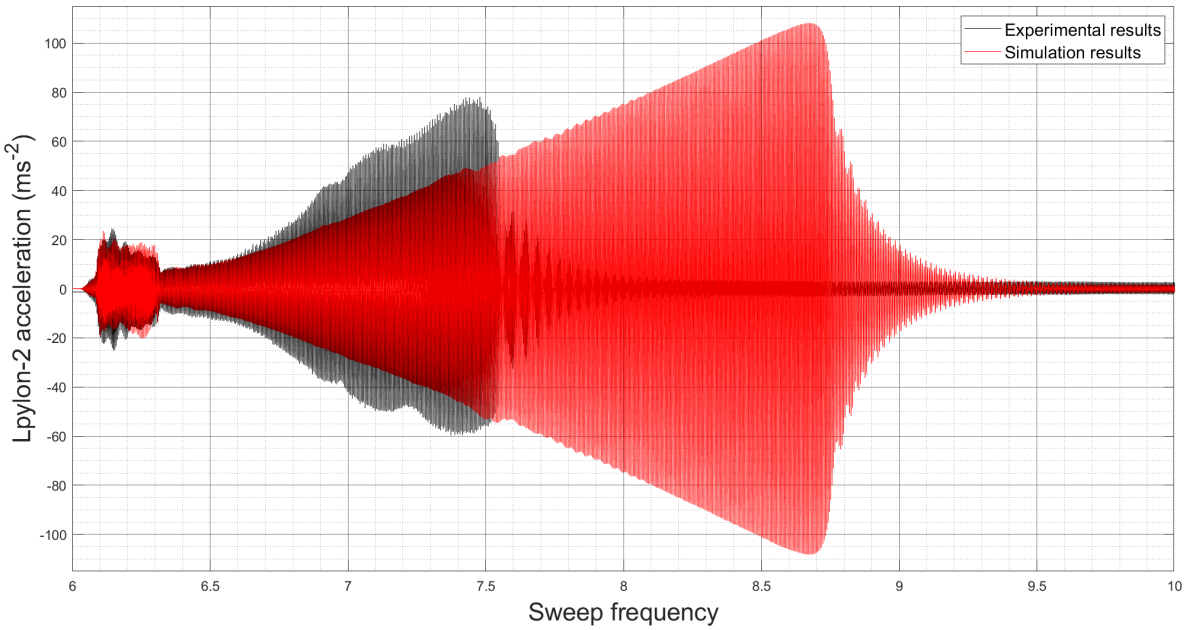


Figure 8.23: Simulated and experimental results for *LPylon:2* at *sweep1* with the excitation level of 0.06 V and with $\zeta_1 = 0.50\%$ and $\zeta_2 = 1.30\%$ using a cubic stiffness

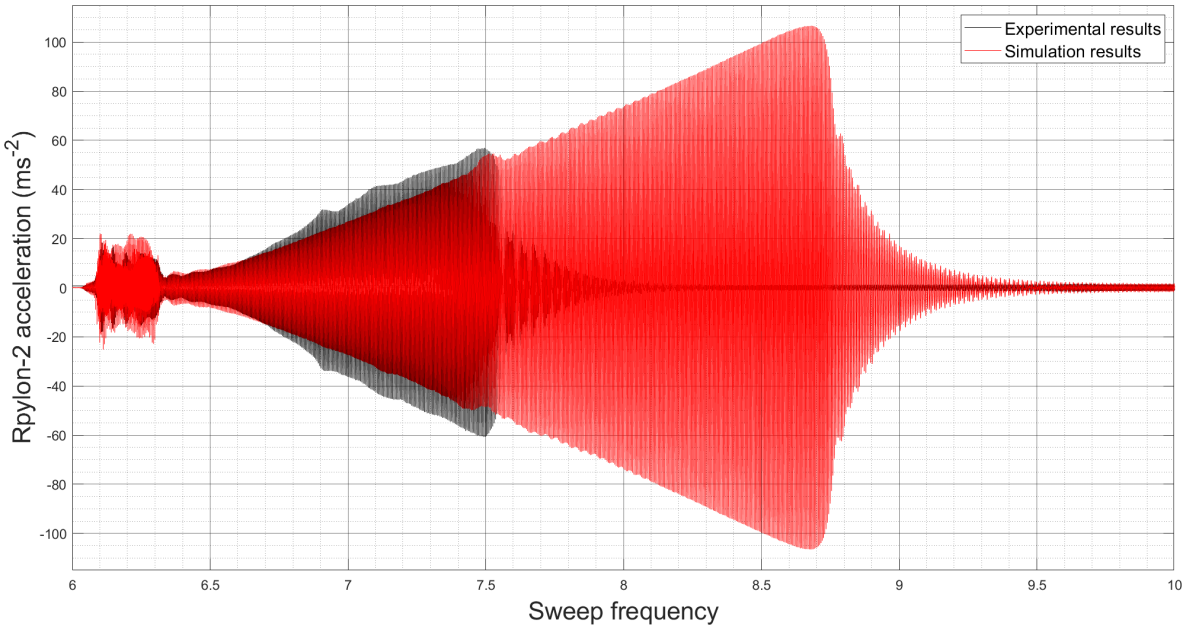


Figure 8.24: Simulated and experimental results for *RPylon:2* at *sweep1* with the excitation level of 0.06 V and with $\zeta_1 = 0.50\%$ and $\zeta_2 = 1.30\%$ using a cubic stiffness

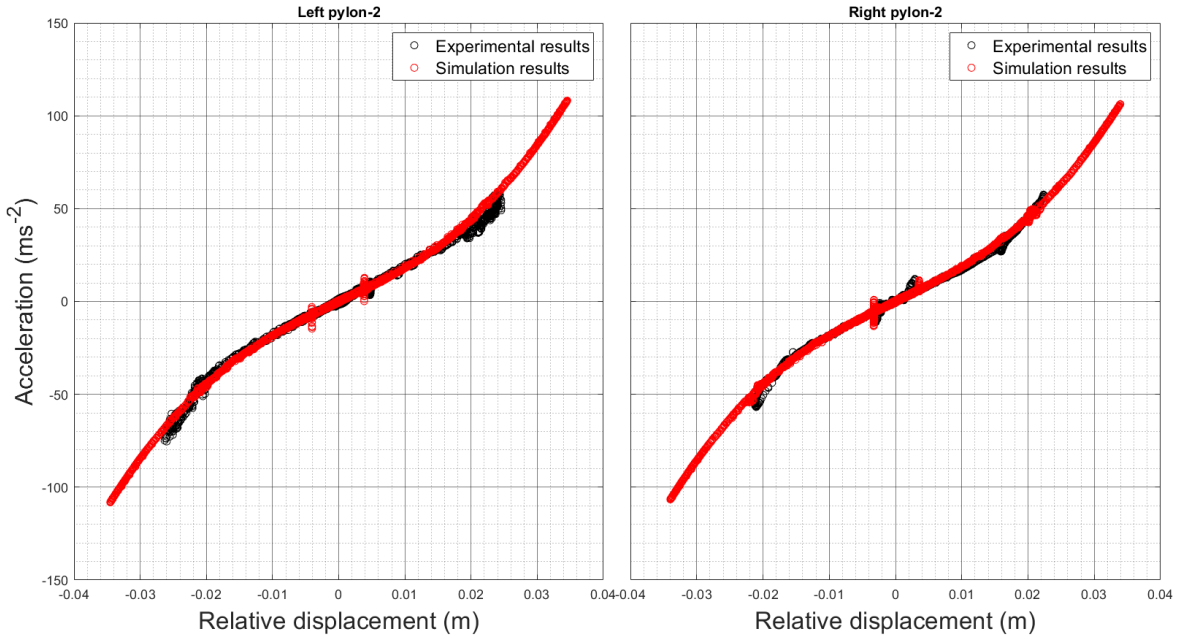


Figure 8.25: Simulated and experimental stiffness curves for *RPylon:2* and *LPylon:2* at *sweep1* with the excitation level of 0.06 V and with $\zeta_1 = 0.50\%$ and $\zeta_2 = 1.30\%$ using a cubic stiffness

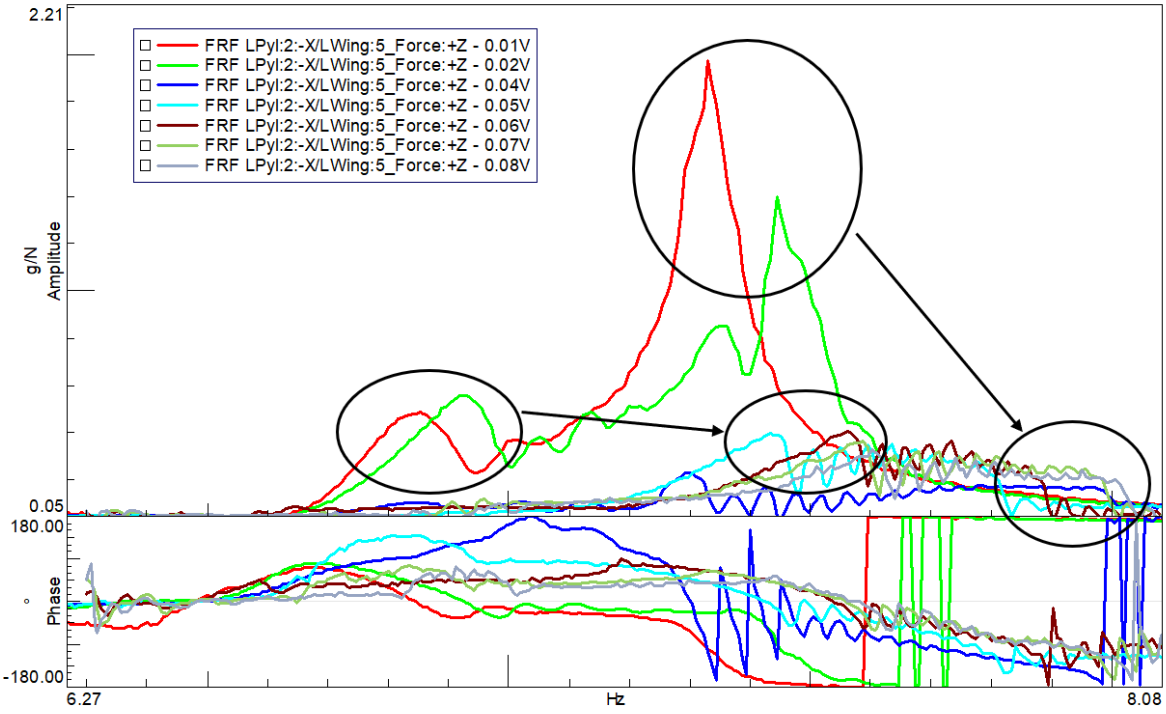


Figure 8.26: Accelerance curves *LPylon:2-LWing:5_force* for the different excitation levels using a cubic stiffness

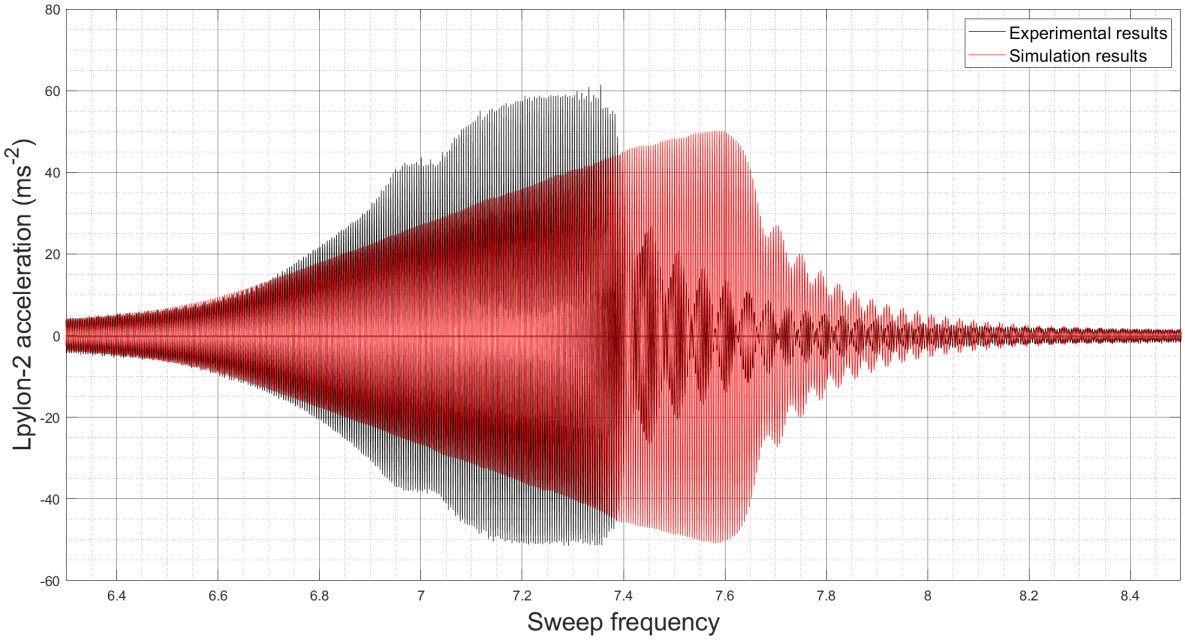


Figure 8.27: Simulated and experimental results for *LPylon:2* at *sweep1* with the excitation level of 0.04 V and with $\zeta_1 = 0.52\%$ and $\zeta_2 = 5.00\%$ using a cubic stiffness

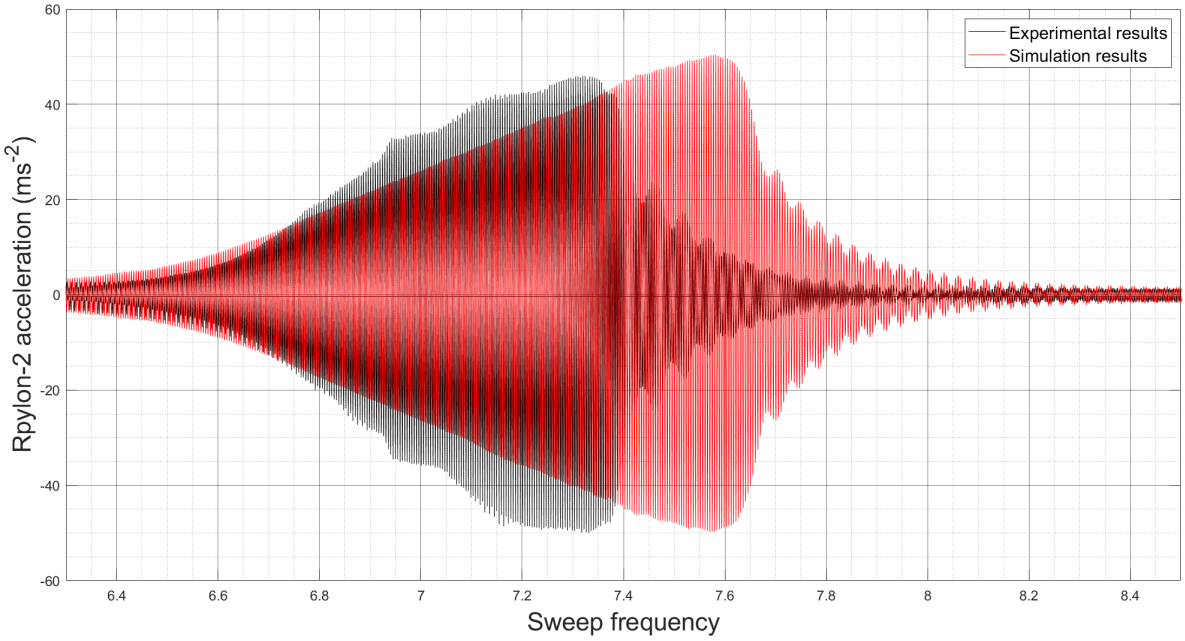


Figure 8.28: Simulated and experimental results for *RPylon:2* at *sweep1* with the excitation level of 0.04 V and with $\zeta_1 = 0.52\%$ and $\zeta_2 = 5.00\%$ using a cubic stiffness

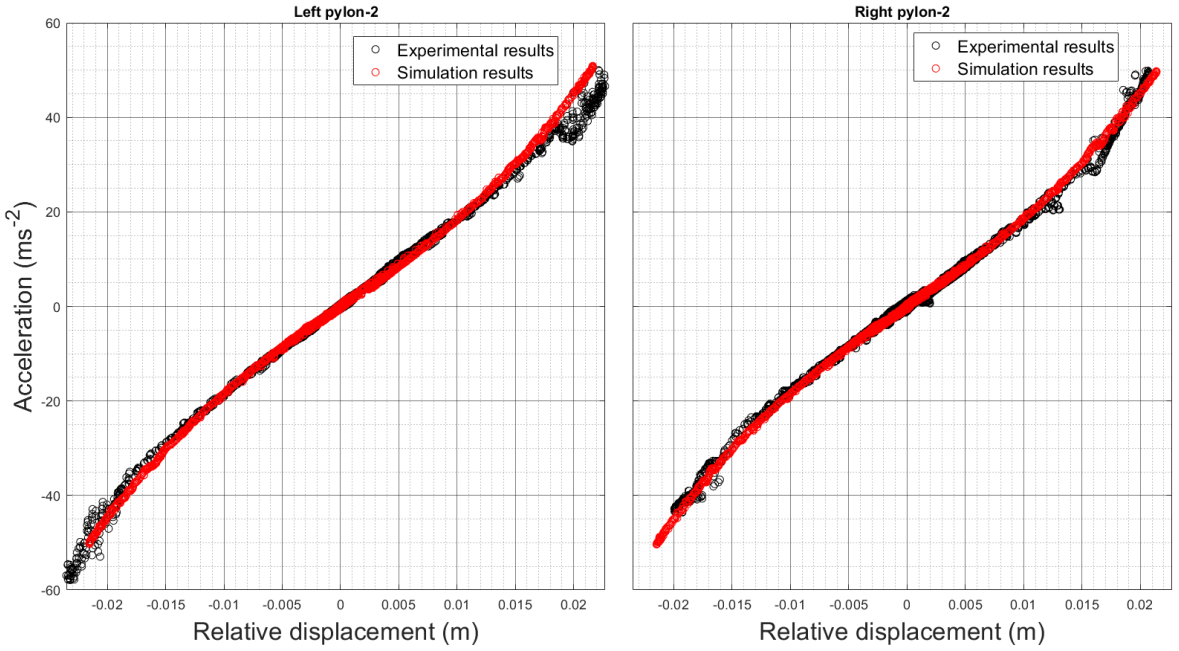


Figure 8.29: Simulated and experimental stiffness curves for *RPylon:2* and *LPylon:2* at *sweep1* with the excitation level of 0.04 V and with $\zeta_1 = 0.52\%$ and $\zeta_2 = 5.00\%$ using a cubic stiffness

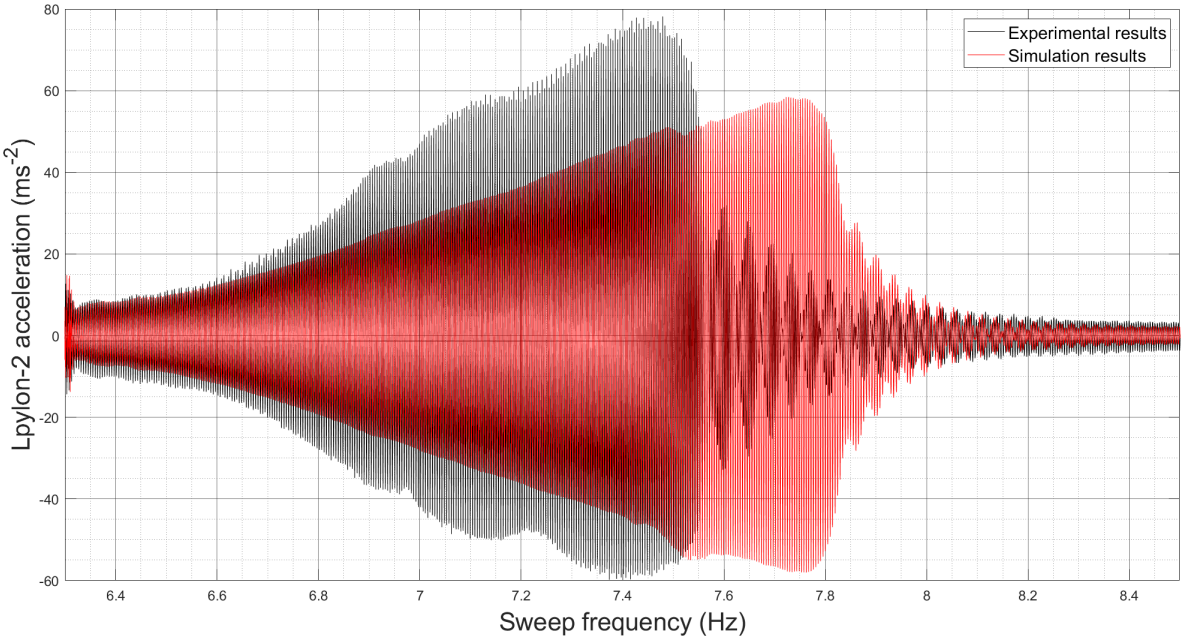


Figure 8.30: Simulated and experimental results for *LPylon:2* at *sweep1* with the excitation level of 0.06 V and with $\zeta_1 = 0.73\%$ and $\zeta_2 = 7.00\%$ using a cubic stiffness

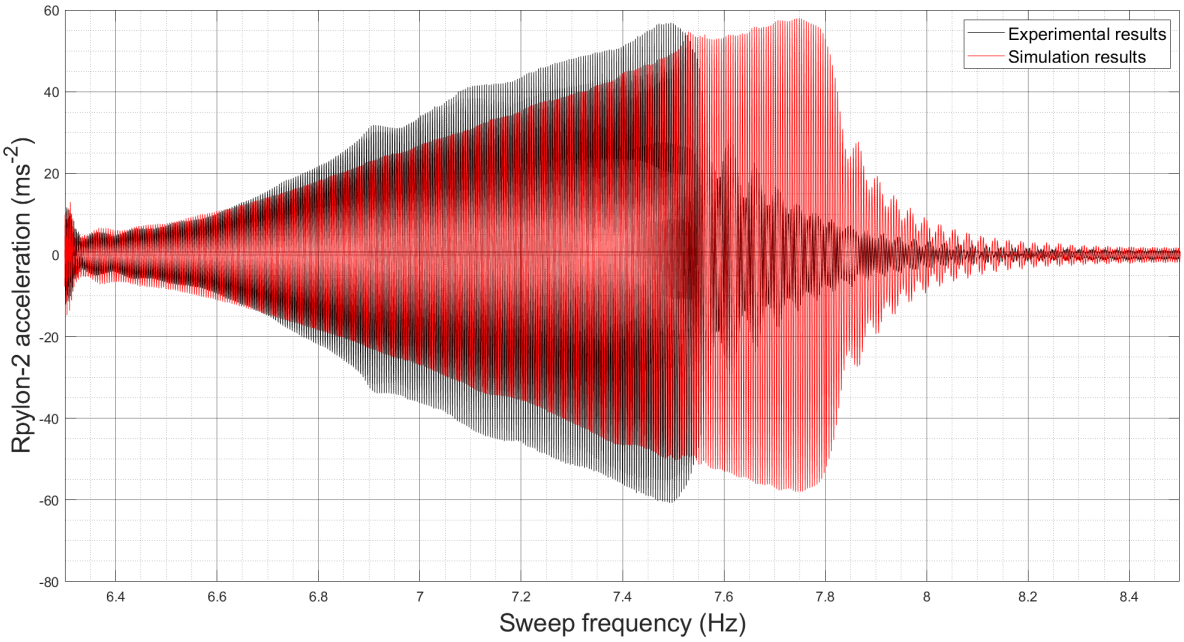


Figure 8.31: Simulated and experimental results for *RPylon:2* at *sweep1* with the excitation level of 0.06 V and with $\zeta_1 = 0.73\%$ and $\zeta_2 = 6.00\%$ using a cubic stiffness

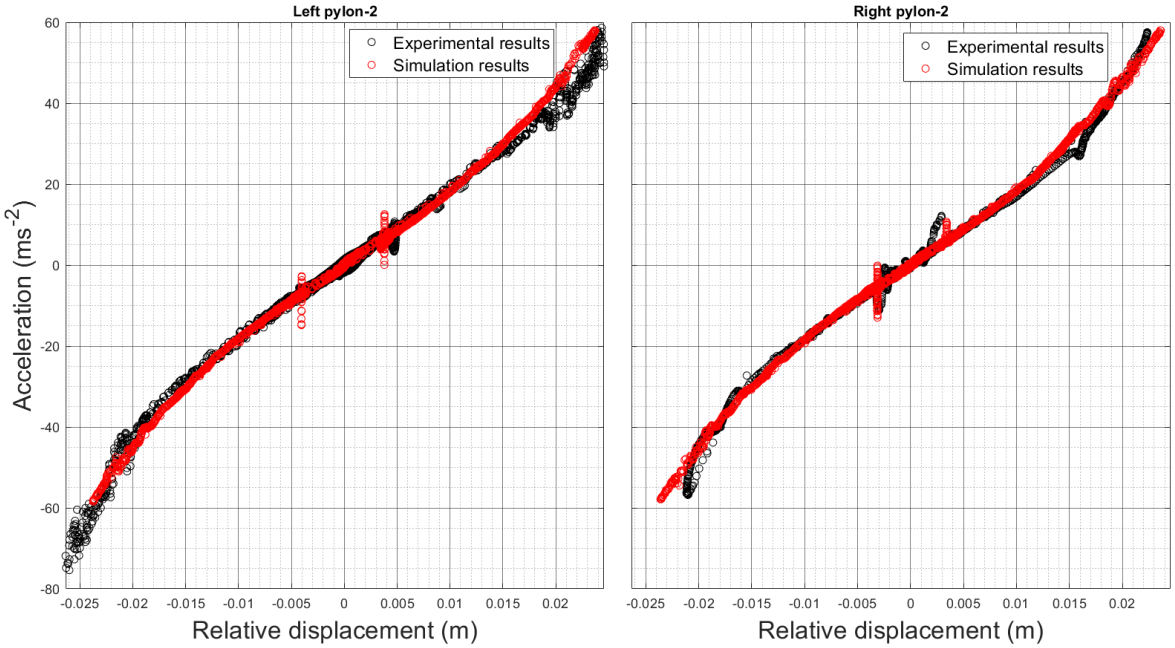


Figure 8.32: Simulated and experimental stiffness curves for *RPylon:2* and *LPylon:2* at *sweep1* with the excitation level of 0.06 V and with $\zeta_1 = 0.73\%$ and $\zeta_2 = 6.00\%$ using a cubic stiffness

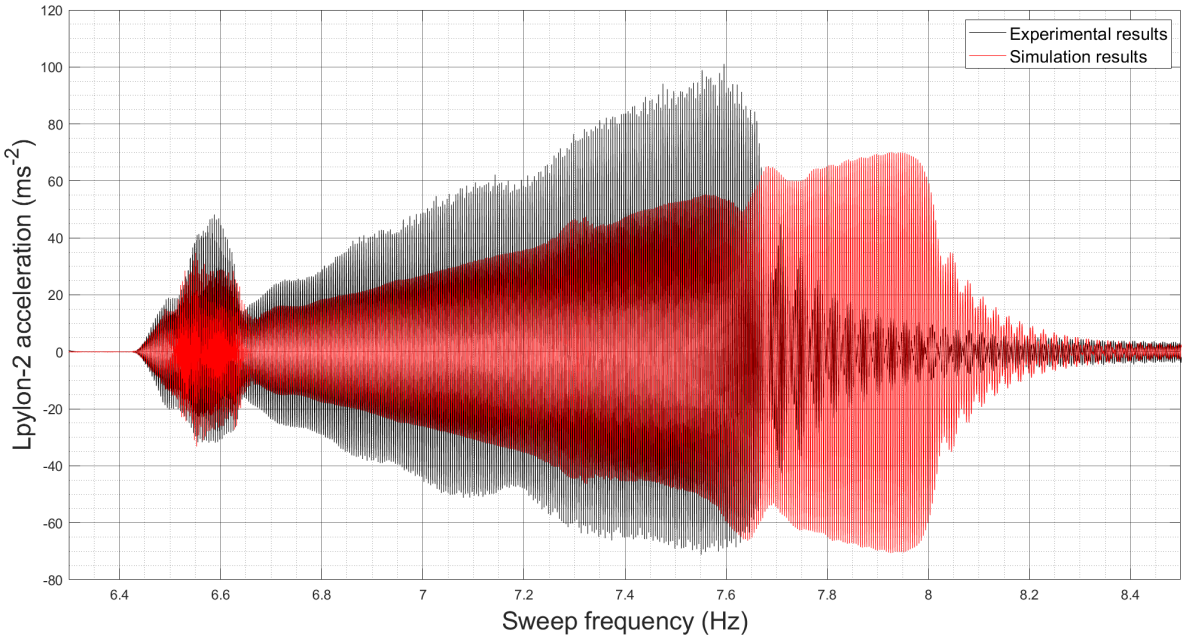


Figure 8.33: Simulated and experimental results for *LPylon:2* at *sweep1* with the excitation level of 0.07 V and with $\zeta_1 = 0.73\%$ and $\zeta_2 = 6.00\%$ using a cubic stiffness

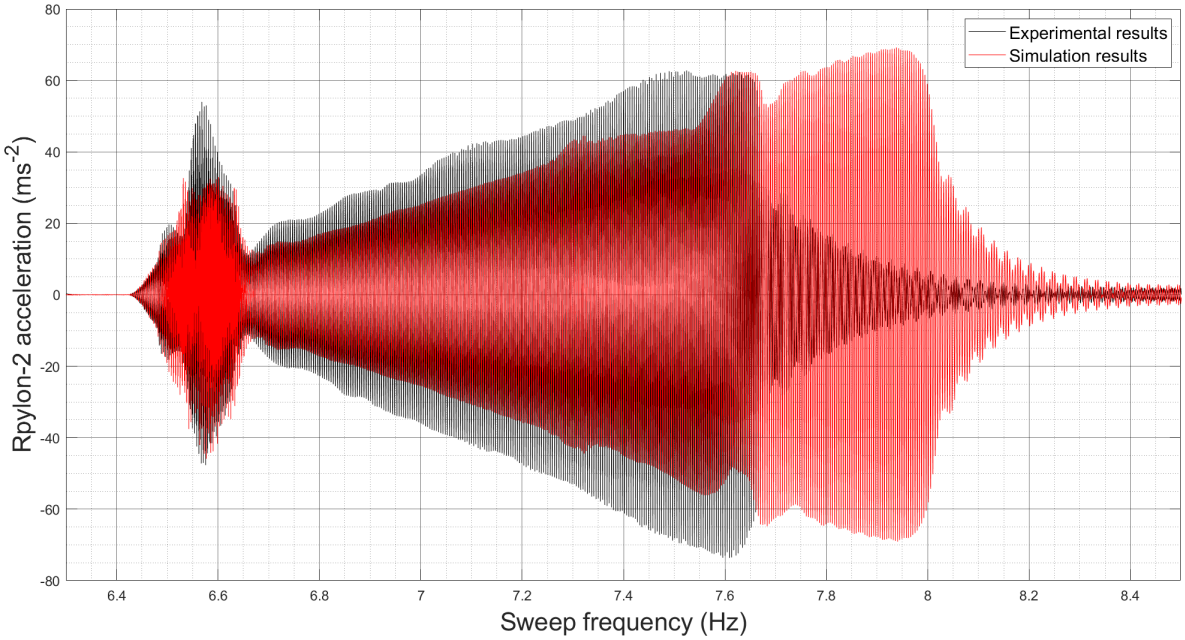


Figure 8.34: Simulated and experimental results for *RPylon:2* at *sweep1* with the excitation level of 0.07 V and with $\zeta_1 = 0.73\%$ and $\zeta_2 = 6.00\%$ using a cubic stiffness

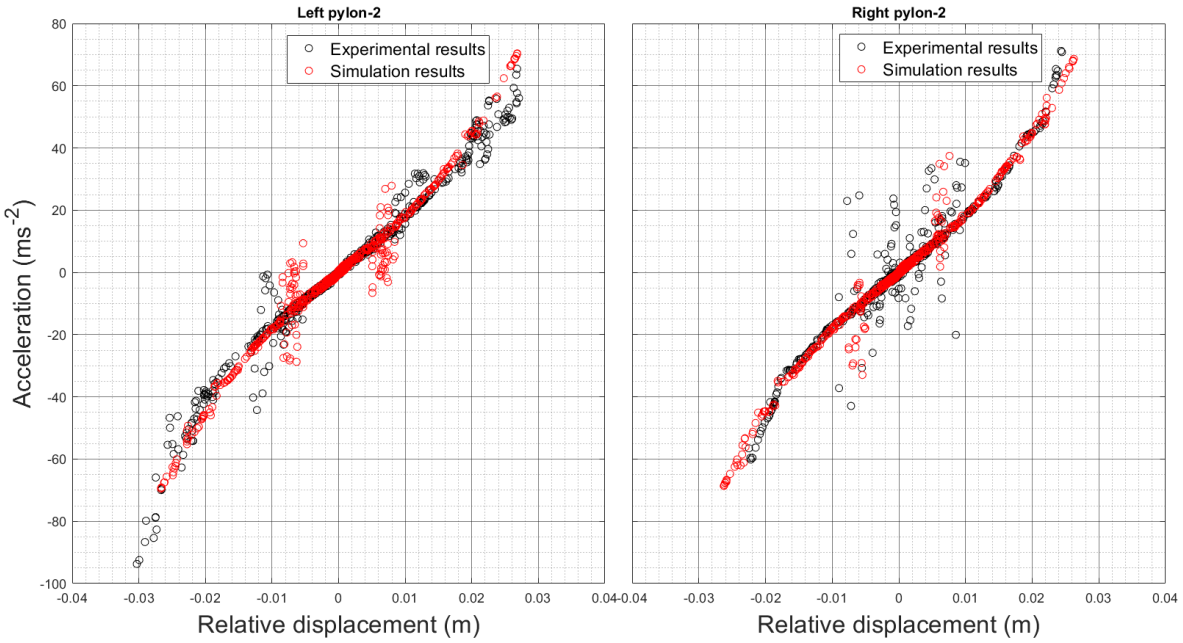


Figure 8.35: Simulated and experimental stiffness curves for *RPylon:2* and *LPylon:2* at *sweep1* with the excitation level of 0.07 V and with $\zeta_1 = 0.73\%$ and $\zeta_2 = 6.00\%$ using a cubic stiffness

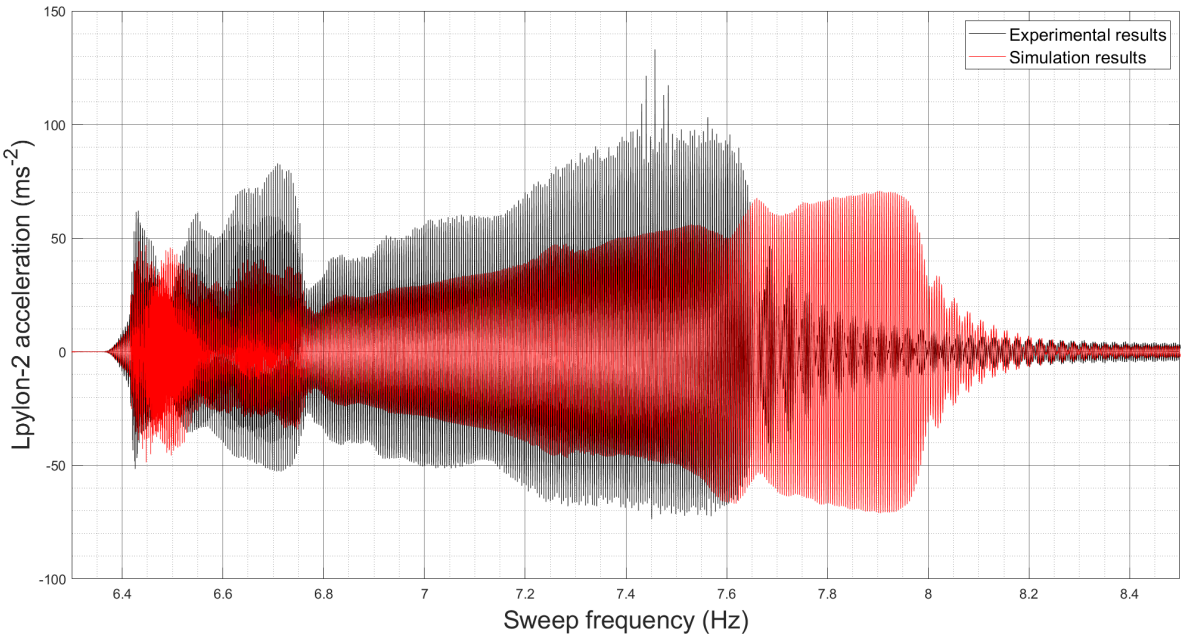


Figure 8.36: Simulated and experimental results for *LPylon:2* at *sweep1* with the excitation level of 0.08 V and with $\zeta_1 = 0.83\%$ and $\zeta_2 = 6.40\%$ using a cubic stiffness

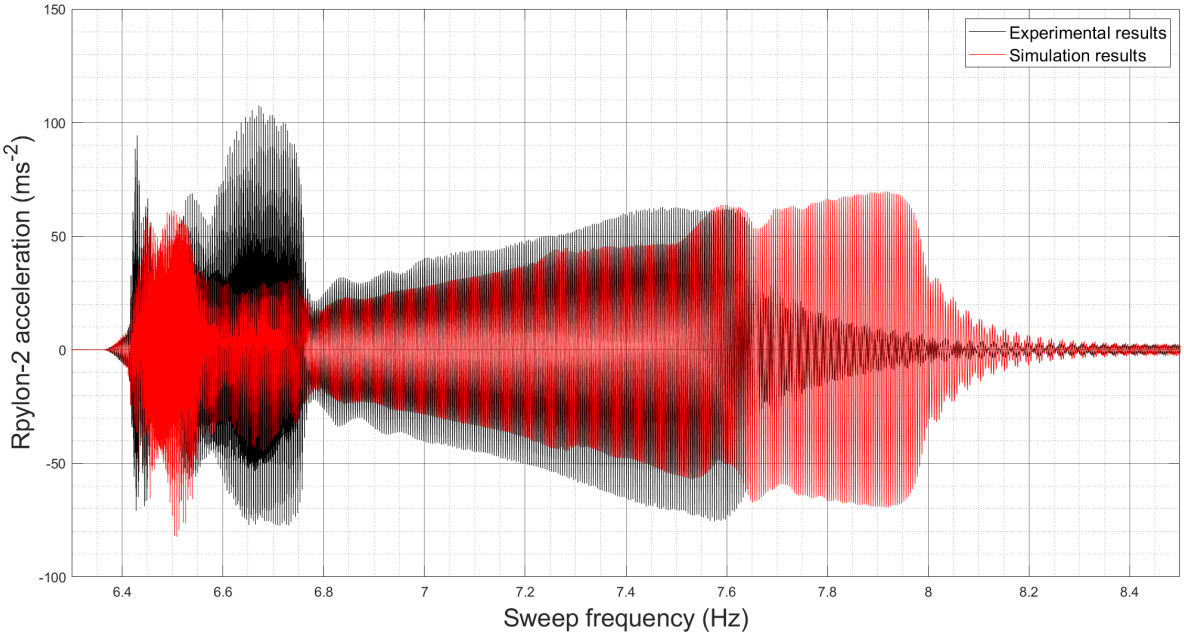


Figure 8.37: Simulated and experimental results for *RPylon:2* at *sweep1* with the excitation level of 0.08 V and with $\zeta_1 = 0.83\%$ and $\zeta_2 = 6.40\%$ using a cubic stiffness

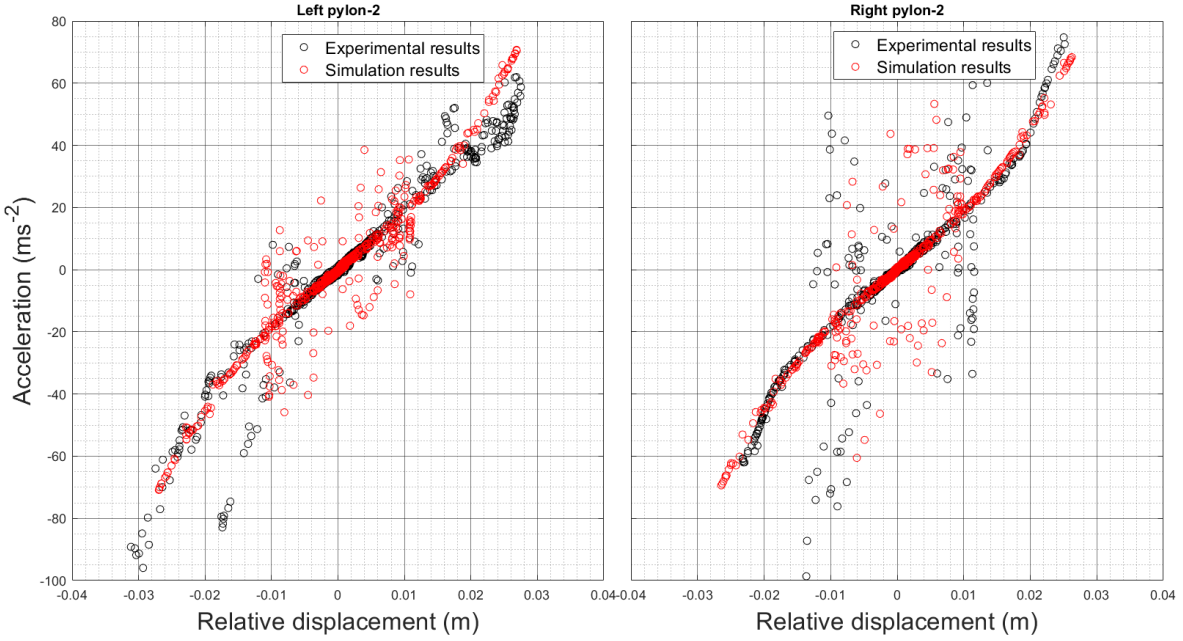


Figure 8.38: Simulated and experimental stiffness curves for *RPylon:2* and *LPylon:2* at *sweep1* with the excitation level of 0.08 V and with $\zeta_1 = 0.83\%$ and $\zeta_2 = 6.40\%$ using a cubic stiffness

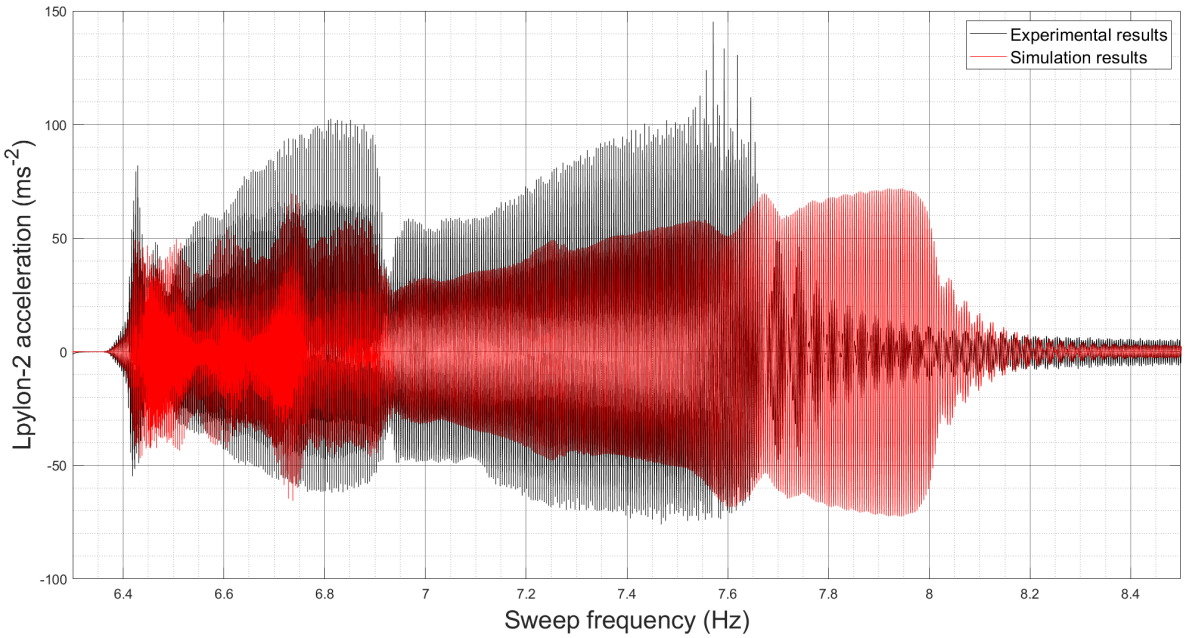


Figure 8.39: Simulated and experimental results for *LPylon:2* at *sweep1* with the excitation level of 0.09 V and with $\zeta_1 = 0.93\%$ and $\zeta_2 = 6.30\%$ using a cubic stiffness

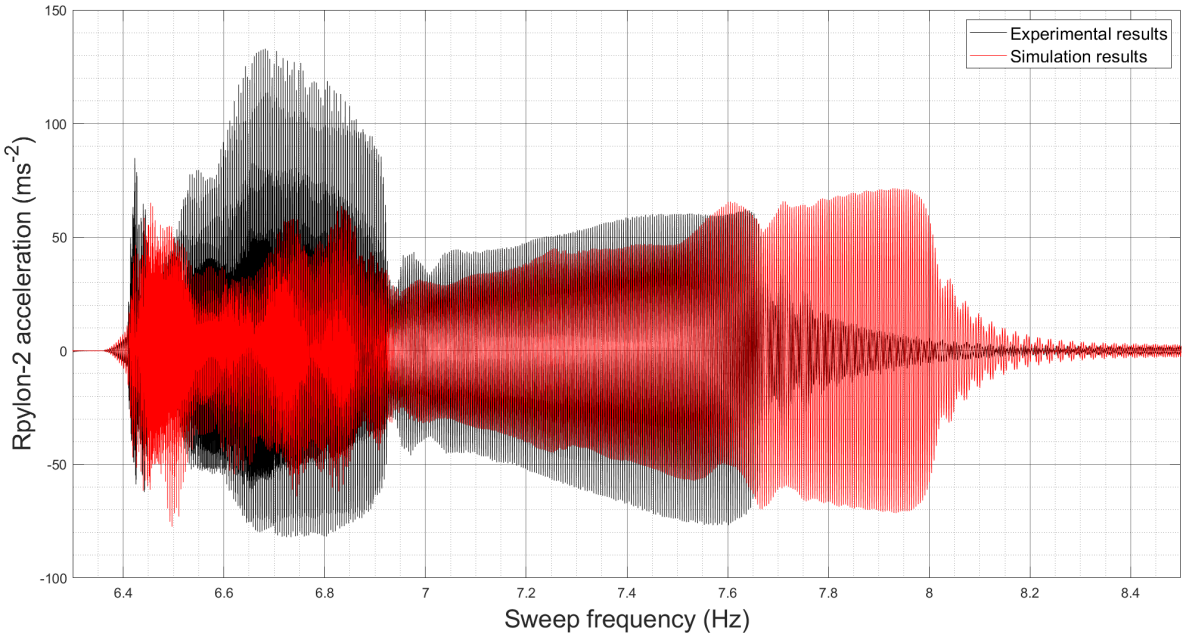


Figure 8.40: Simulated and experimental results for *RPylon:2* at *sweep1* with the excitation level of 0.09 V and with $\zeta_1 = 0.93\%$ and $\zeta_2 = 6.30\%$ using a cubic stiffness

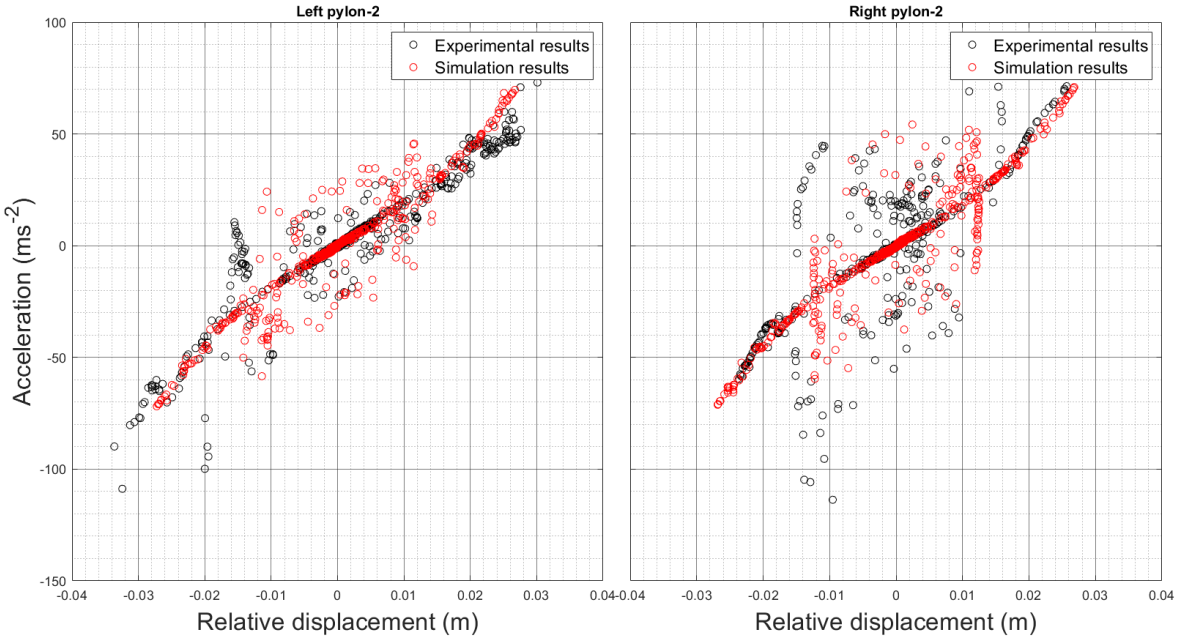


Figure 8.41: Simulated and experimental stiffness curves for *RPylon:2* and *LPylon:2* at *sweep1* with the excitation level of 0.09 V and with $\zeta_1 = 0.93\%$ and $\zeta_2 = 6.30\%$ using a cubic stiffness

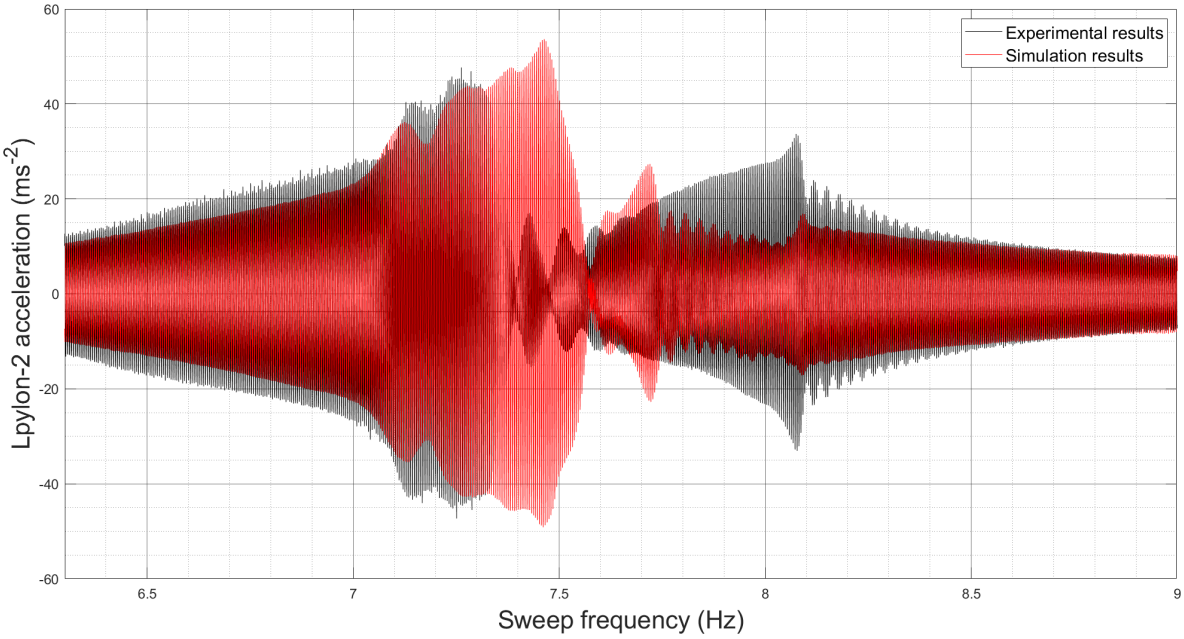


Figure 8.42: Simulated and experimental results for *LPylon:2* at *sweep2* with the excitation level of 0.04 V and with $\zeta_1 = 0.52\%$ and $\zeta_2 = 5.00\%$ using a cubic stiffness

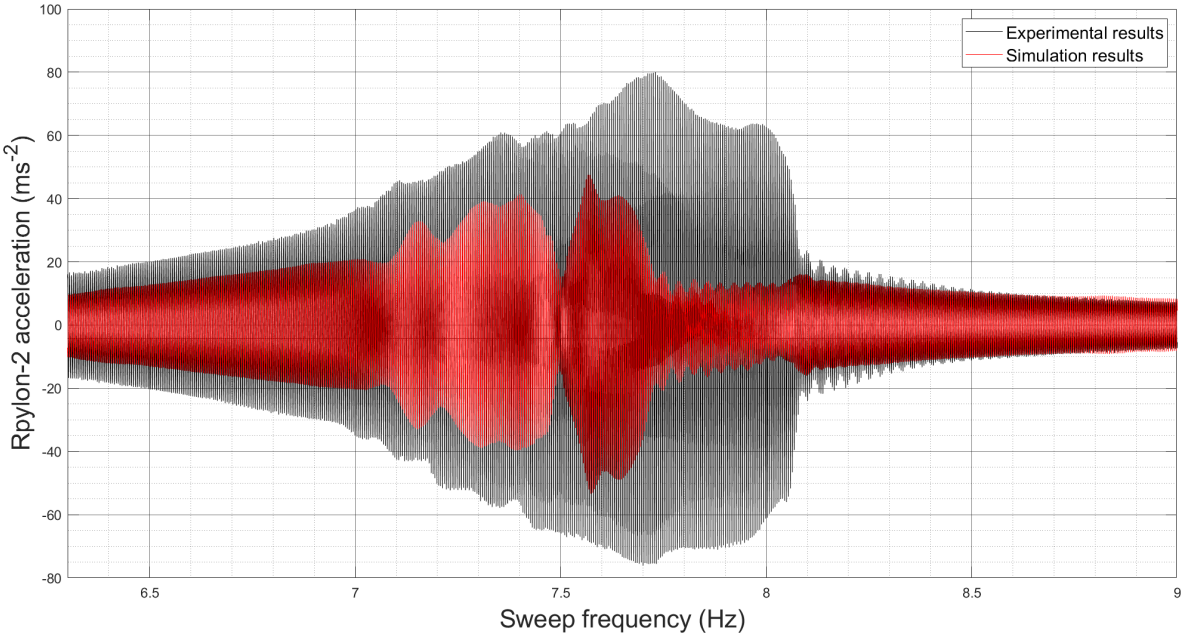


Figure 8.43: Simulated and experimental results for *RPylon:2* at *sweep2* with the excitation level of 0.04 V and with $\zeta_1 = 0.52\%$ and $\zeta_2 = 5.00\%$ using a cubic stiffness

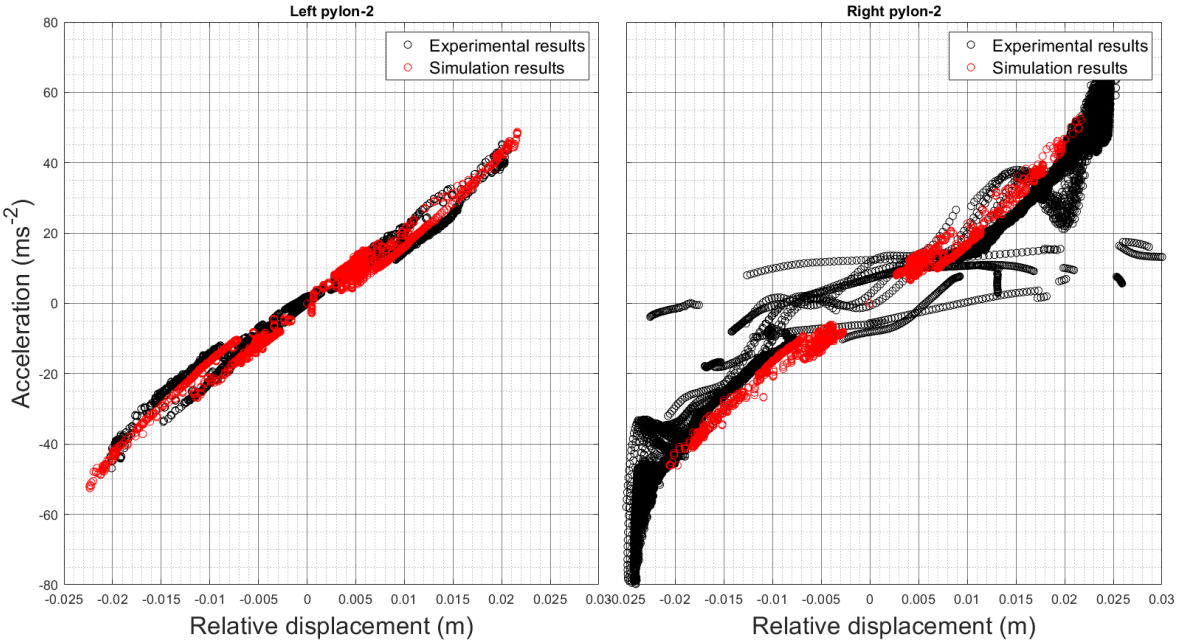


Figure 8.44: Simulated and experimental stiffness curves for *RPylon:2* and *LPylon:2* at *sweep2* with the excitation level of 0.04 V and with $\zeta_1 = 0.52\%$ and $\zeta_2 = 5.00\%$ using a cubic stiffness

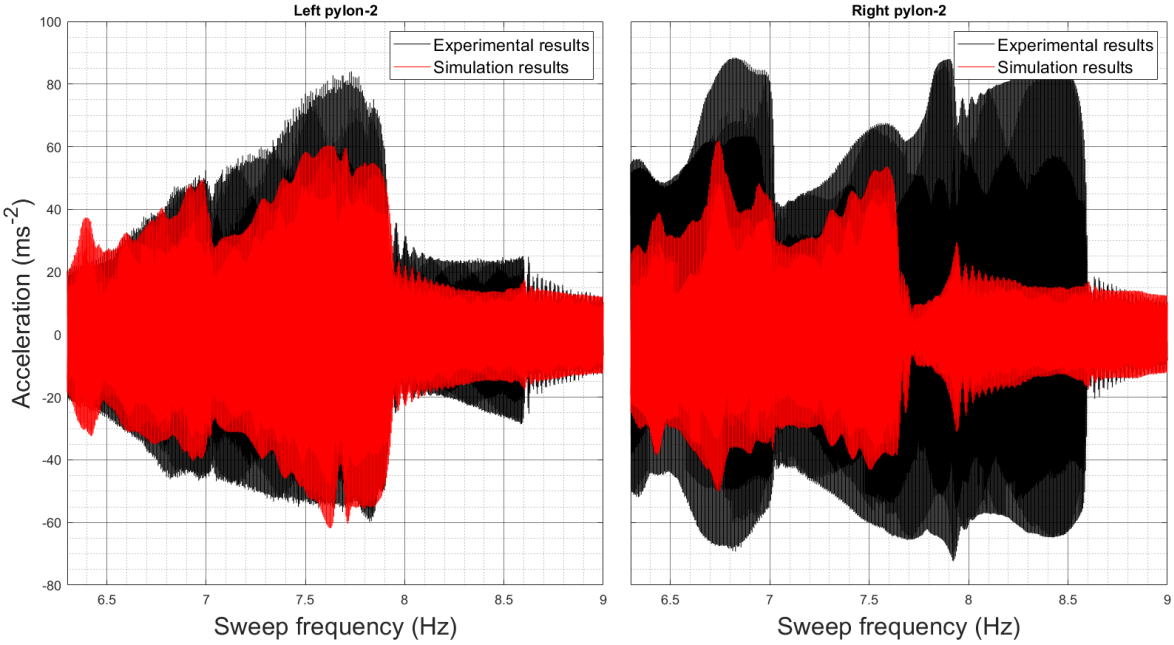


Figure 8.45: Simulated and experimental results for *LPylon:2* and *RPylon:2* at *sweep2* with the excitation level of 0.06 V and with $\zeta_1 = 0.73\%$ and $\zeta_2 = 7.00\%$ using a cubic stiffness

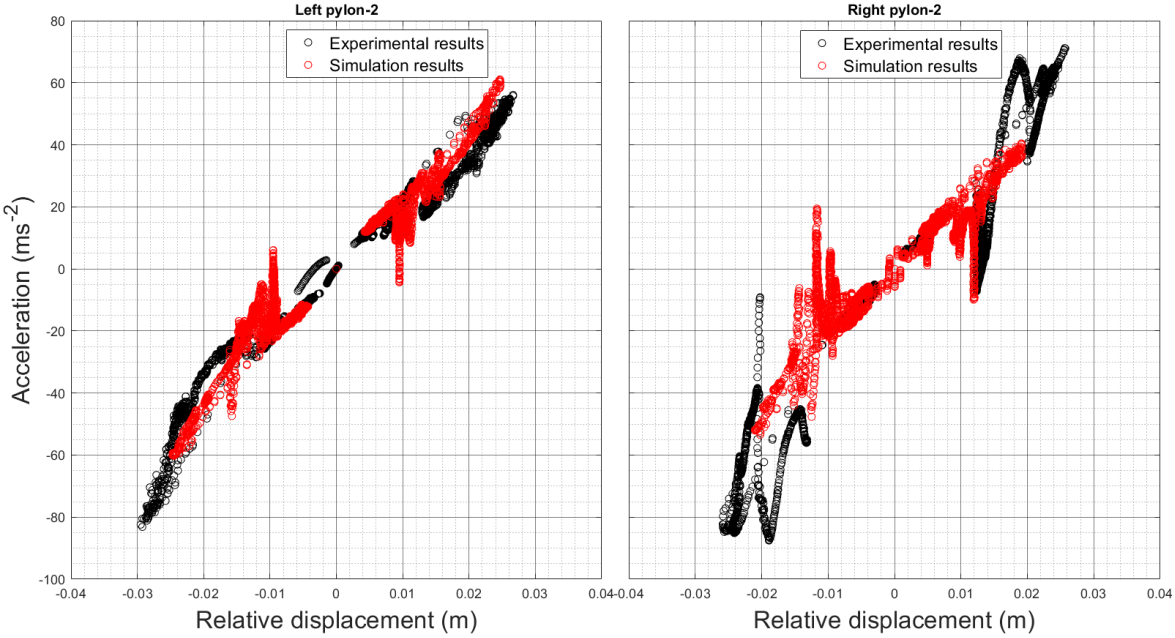


Figure 8.46: Simulated and experimental stiffness curves for *RPylon:2* and *LPylon:2* at *sweep2* with the excitation level of 0.06 V and with $\zeta_1 = 0.73\%$ and $\zeta_2 = 6.00\%$ using a cubic stiffness

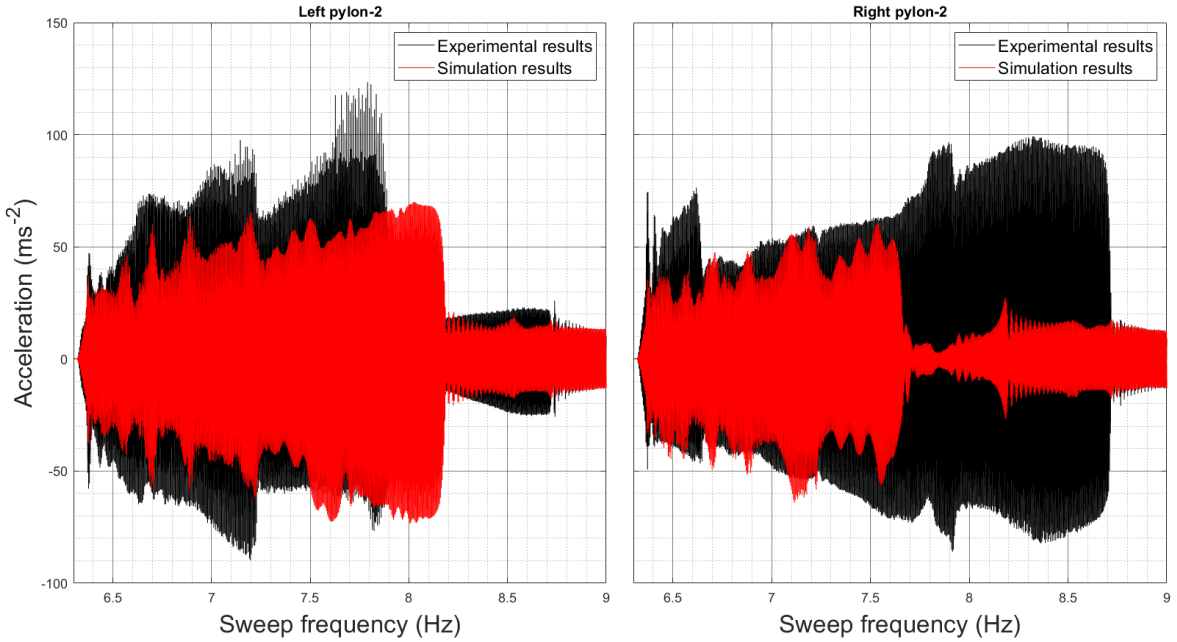


Figure 8.47: Simulated and experimental results for *LPylon:2* and *RPylon:2* at *sweep2* with the excitation level of 0.07 V and with $\zeta_1 = 0.73\%$ and $\zeta_2 = 6.00\%$ using a cubic stiffness

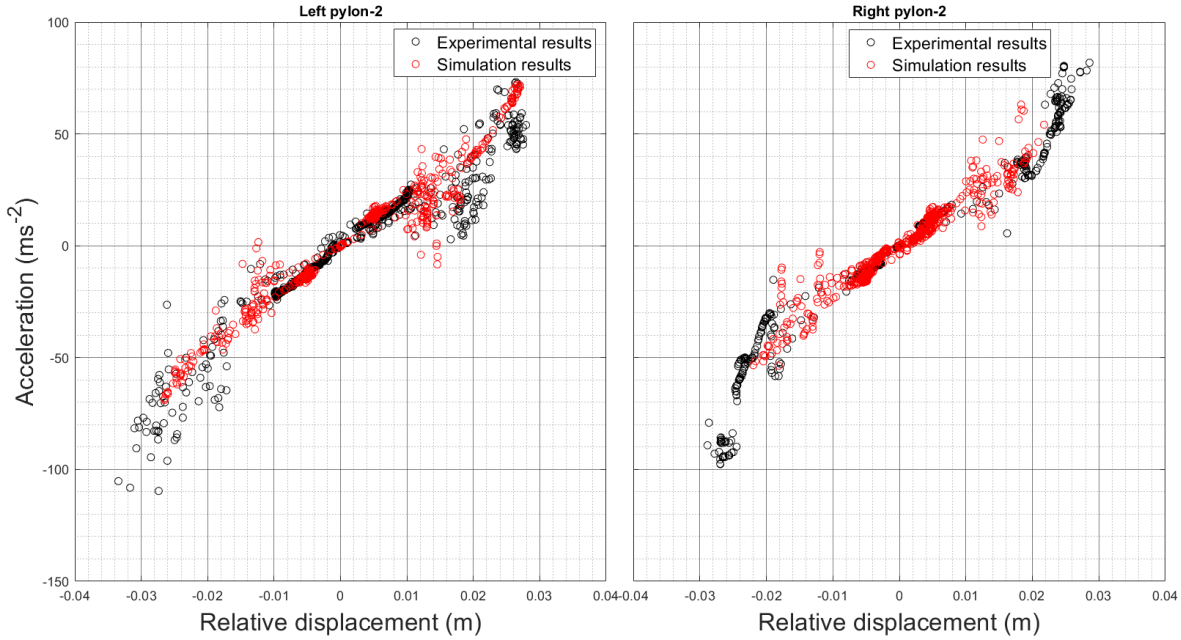


Figure 8.48: Simulated and experimental stiffness curves for *RPylon:2* and *LPylon:2* at *sweep2* with the excitation level of 0.07 V and with $\zeta_1 = 0.73\%$ and $\zeta_2 = 6.00\%$ using a cubic stiffness

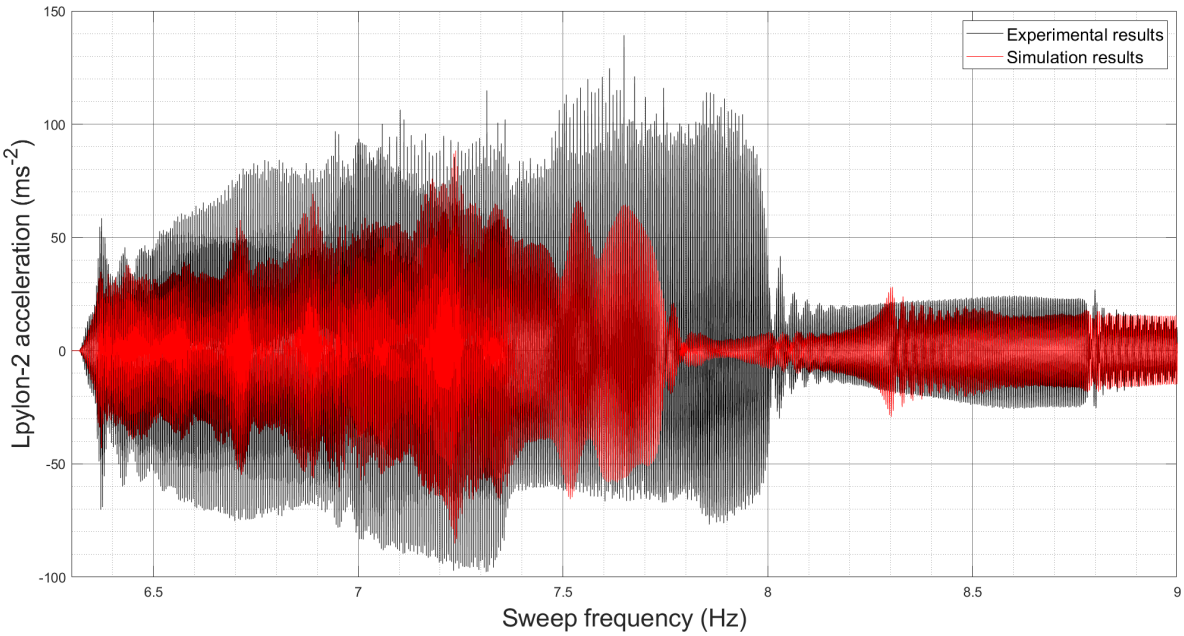


Figure 8.49: Simulated and experimental results for *LPylon:2* at *sweep2* with the excitation level of 0.08 V and with $\zeta_1 = 0.83\%$ and $\zeta_2 = 6.40\%$ using a cubic stiffness

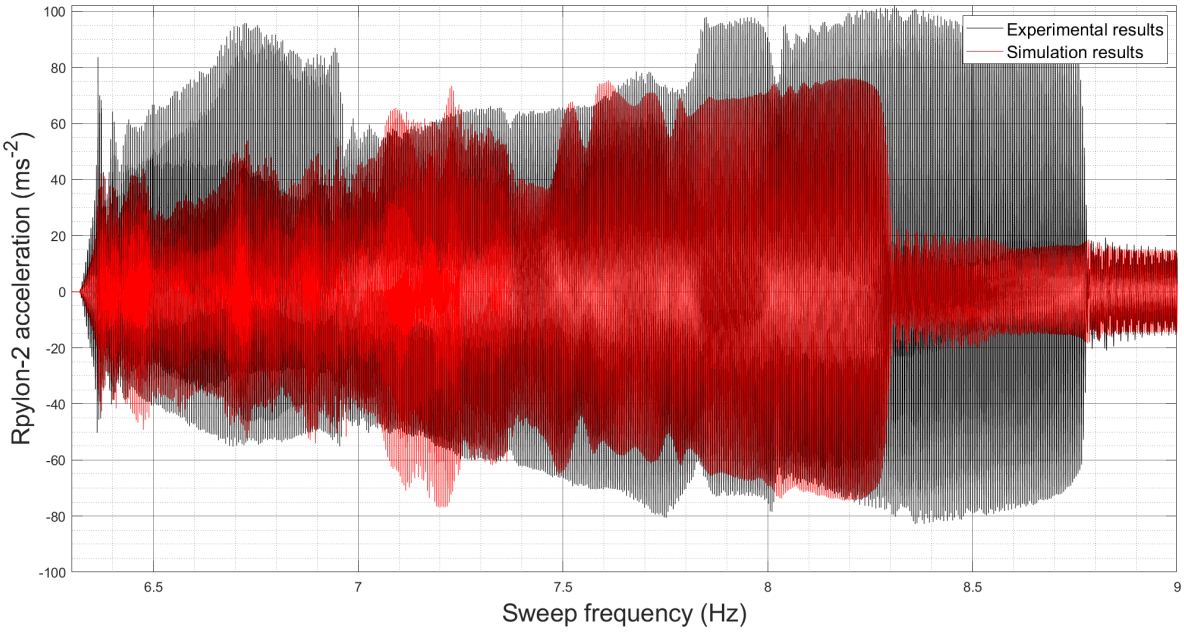


Figure 8.50: Simulated and experimental results for *RPylon:2* at *sweep2* with the excitation level of 0.08 V and with $\zeta_1 = 0.83\%$ and $\zeta_2 = 6.40\%$ using a cubic stiffness

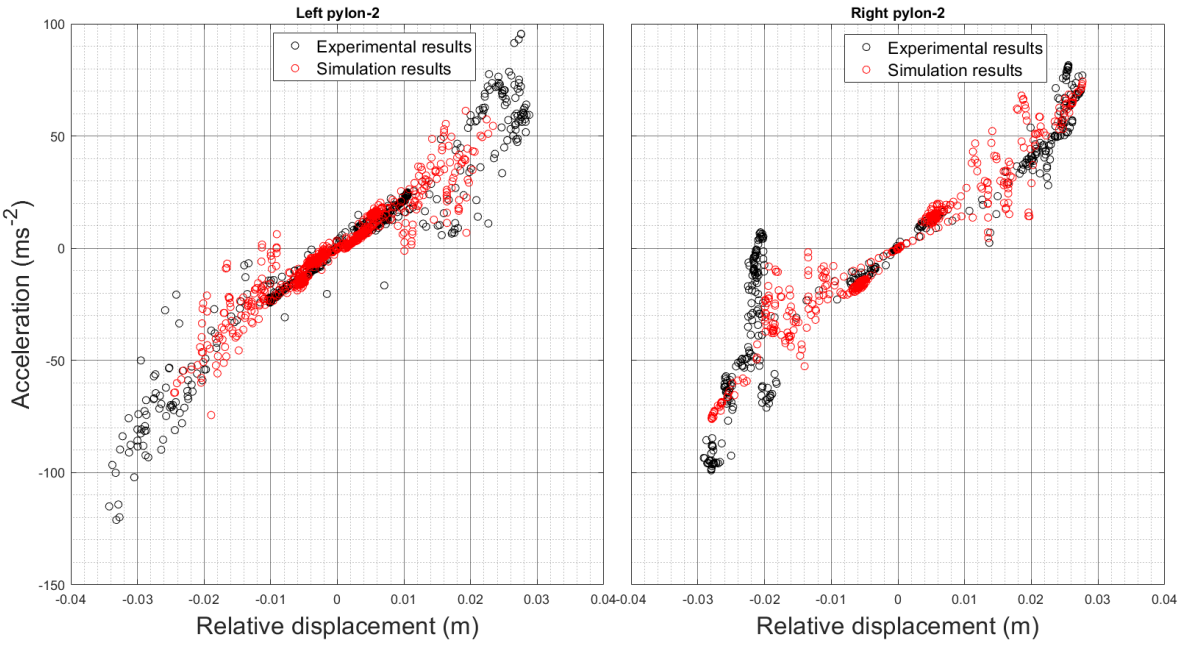


Figure 8.51: Simulated and experimental stiffness curves for *RPylon:2* and *LPylon:2* at *sweep2* with the excitation level of 0.08 V and with $\zeta_1 = 0.83\%$ and $\zeta_2 = 6.40\%$ using a cubic stiffness

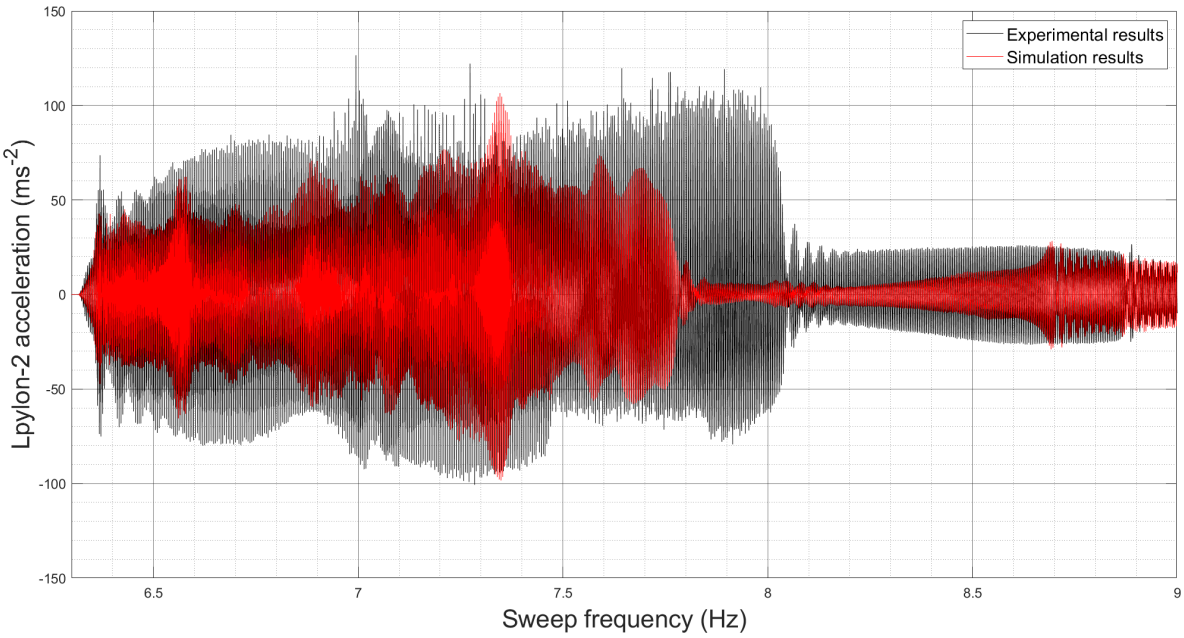


Figure 8.52: Simulated and experimental results for *LPylon:2* at *sweep2* with the excitation level of 0.09 V and with $\zeta_1 = 0.93\%$ and $\zeta_2 = 6.30\%$ using a cubic stiffness

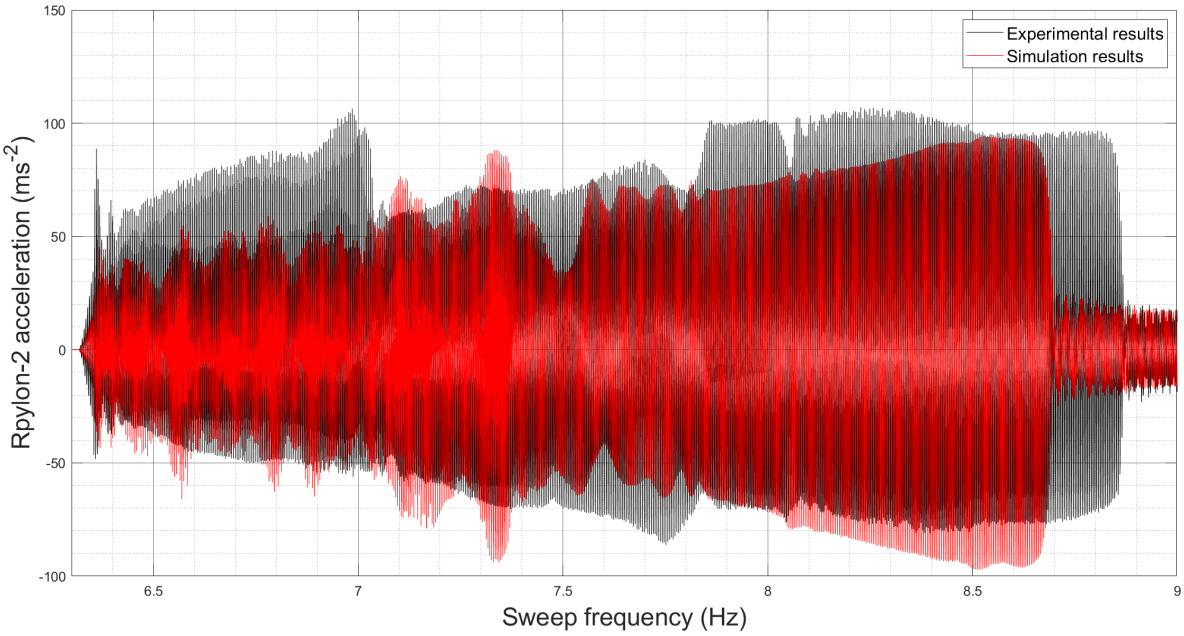


Figure 8.53: Simulated and experimental results for *RPylon:2* at *sweep2* with the excitation level of 0.09 V and with $\zeta_1 = 0.93\%$ and $\zeta_2 = 6.30\%$ using a cubic stiffness

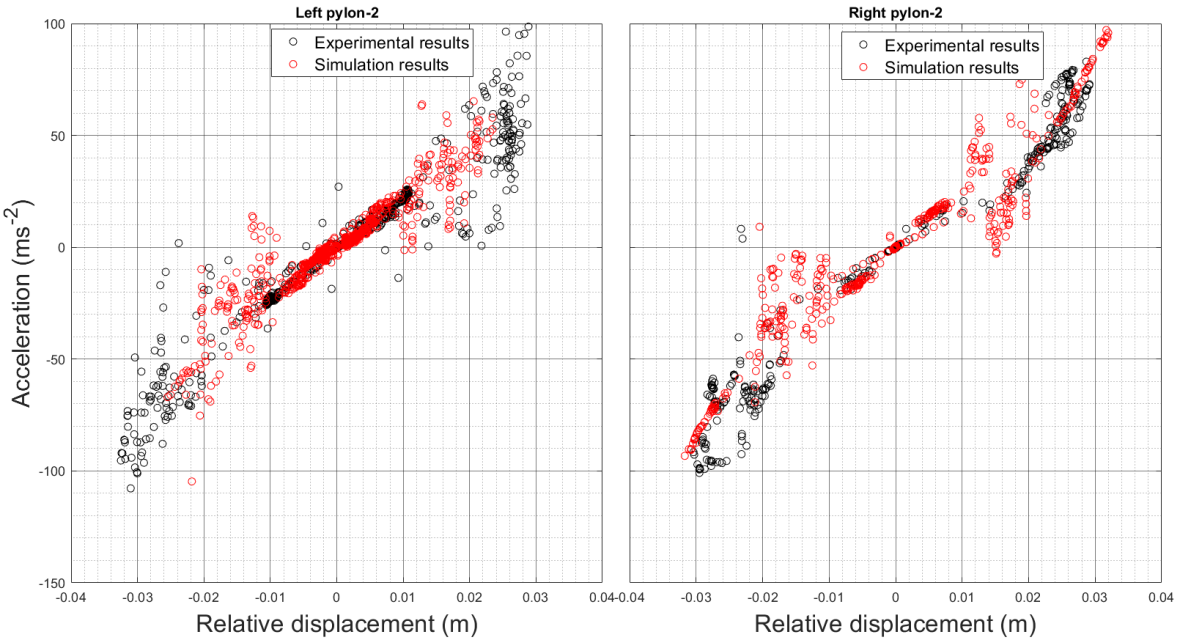


Figure 8.54: Simulated and experimental stiffness curves for *RPylon:2* and *LPylon:2* at *sweep2* with the excitation level of 0.09 V and with $\zeta_1 = 0.93\%$ and $\zeta_2 = 6.30\%$ using a cubic stiffness

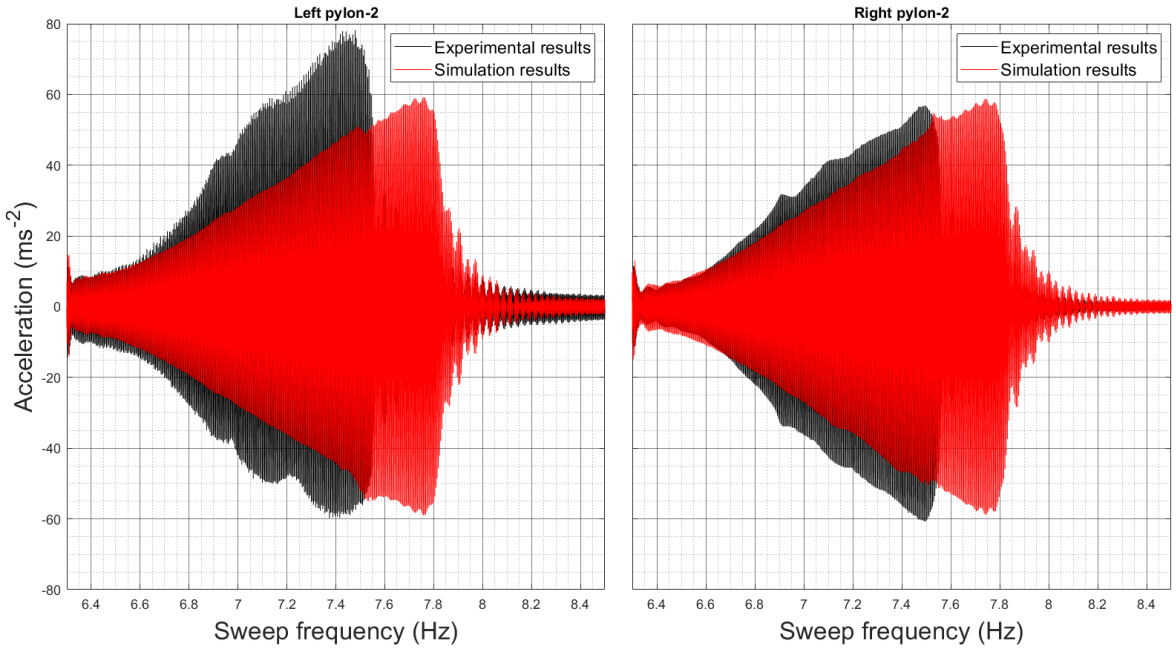


Figure 8.55: Simulated and experimental results for *LPylon:2 RPylon:2* at *sweep1* with the excitation level of 0.06 V and with $\zeta_1 = 0.73\%$ and $\zeta_2 = 0.73\%$ using a cubic stiffness

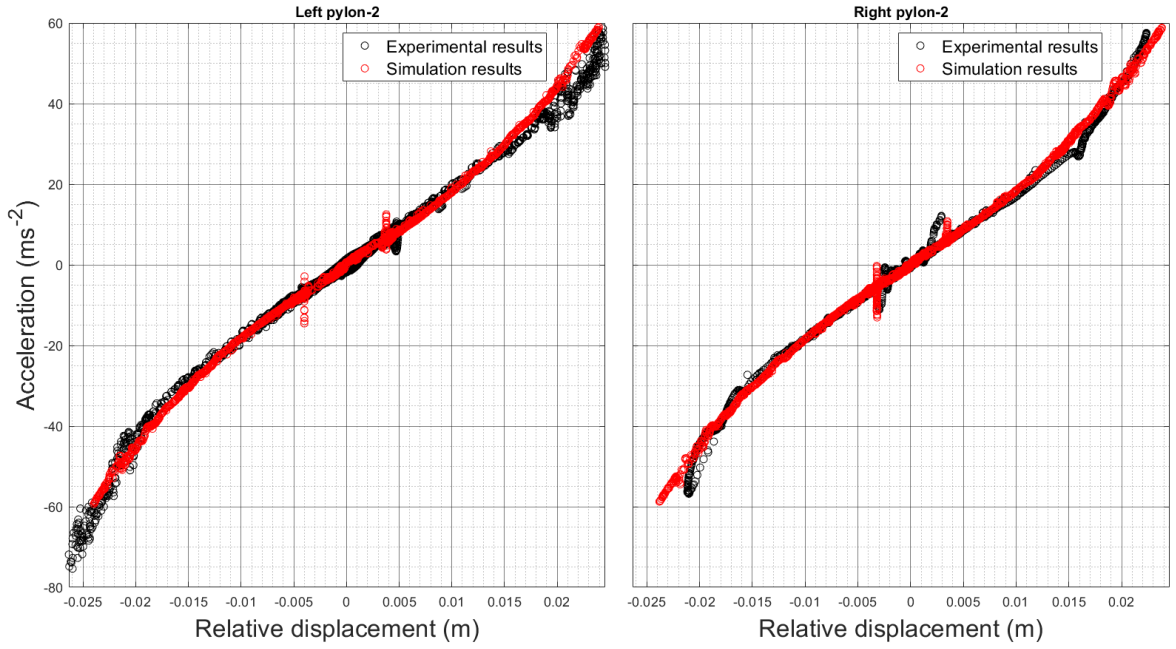


Figure 8.56: Simulated and experimental stiffness curves for *RPylon:2* and *LPylon:2* at *sweep1* with the excitation level of 0.06 V and with $\zeta_1 = 0.73\%$ and $\zeta_2 = 0.73\%$ using a cubic stiffness

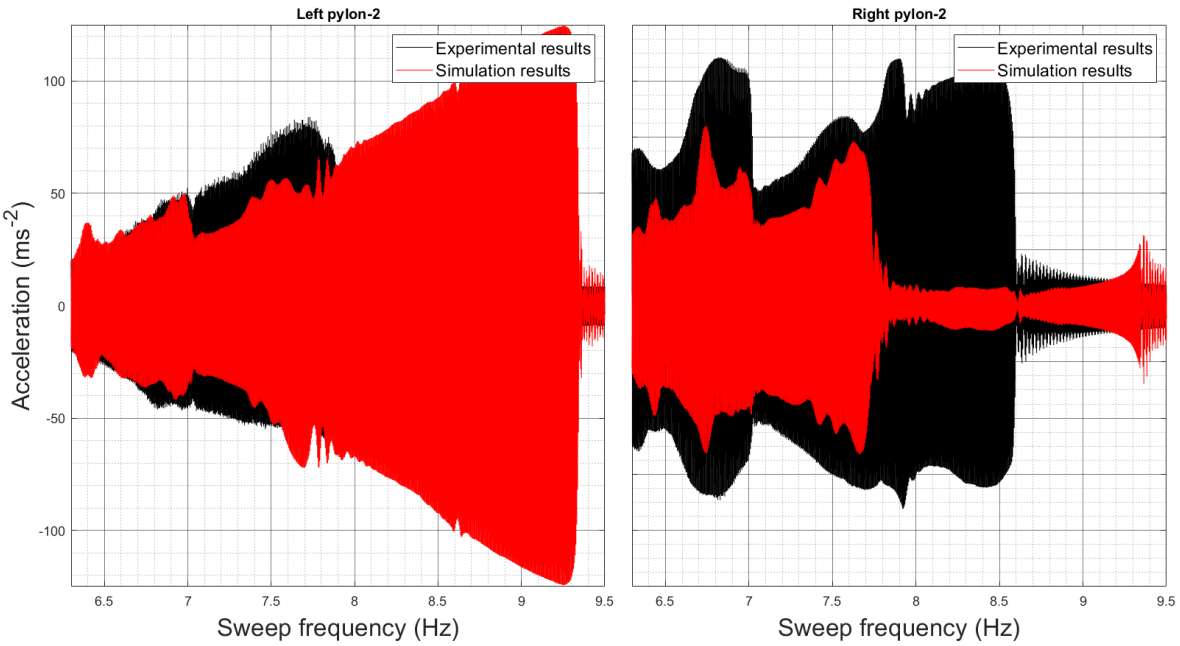


Figure 8.57: Simulated and experimental results for *LPylon:2 RPylon:2* at *sweep2* with the excitation level of 0.06 V and with $\zeta_1 = 0.73\%$ and $\zeta_2 = 4.00\%$ using a cubic stiffness

8.2.2 Polynomial stiffness

With the utilization of a polynomial function to describe the nonlinearity, for the lower excitations level no changes are expected, while for the nonlinear model changes may happen or not because the previous results were already quite good with the simulated stiffness curve approaching closely the experimental one, but at the same time a better curve fitting, even if the improvement is small, may generate better results, and most importantly the incorporation of new harmonics may allow the obtention of the asymmetric accelerations. From the different polynomial functions presented at table 7.4, the one that considers until the term of power 7^{th} will be considered, just for being the one containing more orders.

To confirm what was told about that the linear model, the results for *sweep1* at 0.02 V are presented in fig. 8.58 and 8.59, where no changes happened comparatively with the cubic model. The results for *sweep2* at 0.01 V are also presented at fig. 8.60 and 8.61 to show that the results remain bad and by last for 0.02 V, the results for *sweep2* are also presented at fig. 8.62 and 8.63, although the behaviour is already nonlinear, specially in the left pylon, like it was said in the first section. In the last two figures, comparatively with what was obtained with the cubic stiffness there are some changes, but the overall quality of the performance remains equal.

Before presenting the results it is important to indicate that it was necessary to change the damping values. Initially the first idea was obviously the utilization of the same damping values used with the cubic stiffness, because the damping values are properties of the system and they should not change for using a different way to describe the stiffness. But looking at fig. 8.64 and 8.65 for *sweep1* at 0.04 V, and comparing these plots with the ones obtained at fig. 8.27, 8.28 and 8.29, the point of having at least the "symmetric amplitude" equal at the simulated and experimental answers in the acceleration plot doesn't exist, and consequently there is also a decrease in the quality of the stiffness curves. So, after adjusting the damping

values the following results were obtained:

- 0.04 V - Fig. 8.66, 8.67 and 8.68 for *sweep1* and fig. 8.81, 8.82 and 8.83 for *sweep2* with $\zeta_1 = 0.46\%$ and $\zeta_2 = 4.50\%$;
- 0.06 V - Fig. 8.69, 8.70 and 8.71 for *sweep1* and fig. 8.84, 8.85 and 8.86 for *sweep2* with $\zeta_1 = 0.65\%$ and $\zeta_2 = 5.90\%$;
- 0.07 V - Fig. 8.72, 8.73 and 8.74 for *sweep1* and fig. 8.87 and 8.89 for *sweep2* with $\zeta_1 = 0.65\%$ and $\zeta_2 = 5.90\%$;
- 0.08 V - Fig. 8.75, 8.76 and 8.77 for *sweep1* and fig. 8.90, 8.91 and 8.92 for *sweep2* with $\zeta_1 = 0.75\%$ and $\zeta_2 = 6.90\%$;
- 0.09 V - Fig. 8.78, 8.79 and 8.80 for *sweep1* and fig. 8.93, 8.94 and 8.95 for *sweep2* with $\zeta_1 = 0.80\%$ and $\zeta_2 = 7.70\%$;

About the obtained results, firstly, it is important to point out the improvement at 0.04 V after adjusting the damping values, which confirms what was previously stated. Now, in terms of performance it can be said that for *sweep1* there is a very good performance because comparatively with previous results, it was possible to replicate the nonsymmetric oscillations around the equilibrium position, which proves that the behaviour is caused by a nonlinear phenomenon and not by physical defects on the pylon. The cause of that, was the incorporation of even and odd harmonics, which makes physically possible to have a nonsymmetric behaviour, and not the better curve fitting. But despite of that improvement there still exists that difference of amplitude in the acceleration answers between 6.8-7.6 Hz and the reason for why is that happening is the same that was indicated with the cubic stiffness, and the hypothesis of the existence of nonlinear damping remains applicable to this situation. Besides that, the first resonance around 6.7 Hz for tensions equal or higher than 0.08 V was also not possible to replicate, similarly to what happened with the cubic stiffness. A particular detail of these results is that at 0.06 V the "jump" frequency is higher than expected considering the evolution of the peak frequency with the applied force obtained experimentally and in the previous section when using a cubic stiffness. A last comment that must be done is about the used damping values, because although there still exists an evolution on mode 1 similar to what happened in the previous section, the damping value at 0.04 V is inferior to the one used in the linear model and for that, unfortunately, no explanation was found. It is true, when looking to fig. 8.26 that the curve associated to this voltage doesn't follow the "normal pattern" of the other curves, but it is not a valid justification, because it should be equal or higher than the linear one. On the other hand, the difference between the values is only of 0.02%. On mode 2, the damping increases always as it is suppose to be, unlike what happen with the cubic stiffness, where the damping at mode 2 for 0.09 V was lower than at 0.08 V.

About *sweep2* the overall results have improved, specially in terms of amplitude and frequency location of the "jumps", but the improvements were more significant at 0.06, 0.07 and 0.08 V, with special emphasis at 0.06 and 0.07 V. About the cause of these improvements it is difficult to find a reason, because although the incorporation of odd harmonics has allowed to have asymmetric oscillations, the obtained asymmetries are quite low when compared with the ones that are seen in the experimental results, and for that reason, maybe the cause can be the better fitting of the experimental stiffness curve, although the improvements on that parameter are low. To finalise, like it was proved in the previous sections the damping value in mode 2 is not making the mode 1 dominant at *sweep1*.

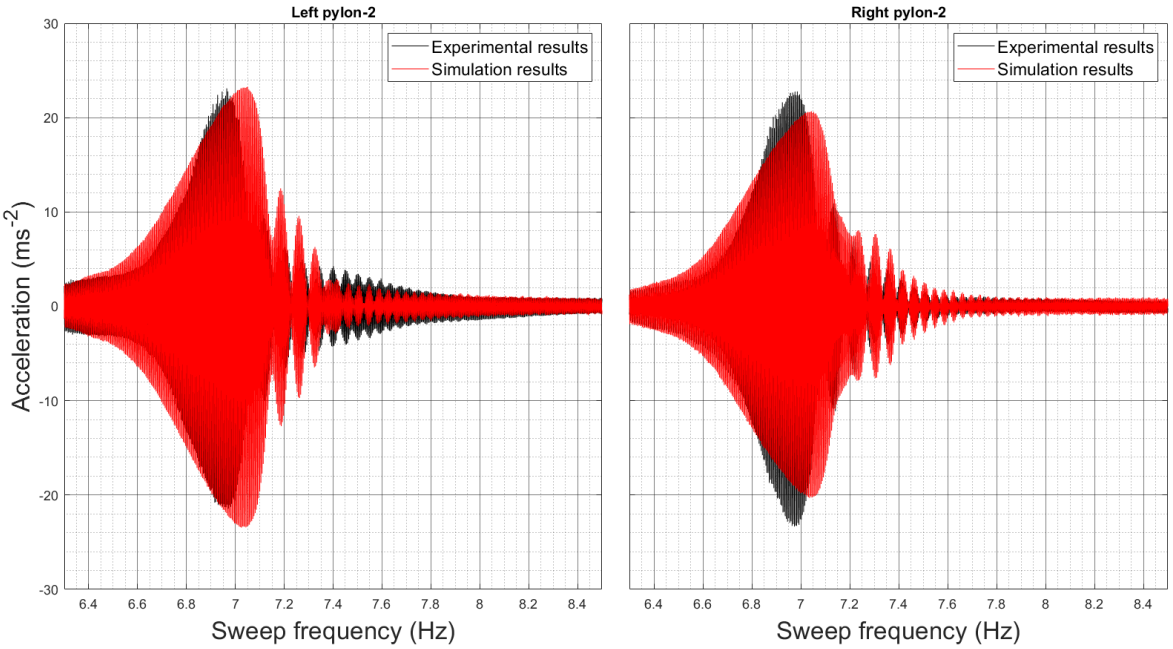


Figure 8.58: Simulated and experimental results for *LPylon:2* and *RPylon:2* at *sweep1* with the excitation level of 0.02 V and with $\zeta_1 = 0.50\%$ and $\zeta_2 = 1.30\%$ using a polynomial stiffness

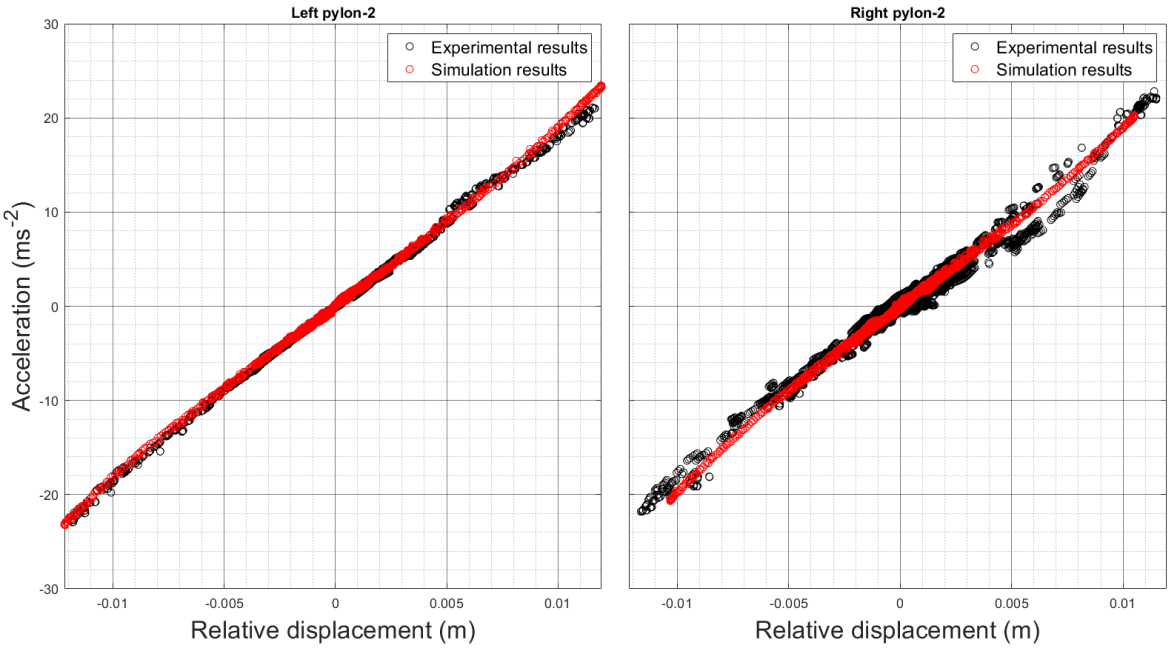


Figure 8.59: Simulated and experimental stiffness curves for *RPylon:2* and *LPylon:2* at *sweep1* with the excitation level of 0.02 V and with $\zeta_1 = 0.50\%$ and $\zeta_2 = 1.30\%$ using a polynomial stiffness

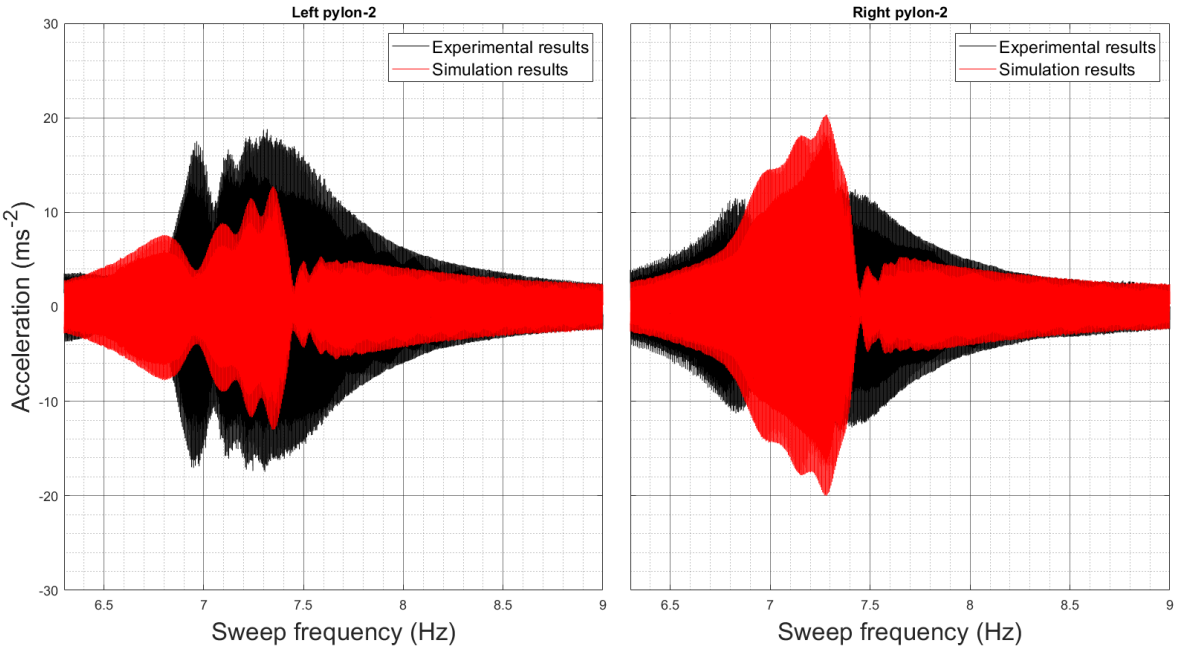


Figure 8.60: Simulated and experimental results for *LPylon:2* and *RPylon:2* at *sweep2* with the excitation level of 0.01 V and with $\zeta_1 = 0.50\%$ and $\zeta_2 = 1.30\%$ using a polynomial stiffness

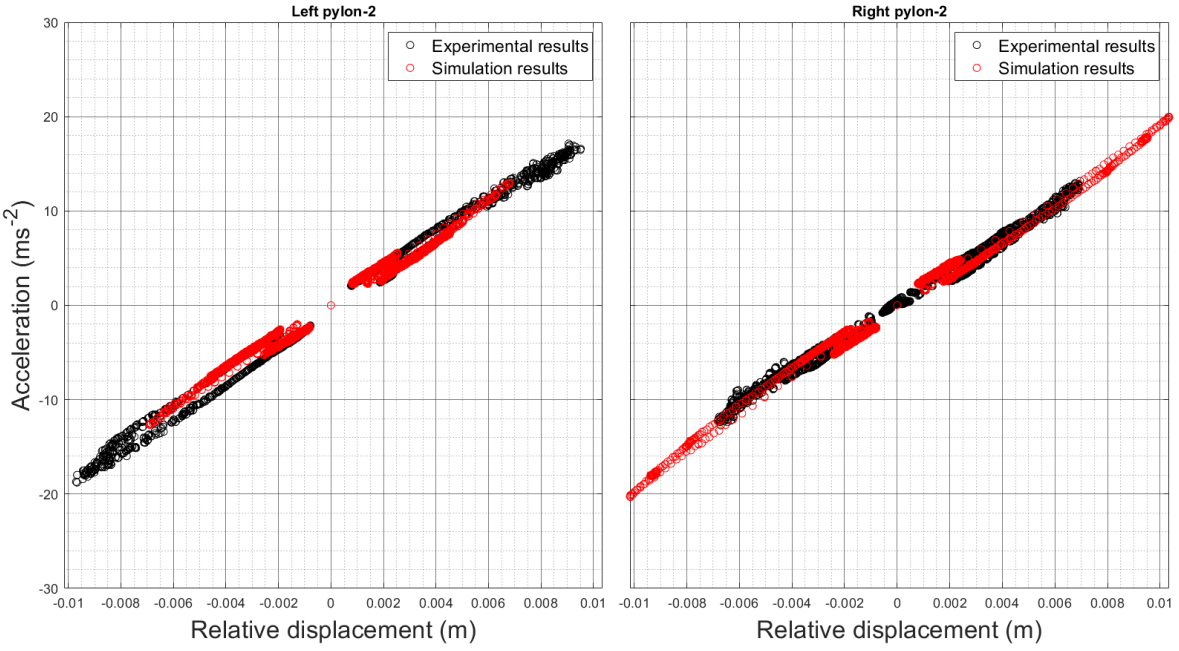


Figure 8.61: Simulated and experimental stiffness curves for *RPylon:2* and *LPylon:2* at *sweep2* with the excitation level of 0.01 V and with $\zeta_1 = 0.50\%$ and $\zeta_2 = 1.30\%$ using a polynomial stiffness

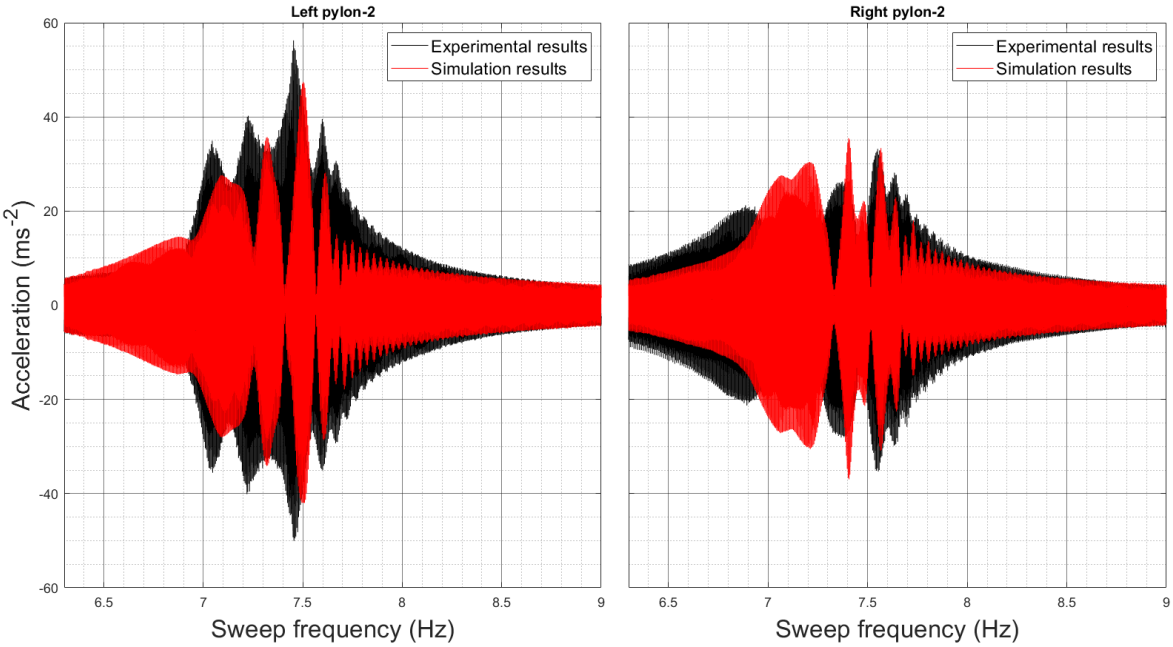


Figure 8.62: Simulated and experimental results for *LPylon:2* and *RPylon:2* at *sweep2* with the excitation level of 0.02 V and with $\zeta_1 = 0.50\%$ and $\zeta_2 = 1.30\%$ using a polynomial stiffness

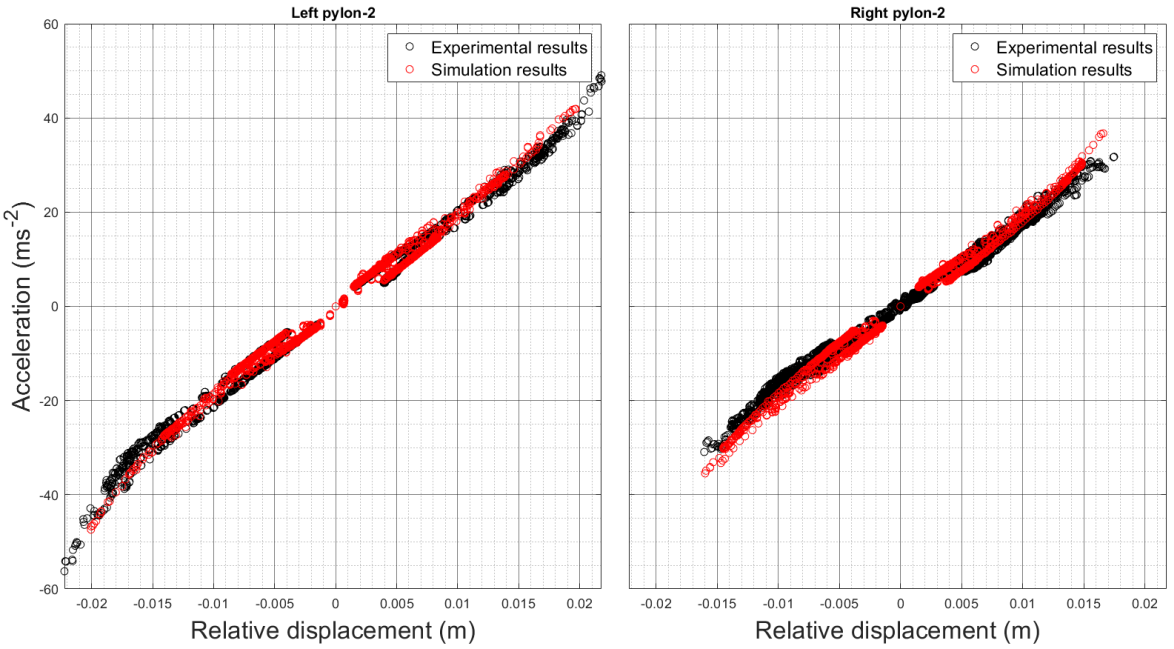


Figure 8.63: Simulated and experimental stiffness curves for *RPylon:2* and *LPylon:2* at *sweep2* with the excitation level of 0.02 V and with $\zeta_1 = 0.50\%$ and $\zeta_2 = 1.30\%$ using a polynomial stiffness

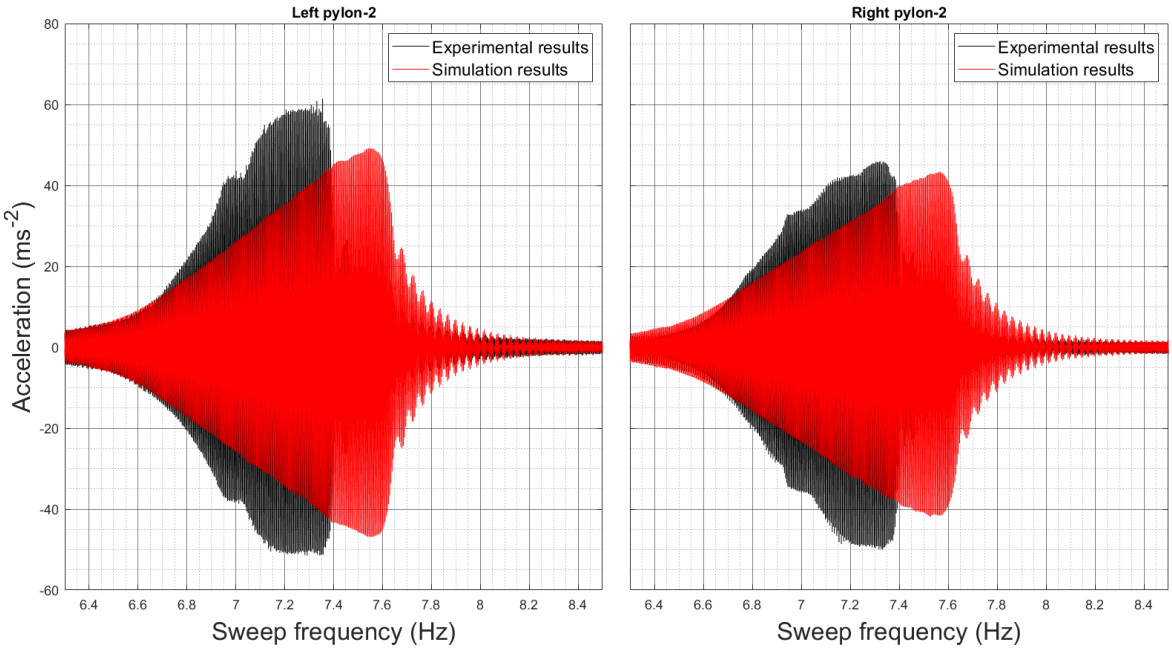


Figure 8.64: Simulated and experimental results for *LPylon:2* and *RPylon:2* at *sweep1* with the excitation level of 0.04 V and with $\zeta_1 = 0.52\%$ and $\zeta_2 = 5.00\%$ using a polynomial stiffness

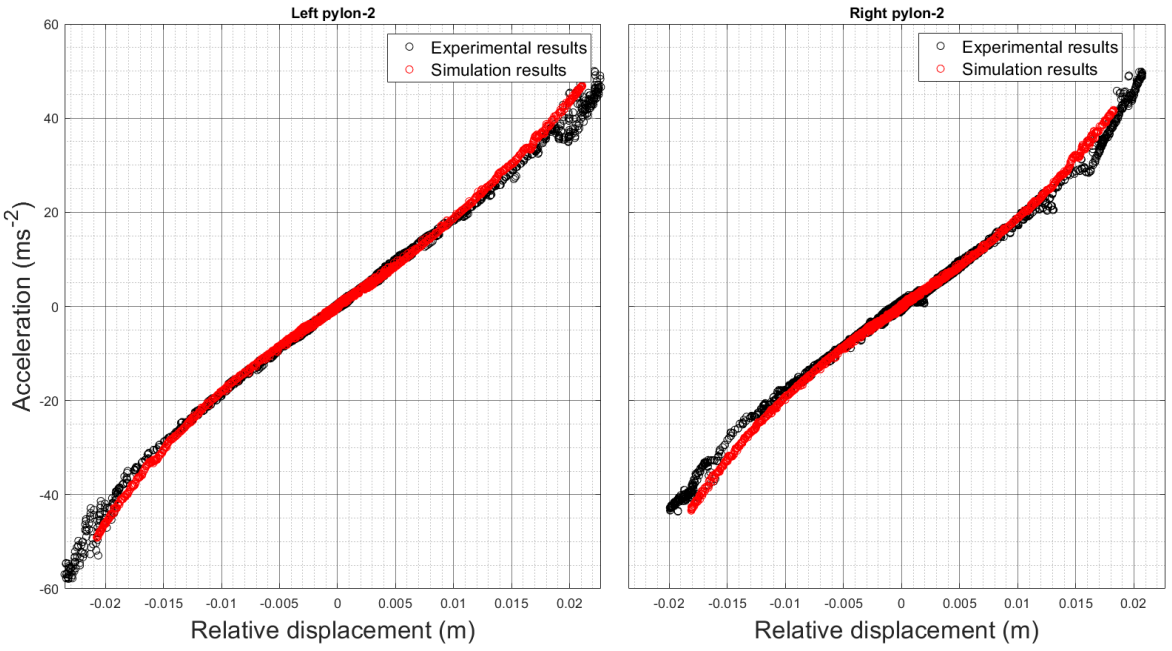


Figure 8.65: Simulated and experimental stiffness curves for *RPylon:2* and *LPylon:2* at *sweep1* with the excitation level of 0.04 V and with $\zeta_1 = 0.52\%$ and $\zeta_2 = 5.00\%$ using a polynomial stiffness

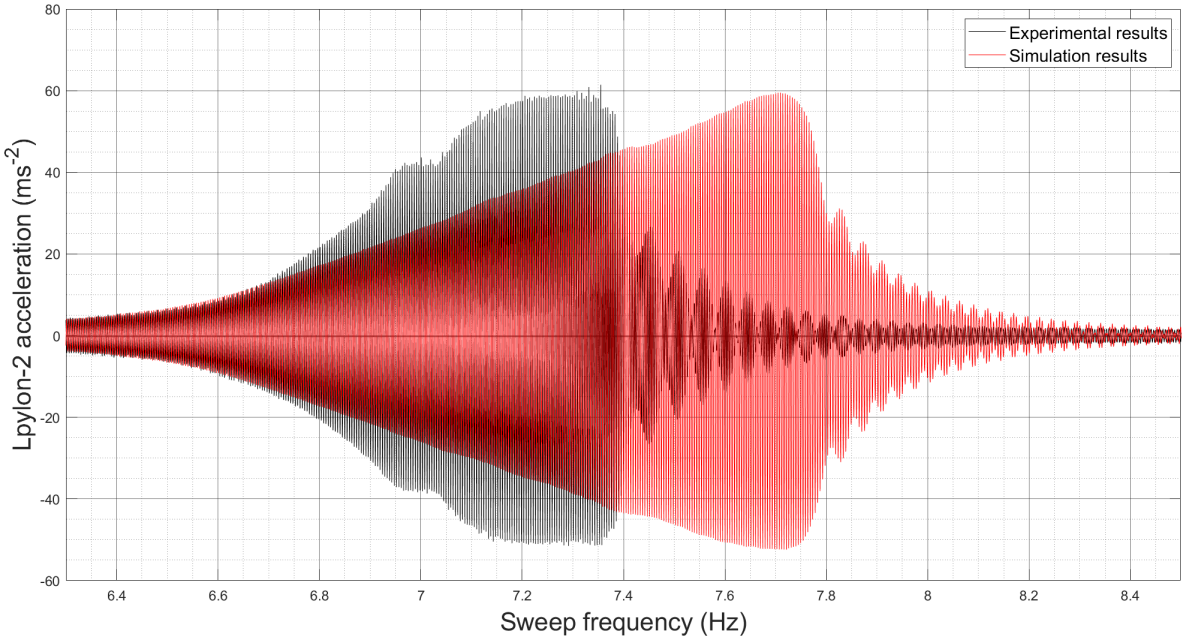


Figure 8.66: Simulated and experimental results for *LPylon:2* at *sweep1* with the excitation level of 0.04 V and with $\zeta_1 = 0.46\%$ and $\zeta_2 = 4.50\%$ using a polynomial stiffness

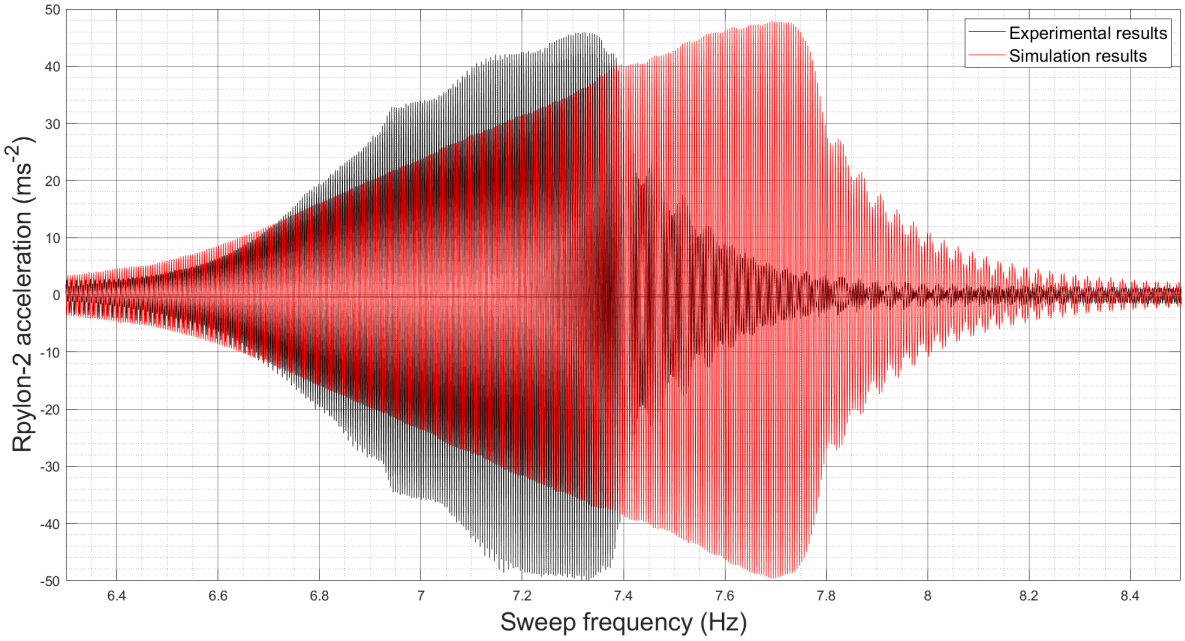


Figure 8.67: Simulated and experimental results for *RPylon:2* at *sweep1* with the excitation level of 0.04 V and with $\zeta_1 = 0.46\%$ and $\zeta_2 = 4.50\%$ using a polynomial stiffness

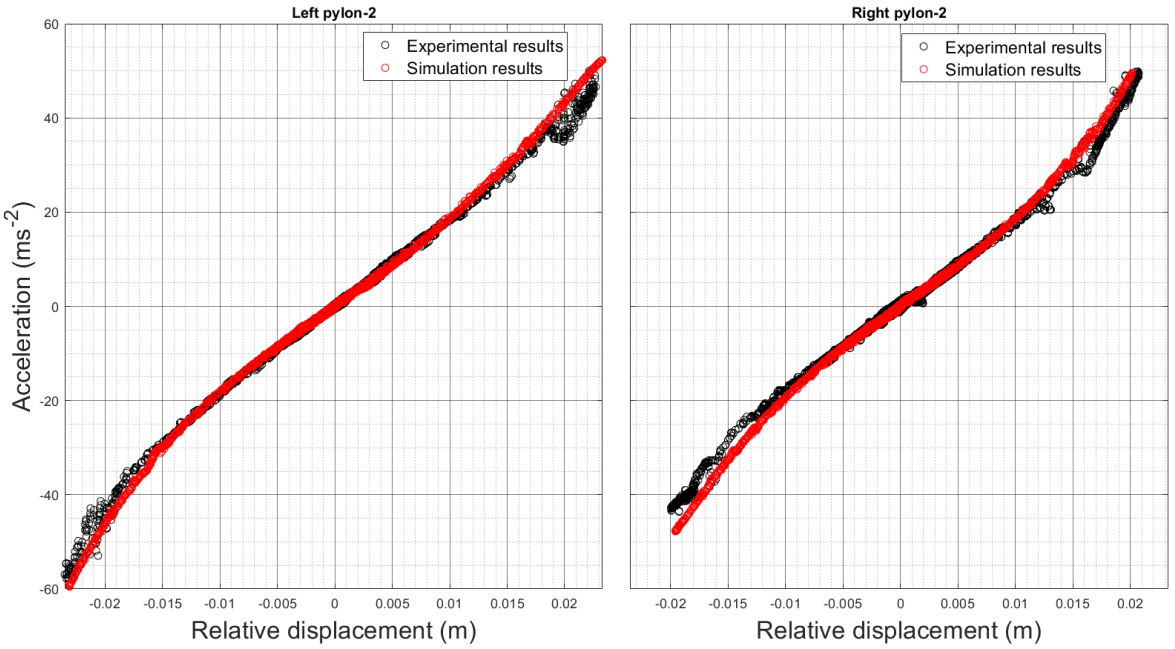


Figure 8.68: Simulated and experimental stiffness curves for *RPylon:2* and *LPylon:2* at *sweep1* with the excitation level of 0.04 V and with $\zeta_1 = 0.46\%$ and $\zeta_2 = 4.50\%$ using a polynomial stiffness

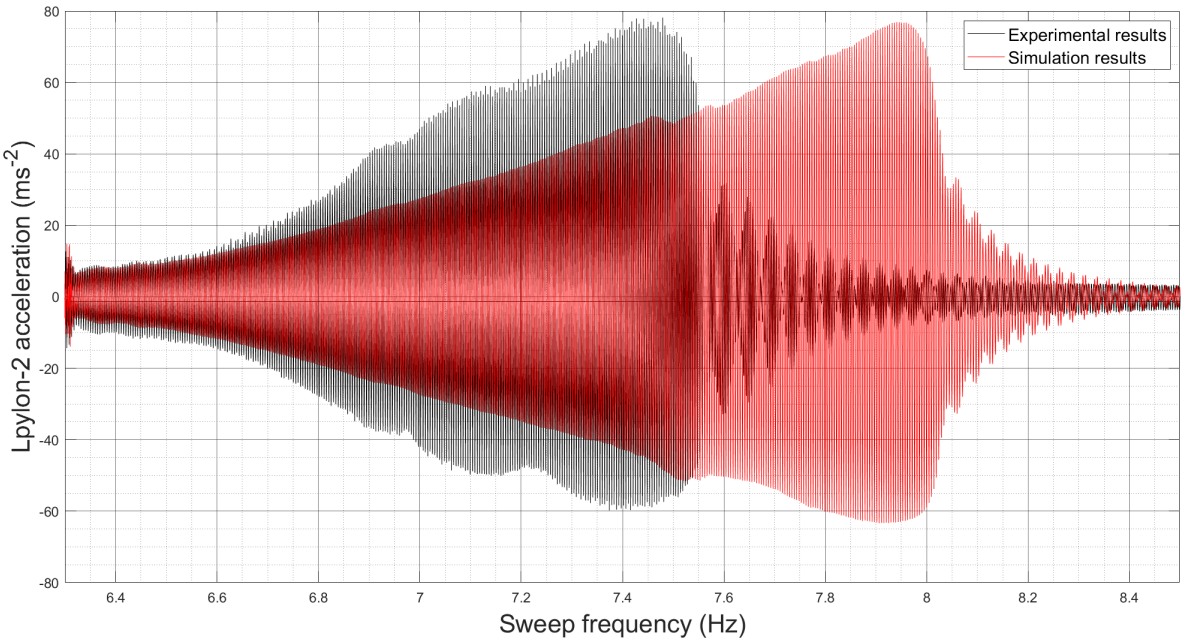


Figure 8.69: Simulated and experimental results for *LPylon:2* at *sweep1* with the excitation level of 0.06 V and with $\zeta_1 = 0.65\%$ and $\zeta_2 = 5.90\%$ using a polynomial stiffness

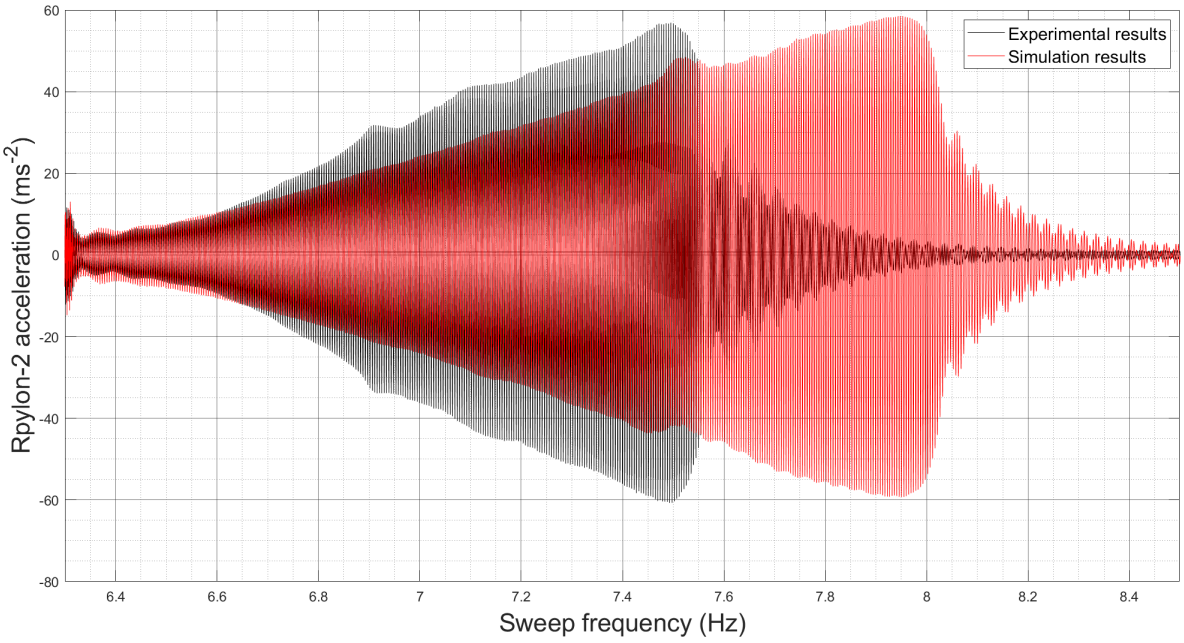


Figure 8.70: Simulated and experimental results for *RPylon:2* at *sweep1* with the excitation level of 0.06 V and with $\zeta_1 = 0.65\%$ and $\zeta_2 = 5.90\%$ using a polynomial stiffness

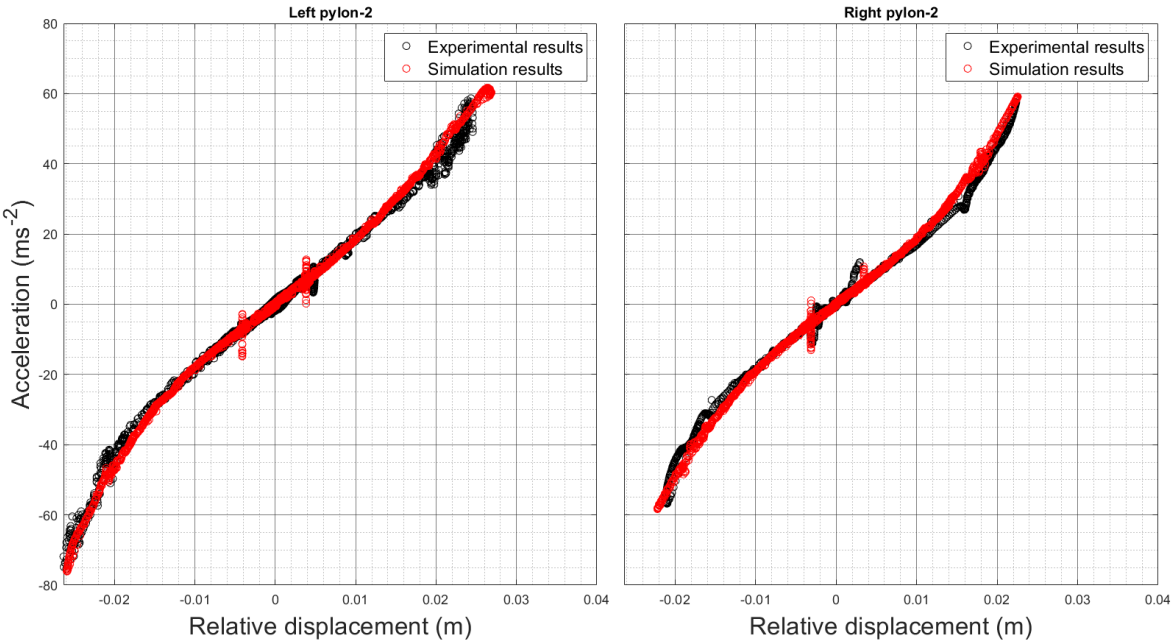


Figure 8.71: Simulated and experimental stiffness curves for *RPylon:2* and *LPylon:2* at *sweep1* with the excitation level of 0.06 V and with $\zeta_1 = 0.65\%$ and $\zeta_2 = 5.90\%$ using a polynomial stiffness

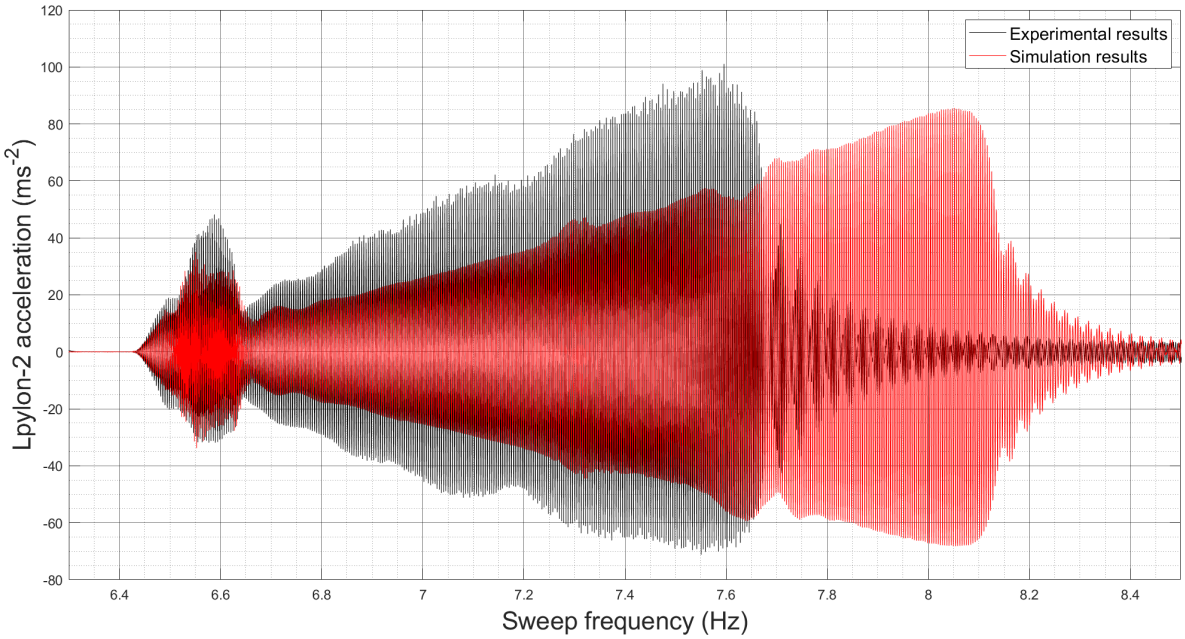


Figure 8.72: Simulated and experimental results for *LPylon:2* at *sweep1* with the excitation level of 0.07 V and with $\zeta_1 = 0.65\%$ and $\zeta_2 = 5.90\%$ using a polynomial stiffness

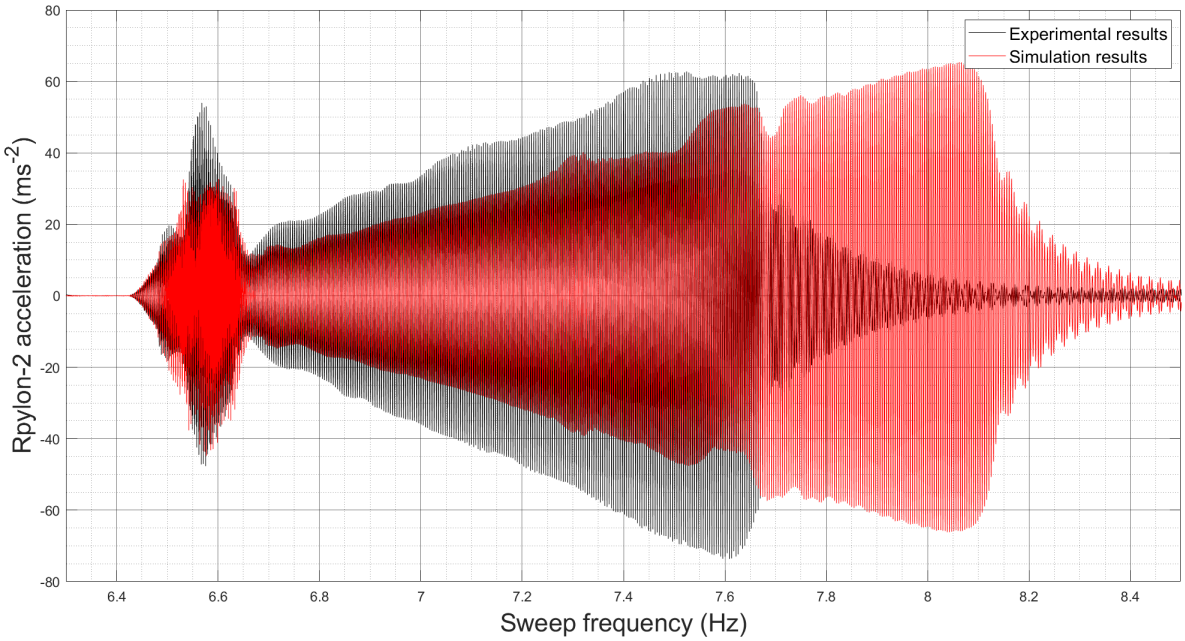


Figure 8.73: Simulated and experimental results for *RPylon:2* at *sweep1* with the excitation level of 0.07 V and with $\zeta_1 = 0.65\%$ and $\zeta_2 = 5.90\%$ using a polynomial stiffness

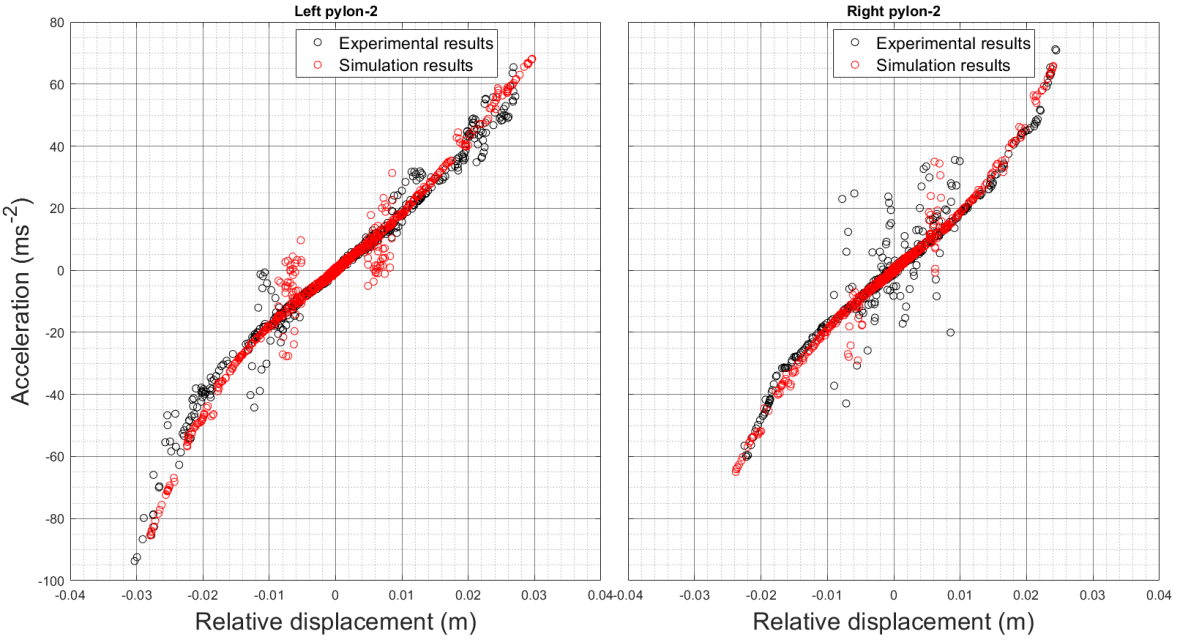


Figure 8.74: Simulated and experimental stiffness curves for *RPylon:2* and *LPylon:2* at *sweep1* with the excitation level of 0.07 V and with $\zeta_1 = 0.65\%$ and $\zeta_2 = 5.90\%$ using a polynomial stiffness

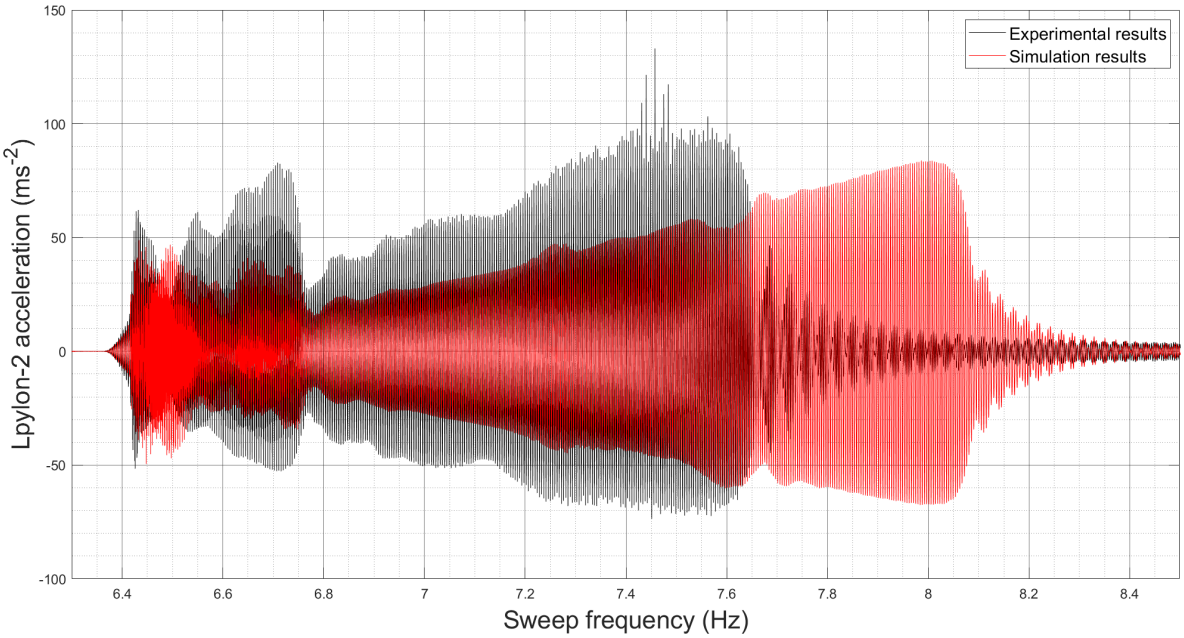


Figure 8.75: Simulated and experimental results for *LPylon:2* at *sweep1* with the excitation level of 0.08 V and with $\zeta_1 = 0.75\%$ and $\zeta_2 = 6.90\%$ using a polynomial stiffness

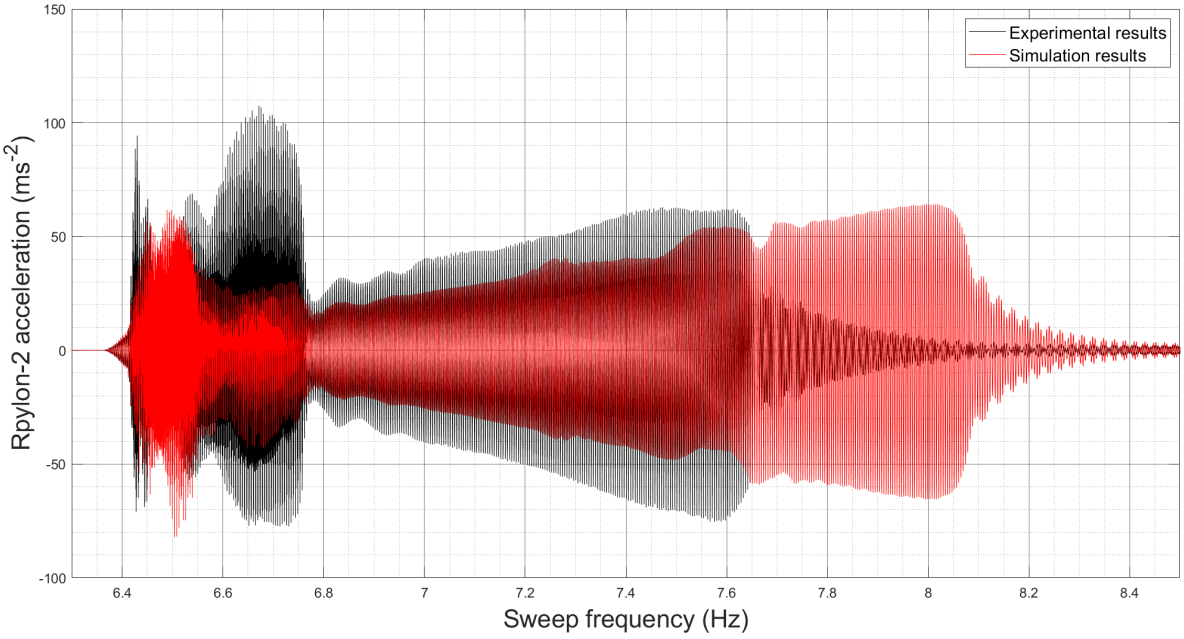


Figure 8.76: Simulated and experimental results for *RPylon:2* at *sweep1* with the excitation level of 0.08 V and with $\zeta_1 = 0.75\%$ and $\zeta_2 = 6.90\%$ using a polynomial stiffness

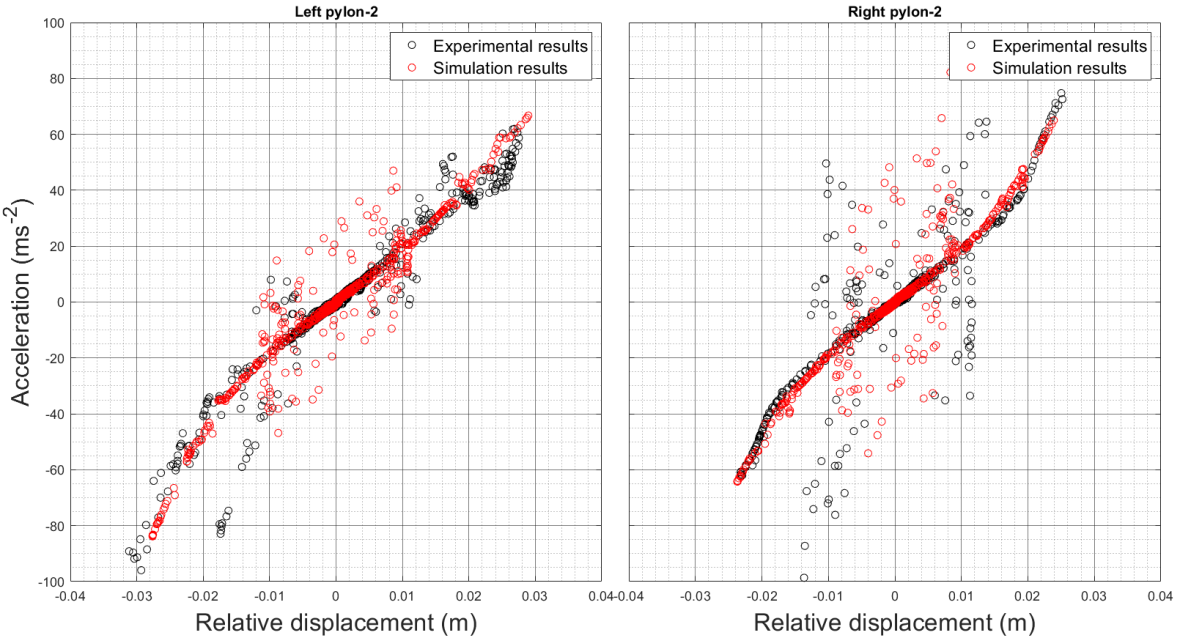


Figure 8.77: Simulated and experimental stiffness curves for *RPylon:2* and *LPylon:2* at *sweep1* with the excitation level of 0.08 V and with $\zeta_1 = 0.75\%$ and $\zeta_2 = 6.90\%$ using a polynomial stiffness

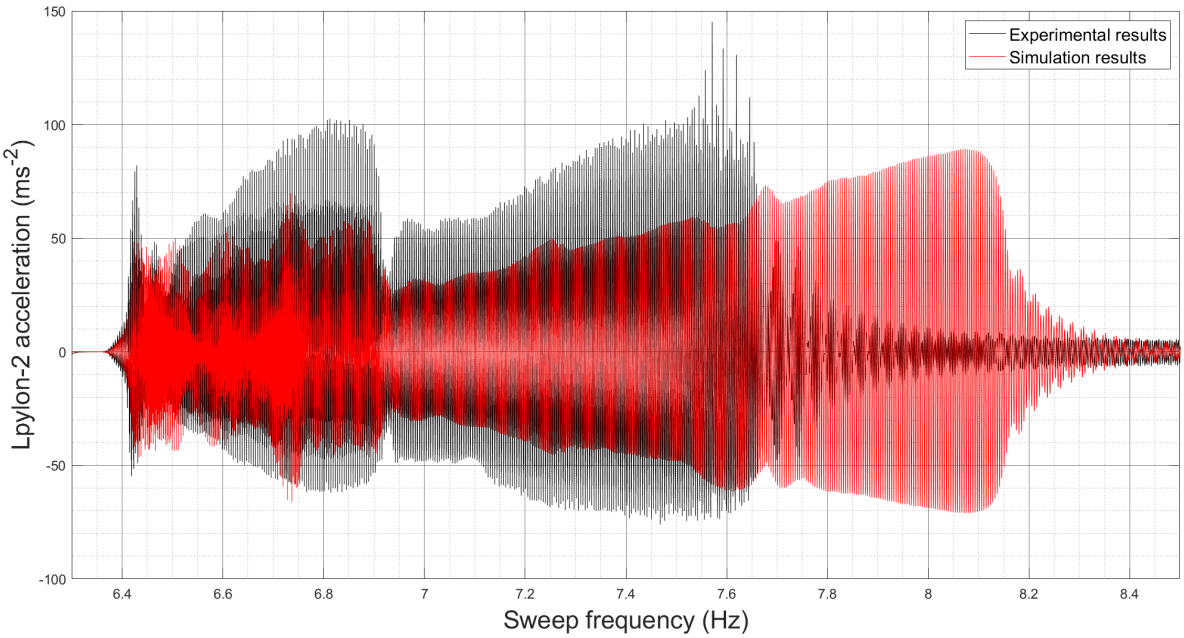


Figure 8.78: Simulated and experimental results for *LPylon:2* at *sweep1* with the excitation level of 0.09 V and with $\zeta_1 = 0.80\%$ and $\zeta_2 = 7.70\%$ using a polynomial stiffness

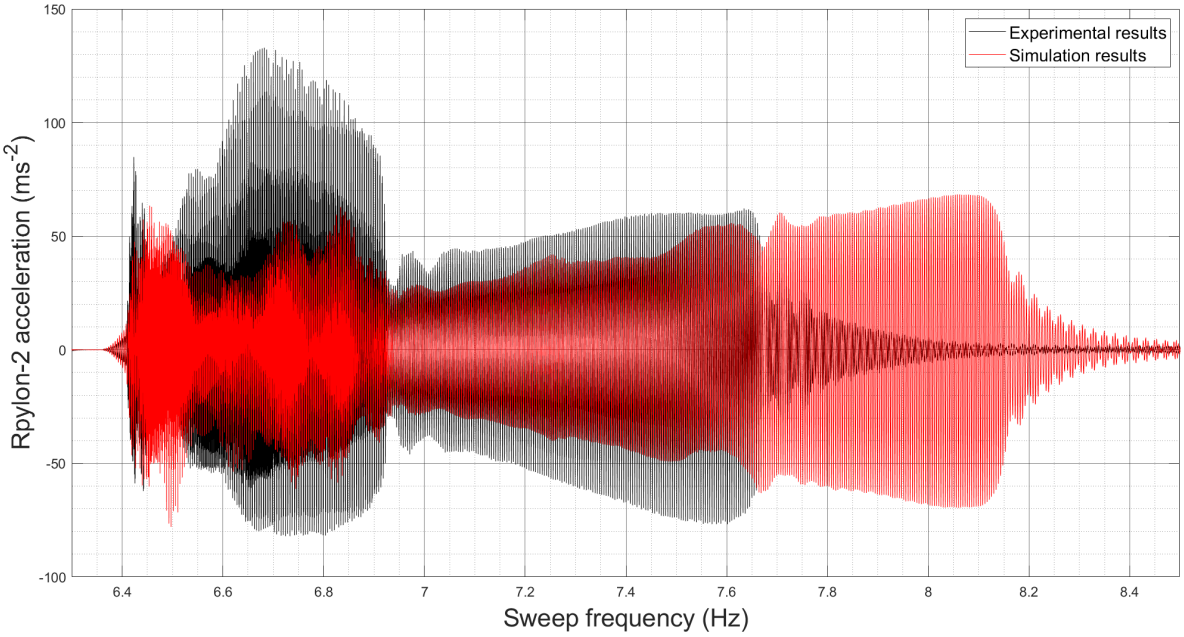


Figure 8.79: Simulated and experimental results for *RPylon:2* at *sweep1* with the excitation level of 0.09 V and with $\zeta_1 = 0.80\%$ and $\zeta_2 = 7.70\%$ using a polynomial stiffness

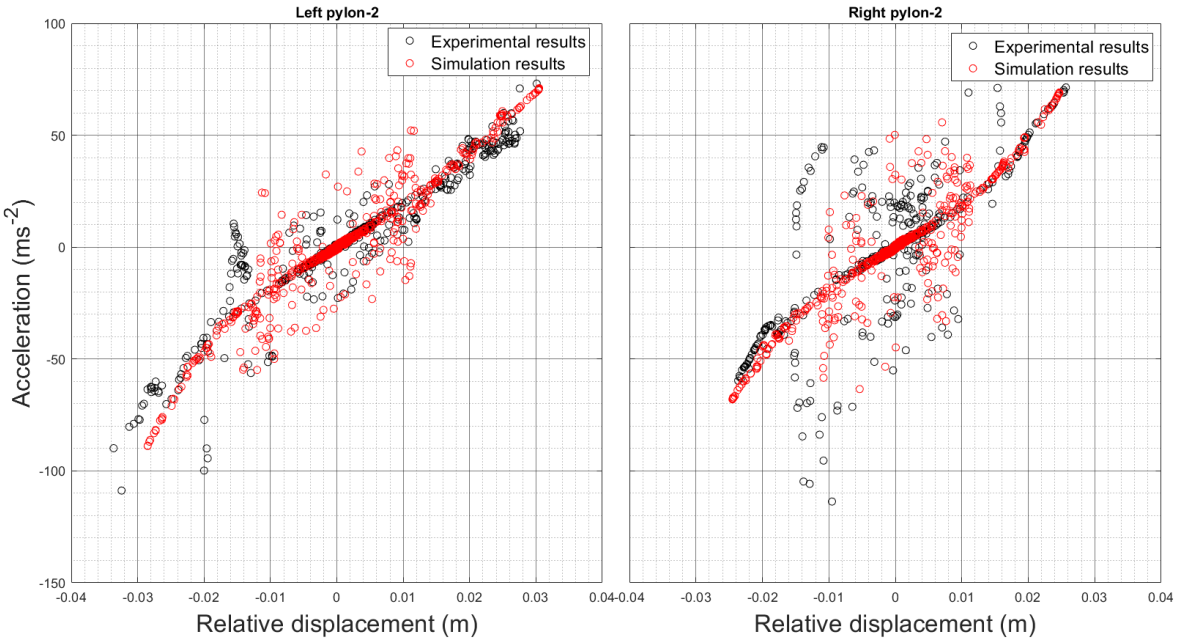


Figure 8.80: Simulated and experimental stiffness curves for *RPylon:2* and *LPylon:2* at *sweep1* with the excitation level of 0.09 V and with $\zeta_1 = 0.80\%$ and $\zeta_2 = 7.70\%$ using a polynomial stiffness

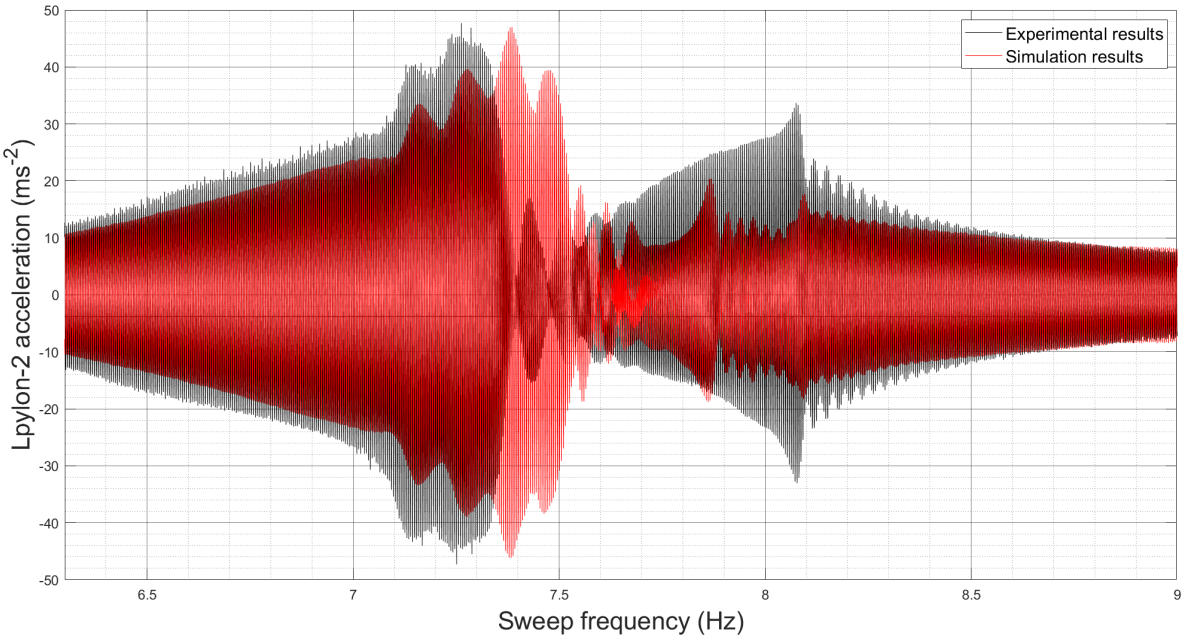


Figure 8.81: Simulated and experimental results for *LPylon:2* at *sweep2* with the excitation level of 0.04 V and with $\zeta_1 = 0.46\%$ and $\zeta_2 = 4.50\%$ using a polynomial stiffness

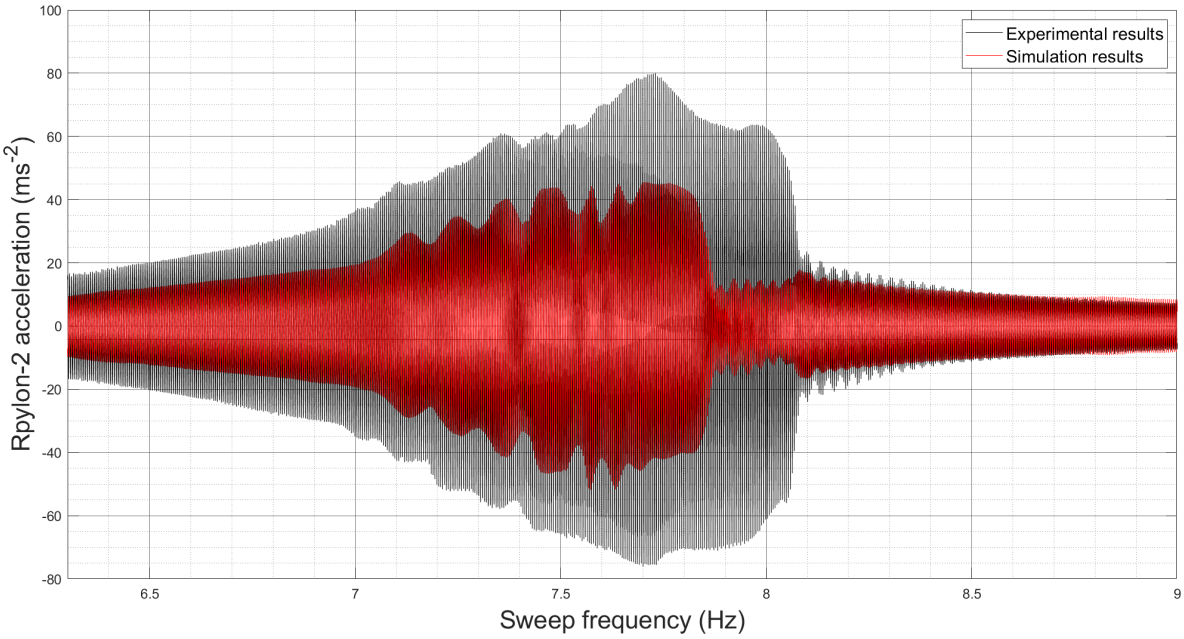


Figure 8.82: Simulated and experimental results for *RPylon:2* at *sweep2* with the excitation level of 0.04 V and with $\zeta_1 = 0.46\%$ and $\zeta_2 = 4.50\%$ using a polynomial stiffness

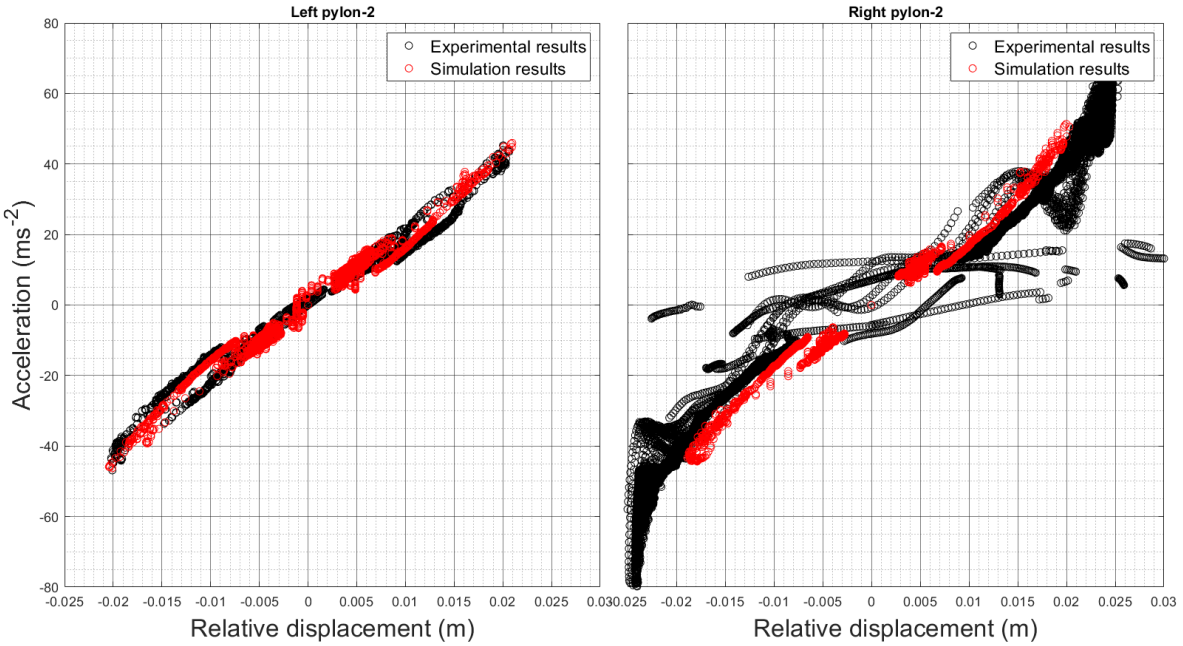


Figure 8.83: Simulated and experimental stiffness curves for *RPylon:2* and *LPylon:2* at *sweep2* with the excitation level of 0.04 V and with $\zeta_1 = 0.46\%$ and $\zeta_2 = 4.50\%$ using a polynomial stiffness

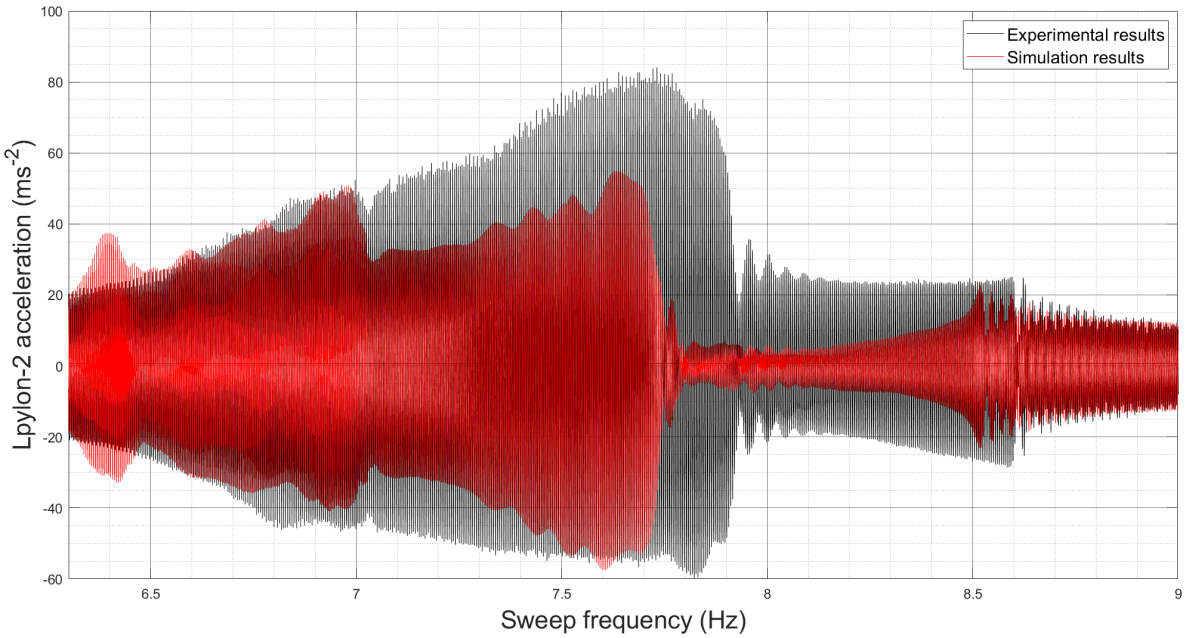


Figure 8.84: Simulated and experimental results for *LPylon:2* at *sweep2* with the excitation level of 0.06 V and with $\zeta_1 = 0.65\%$ and $\zeta_2 = 5.90\%$ using a polynomial stiffness

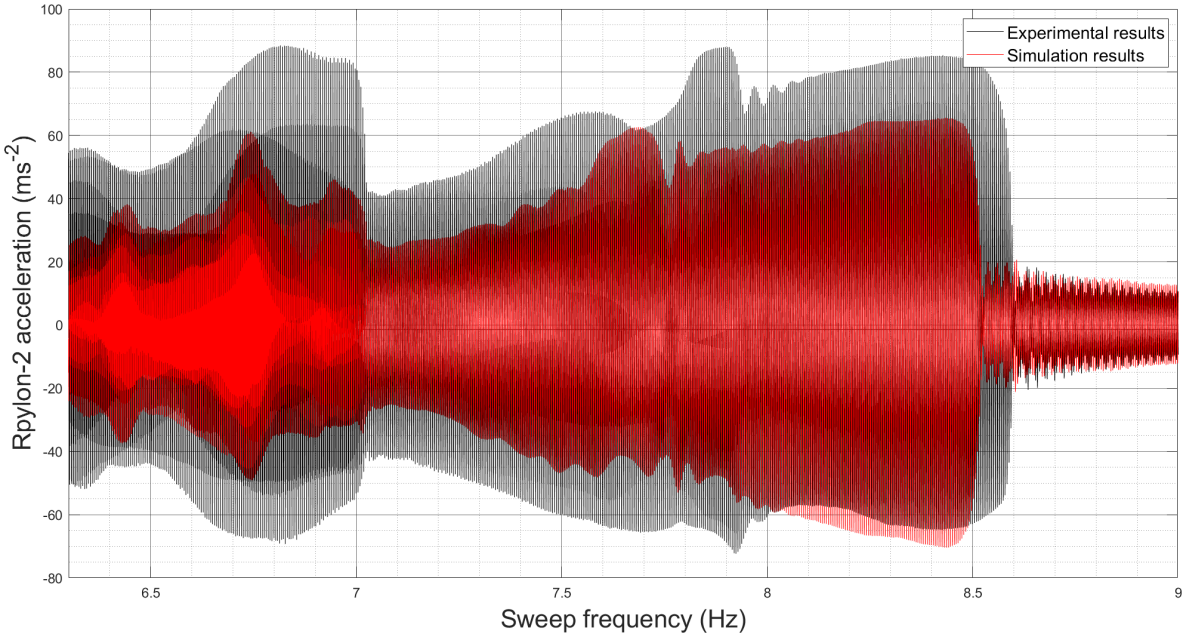


Figure 8.85: Simulated and experimental results for *RPylon:2* at *sweep2* with the excitation level of 0.06 V and with $\zeta_1 = 0.65\%$ and $\zeta_2 = 5.90\%$ using a polynomial stiffness

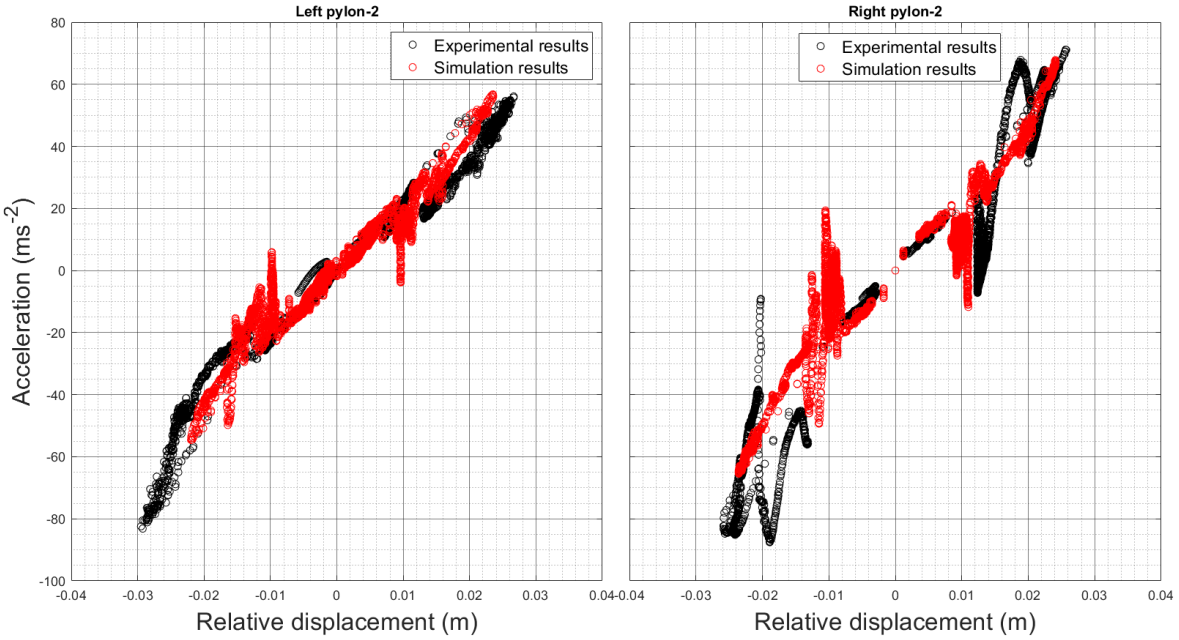


Figure 8.86: Simulated and experimental stiffness curves for *RPylon:2* and *LPylon:2* at *sweep2* with the excitation level of 0.06 V and with $\zeta_1 = 0.65\%$ and $\zeta_2 = 5.90\%$ using a polynomial stiffness

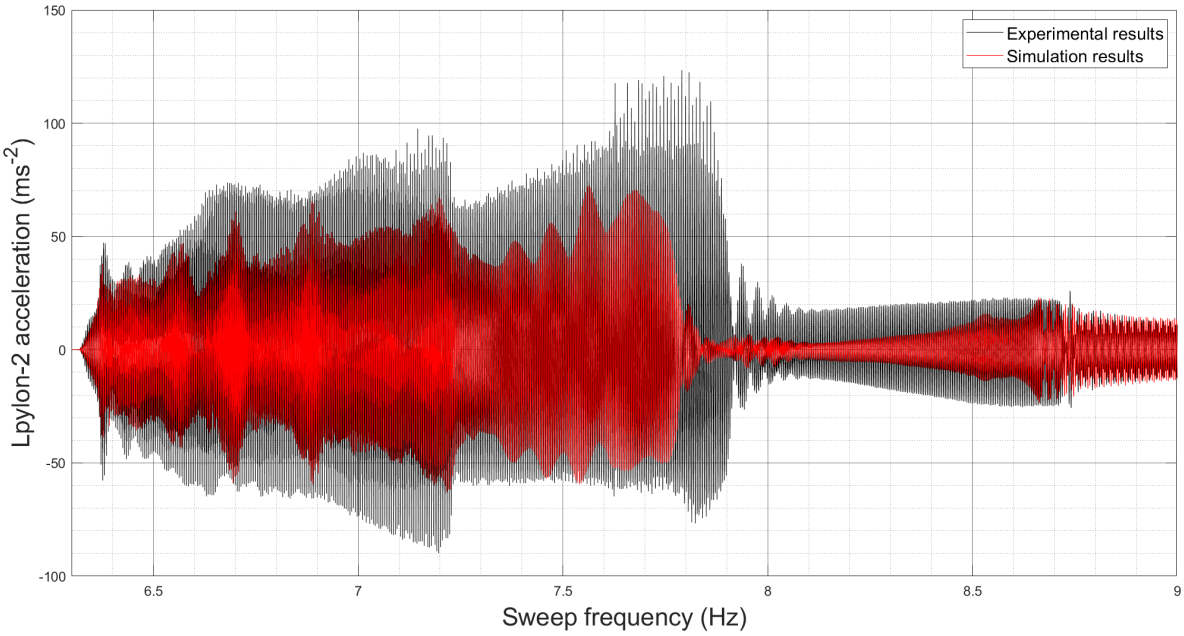


Figure 8.87: Simulated and experimental results for *LPylon:2* at *sweep2* with the excitation level of 0.07 V and with $\zeta_1 = 0.65\%$ and $\zeta_2 = 5.90\%$ using a polynomial stiffness

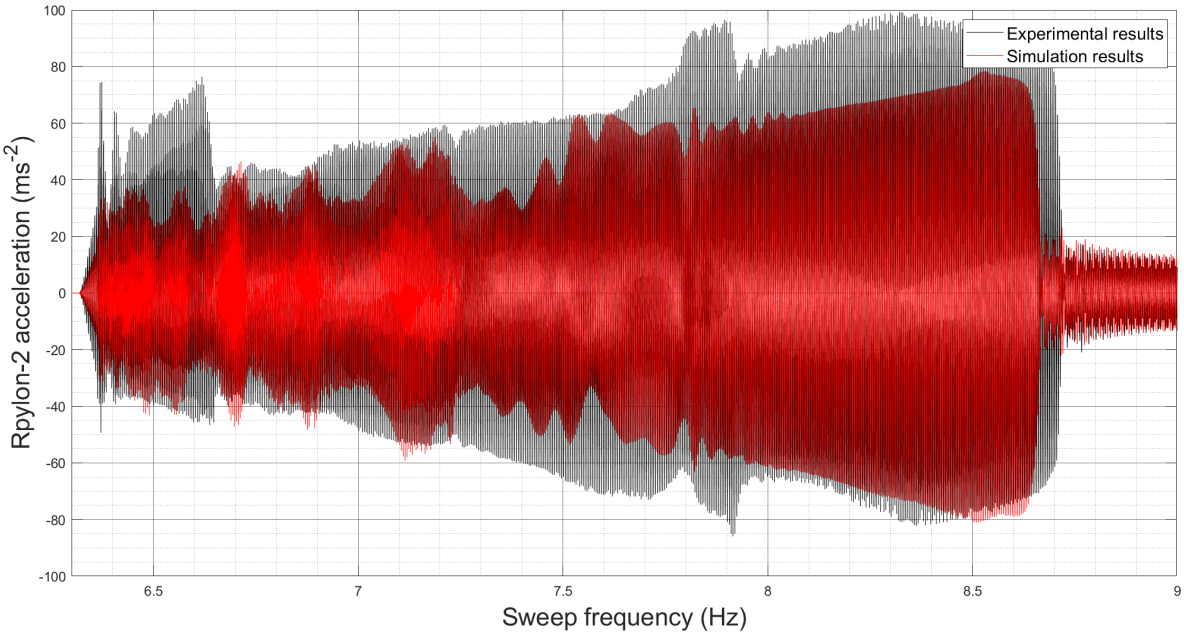


Figure 8.88: Simulated and experimental results for *RPylon:2* at *sweep2* with the excitation level of 0.07 V and with $\zeta_1 = 0.65\%$ and $\zeta_2 = 5.90\%$ using a polynomial stiffness

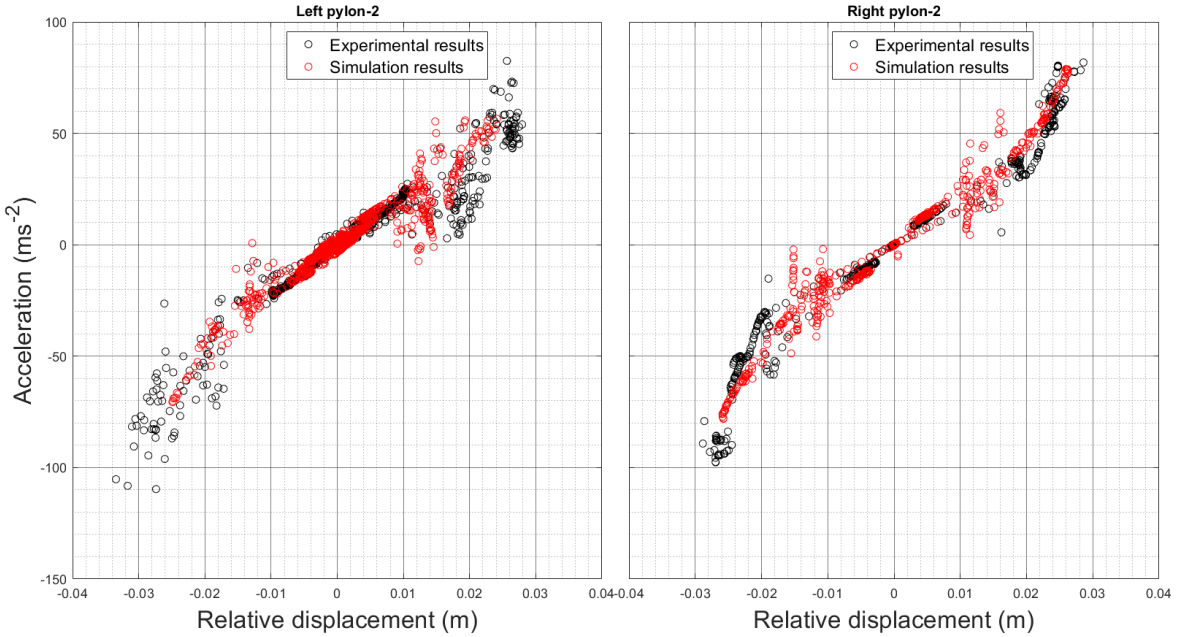


Figure 8.89: Simulated and experimental stiffness curves for *RPylon:2* and *LPylon:2* at *sweep2* with the excitation level of 0.07 V and with $\zeta_1 = 0.65\%$ and $\zeta_2 = 5.90\%$ using a polynomial stiffness

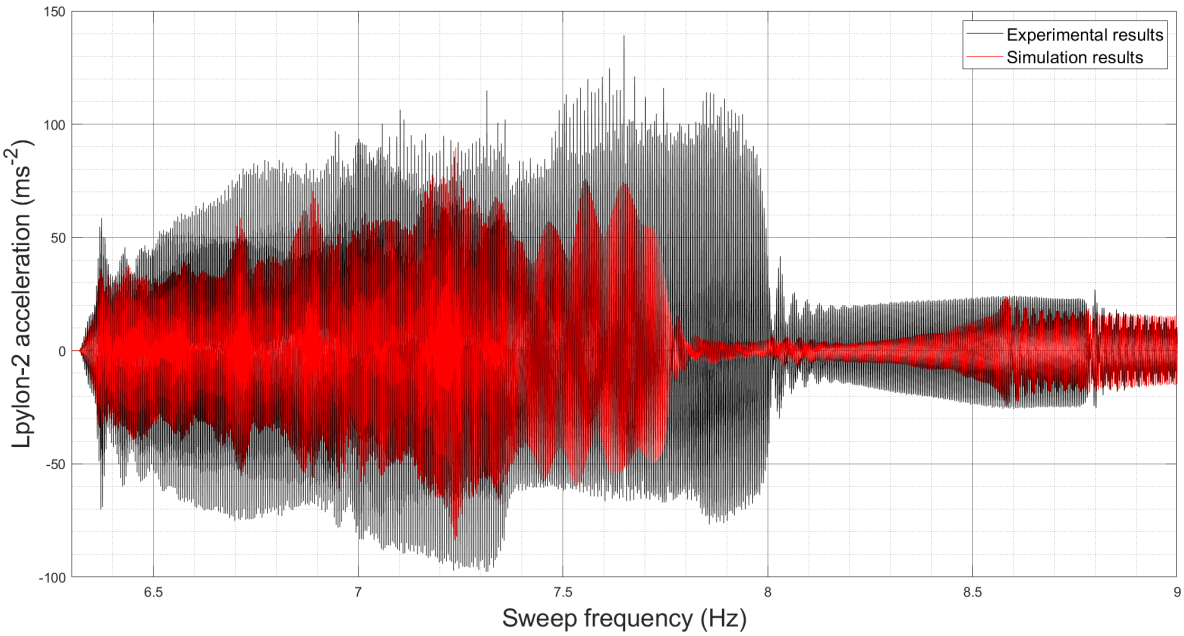


Figure 8.90: Simulated and experimental results for *LPylon:2* at *sweep2* with the excitation level of 0.08 V and with $\zeta_1 = 0.75\%$ and $\zeta_2 = 6.90\%$ using a polynomial stiffness

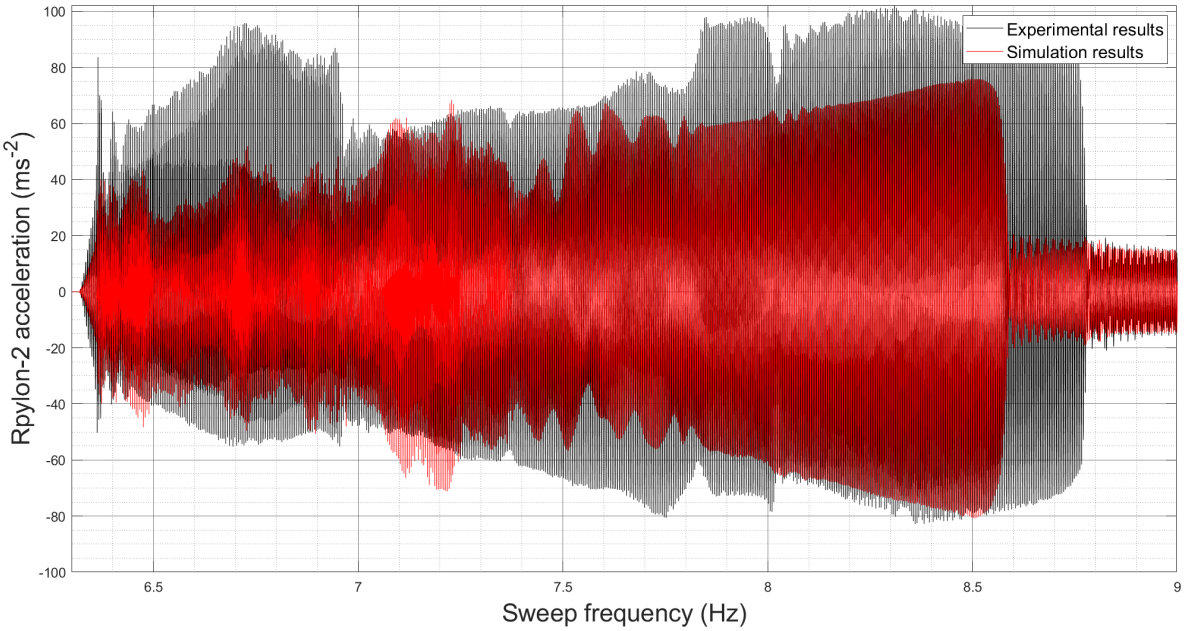


Figure 8.91: Simulated and experimental results for *RPylon:2* at *sweep2* with the excitation level of 0.08 V and with $\zeta_1 = 0.75\%$ and $\zeta_2 = 6.90\%$ using a polynomial stiffness

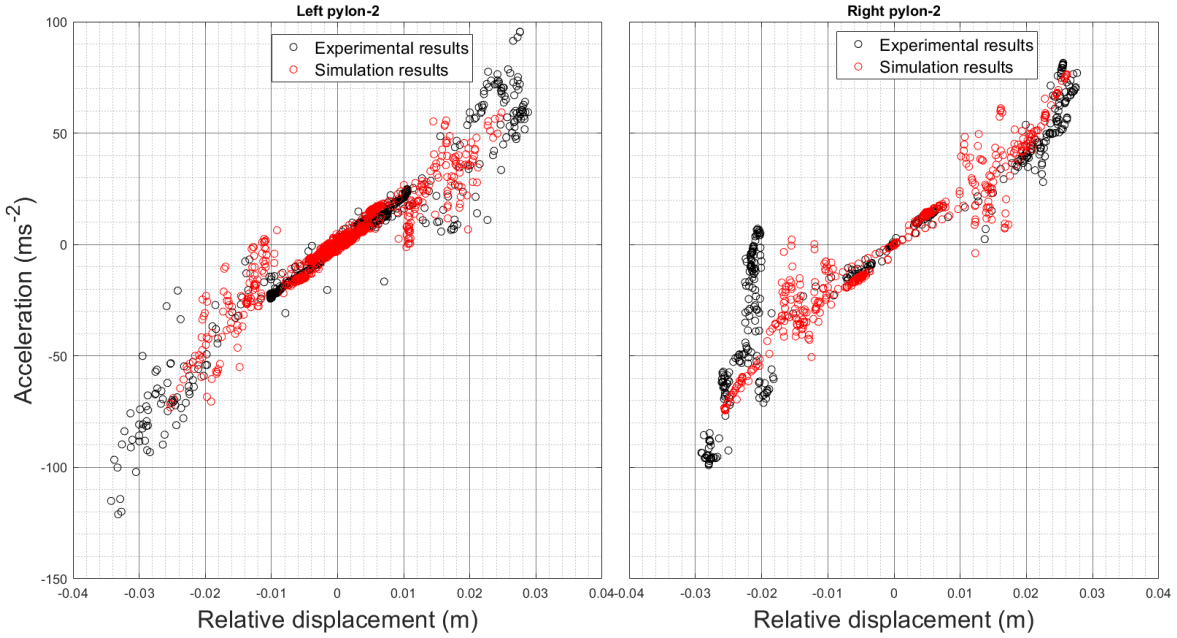


Figure 8.92: Simulated and experimental stiffness curves for *RPylon:2* and *LPylon:2* at *sweep2* with the excitation level of 0.08 V and with $\zeta_1 = 0.75\%$ and $\zeta_2 = 6.90\%$ using a polynomial stiffness

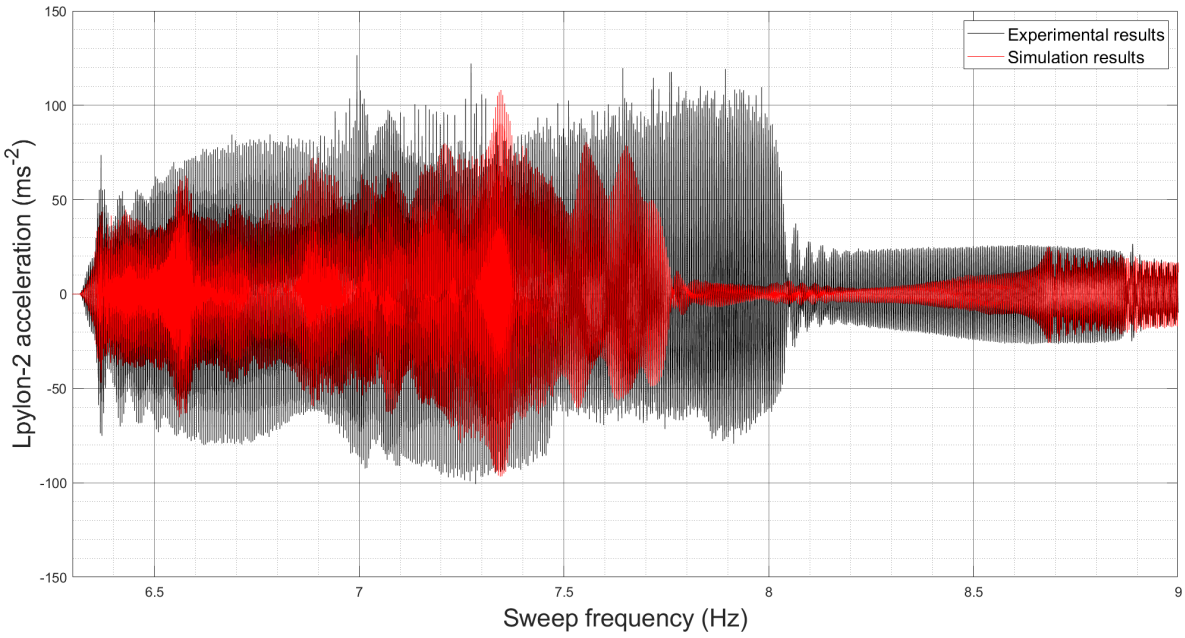


Figure 8.93: Simulated and experimental results for *LPylon:2* at *sweep2* with the excitation level of 0.09 V and with $\zeta_1 = 0.80\%$ and $\zeta_2 = 7.70\%$ using a polynomial stiffness

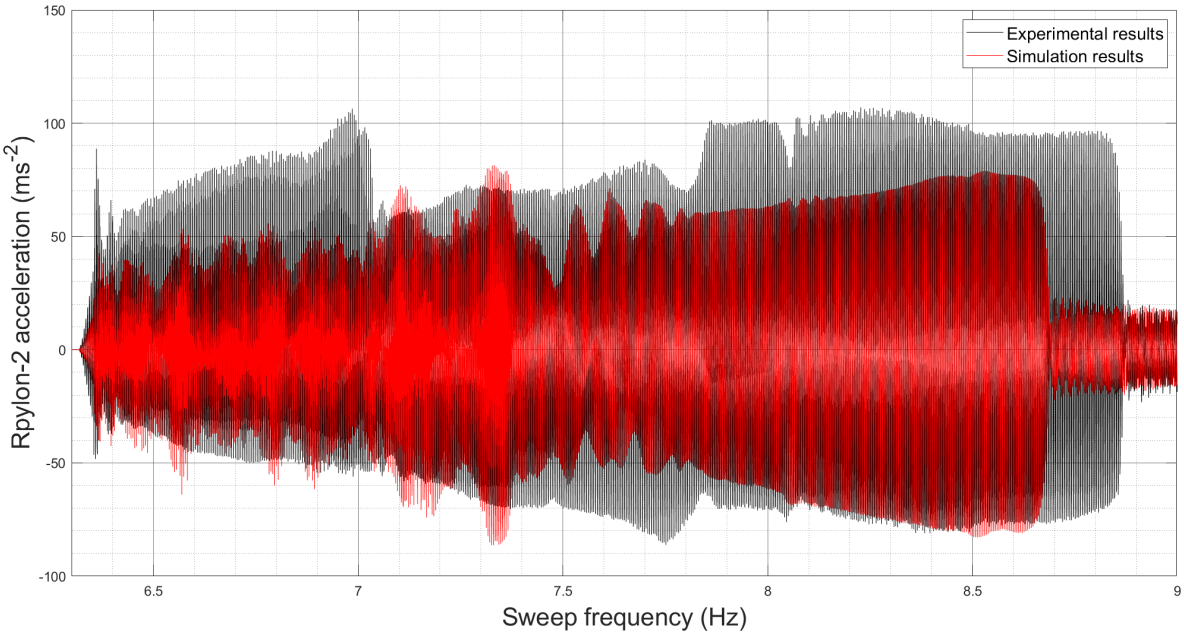


Figure 8.94: Simulated and experimental results for *RPylon:2* at *sweep2* with the excitation level of 0.09 V and with $\zeta_1 = 0.80\%$ and $\zeta_2 = 7.70\%$ using a polynomial stiffness

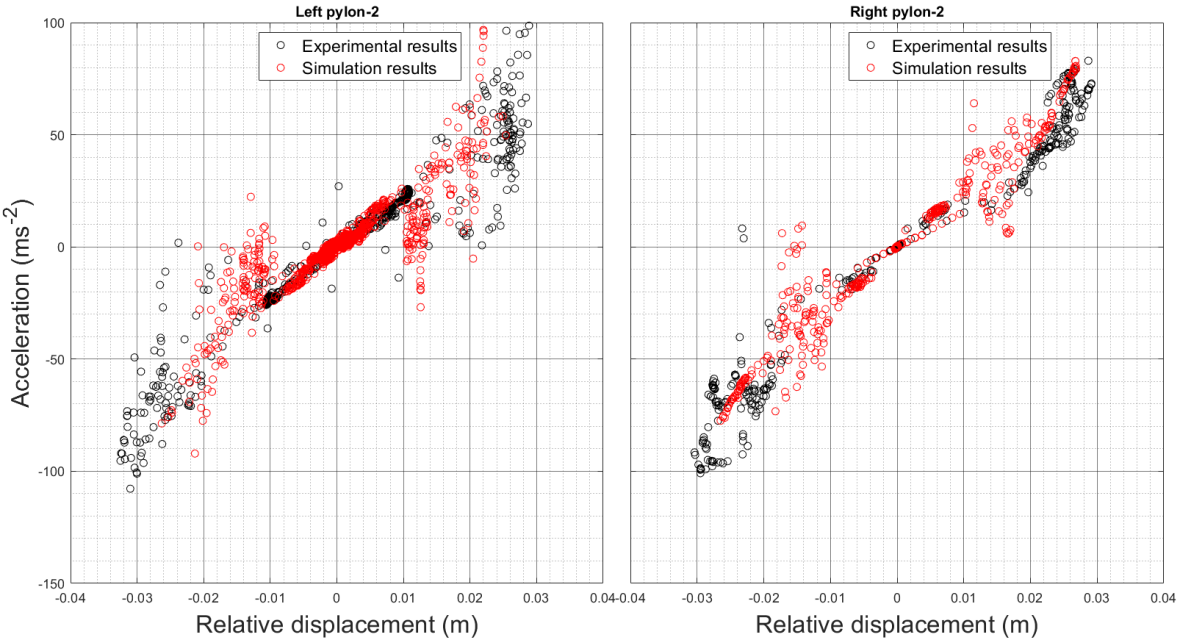


Figure 8.95: Simulated and experimental stiffness curves for *RPylon:2* and *LPylon:2* at *sweep2* with the excitation level of 0.09 V and with $\zeta_1 = 0.80\%$ and $\zeta_2 = 7.70\%$ using a polynomial stiffness

8.2.3 Piecewise stiffness

To exemplify the utilization of this option, the results for *sweep1* at 0.06 V, with the same damping values used with the cubic stiffness, are presented at fig. 8.96 and 8.97.

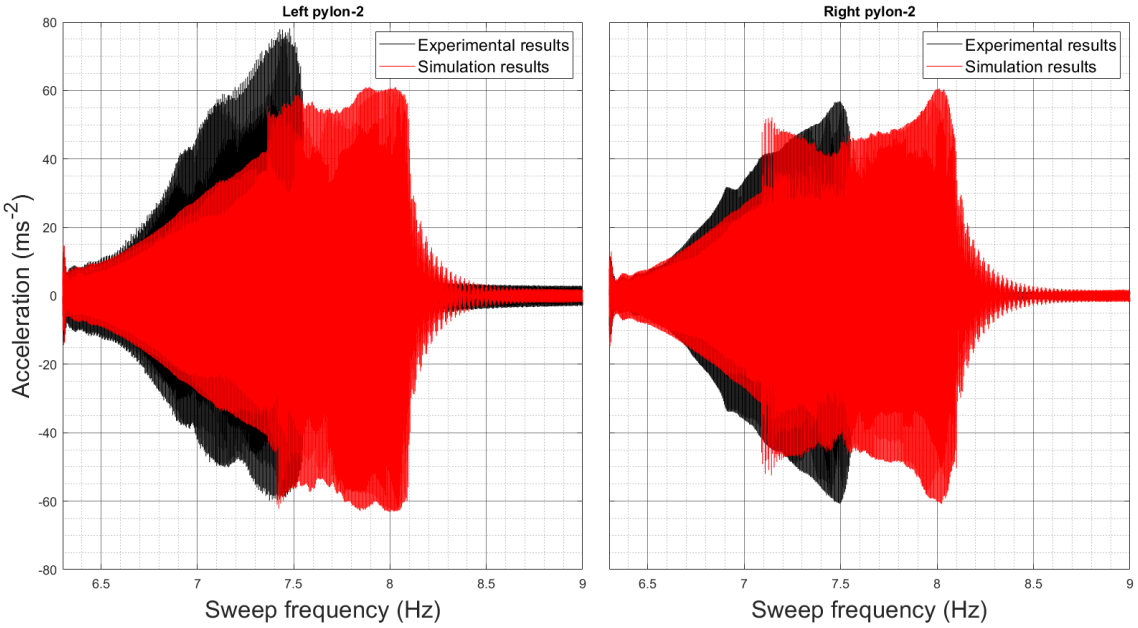


Figure 8.96: Simulated and experimental results for *LPylon:2* and *RPylon:2* at *sweep1* with the excitation level of 0.06 V and with $\zeta_1 = 0.73\%$ and $\zeta_2 = 5.50\%$ using a piecewise stiffness

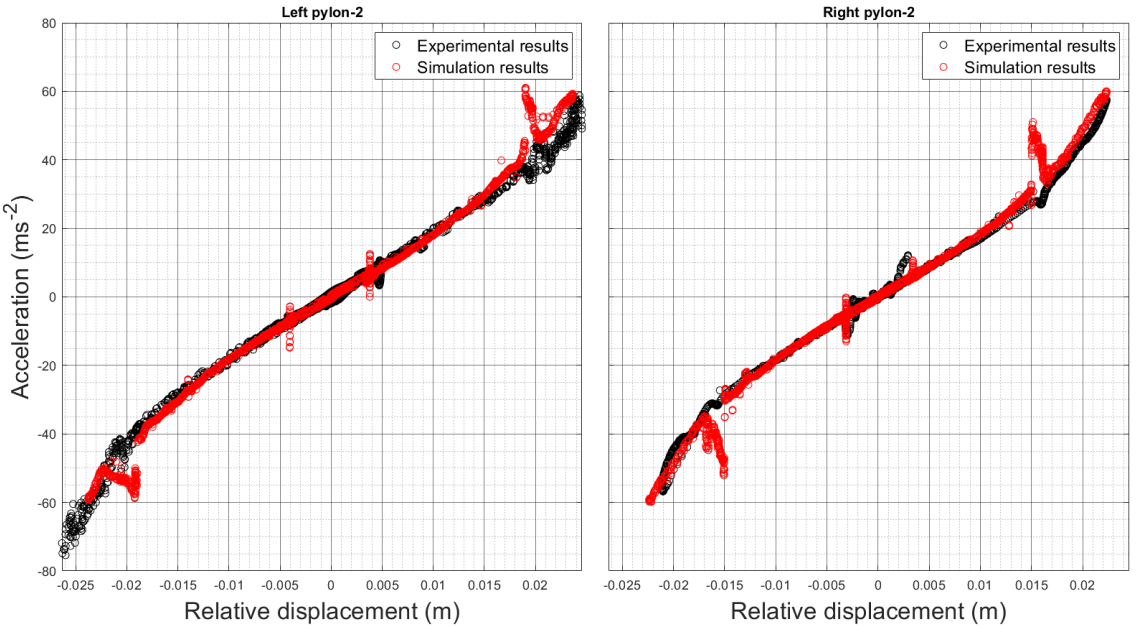


Figure 8.97: Simulated and experimental stiffness curves for *RPylon:2* and *LPylon:2* at *sweep1* with the excitation level of 0.06 V and with $\zeta_1 = 0.73\%$ and $\zeta_2 = 5.50\%$ using a piecewise stiffness

This way of modelling the stiffness was not very explored due to problems in getting a continuous stiffness curve (fig. 8.97) and because of the appearing of "strange jumps" generated in regions where they should not happen (fig. 8.96). On those plots a cubic function was considered in the linear region to attempt to improve the results and maybe allow a better continuity, but it revealed to be useless.

8.3 Conclusions on the structural model updating

Looking at the results obtained at this chapter it is safe to say that the construction of the hybrid linear nonlinear model was well succeed or otherwise it would not have been possible to reproduce the input stiffness curve values, and to have simulation times of 25s to 500.000 time iterations, which reveals that the concept utilized on this thesis was a success. It is true that for *sweep2* the results were not that good, but it was possible to replicate the stiffness curve and the shape of acceleration plots, which certainly deny any suspicions about the linear part of the model. Moreover, if it was possible to replicate the shape of the acceleration plots, maybe this means that the cause of the less good results is indeed the damping. Damping revealed to be a great obstacle not only because prevented the obtention of better results but also because the system revealed a big sensitivity to the damping values, which is easily explained for their low values and by the fact that the simulated area is in the region of two resonances, which means that any small increase can cause big variations. Additionally the damping also defines the phase answer of the modes and if the modes phase are not well related, bad results are obtained. Dozens or even hundreds of simulations were made to get the presented results.

The increase in damping values with the excitation force, is certainly related with the structure itself, but the plastic stingers that connect the shakers to the airplane may have had also some influence because they are made of plastic and for that reason they are not very stiff, and their deformation may induce some additional damping. In a normal procedure, stingers with different lengths and materials are tested, but like it was told, a linear validated finite element model of the airplane without the pylons was provided by the company from a previous work done by a student, and in the validation of that model these stingers were used during the experiments, and for that reason it was decided to also use them at this work, because if in the validation done in that previous work no problems occurred, there is no reason to use different stingers. But since higher excitation levels were applied, it is possible that the stingers that revealed to be good for linear excitation levels may not be good enough for nonlinear excitation levels.

A detail that is still need to be clarified is the nature of the nonlinearity, which considering the simulations, it can be declared with a high probability, that it is not cubic, or otherwise it is a very big coincidence that with the consideration of the polynomial stiffness the asymmetric accelerations and displacements were so well reproduced. But at the same time with the curve fitting operations, when considering the cubic stiffness, the natural frequency of the pylon was returned automatically by the software. To finalise there are some open questions for which a answer is not known:

- On *sweep1* what is that first "jump" around 6.8-6.9 Hz that appear specially at 0.08 and 0.09 V?
- If a nonlinear damping exists, why it wasn't detected at acceleration surface method? (Probably because it is really low and difficult to visualize nonparametrically...)

- Why 0.04 V curve doesn't follow the same evolution of the others excitation levels on the FRF plot of the fig. 8.26?

CHAPTER 9

Conclusion

Regarding the challenge "linear dynamics" and "nonlinear dynamics" the main goal leading to the start of this work was to make the linear finite element model of the airplane capable of simulate and predict nonlinear answers and simultaneously assure a low computational cost. To achieve that goal two main topics were studied, the Structural Model Updating and the Model Order Reduction techniques. The main conclusions and future works that need to be developed are addressed in the next two sections of this chapter.

9.1 Main conclusions

Regarding the process of structural model updating, on this thesis it was presented in three main chapters, one where the numerical model and experimental procedure were presented, a second one where the linear model validation and the nonlinear characterization were made, and a final one where the update itself was performed. Regarding the success of the first two chapters, whose success is associated to each other, the obtainment of a linear validated model was well succeeded, despite of the unsuccess in the validation of the modes associated to second bending mode of the pylons. But since the focus of the simulations were in the first two modal modes of the airplane, that problem ended up being irrelevant. Relatively to the characterization of the nonlinearity, this phase was only partially well succeeded, because it was not possible to do a correct characterization of the damping. Regarding the Acceleration Surface Method (presented in 2019 in [19]) that was used to do the nonlinear characterization, it is important to note that the method revealed big limitations in characterizing low damping values, that led to the non-characterization of the nonlinear damping, that like it was already indicated, it prevented the obtention of better results. Nevertheless, this method revealed to be very effective in the characterization of the nonlinear stiffness, since it was possible to witness the evolution of the stiffness curve for different excitation levels with the growing of the curve on its extremities, and moreover, the ASM was even used as a means to identify a subharmonic resonance. Relatively to the final step, the success of the update can be seen in two different perspectives, one which is related with the fact that it was possible to input with the accuracy the desired nonlinear stiffness to the model, and a second perspective that is related with the generated results, that like it was already observed, for *sweep1* good results were obtained and for *sweep2* less good results were achieved.

The second main topic of study were the Model Order Reduction techniques, that fulfilled their purpose of assure a low computational cost for the numerical model with big success, because like already pointed, it was possible to simulate 500 000 time iterations in only 25 seconds. This topic revealed to be decisive in the progress of this work, because without the reduced simulation time that this tool allowed, it would have been impossible to perform the many iterations that were made regarding the damping values of the system, and consequently achieve the results presented in this thesis. This necessity of performing many iterations also highlights the importance of doing a precise characterization of the system, not only because it saves time and allows the achievement of better results, but also because it may make the process of structural model updating a total failure, since without a reduced computational cost, the tuning that was done is not possible, and in some circumstances the generation of a reduced order model may not be possible.

There are some external influences that must be indicated, and one of them is related with a defect that was found in the connection between one of the pylons and the wing. As it can be seen in fig. 9.1 the holes are not aligned as they should be, and that might have some influence in the obtained results, and it is probably the cause of the problem in the linear modes associated to the second pylon bending mode. But the answers were simulated until 10 Hz, and considering the obtained MAC plot in model correlation, it is hard to say if it had any influence in the results presented at chapter 8. Another external variable that could also had some impact in the results is the accumulated damage in the pylons, because as it can be seen at fig. 9.1 fatigue cracks were developed. In the linear model they had no influence for sure because they were the first experiments to be done, and on the nonlinear experiments it is hard to say if it had any influence because the experimental results, as witnessed at section 7.2, present the standard evolution of a nonlinear system. Besides that, more experiments were made than the presented ones, some of them before and others after the presented nonlinear measurements, which makes even more difficult to evaluate the real impact of the crack formation. But regarding the development of the fatigue crack, it is important to have in mind that its appearance is associated to the occurrence of a softening behaviour, which according to the presented results seemed to not have happened, and due to the low thickness of the plate (1.5 mm), the crack growth, once initiated happens faster than in a thicker plate, and that was why the crack had already that size when it was detected.

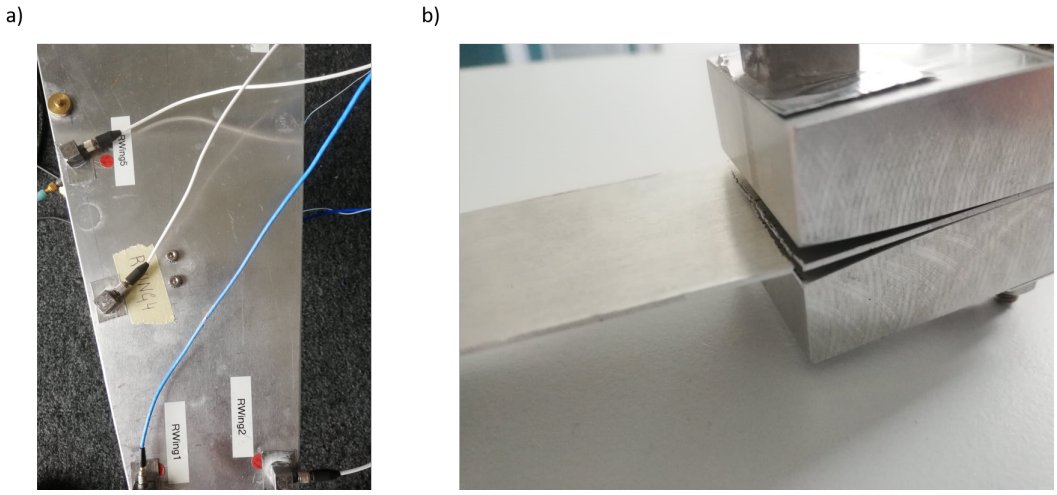


Figure 9.1: Exterior factors: a) holes misalignment; b) fatigue fracture

9.2 Future works

Concerning some of the conclusions that were made but also some additional tasks that could have been done, the following tasks could have been made to improve the quality of this work:

- The study of other techniques in order to characterize a possible nonlinear damping. With this perhaps it could have been possible to replicate perfectly the experimental results;
- The creation of a numerical tool to allow a faster tunning of the damping values, because this operation revealed to be very time consuming due to the high sensitivity of the simulations to this variable;
- The realization of simulations around 45-65 Hz to see if it is possible to predict the occurrence of the subharmonic resonance. This last task was not done because it would require the tunning of the damping on all modes used on the last chapter;
- Model the stiffness with FEM simulations;

To finalise this chapter, it can be said that all proposed goals were at least, partially achieved.

References

[1] J. J. Thomsen, *Nonlinear Vibrations: Classical Local Theory*, pp. 65–136. Berlin, Heidelberg: Springer Berlin Heidelberg, 2003.

[2] G. Kerschen, K. Worden, A. F. Vakakis, and J.-C. Golinval, "Past, present and future of nonlinear system identification in structural dynamics," *Mechanical Systems and Signal Processing*, vol. 20, no. 3, pp. 505–592, 2006.

[3] G. Kerschen, M. Peeters, J. Golinval, and A. Vakakis, "Nonlinear normal modes, part i: A useful framework for the structural dynamicist," *Mechanical Systems and Signal Processing*, vol. 23, no. 1, pp. 170–194, 2009. Special Issue: Non-linear Structural Dynamics.

[4] A. Bajaj and C. Krousgrill, "Nonlinear system resonance phenomena," in *Encyclopedia of Vibration* (S. Braun, ed.), pp. 928–943, Oxford: Elsevier, 2001.

[5] A. Haddow, "Testing, nonlinear system," in *Encyclopedia of Vibration* (S. Braun, ed.), pp. 1285–1289, Oxford: Elsevier, 2001.

[6] J. Noël and G. Kerschen, "Nonlinear system identification in structural dynamics: 10 more years of progress," *Mechanical Systems and Signal Processing*, vol. 83, pp. 2–35, 2017.

[7] J. Dias Rodrigues, "Integração directa da equação de movimento." Faculdade de Engenharia da Universidade do Porto, 2019.

[8] K.-J. Bathe, *Solution of Equilibrium Equations in Dynamic Analysis*, pp. 768–837. London, United Kingdom: Pretince-Hall, Inc., 1996.

[9] M. Géradin and D. Rixen, *Direct Time-Integration Methods*, pp. 511–576. The Atrium, SouthernGate, Chichester, West Sussex, PO19 8SQ, United Kingdom: John Wiley & Sons, Ltd, 2014.

[10] E. Chatzi, G. Abbiati, and K. Agathos, "The finite element method for the analysis of non-linear and dynamic systems: Non-linear dynamics part i." ETH Zurich, 2017.

[11] K. Wirsing, "Time frequency analysis of wavelet and fourier transform," in *Wavelet Theory* (S. Mohammady, ed.), ch. 1, Rijeka: IntechOpen, 2021.

[12] C. Rice, "Wavelets/time frequency analysis." community.sw.siemens.com/s/article/wavelets-time-frequency-analysis, Aug 2019.

[13] T. Dossogne, J.-P. Noël, C. Grappasonni, G. Kerschen, B. Peeters, J. Debille, M. Vaes, and J. Schoukens, "Nonlinear ground vibration identification of an f-16 aircraft - part ii understanding nonlinear behaviour in aerospace structures using sine-sweep testing," in *International Forum on Aeroeslasticity and Structural Dynamics*, 06 2015.

[14] M. O. Oliveira, J. H. Reversat, and L. A. Reynoso, "Wavelet transform analysis to applications in electric power systems," in *Wavelet Transform and Complexity* (D. Baleanu, ed.), ch. 5, Rijeka: IntechOpen, 2019.

[15] MathWorks, "Estimate instantaneous frequency - matlab." mathworks.com/help/signal/ref/instfreq.html, 2021.

[16] Letswave, "Chapter 1-5. time-frequency analysis." letswave.cn/tu_ch1_5.html, 2018.

[17] S. Masri and T. Caughey, "A nonparametric identification technique for nonlinear dynamic problems," *Journal of Applied Mechanics*, vol. 46, pp. 433–447, 1979.

[18] S. Sani, H. Ouyang, J. Cooper, and C. Nizwan, "Smart methodology of stiffness nonlinearity identification vibration system," in *International Conference on Mechanical Engineering Research*, 07 2013.

[19] T. Dossogne, L. Masset, B. Peeters, and J. P. Noël, "Nonlinear dynamic model upgrading and updating using sine-sweep vibration data," *Proceedings of the Royal Society A: Mathematical, Physical and Engineering Sciences*, vol. 475, no. 2229, p. 20190166, 2019.

[20] R. R. Craig Jr. and M. C. C. Bampton, "Coupling of substructures for dynamic analyses," *AIAA Journal*, vol. 6, no. 7, pp. 1313–1319, 1968.

[21] R. R. Craig Jr. and C. J. Chang, "A review of substructure coupling methods for dynamic analysis," tech. rep., National Aeronautics and Space Administration. NASA Technical Reports Server: NTRS, 1976.

[22] R. R. Craig Jr., "On the use of attachment modes in substructure coupling for dynamic analysis," in *18th Structural Dynamics and Materials Conference*, pp. 89–99, 03 1977.

[23] R. R. Craig Jr., "A review of time-domain and frequency-domain component mode synthesis methods," *International Journal of Analytical and Experimental Modal Analysis*, vol. 2, no. 2, pp. 59–72, 1987.

[24] R. Rodriguez Sanchez, M. Buchschmid, and G. Müller, "Model order reduction in structural dynamics," in *European Congress on Computational Methods in Applied Sciences and Engineering*, pp. 4221–4247, 06 2016.

[25] R. R. Craig Jr. and C. J. Chang, "Substructure coupling for dynamic analysis and testing," tech. rep., National Aeronautics and Space Administration. NASA Technical Reports Server: NTRS, 1977.

[26] A. Borzacchiello, "An engineering approach to identify and model localized nonlinearities in structural dynamics." University of Trieste, 2018.

[27] W. Heylen, S. Lammens, and P. Sas, *Modal Analysis Theory and Testing*. Katholieke Universteit Leuven, Departement Werktuigkunde; Leuven, 2000.

[28] S. Vettori, E. D. Lorenzo, B. Peeters, and A. Carcaterra, "Development and validation of data processing techniques for aircraft ground vibration testing," in *Topics in Modal Analysis & Testing, Volume 8* (M. L. Mains and B. J. Dilworth, eds.), (Cham), pp. 225–236, Springer International Publishing, 2020.

[29] P. Schaldenbrand, "Getting started with modal curvefitting." community.sw.siemens.com/s/article/getting-started-with-modal-curvefitting, Aug 2020.

[30] G. Kerschen, J.-C. Golinval, and K. Worden, "Theoretical and experimental identification of a non-linear beam," *Journal of Sound and Vibration*, vol. 244, no. 4, pp. 597–613, 2001.

[31] Y. Zhu, W. Jiang, X. Kong, Z. Zheng, and H. Hu, "An accurate integral method for vibration signal based on feature information extraction," *Shock and Vibration*, vol. 2015, pp. 1–13, 2015.

[32] NationalInstruments, "Filter specifications (digital filter design toolkit)." zone.ni.com/reference/en-XX/help/371325F-01/lvdfdtconcepts/dfd_filter_spec/, 2011.